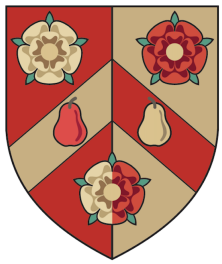


Sensitive External Quantum Efficiency Measurements for Studying Charge Transfer in Organic Solar Cells

Anna Jungbluth

Wolfson College



University of Oxford

A thesis submitted for the degree of

Doctor of Philosophy

Trinity 2022

This thesis is dedicated to my grandparents,
Opa Alfred, Oma Annemie, Opa Horst, and Oma Anni,
who taught me that hard work always pays off.

Acknowledgements

This thesis is the culmination of 5 wonderful (and demanding) years in Oxford. I would first like to thank my supervisor, Prof. Moritz Riede, for his guidance and support throughout my PhD. I am especially thankful for the encouragement and freedom to explore interests outside of my research (and that he allowed me to pause my PhD and go to California for the internship of a lifetime.) Secondly, I would like to thank Dr. Pascal Kaienburg for the invaluable discussions, feedback, and support over the last years. My research (and this thesis) would not be same without it. Thanks to my friends and colleagues in the AFMD group, especially Dr. Alberto Privitera for fruitful collaborations and for sharing his enthusiasm for EPR spectroscopy with me, and Andreas E. Lauritzen for his friendship and for keeping his snack drawer stocked. My time at work was made immensely more enjoyable by the wonderful people around me, especially Laura, Melissa, Robbie, Augustin, Mike, and Leo, just to name a few. A very special thank you goes to my dear friend, role model, and future Prof. Alex Ramadan. Her passion for research and her drive to make Physics more welcoming and inclusive is truly inspiring. Outside of my research in Oxford, I would like to thank the Frontier Development Lab, and especially my friend and mentor Dr. Andrés Muñoz-Jaramillo, for helping me grow as a leader. After a brief 6 months in College accommodation, I was fortunate to find the most wonderful housemates, April, Emily, Frankie, Maria, and Sasheenie, who made me feel truly at home in the UK. Thank you for all the house dinners, weekend walks, and evening chats to take my mind off work. I would also like to thank my friends from Cowleyfornia, Sofia, Caroline, KC, James, Maarten, and Vangelis, for the many burger Mondays, College balls, Greece holidays, and generally wonderful times in Oxford. Thank you to my Hackathon team, Amy, Odhran, Robin, and Vid, for the many shared adventures, and thanks to my wonderful friend Julianne for supplying me with photos of her puppy. While I inevitably can't name everyone in these acknowledgements, I am hugely grateful for the wonderful people I have met in Oxford over the last 5 years, and the friendships that have lasted from my time at MIT, especially with the Party Lounge and my Fantastic Five. Finally, I would like to thank my partner and best friend Sam for always being by my side, and my family, especially my parents, grandparents, and my sister, for their love and support in helping me reach this milestone. None of this would have been possible without them.

Abstract

Charge transfer (CT) states, which form at the interface between donor and acceptor molecules in organic solar cells (OSCs), strongly influence device performance, in particular the open-circuit voltage and the photogeneration of free charges. However, the connection between molecular properties, the resulting energetics at the donor-acceptor interface, and ultimately device performance is still incompletely understood. To address this knowledge gap, this thesis studies the impact of (1) molecular energy levels and donor:acceptor mixing ratios on exciton separation, and (2) blend morphologies on interfacial energetic disorder and voltage losses. CT state properties are studied via a custom-built sensitive external quantum efficiency (EQE) setup and fit from the resulting spectra. In the first part of this thesis, we establish a reliable and reproducible fitting methodology that considers both singlet and CT state absorption contributions in the EQE. We first apply this methodology to study the impact of molecular energy levels on exciton separation in low donor content blends of ZnPc or its fluorinated derivatives (F_xZnPc, with $x = 0, 4, 8, 16$) and C_{60}. We find that the fluorination-induced shifts of the donor energy levels result in an increasing CT state energy with C_{60} and a decreasing offset between local excitation (LE) and CT states. Through in-depth characterization of molecular and blend energy levels, we draw a comprehensive picture of how LE, CT, and charge separated (CS) energy levels and the energetic transitions between states change upon fluorination of ZnPc. We find that the CT $\rightarrow$ CS transition presents a major bottleneck for free charge generation in the low offset F_8ZnPc and F_{16}ZnPc blends. This study is further extended beyond the low donor content blends by gradually varying the donor:acceptor mixing ratio from neat F_xZnPc to neat C_{60}. We find that with increasing F_8ZnPc or F_{16}ZnPc content, the CT dissociation efficiency is further reduced, leading to very low photocurrents in these blends. The dependence of CT dissociation on donor concentration is attributed to charge-quadruple induced electrostatic shifts, caused by the positive quadrupole moments of F_8ZnPc/F_{16}ZnPc, which increase the CT dissociation barrier with increasing donor content. In comparison, ZnPc/F_4ZnPc, which have negative quadrupole moments, experience the opposite electrostatic shifts and show efficient CT dissociation across all donor:C_{60} mixing ratios. These results not only motivate further studies of the CS state, but also show that improving the CT $\rightarrow$ CS transition, for instance via the design of molecules with suitable quadrupole moments, is an effective route for increasing the

photocurrents of OSCs. Finally, we study the impact of interfacial energetic disorder on device performance and voltage losses for five small molecule donor:C_{60} systems. Through temperature-dependent EQE measurements, we disentangle the contributions of static (i.e. temperature independent) and dynamic (i.e. temperature-dependent) disorder. Contrary to what is often stated for evaporated blends of small molecules, static disorder is found to be significant, and often exceed the contribution of dynamic disorder in the CT linewidth. This motivates future studies of interfacial disorder in OSCs, linking bulk and interface morphologies to device performance, and finding ways to reduce disorder to decrease voltage losses.

Table of Contents

Publication List i

1 Introduction **1**

1.1 Climate Change & Renewable Energies 1

1.2 Opportunities & Challenges of OPV 2

1.3 Thesis Outline 3

2 The Physics of Organic Solar Cells **5**

2.1 Organic Semiconducting Molecules 6

2.1.1 Orbitals & Energy Levels 6

2.1.2 Optoelectronic Transitions 7

2.2 Organic Molecular Solids 13

2.2.1 Polarization & Electrostatic Effects 13

2.2.2 Excitons 15

2.3 Working Principles of Organic Solar Cells 16

2.3.1 The Donor-Acceptor Concept 16

2.3.2 Charge Generation & Recombination 18

2.3.3 Current Density-Voltage Characteristics 21

2.3.4 Reciprocity 23

2.3.5 Voltage Losses 25

2.3.5.1 Reference Energies 25

2.3.5.2 Radiative Limit 26

2.3.5.3 Voltage Losses - Detailed Balance Picture 28

2.3.5.4 Voltage Losses - Energetic State Picture 29

3 The Physics of Charge Transfer States **32**

3.1 Marcus Theory 33

3.1.1 Charge Transfer Events & Transition Rates 33

3.1.2 Determination of CT State Properties 38

3.1.3 Static & Dynamic Disorder 40

3.1.4 Limitations of Classical Marcus Theory 41

3.1.4.1 Interference Effects . . . 41
3.1.4.2 Low Offset Systems . . . 43
3.2 Marcus-Levich-Jortner Theory . . . 45
3.2.1 Phonon Modes & Transition Rates . . . 45
3.2.2 CT State Properties in the MLJ Framework . . . 47
3.2.3 Multiple Phonon Modes . . . 48
3.3 Sources of Spectral Broadening . . . 49
3.4 Three-State Models . . . 52
3.4.1 Diabatic vs. Adiabatic States . . . 53
3.4.2 CT State Modeling using Three-State Approaches . . . 53
3.5 Discussion of Advanced CT State Models . . . 54

4 Materials & Methods 60
4.1 Materials . . . 61
4.2 Sample Fabrication . . . 63
4.2.1 Vacuum Thermal Deposition . . . 63
4.2.2 Device Architectures . . . 64
4.3 Thin Film Characterization . . . 66
4.3.1 Absorption Measurements . . . 66
4.3.2 Spectroscopic Ellipsometry . . . 66
4.3.3 Electron Paramagnetic Resonance Spectroscopy . . . 66
4.3.4 Grazing Incidence Wide Angle X-Ray Scattering . . . 68
4.4 Device Characterization . . . 70
4.4.1 Current Density-Voltage Measurements . . . 70
4.4.2 Mismatch Correction . . . 70
4.4.3 External Quantum Efficiency Measurements . . . 71
4.4.3.1 Room Temperature Measurements . . . 71
4.4.3.2 Temperature-Dependent Measurements . . . 71
4.5 Computational Methods . . . 72
4.5.1 Transfer Matrix Modelling . . . 72
4.5.2 Density Functional Theory . . . 72

5 Sensitive External Quantum Efficiency Measurements & Analysis 74
5.1 Measurement Setup . . . 75
5.2 Measurement Control Software . . . 78
5.3 Charge Transfer State Analysis . . . 81
5.3.1 Analysis Program . . . 81
5.3.2 Fit Example . . . 83
5.3.3 Fitting Singlet & CT State Absorption . . . 84
5.3.4 Fit Approach Comparison . . . 87

6 Charge transfer in dilute OSCs based on fluorinated ZnPc and C_{60} 90
6.1 Introduction . . . 91
6.2 Materials & Devices . . . 93
6.3 Device Performance . . . 94
6.4 Energy Levels . . . 96
6.5 Charge Separation & Recombination . . . 102
6.6 Conclusions . . . 107

7 The impact of donor concentration on the performance of OSCs based on fluorinated ZnPc and C_{60} 109
7.1 Introduction . . . 110
7.2 Materials & Devices . . . 111
7.3 Device Performance . . . 113
7.3.1 Comparison across D:C_{60} Mixing Ratios . . . 113
7.3.2 Comparison across Donor Molecules . . . 116
7.4 CT State Analysis . . . 119
7.5 Voltage Losses . . . 124
7.6 Discussion . . . 127
7.7 Conclusions . . . 129

8 The impact of static and dynamic disorder on the performance of OSCs based on dilute and intermixed D:A blends 131
8.1 Introduction . . . 132

8.2 Materials & Devices . . . 135
8.3 Device Performance . . . 137
8.4 GIWAXS Analysis . . . 140
8.5 Disorder Analysis . . . 142
8.5.1 Determination of Static & Dynamic Disorder . . . 142
8.5.2 Marcus vs. MLJ Theory . . . 144
8.5.3 Material Comparison . . . 147
8.6 Voltage Losses . . . 154
8.7 Discussion . . . 157
8.8 Conclusions . . . 159

9 Conclusions & Outlook **161**

Appendix A Appendix **195**

Appendix B Appendix **196**
B.1 GIWAXS Analysis . . . 196
B.2 DFT Calculations . . . 198
B.3 EPR Analysis . . . 203

Appendix C Appendix **206**

Appendix D Appendix **210**

List of Figures

1.1 Global CO_2 emissions & temperature anomalies . . . 2

2.1 Schematic orbital energy levels of carbon . . . 7
2.2 Schematic transitions of orbital energy levels from atoms to molecules . . . 8
2.3 Jablonski diagram of molecular energetic states . . . 9
2.4 Schematic potential energy curves of two-atomic molecules . . . 11
2.5 Schematic potential energy curves & absorption spectra with varying equilibrium reaction coordinates . . . 12
2.6 Schematic transitions of energy levels from molecules to molecular solids . . . 13
2.7 Schematic of excitons in semiconducting solids . . . 15
2.8 Schematic of molecular orbitals at the donor-acceptor interface . . . 17
2.9 Schematic of donor-acceptor heterojunctions . . . 18
2.10 Jablonski diagram of charge generation & recombination in molecular blends 20
2.11 Schematic $J - V$ curve . . . 24
2.12 Schematic of energy levels & voltage losses . . . 30

3.1 Schematic of free energy curves . . . 35
3.2 Schematic of transition rates between initial & final states . . . 37
3.3 Schematic of simulated EQE & EL spectra . . . 44
3.4 Schematic comparison of Marcus & MLJ theory . . . 50
3.5 Schematic potential energy curves of diabatic & adiabatic states . . . 53
3.6 Schematic of energetic hybridization . . . 58

4.1 Molecular structure of materials . . . 62
4.2 Schematic of the Evaporation CHamber Oxford (ECHO) . . . 64
4.3 Schematic device stack . . . 65
4.4 Schematic of Zeeman splitting . . . 67

5.1 Schematic of custom-built $sEQE$ setup . . . 75
5.2 GUI of $sEQE$ control software . . . 79
5.3 Example $sEQE$ measurement output . . . 80

5.4 GUI of $sEQE$ analysis program . . . 82
5.5 Example $sEQE$ spectra measured with different spectral filters . . . 83
5.6 Example CT state fits & heat maps . . . 85
5.7 Example CT state fits for low-offset systems . . . 86
5.8 Comparison of CT state fitting approaches . . . 88

6.1 Extinction coefficient of dilute F_xZnPc:C_{60} & neat F_xZnPc thin films . . . 93
6.2 $J-V$ & EQE characteristics of dilute F_xZnPc:C_{60} devices . . . 94
6.3 Comparison of photon absorption & EQE of dilute F_xZnPc:C_{60} . . . 96
6.4 DFT calculations of blend & molecular energy levels for F_xZnPc:C_{60} . . . 97
6.5 CT state fits of dilute F_xZnPc:C_{60} . . . 100
6.6 Three-state vibronic fits of sensitive EQE spectra . . . 101
6.7 trEPR spectra of dilute F_xZnPc:C_{60} . . . 104
6.8 Schematic of charge transition processes in dilute F_xZnPc:C_{60} . . . 106

7.1 Molecular structure & quadrupole moments of F_xZnPc & C_{60} . . . 111
7.2 Normalized absorbance of neat F_xZnPc & neat C_{60} . . . 112
7.3 $J-V$ & EQE characteristics of F_xZnPc:C_{60} devices . . . 114
7.4 $J-V$ characteristics with donor fluorination & content . . . 117
7.5 Transfer matrix modelling of the photocurrents of F_xZnPc:C_{60} . . . 119
7.6 Logarithmic EQE of F_xZnPc:C_{60} . . . 120
7.7 Example CT state fits of F_xZnPc:C_{60} . . . 121
7.8 CT state energies with donor fluorination & content . . . 122
7.9 Comparison of CT & singlet state energies with ZnPc content . . . 123
7.10 Overview of energy levels & voltage losses of F_xZnPc:C_{60} . . . 126
7.11 Impact of donor quadrupole moments on molecular energy levels . . . 128

8.1 Schematic of static & dynamic disorder . . . 133
8.2 Simulated EQE spectra with varying static & dynamic disorder . . . 134
8.3 Molecular structure & electronic quality of chosen molecules . . . 136
8.4 $J-V$ characteristics of donor:C_{60} devices . . . 138
8.5 Example CT state fits including disorder . . . 143
8.6 Schematic comparison of MLJ theory fitting parameters . . . 146

8.7 Correlation plots of Marcus vs. MLJ theory fit results 147
8.8 Normalized temperature-dependent EQE of donor:C_{60} devices 149
8.9 Gaussian variance fit results for donor:C_{60} devices 151
8.10 Static & dynamic disorder fit results for donor:C_{60} devices 152
8.11 Comparison of static disorder with donor choice and content 153
8.12 Comparison of energy levels & voltage losses with donor choice & content 156
8.13 Normalized temperature-dependent EQE of NFA blends 157
8.14 Radiative V_{oc} vs. total disorder 158

A.1 Photo of custom-built $sEQE$ setup 195

B.1 2D GIWAXS scattering of dilute F_xZnPc:C_{60} & neat F_xZnPc thin films . . . 197
B.2 trEPR spectra of neat F_xZnPc 204

C.1 Photo of the F_xZnPc:C_{60} samples 206
C.2 Spectral mismatch correction of F_xZnPc:C_{60} blends 208
C.3 Comparison of CT & singlet state energies with F_4ZnPc content 208
C.4 Comparison of CT & singlet state energies with F_8ZnPc content 209
C.5 Comparison of CT & singlet state energies with F_{16}ZnPc content 209

D.1 Photo of the disorder samples 210
D.2 2D GIWAXS scattering of dilute donor & intermixed donor:acceptor blends 213
D.3 2D GIWAXS scattering of dilute acceptor & neat donor films 214
D.4 Spectral mismatch correction of donor:C_{60} blends 215
D.5 Absorbance of neat donor films 215
D.6 Radiative V_{oc} vs. dynamic disorder 216
D.7 Radiative V_{oc} vs. static disorder 216
D.8 Radiative V_{oc} vs. CT state energy 217

List of Tables

4.1 Material properties & supplier details 61

5.1 Comparison of EQE fit results for ZnPc:C_{60} 88
5.2 Comparison of EQE fit results for F_4ZnPc:C_{60} 89

6.1 DFT calculations of singlet, triplet, & CT state energies for F_xZnPc:C_{60} . . 97
6.2 DFT calculations of CS & CT state energies for F_xZnPc:C_{60} 98
6.3 Subset of the best-fit values for trEPR analysis of dilute F_xZnPc:C_{60} 105

8.1 Summary of acceptor aggregation features as measured via GIWAXS . . . 140
8.2 Summary of donor aggregation features as measured via GIWAXS 141

B.1 DFT calculations of singlet, triplet, & CT state energies for ZnPc:C_{60} 198
B.2 DFT calculations of singlet, triplet, & CT state energies for F_4ZnPc:C_{60} . . 199
B.3 DFT calculations of singlet, triplet, & CT state energies for F_8ZnPc:C_{60} . . 200
B.4 DFT calculations of singlet, triplet, & CT state energies for F_{16}ZnPc:C_{60} . . 201
B.5 DFT calculations of molecular orbital energies for F_xZnPc & C_{60} 201
B.6 DFT calculations of dipole moments & electronic coupling for F_xZnPc:C_{60} 202
B.7 Fit parameters for three-state vibronic analysis of dilute F_xZnPc:C_{60} 202
B.8 Best-fit values for trEPR analysis of neat F_xZnPc 205
B.9 Best-fit values for trEPR analysis of dilute F_xZnPc:C_{60} 205

C.1 Device performances & energy levels of F_xZnPc:C_{60} blends 207

D.1 Electronic quality & Scharber efficiency for donor:C_{60} blends 211
D.2 Device performances & energy levels of donor:C_{60} blends 212

List of Abbreviations

A ..... Acceptor

Al ..... Aluminium

AM ..... Air Mass

a-Si ..... Amorphous Silicon

BHJ ..... Bulk Heterojunction

CdTe ..... Cadmium Telluride

CS ..... Charge Separated State

c-Si ..... Crystalline Silicon

CT ..... Charge Transfer

CT State ..... Charge Transfer State

CO_2 ..... Carbon Dioxide

D ..... Donor

DFT ..... Density Functional Theory

DOS ..... Density of States

EA ..... Electron Affinity

ECHO ..... Evaporation CHamber Oxford

E_{CT} ..... Charge Transfer State Energy

EL ..... Electroluminescence

EQE ..... External Quantum Efficiency

FC ..... Franck-Condon Factor

FF ..... Fill Factor

FRET ..... Förster Resonance Energy Transfer [GaAs] Gallium Arsenide

GHG . . . . . Greenhouse Gases

HOMO . . . . . Highest Occupied Molecular Orbital

IP . . . . . Ionization Potential

IPES . . . . . Inverse Photoemission Spectroscopy

IQE . . . . . Internal Quantum Efficiency

IR . . . . . Infrared

ISC . . . . . Inter-system Crossing

$\mathbf{J_{sc}}$ . . . . . Short-circuit Current Density

J-V . . . . . Current Density-Voltage

LUMO . . . . . Lowest Unoccupied Molecular Orbital

MLJ . . . . . Marcus-Levich-Jortner

MPP . . . . . Maximum Power Point

NFA . . . . . Non-Fullerene Acceptor

NIR . . . . . Near-Infrared

OLED . . . . . Organic Light Emitting Diode

OPV . . . . . Organic Photovoltaics

OSC . . . . . Organic Solar Cells

PCE . . . . . Photon Conversion Efficiency

PHJ . . . . . Planar Heterojunction

PL . . . . . Photoluminescence

PV . . . . . Photovoltaic

QCM . . . . . Quartz Crystal Microbalance

RT . . . . . Room Temperature

sEQE ..... Sensitive External Quantum Efficiency

SM ..... Small Molecule

SOMO ..... Single Occupied Molecular Orbital

SQ ..... Shockley-Queisser

S_0 ..... Singlet Ground State

S_1 ..... Singlet Excited State

S_n ..... n^{th} Singlet Excited State

T_1 ..... Triplet Excited State

T_n ..... n^{th} Triplet Excited State

TMM ..... Transfer Matrix Method

UPS ..... Ultraviolet Photoelectron Spectroscopy

UV ..... Ultraviolet

V_{MPP} ..... Voltage at Maximum Power Point

V_{oc} ..... Open-Circuit Voltage

XPS ..... X-Ray Photo-Electron Spectroscopy

ZFS ..... Zero Field Splitting

List of Publications

Peer-Reviewed Articles

1. A. Jungbluth, P. Kaienburg, and M. Riede, "Charge transfer state characterization and voltage losses of organic solar cells," *Journal of Physics: Materials*, vol. 5, p. 024002, Jan 2022

2. P. Kaienburg, A. Jungbluth, I. Habib, S. V. Kesava, M. Nyman, and M. Riede, "Assessing the photovoltaic quality of vacuum-thermal evaporated organic semiconductor blends," *Advanced Materials*, p. 2107584, Dec 2021

3. I. Ramirez, A. Privitera, S. Karuthedath, A. Jungbluth, J. Benduhn, A. Sperlich, D. Spoltore, K. Vandewal, F. Laquai, and M. Riede, "The role of spin in the degradation of organic photovoltaics," *Nature Communications*, vol. 12, Jan 2021

4. G. J. Moore, M. Causa', J. F. M. Hardigree, S. Karuthedath, I. Ramirez, A. Jungbluth, F. Laquai, M. Riede, and N. Banerji, "Ultrafast charge dynamics in dilute-donor versus highly intermixed TAPC:C60 organic solar cell blends," *The Journal of Physical Chemistry Letters*, vol. 11, pp. 5610–5617, Jun 2020

Conference Presentations (First Author Only)

1. A. Jungbluth, A. Privitera, E. K. Cho, P. Kaienburg, A. E. Lauritzen, S. V. Kesava, T. Derrien, J.-L. Bredas, V. Coropceanu, M. Riede, "Charge transfer processes and voltage losses of dilute solar cells based on fluorinated ZnPc," *International Workshop on Charge Transport and Excited State Processes in Organic Materials (IWOM)*, 2021, London, UK. **(Oral Presentation)**

2. A. Jungbluth, P. Kaienburg, A. E. Lauritzen, M. Riede, "Charge Transfer States and Reorganization Energies of Organic Solar Cells as a Function of Electron Donor Concentration," *Materials Research Society (MRS) Fall Meeting*, 2019, Boston, USA. **(Poster Presentation)**

3. A. Jungbluth, G. Moore, A. Privitera, I. Ramirez, J. Hardigree, M. Causa', N. Banerji, M. Riede, "Charge generation and recombination in dilute organic solar cells," *Materials Research Society (MRS) Fall Meeting*, 2018, Boston, USA. **(Oral Presentation)**

1 | Introduction

1.1 Climate Change & Renewable Energies

Anthropogenic climate change presents one of the biggest challenges of the 21st century. The increased emission of greenhouse gases (GHG) like carbon dioxide (CO_2; Figure 1.1a) that arose with societal industrialization has caused a rise in global averages temperatures and severe temperature anomalies (Figure 1.1b). Without a rapid decrease in GHG emissions to net zero, temperatures are projected to continue rising, threatening life on Earth as we know it [5]. Extreme weather events, biodiversity loss, and forced migration are only some of the adverse consequences of global warming and climate change.

In 2016, more than 73% of GHG emissions came from the energy sector (i.e. electricity, heat, and transportation) [6]. Renewable energy resources (like solar, wind, and hydro energy) are crucially important for helping us transition away from the burning of fossil fuels and reach climate targets like the Paris Agreement [7] that aim to limit global warming to $< 2°C$ compared to pre-industrial levels. Especially the direct use of solar energy is an attractive choice since radiation from the Sun is extremely abundant. In fact, enough solar radiation reaches the Earth each hour to cover our global annual energy demand [8].

Solar energy is classified into two categories, i.e. solar thermal energy, which captures the Sun's heat for indirect electricity generation and heat transfer, and solar photovoltaic (PV) energy, which directly converts solar radiation into electricity via the absorption of photons. As of 2020, 95% of PV production was dominated by crystalline Silicon (c-Si) [9], followed by other inorganic materials like amorphous silicon (a-Si), cadmium telluride (CdTe), and gallium arsenide (GaAs). Over the last decades, silicon solar cells reached $> 25\%$ efficiencies of converting sunlight into electricity under laboratory conditions [10], with commercial modules reaching $\geq 20\%$. Increased efficiencies, coupled with the decreasing cost of silicon, and expanded manufacturing capabilities have recently led to silicon PV producing the cheapest electricity recorded in history [11].

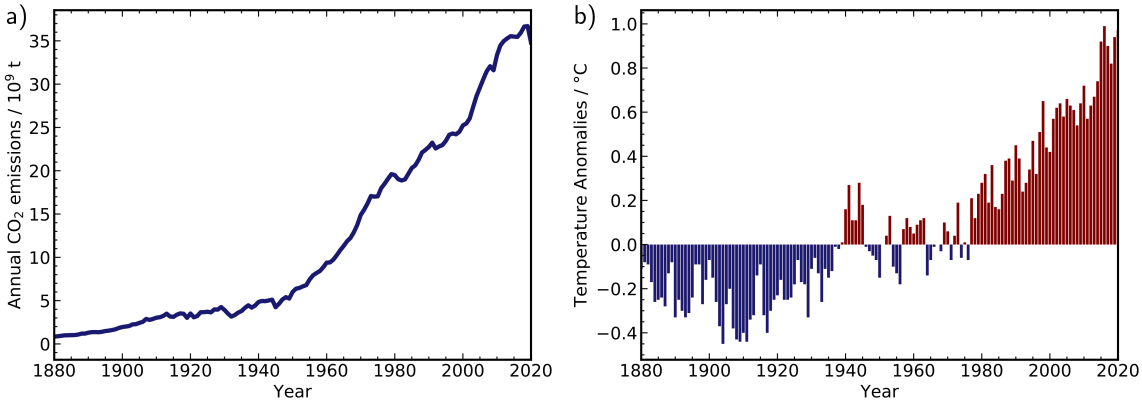


Figure 1.1: a) Annual global CO_2 emissions (in billion tons) from fossil fuels and industry. The emission data was obtained with permission under CC BY 4.0 from Our World in Data [6]. b) Temperature anomalies, obtained from the National Center for Environmental Information at NOAA [12].

Despite this immense success, research focused on discovering and improving alternative materials for PV applications has remained important. Perovskites and organic semiconductors are amongst the most promising candidates for inexpensive and well-performing solar cells. However, new and emerging PV technologies are unlikely to replace existing silicon solar cells unless they come with a severe reduction in cost or increase in power conversion efficiencies. Instead, alternative materials will likely enter the market in tandem and multi-junction devices with silicon, and for locations and applications that are unsuited for existing technologies. In this context, PV technologies based on organic semiconductors - known as organic photovoltaics (OPV) or organic solar cells (OSCs) - present a range of interesting properties and unique advantages that are discussed in more detail in the following sections.

1.2 Opportunities & Challenges of OPV

Organic solar cells have attracted interest over the last decades for their potential to generate inexpensive electricity for a growing population. In fact, OSCs demonstrate the potential to become the cheapest source of electricity, undercutting even silicon PV [13]. One key advantage of OSCs is that the chemical structure of the organic semiconducting molecules can be tuned and adapted depending on the application. This leads to an exhaustive parameter space for exploration. In addition, OSCs are based on abundant and non-toxic raw materials,

have low active-layer material consumption ($\sim$ 1g/m^2), and can be processed at reduced temperatures using inexpensive and scalable fabrication methods [13], [14], [15].

Compared to most inorganic PV materials, organic semiconductors can be deposited onto flexible substrates like sheets of plastic. This not only reduces their weight and cost, but also allows OSCs to be installed onto curved surfaces, increasing their range of possible applications. This, coupled with the potential to synthesize molecules that absorb outside the visible spectrum [16], paves the way for integrating OSCs into buildings, windows, and greenhouses for additional electricity generation, and makes OSCs an excellent choice for electrifying lightweight housing constructions in low-income countries. Recent lifecycle analyses also reveal that OSCs have the lowest carbon footprint of all PV technologies [13], highlighting their importance for a more sustainable energy landscape.

Apart from stability issues for some material systems, the key challenge of OSCs are the low light-to-electricity conversion efficiencies resulting from large energy losses in the light absorbing layers. These energy losses manifest in losses in voltage compared to the upper limit predicted by the absorption profile of the semiconducting molecules. Voltage losses can be of radiative (i.e. photon emitting) or non-radiative (i.e. heat emitting) nature and easily span 100s mV for OSCs. While both radiative and non-radiative losses are significant, non-radiative recombination was shown to couple with intra-molecular vibrations of organic semiconducting molecules [17], and is possibly intrinsic to this class of materials [13]. A major focus of current research (including the work presented in this thesis) is therefore centered on identifying, understanding, and mitigating radiative and non-radiative recombination pathways in OSCs. An improved understanding of dominant loss mechanisms aids in the creation of molecular design rules for the development of molecules with improved performance. This is with the ultimate goal of increasing light-to-electricity conversion efficiencies and aiding the commercial success of OPV.

1.3 Thesis Outline

The main focus of this thesis is on investigating the physics of charge transfer (CT) states, i.e. energetic states that form at the interface between donor and acceptor molecules in

OSCs, and relating this understanding to charge separation, voltage losses, and dominant recombination pathways. Sensitive external quantum efficiency ($sEQE$) measurements are used as the primary experimental technique to study the weak light absorption of CT states.

Chapter 2 introduces the physics of OSCs, starting with the optoelectronic properties of organic semiconducting molecules and the formation of organic molecular solids. The fundamental working principles of OSCs are discussed, and two primary frameworks for evaluating voltage losses are introduced. While one framework (the detailed balance picture) is based on thermodynamic principles and therefore applicable to all PV technologies, the second framework (the energetic state picture) relates to CT state properties and is uniquely applicable to OSCs. Chapter 3 discusses the physics of CT states, and introduces three frameworks (i.e. Marcus theory, Marcus-Levich-Jortner theory, and a three-state model) for fitting CT state properties from absorption and emission spectra. Chapter 4 summarizes the materials used in this thesis, and introduces the experimental and computational techniques employed. Chapter 5 provides a detailed description of the custom-built sensitive external quantum efficiency setup assembled and programmed as part of this thesis. In addition, the custom python program written to fit CT state properties from $sEQE$ spectra is detailed.

Chapter 6 investigates charge transfer and exciton separation in low donor content OSCs based on ZnPc and its fluorinated derivatives (F_xZnPc, with $x = 4, 8, 16$) as donors and C_{60} as the electron acceptor. Chapter 7 expands on the previous chapter and studies device performance, CT state properties, and voltage losses as a function of donor content and fluorination for F_xZnPc:C_{60} OSCs. The scientific objective of these two results chapters is on understanding the trade off between efficient free charge generation and low voltage losses facilitated via close energetic matching of molecular and CT state energy levels. Chapter 8 investigates the impact of energetic disorder on device performance and voltage losses for a variety of donor:C_{60} blends. The focus of this chapter is on establishing a suitable methodology for disentangling the contributions of static and dynamic disorder, and relating this understanding to device measurements and microstructural characterization of the active layers. Chapter 9 summarizes the key results of this thesis and provides an outlook for future research. Finally, additional results are provided for the interested reader in the appendix.

2 | The Physics of Organic Solar Cells

In this chapter, we discuss the properties of organic semiconducting molecules and cover how molecular solids, and their effective energy bands, are formed. Books such as [18], [19] are used as the main sources. Comparing mono-molecular and bi-molecular thin films, we introduce the main pathways for exciton generation, separation, and recombination. This knowledge is applied when discussing the underlying working principles of organic solar cells. More specifically, we explain the origin of the open-circuit voltage in organic solar cells based on two frameworks, (1) the detailed balance picture based on thermodynamic principles, which is applicable to all types of solar cells, and (2) the charge transfer state picture which is uniquely applicable to organic semiconductor blends. The former heavily draws on the work of Rau et al. [20], [21], while the latter primarily follows the discussion of Vandewal et al. [22], [23], [24]. For each framework, we provide a clear guide on how to quantify voltage losses, and establish how voltage losses are calculated in this thesis.

This chapter is based on A. Jungbluth, P. Kaienburg, M. Riede. Charge transfer state characterization and voltage losses of organic solar cells. J. Phys. Mater. ***5*** *024002 (2022) [1]. Text and figures were reproduced or adapted with permission under CC BY 4.0.*

2.1 Organic Semiconducting Molecules

2.1.1 Orbitals & Energy Levels

Carbon is a fundamental building block of organic semiconductors and contains six electrons including four valence electrons. In a simplified picture, these electrons are distributed in shells around the atomic core. In each shell, the wave-like behavior of the electrons is described through wave functions and orbitals, which are calculated by solving Schrödinger's equation. Each orbital can be occupied by two electrons with opposing spins.

The electronic configuration of carbon ($1s^2 2s^2 2p^2$) shows that the s-orbital of the first and second shell are fully occupied. The p-orbital of the second shell, which consists of three degenerate states, is occupied by the remaining two electrons. To form bonds between elements, the atomic orbitals of the valence electrons overlap to "share" electrons and fully occupy shells. Bonds between carbon and hydrogen, for instance, arise from an overlap of the $2s$ and $2p$ valence electrons of carbon with the $1s$ valence electron of hydrogen, forming sp-hybrid orbitals (Figure 2.1). In the case of methane (CH_4), one $2s$ electron of carbon is promoted into the $2p_z$ orbital, resulting in an sp^3 hybridization. The energetic cost of rearranging the electrons is compensated by the energetic gain of forming inter-atomic bonds.

In the case of ethene (C_2H_4), each carbon atom forms one C−C and two C−H bonds through an sp^2 hybridization. For each carbon atom, the remaining $2p_z$ orbitals overlap out of plane to form a π-bond (Figure 2.2). Depending on the spin-configuration, this π-bond is classified as being bonding (π) or anti-bonding (π*), with the bonding state being lower in energy. For molecules like benzene (C_6H_6), the alternating π-bonds (also called conjugated π-bonds) are effectively delocalized across the whole molecule. The more π-bonds are formed in a molecule, the smaller the energetic spacing between the respective bonding and anti-bonding states (Figure 2.2).

The highest occupied bonding state (highest occupied molecular orbital; HOMO), and the lowest unoccupied anti-bonding state (lowest unoccupied molecular orbital; LUMO) are the closest equivalents to the valence and conduction bands of inorganic semiconductors. However, compared to inorganic semiconductors, where the strong interactions in crystal

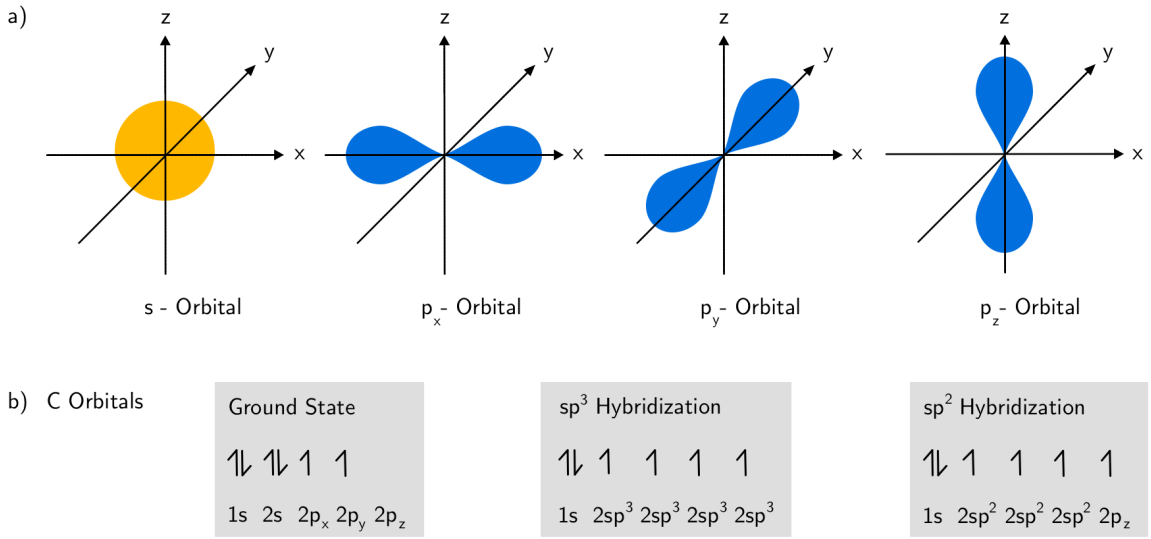


Figure 2.1: a) s and p orbitals. b) Orbitals of a carbon atom in the ground, sp^2 and sp^3 hybridized state. Redrawn and adapted with permission from Tress [18], Copyright 2014 Springer Nature.

lattices create bands with high conductivity, the energy levels of organic semiconductors are governed by disorder, resulting in a distribution of energy levels and low charge mobilities [18]. The energetic difference between the HOMO and LUMO can be equated with the transport gap (E_{trans}) of inorganic semiconductors, which will be discussed in more detail in the following sections.

2.1.2 Optoelectronic Transitions

Electrons can transition between ground and excited states via absorption and emission of light and vibrational energy. In absorption and emission experiments, the π - π* transitions are not detected as sharp lines but rather as broad features due to the vibrational, rotational, and translational manifolds in organic molecules [18]. Vibrational manifolds, which arise from the oscillation of molecules and their nuclei at temperatures > 0 K, are spaced around 100 meV apart, while rotational and translational sub levels are in range of 10s meV [18].

Figure 2.3 summarizes the different transitions (including lifetimes) that occur in organic semiconducting molecules. Through absorption of a photon, an electron is excited from the ground state (S_0) to an excited singlet state (S_1, S_2, etc.). Here, the term "singlet" refers

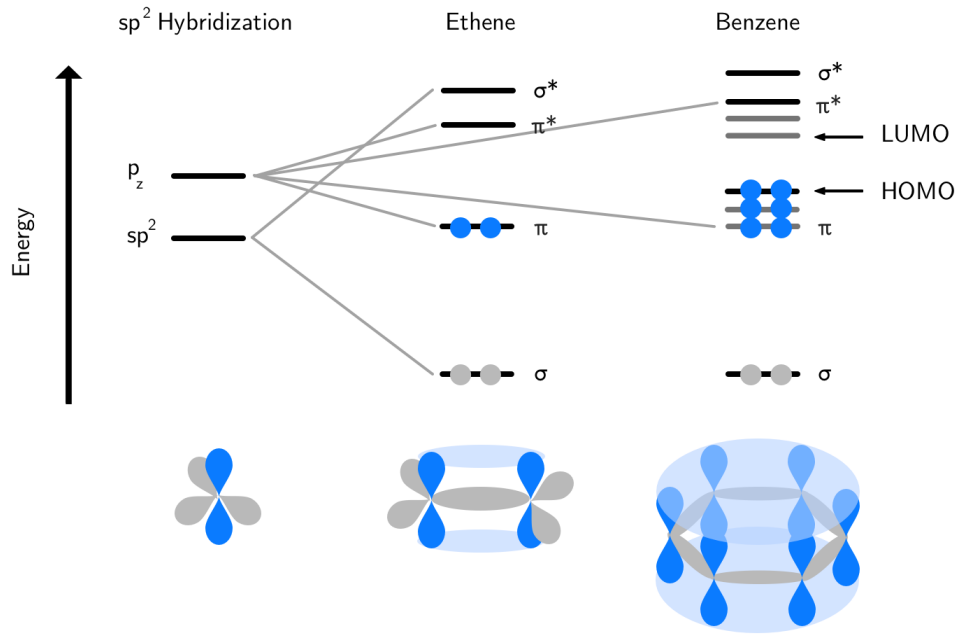


Figure 2.2: Transitions of orbital energy levels from a single carbon atom, to ethene (C_2H_4), and benzene (C_6H_6). π-bonds form from overlapping p_z orbitals, and can be either bonding or anti-bonding (marked with an asterisk). Redrawn and adapted with permission from reference [25], Copyright 2006 Springer-Verlag Berlin Heidelberg.

to an energetic state with spin-paired electrons. Electrons that are excited above S_1 relax through non-radiative internal conversion and within picoseconds to the first excited state. Transitions from S_1 to S_0 can be of radiative or non-radiative nature.

In contrast to singlets, triplet states refer to energetic states with unpaired electrons. Direct transitions to a triplet excited state (T_1, T_2, etc.) are spin-forbidden and therefore unlikely. Singlet-triplet transitions are also spin-forbidden, but can occur due to spin-orbit coupling and via a process called inter-system crossing (ISC). Since ISC occurs with low probability, triplet states are often orders of magnitude longer lived than singlets. The probability of ISC can be enhanced by adding heavy atoms to a molecule to increase spin-orbit coupling [19].

Following from this initial assessment, we now turn to discussing the quantum mechanical origins and implications of the different optoelectronic transitions in organic semiconducting molecules. According to the Born-Oppenheimer approximation, the total wave function (Ψ_{total}), describing the state of a molecule, is made up of electronic (Ψ_{el}), vibrational (Ψ_{vib}), and spin contributions (Ψ_{spin}) that can be treated independently,

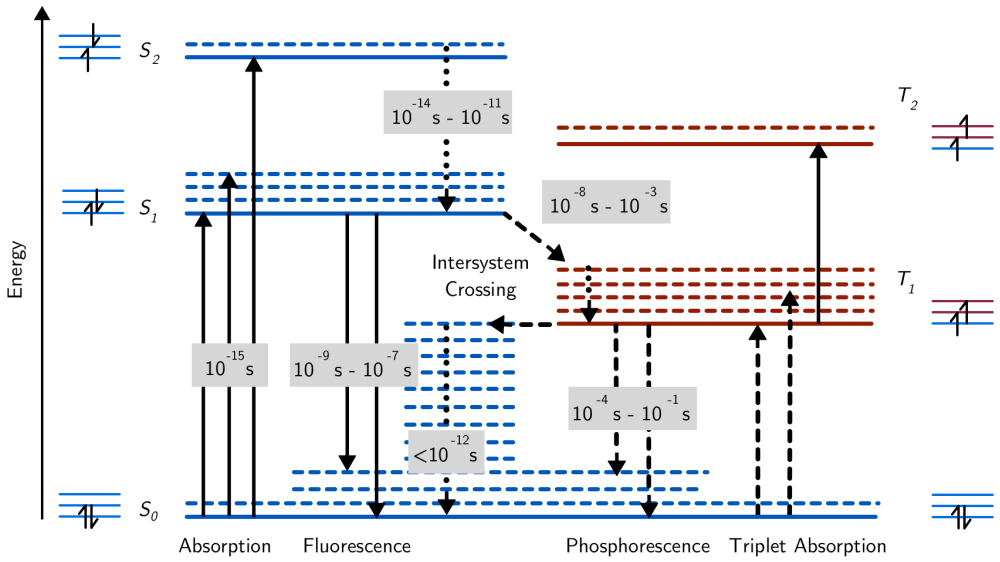


Figure 2.3: Jablonski diagram of singlet (S_n) and triplet (T_n) states. Transitions between the lowest energetic states (solid horizontal lines), and vibrational manifolds (dashed horizontal lines), can be radiative (solid arrows), non-radiative (dotted arrows), or spin-forbidden (dashed arrows). The numbers in the grey boxes indicated typical lifetimes of the processes. Redrawn and adapted with permission from Tress [18], Copyright 2014 Springer Nature.

$$\Psi_{total} = \Psi_{el}\Psi_{vib}\Psi_{spin}, \tag{2.1}$$

where the Ψ_{vib} depends on the position of the nucleus, Ψ_{spin} depends on the position of electrons, and Ψ_{el} depends on the position of the nucleus and electrons. The square of Ψ_{total} describes the probability of finding electrons, their spins, and the nucleus in a specific state.

Upon light absorption, the energy of a molecule is increased, and upon light emission, the energy of a molecule is decreased. The rate of transition (k), depends on the number (n) of transitions that occur per unit time (t), i.e. $k = dn/dt$, and is inversely related to the transition lifetime. The rate of transition between an initial state Ψ_i and a final state Ψ_j due to a perturbing Hamiltonian H' is described by Fermi's golden rule,

$$k_{ij} = \frac{2\pi}{\hbar}|\langle\Psi_j|H'|\Psi_i\rangle|^2\rho, \tag{2.2}$$

where ρ is the density of final states. Inserting Ψ_{total} into equation 2.2 yields

$$k_{ij} = \frac{2\pi}{\hbar}|\langle\Psi_{el,j}\Psi_{spin,j}\Psi_{vib,j}|H'|\Psi_{el,i}\Psi_{spin,i}\Psi_{vib,i}\rangle|^2\rho. \tag{2.3}$$

In the case of light-matter interactions, the perturbing Hamiltonian H' can be related to the properties of electromagnetic waves as $H' = \mu_{el}$, where μ_{el} is the electric dipole operator. Incident light and its time-dependent electric fields cause electrons to move in resonance [19]. Atomic nuclei, on the other hand, are too heavy to move on the same timescale [26], [27], [28], and electron spins are unaffected by electric oscillations. In addition, the changing magnetic fields of electromagnetic waves are too small to affect spins. Consequently, according to the Franck-Condon principle, only the electronic part of the wave function is impacted, and the vibrational and spin components can be considered constant,

$$k_{ij} = \frac{2\pi}{\hbar}|\langle\Psi_{el,j}|\mu_{el}|\Psi_{el,i}\rangle|^2|\langle\Psi_{vib,j}|\Psi_{vib,i}\rangle|^2|\langle\Psi_{spin,j}|\Psi_{spin,i}\rangle|^2\rho. \tag{2.4}$$

Regarding the spin contribution of an optical transition, the integral $\langle\Psi_{spin,j}|\Psi_{spin,i}\rangle$ is either 0, if the spins of the initial and final state differ, or 1 if they remain the same. Transitions between singlet states (i.e. $S_1 \rightarrow S_0$) and triplet states (i.e. $T_2 \rightarrow T_1$) are spin-allowed since electron spins are conserved. As briefly noted earlier, while singlet to triplet transitions are technically spin-forbidden, they are detected experimentally due to spin-orbit coupling.

If the electronic contribution $\langle\Psi_{el,j}|\mu_{el}|\Psi_{el,i}\rangle$ is non-zero, then optoelectronic transitions are dipole-allowed [19]. Furthermore, the value of the integral scales with increasing overlap between the wave functions of the initial and the final state [19]. This means that transition rates between states on similar areas of the same molecule are larger than those between areas that are further apart, or between electronic states of different molecules. Compared to the electronic contribution, which controls the intensity of a transition, the vibrational contribution $\langle\Psi_{vib,j}|\Psi_{vib,i}\rangle$ controls the spectral shape [19].

Figure 2.4a shows a schematic of the potential energy curves of a two-atomic molecule for ground and excited states as modelled via the Morse potential. Each state has an interatomic equilibrium distance for which energy is minimized. The vibrational energy levels within each electronic state are calculated as the eigenvalues of the Schrödinger equation

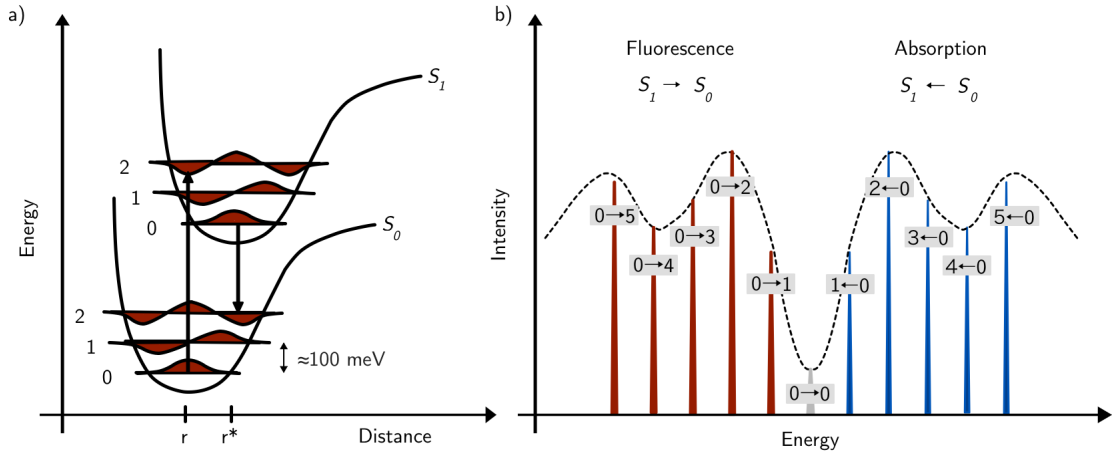


Figure 2.4: a) Schematic potential energy curves of the ground and excited states of a two-atomic molecule. The inter-atomic equilibrium distance increases from the ground state (r) to the excited state (r*). b) Reciprocity between absorption and emission for the vibrational manifolds of the ground state (S_0) and first excited singlet state (S_1). Emission occurs at lower energies than absorption (Stokes shift). Redrawn and adapted with permission from Tress [18], Copyright 2014 Springer Nature.

of the Morse potential. The energy splitting between energy levels is larger than between vibrational levels. The latter are usually spaced around 100 meV apart, and can be attributed to the vibrational modes of C−C or C−H bonds [29], [30]. At room temperature and with thermal energy of 25 meV, only the lowest vibrational energy levels are occupied. As shown in the schematic of Figure 2.4a, the equilibrium distance of excited electronic states is usually right-shifted. This is attributed to reduced electron densities when electrons move from bonding to anti-bonding orbitals, requiring larger spacing between atomic cores [19].

According to the Franck-Condon principle, optical transitions between states occur more likely for large overlaps of vibrational wave functions and at constant molecular coordinates. This can be rationalized considering that, upon photon absorption, electron distributions change their positions faster than atoms change their positions within molecules [26], [27], [28]. Direct optical transitions are followed by quick internal conversion and molecular reorganization to a new equilibrium coordinate. The latter is a non-radiative process. Consequently, fluorescence is red-shifted compared to absorption (Stokes shift) (Figure 2.4b).

The probability of a transition from the 0th vibrational level of the ground state to the nth vibrational level of the excited state (I_{0-n}) is Poisson distributed if the energy of the vibrational quanta $\hbar\omega_n >> k_B T$,

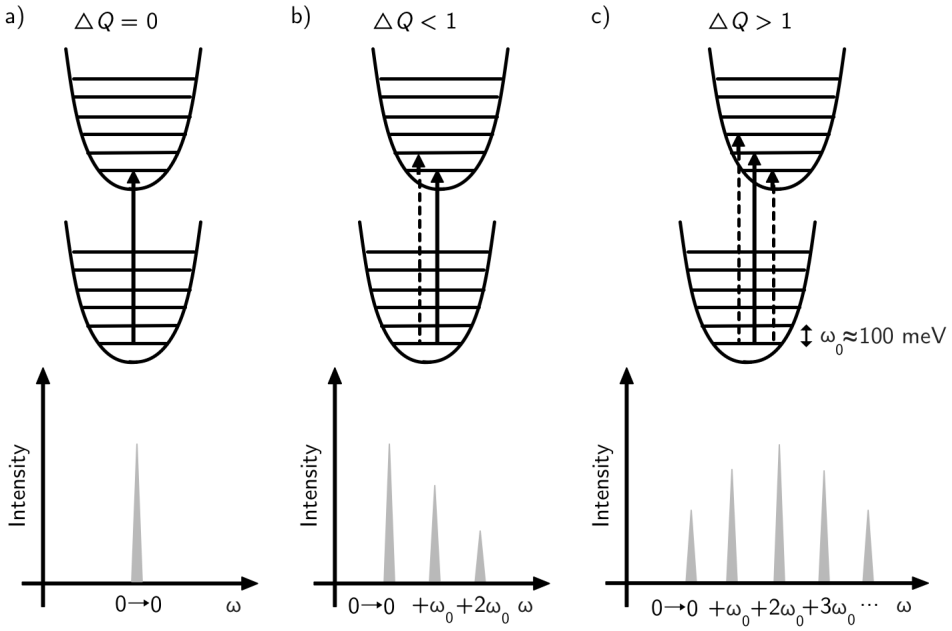


Figure 2.5: Schematics of potential energy curves and absorption spectra for a) no, b) small, and c) large differences between the equilibrium reaction coordinate (ΔQ) of ground and excited states. ΔQ depends on the geometry and rigidity of the molecules. The bottom graphs show the absorption linewidths associated with the different optoelectronic transitions. The envelope that describes the sum of all linewidths can be modelled via a Poisson distribution. Redrawn and adapted from Lecture 8, MIT Open Courseware, Introduction to Quantum Mechanics 2, with permission under CC BY 4.0.

$$I_{0-n} = |\langle \Psi_{vib,n} | \Psi_{vib,0} \rangle|^2 = \frac{S^n}{n!} e^{-S}. \tag{2.5}$$

In equation 2.5, S describes the Huang-Rhys parameter, a dimensionless quantity that depends on the change in the equilibrium reaction coordinates (ΔQ) between ground and excited states as $S \propto \Delta Q^2$. Q is a generalized quantity that encompasses information on the inter-atomic equilibrium distance of a specific energetic state. For stiff molecules with rigid bonds, ΔQ is small, resulting in strong wave function overlap for $0-0$ transitions (Figure 2.5a). In comparison, flexible molecules with large ΔQ show stronger wave function overlap for higher vibrational energy levels of the excited state (Figure 2.5c).

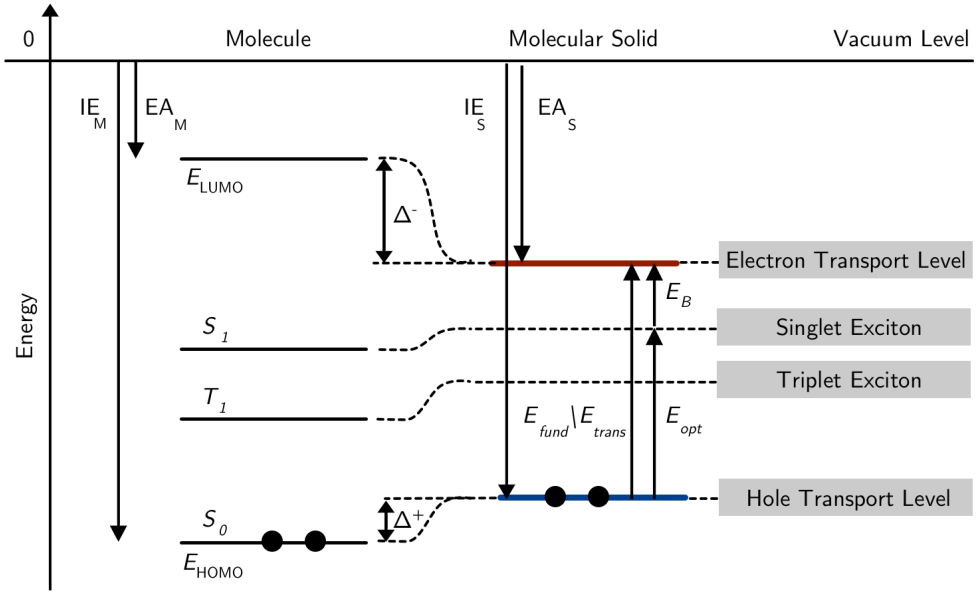


Figure 2.6: Schematic energy level changes from a single molecule to a molecular solid. Electrostatic polarization effects (Δ^-, Δ^+) decrease the energy gap. The ionization energy (IE) denotes the energy needed to remove an electron from the molecule (M) or solid (S). The electron affinity (EA) denotes the energy gained when adding an electron to a neutral molecule. The fundamental (E_{fund}) or transport gap (E_{trans}) describe the energetic difference between the LUMO and HOMO of organic molecules and solids respectively. In comparison, the optical gap (E_{opt}) marks the first allowed optical transition. For organic semiconductors, E_{trans} and E_{opt} are not the same, and the difference describes the exciton binding energy (E_B). Redrawn and adapted with permission from Tress [18], Copyright 2014 Springer Nature, and Brédas [31], Copyright The Royal Society of Chemistry 2014.

2.2 Organic Molecular Solids

2.2.1 Polarization & Electrostatic Effects

Having introduced the energetic bands and optoelectronic transitions in organic molecules, we next turn to discussing the formation of organic molecular solids. When organic molecules are brought together to form crystalline or amorphous thin films, polarization effects cause weak van der Waals interactions that change the energy landscape with respect to the vacuum level. Figure 2.6 shows a schematic of the expected energy level shifts.

Koopmans' theorem states that the energy of the HOMO (LUMO) of a molecule is equal in magnitude to the ionization energy IE (electron affinity EA) [32]. The terms HOMO and

LUMO are often also applied to thin films, although this is technically incorrect [33]. When molecules are brought together to form solids, molecular properties like absorption spectra and energy levels are shifted due to polarization effects. The changing polarization environments in thin films are caused by electrostatic inductions (U_{ind}) of neighboring molecules that increase EA and decrease IE. In comparison, charge distributions of the environment cause electrostatic contributions (U_{el}) that shift EA and IE equally [34], [35], [36], [37]. Both effects combined lead to electrostatic corrections for holes (Δ^+) and electrons (Δ^-) as

$$\Delta^+ = \mathrm{IE} - E_{\mathrm{HOMO}} = -U_{ind} + U_{el}, \tag{2.6}$$

$$\Delta^- = \mathrm{EA} - E_{\mathrm{LUMO}} = U_{ind} + U_{el}. \tag{2.7}$$

When molecules are placed in a static electric field, distortions of their charge distributions can cause electrostatic multipoles [37]. U_{ind} depends on the dipole moment and static polarisability [38]. For organic molecules with large clouds of delocalized π-electrons, induction effects of energy levels in a gas-phase and thin films are typically around $1-2$ eV [39], [37].

In comparison, electrostatic interactions occur without changes to the electron distributions and arise from charge-charge, charge-dipole, dipole-dipole, and charge-quadrupole interactions as the leading terms [37]. In simple terms, for neutral molecules with negligible dipole-dipole interactions, e.g. for co-planar stacking with alternating dipole alignment [37], [36] or molecules with vanishing static dipole moments, charge-quadrupole interactions become the dominant contribution to electrostatic shifts [37], [38].

Charge-quadrupole interactions mainly impact nearest neighbors [40] since their contribution decreases with $1/r^3$. Nonetheless, charge-quadrupole interactions strongly impact thin film energy levels, as modelled theoretically and measured experimentally for thin films and devices [34], [41], [40], [42], [35]. More specifically, charge-quadrupole interactions were found to strongly impact charge dissociation and the open-circuit voltage of OSCs [41]. Chapter 7 of this thesis builds on this work and further explores the role of charge-quadrupole interactions on OSC device performance.

Returning to Figure 2.6, the energetic difference between the IE and EA of a molecule is defined as the fundamental gap (E_{fund}) [31]. In a solid, IE $-$ EA marks the transport gap (E_{trans}), as charge transport occurs in the LUMO for electrons and HOMO for holes [18]. Compared to inorganic semiconductors, E_{fund}/E_{trans} of organic semiconductors are not the same as the optical gap (E_{opt}). Instead, the optical gap is defined as the first allowed optical transition between the singlet ground state (S_0) and the lowest excited singlet state (S_1) [18]. Triplet (T_1) states are energetically located below S_1.

2.2.2 Excitons

Charge generation in organic semiconducting molecules occurs via excitons, i.e. bound electron and hole pairs. Frenkel excitons describe excitons that are located on the same molecule after photon absorption (Figure 2.7a). The exciton binding energy (E_B), classifies how strongly bound electrons and holes are, and is usually on the order of 100s meV due to the low dielectric constant ($\eta \approx$ 3-5) of organic molecules [31], [18]. Looking back at Figure 2.6, E_B relates to the energy levels of a molecular solid as $E_B = \mathrm{IE_S} - \mathrm{EA_S} - E_{S_1}$, where E_{S_1} is the energy of the first allowed optical transition.

Once excitons are generated, they can move through solids and transfer to neighboring molecules. Exciton transport and diffusion in organic molecular solids usually occurs between $5 - 40$ nm [43], [44]. In highly crystalline solids with strong intermolecular interactions, such as inorganic semiconductors with high dielectric constants ($\eta \geq 10$), excitons

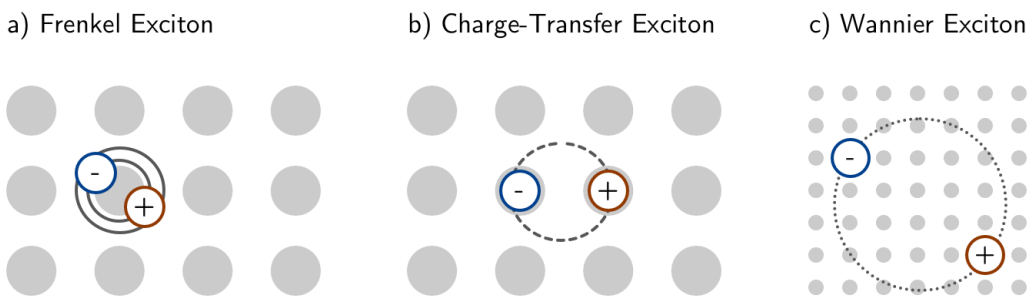


Figure 2.7: a) Frenkel excitons are localized on one molecule and tightly bound. b) Charge-transfer (CT) excitons are localized across molecules and weakly bound. c) Wannier excitons are highly delocalized across molecules and only very weakly bound.

easily delocalize (Figure 2.7c). These so-called Wannier excitons freely dissociate into separated charges, as their binding energy is lower than thermal energy at room temperature.

Excitons that are located across neighboring molecules are classified as charge transfer (CT) excitons, and the associated energetic state is the CT state (Figure 2.7b). CT states in monomolecular solids are challenging to detect, as their absorption peaks are not resolved from that of the $S_0 \rightarrow S_1$ transition. As discussed in the following sections, CT states of bimolecular solids play a crucial role for the performance of organic solar cells (OSCs).

2.3 Working Principles of Organic Solar Cells

2.3.1 The Donor-Acceptor Concept

In order to separate electron-hole pairs before excitons recombine, the exciton binding energy has to be overcome. As briefly discussed earlier, the spontaneous separation of Frenkel excitons in organic semiconducting molecules is unlikely, since $E_B >> k_B T$. To circumvent this constraint, Tang first introduced the concept of organic heterojunctions between electron donating (donors; D) and electron accepting (acceptors; A) molecules [45]. By combining molecules with energy levels that favor energy transfer, Frenkel excitons located on one molecule delocalize to form CT excitons across the D-A interface. Since CT excitons have a lower binding energy than Frenkel excitons, the charge separation probability is enhanced. As sketched out in Figure 2.8, the molecule with the EA closest to the vacuum level acts as the electron donor. Since CT states are coupled to the ground state, they can be assessed through absorption and emission measurements [23], [24].

Ionized molecules in the CT state undergo molecular reorganization that decreases the energy of a hole on the cation, and the electron on the anion. This molecular reorganization creates singly occupied molecular orbitals ($SOMO$) that are slightly lower in energy than the HOMO and LUMO. In addition, E_{S_1} of the individual molecules is larger than the energy of the CT state E_{CT}. While D-A heterojunctions help to facilitate exciton transfer, they also contribute to energy loss pathways in OSCs, as will be discussed in more detail later.

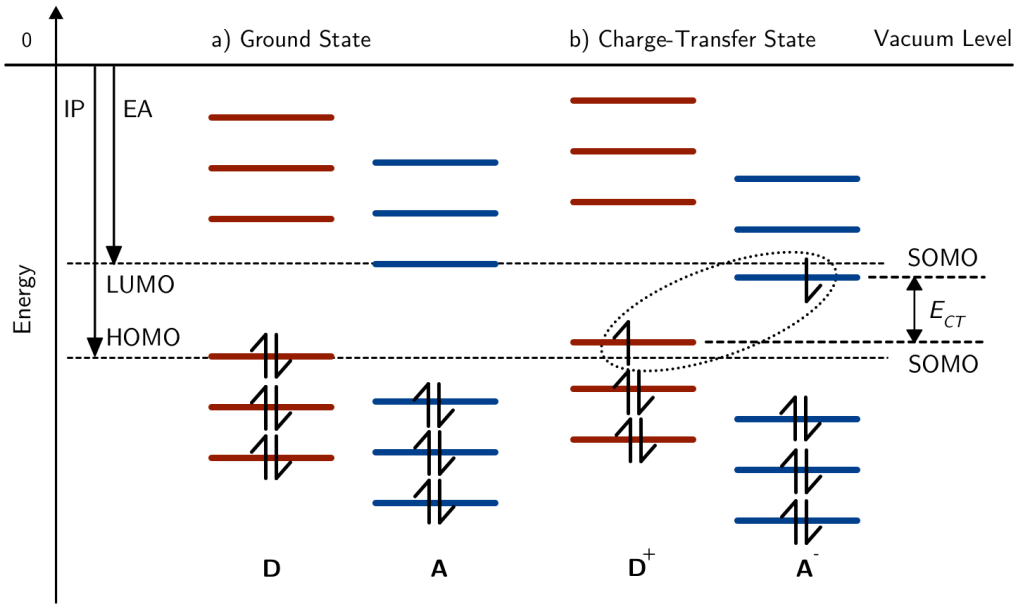


Figure 2.8: a) Ground state, b) Charge transfer (CT) state energy levels. Ionized molecules in the CT state undergo molecular reorganization that decreases the energy of a hole on the cation and the electron on the anion. This reorganization process creates singly occupied molecular orbitals (SOMO). The difference between the HOMO − LUMO gap and the SOMO − SOMO gap is given by the exciton binding energy. Redrawn and adapted with permission from Tress [18], Copyright 2014 Springer Nature.

When Tang first introduced the D-A heterojunction concept, donor and acceptor layers were stacked vertically, creating planar heterojunctions (PHJ) [45] (Figure 2.9a). For many systems, CT at the D-A interface is efficient, provided that excitons can each it [30], and favorable energetic offsets exist. Compared to typical absorption depths of $\sim$ 100 nm, exciton diffusion lengths in organic thin films are usually on the order of 10s nm [46], [43], [47]. While Tang observed improved exciton separation efficiencies, the photocurrents of PHJs are limited, as either not all photons are absorbed, or Frenkel excitons recombine before they can reach the D-A interface. To circumvent this limitation, intermixed bulk heterojunctions (BHJ) were developed (Figure 2.9b). In these systems, donor and acceptor molecules are deposited simultaneously in a desired mixing ratio. As a result, active layer thicknesses can be increased, facilitating better photon absorption while ensuring that excitons can more easily reach D-A interfaces.

The active layer morphology and mixing characteristics of donor and acceptor molecules strongly impacts the overall device performance [48], [49], [50]. For a long time, it was

thought that well-performing devices require large amounts of donor and acceptor molecules. This was centered in the belief that an abundance of donor-acceptor interfaces is needed for charge separation, and that efficient charge transport requires percolation pathways of donor and acceptor aggregates.

However, these assumptions were put into question when Zhang et al. demonstrated improved device performance for TAPC:C_{60} blends with low donor content [49]. For certain molecules, these "dilute" systems (Figure 2.9c), which are usually fabricated with less than 10% donor loading [3], show increased open-circuit voltages and higher photocurrents than their intermixed counterparts. These observations are generally explained considering that D-A interfaces not only facilitate exciton separation, but also provide opportunities for electrons and holes to meet and recombine [51], [52]. Even though the mechanisms of charge transport in dilute BHJs are not yet fully understood, previous research identified long-range tunneling of holes via isolated donor molecules as a potential transport pathway [53]. To build on the current understanding, chapters 7, and 8 of this thesis compare the performances of BHJs based on dilute and intermixed blends and further investigate how D:A mixing ratios impact device performance.

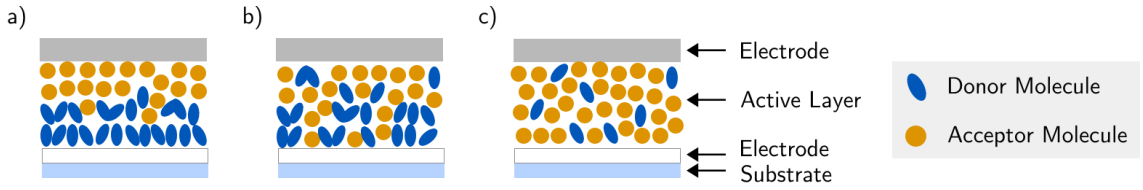


Figure 2.9: Simplified schematics of different heterojunction types: a) Planar heterojunction (PHJ), b) bulk heterojunction (BHJ), c) bulk heterojunction with low donor content.

2.3.2 Charge Generation & Recombination

Having introduced the concepts of D-A heterojunctions and interfacial CT states, we next discuss the charge generation and recombination mechanisms in OSCs in more detail. Figure 2.10 shows an overview of the dominant charge generation and recombination pathways in OSCs, including transition rates and timescales.

The main aim of OSCs is to convert sunlight into usable electric energy. The generation of free charge carriers is a multi-step process, reliant on (1) photon absorption to excite Frenkel excitons, (2) exciton diffusion to the D-A interface, (3) charge transfer, and (4) CT exciton separation. This is followed by free charge collection at the electrodes.

In the simple picture, Frenkel excitons are generated on the donor molecules, and charge transfer occurs via electron transfer to the acceptor. However, depending on the optical gaps of the molecules, an analogous process applies to photon absorption via acceptor molecules that is followed by hole transfer to the donor. The latter process occurs in C_{60} blends with TAPC, which is a transparent donor. While this simple picture of electron or hole transfer generally applies to fullerene-based blends, recent work [54] showed that many well-performing non-fullerene acceptors (NFAs) with low energetic offsets at the D-A interface undergo Förster resonance energy transfer (FRET) from the donor to the NFA, followed by hole transfer back to the donor.

For many material systems, the internal quantum efficiency (IQE) approaches unity [55], [56], meaning that almost all excitons successfully dissociate. For a long time, it was believed that efficient exciton dissociation required large energetic offsets (often termed "driving forces") at the D-A interface. Depending on how the term is used in literature, the driving force relates to different reference energy levels. In the $\mathrm{EA/IE}$ picture, the driving force relates to large $\Delta\mathrm{EA}$ for electron transfer, and large $\Delta\mathrm{IE}$ for hole transfer. In the singlet/CT state picture, the driving force describes the energetic gap between E_{S_1} and E_{CT} ($\Delta E_{CT} = E_{S_1} - E_{CT}$). This manifests in an apparent trade-off between high photocurrents and the conservation of chemical potential, often described as the $EQE - V_{oc}$ trade-off for OSCs [57], [58]. Here, EQE describes the external quantum efficiency, i.e. the spectrally-dependent generation of free charges, and V_{oc} describes the open-circuit voltage.

Current research is still investigating which driving force ($\Delta\mathrm{EA/IE}$ or ΔE_{CT}) is the most relevant for device performance. However, recent advances employing NFAs, which show high photocurrents despite low $\Delta\mathrm{EA/IE}$ or ΔE_{CT} [59], [60], [61], have put the trade-off between high current or voltage into question. The underling working mechanisms of NFA blends are discussed in more detail later.

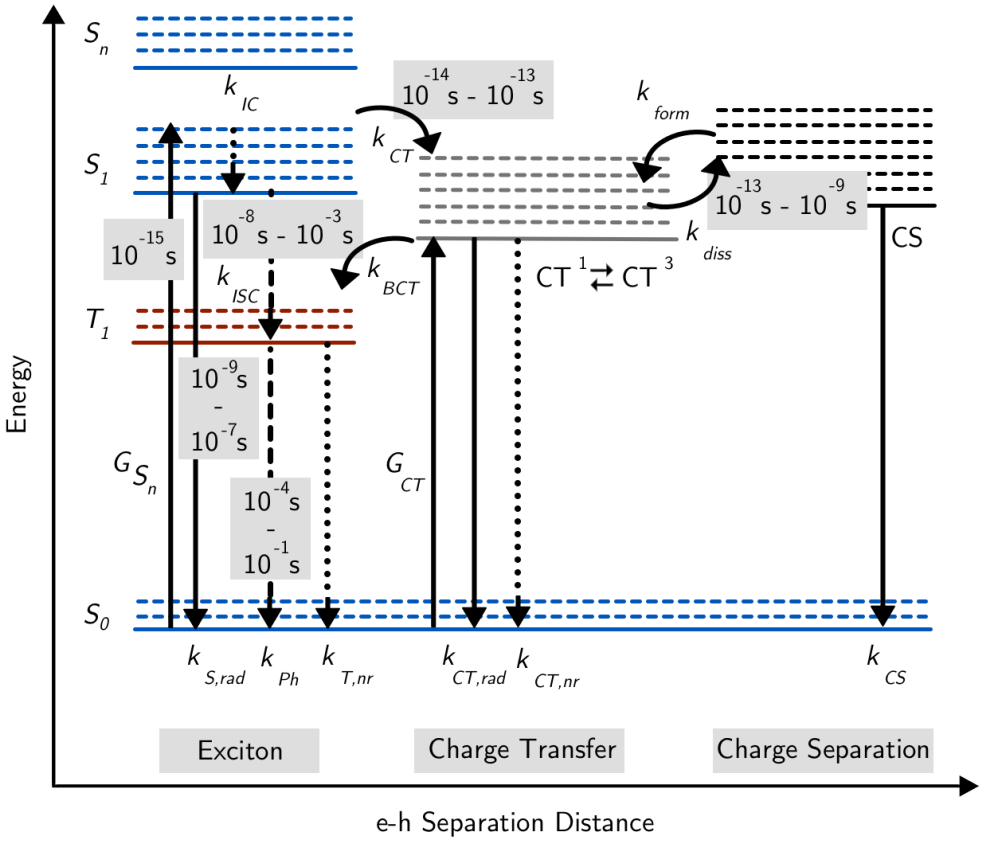


Figure 2.10: Jablonski diagram of charge generation and recombination processes in OSCs. Upon photon absorption, electrons are excited from the ground state (S_0) into excited singlet states (S_n). Depending on the absorption profiles of the donors and acceptors, exciton transfer to the charge transfer (CT) state occurs via electron or hole transfer at rate k_{CT}. Alternatively, CT states can be excited directly. These excitation processes occur at rates of G_{S_n} and G_{CT} respectively. Thermal relaxation, i.e. internal conversion (IC), occurs at rate k_{IC}. Both singlet states and CT states can decay radiatively ($k_{S,rad}$ and $k_{CT,rad}$), or non-radiatively via inter-system crossing (ISC) or back charge transfer (BCT) to triplet states (T_n). Recombination from the CT state competes with charge dissociation into the charge separated (CS) state. Between the CT and CS state, excitons can dissociate and separate as k_{diss} and k_{form}. Solid lines represent optically-allowed transitions, dashed lines spin-forbidden transitions, and dotted lines denote non-radiative pathways. The boxes indicate typical timescales of the processes. The timescales were taken from [62], [63], [18]. Redrawn and adapted with permission from Vandewal et al. [56], Copyright 2013 Springer Nature.

As discussed for optoelectronic transitions of single molecules, absorption and emission of photons are reciprocal processes, with emission being spectrally shifted to lower energies. This Stokes shift between absorption and emission arises from rapid thermalization of ex-

cess energy to the lowest vibrationally excited states. At the D-A interface, CT is ultra-fast and occurs on the order of $20 - 300$ fs, as measured for fullerene blends in reference [63]. Once CT states are formed, dissociation of CT excitons competes with charge recombination. Since both Frenkel and CT excitons are coupled to the ground state, they can recombine radiatively with rates $k_{S,rad}$ and $k_{CT,rad}$. In addition, both singlet and CT states can recombine non-radiatively via vibrational relaxation.

These recombination events are classified into geminate recombination if the recombining charge carriers originate from the same photon, or non-geminate recombination if the charge carriers originate from different photons. CT excitons that successfully dissociate into charge separated (CS) states can reform CT complexes. This reformation process occurs non-geminately, resulting in CT excitons with singlet or triplet character. Singlet and triplet CT states are nearly energetically degenerate [64], and their formation follows spin statistics, meaning $3/4$ of events lead to triplet and $1/4$ lead to singlet excitons.

As a result, non-radiative decay can occur directly from the CT state, or via back charge transfer (BCT) to molecular triplets. Triplet-mediated recombination can also occur geminately via ISC of spin-coupled charge pairs. Geminate recombination, which is further discussed in Chapter 6, can be studied via Electron Paramagnetic Resonance (EPR), while non-geminate recombination is generally studied via spectroscopic techniques like transient absorption spectroscopy (TAS) [65].

Whether CT states dissociate multiple times is still debated. According to Langevin theory, electrons and holes recombine as soon as they meet within their Coulombic radius [66]. While Langevin theory describes recombination in organic light emitting diodes (OLEDs) well [51], recombination rates in OSCs are generally overestimated [67], [68]. Burke et al. demonstrated that reduced Langevin recombination can be well explained if CT states form and dissociate many times, creating an equilibrium between CT and CS states [51].

2.3.3 Current Density-Voltage Characteristics

Having introduced the basic mechanisms for charge generation and recombination, we briefly take a step back to discuss the current density-voltage ($J - V$) characteristics of solar

cells. The following paragraphs present a very simplistic overview of the complex voltage-dependence of the photocurrent. The interested reader is referred to references [18], [19], [69] for a more in-depth discussion.

Shockley [69] derived the $J-V$ characteristics under illumination of $p-n$ junctions based on inorganic semiconductors as

$$J(V,T) = J_0(e^{\frac{qV}{k_BT}} - 1) - J_{ph}(V), \tag{2.8}$$

where J_0 is the dark saturation current, q is the elementary charge, k_B is the Boltzmann constant, T is the temperature, and J_{ph} describes the photocurrent upon light absorption. Equation 2.8 is often discussed assuming that J_{ph} is independent of the applied external field, as is the case for high quality inorganic semiconductors, and that $J_{ph} = J_{sc}$. Here, J_{sc} is the short-circuit current density, i.e. the measured current density when no voltage is applied. However, this assumption is not guaranteed to be true in OSCs, where a strong voltage-dependence of the photocurrent is observed [18]. This can largely be attributed to low charge carrier mobilities, which lead to significant charge populations at OSC operating conditions that partially screen the applied external field. As a result, a number of approaches have been applied to derive the voltage-dependence of the photocurrent of OSCs from e.g. equivalent-circuit models, charge mobility-lifetime relationships [18], [70], [71], [72], [73].

Nonetheless, following from equation 2.8, the open-circuit voltage (V_{oc}), i.e. the voltage under illumination for which all charge carrier recombine and no current is extracted $J(V,T) = 0$, can be derived as

$$V_{oc} = \frac{k_BT}{q} \ln\left(\frac{J_{ph}}{J_0} + 1\right) \approx \frac{k_BT}{q} \ln \frac{J_{ph}}{J_0}. \tag{2.9}$$

Figure 2.11 shows a schematic of a current density-voltage curve following the Shockley diode equation (equation 2.8). We note that equation 2.8 is the ideal diode equation, i.e. describing ideal semiconductors with perfect absorption, charge extraction, and only radiative recombination. Real devices, however, are generally non-ideal, and suffer from internal resistances and non-radiative recombination. The latter is accounted for in the non-ideal

diode equation, $J(V,T) = J_0(e^{\frac{qV}{nk_BT}} - 1)$, and via inclusion of the ideality factor n, which generally ranges from $1-2$ depending on the dominant recombination pathways.

The electrical power generated by a solar cells under illuminated is defined at $P = I \cdot V = J \cdot A \cdot V$, where I is the total current that scales with the active area A of the device. The fill factor (FF), which describes the "squareness" of the $J-V$ curve, is defined as

$$FF = \frac{J_{\mathrm{MPP}} V_{\mathrm{MPP}}}{J_{sc} V_{oc}}, \tag{2.10}$$

where J_{MPP} and V_{MPP} describe the current and voltage at the maximum power point P_{MPP}. The power conversion efficiency (PCE) describes how efficiently incident light is converted into electrical power, and is defined as

$$PCE = \frac{J_{sc} V_{oc} FF}{P_{in}} = \frac{J_{\mathrm{MPP}} V_{\mathrm{MPP}}}{P_{in}}, \tag{2.11}$$

where P_{in} describes the power of the incident light (i.e. the AM1.5g solar spectrum). Even though relationships like equation 2.10 seem simple at first, the underlying principles that govern quantities like the V_{oc}, J_{sc}, FF, and ultimately the PCE of OSCs are highly complex and rely on many confounding parameters. The main focus of this chapter, and this thesis in general, is the V_{oc} and its relationship to the charge transfer state.

2.3.4 Reciprocity

As detailed earlier, absorption and emission are reciprocal optoelectronic processes. Absorption of full device stacks can be measured experimentally via the EQE, which relates the spectral dependence of the number of free charge carriers to incident photons, i.e. $EQE(E) = \frac{\#\text{electron}-\text{hole pairs}/s}{\#\text{photons}(E)/s}$. Emission can be measured via electroluminescence (EL) or photoluminescence (PL) spectroscopy. The former detects light emission after electrical injection of charge carriers [74], and by operating solar cells as light emitting diodes (LEDs). In comparison, PL spectroscopy uses lasers to photoexcite excitons [75] and is generally performed on thin films, but has also been applied to devices [76].

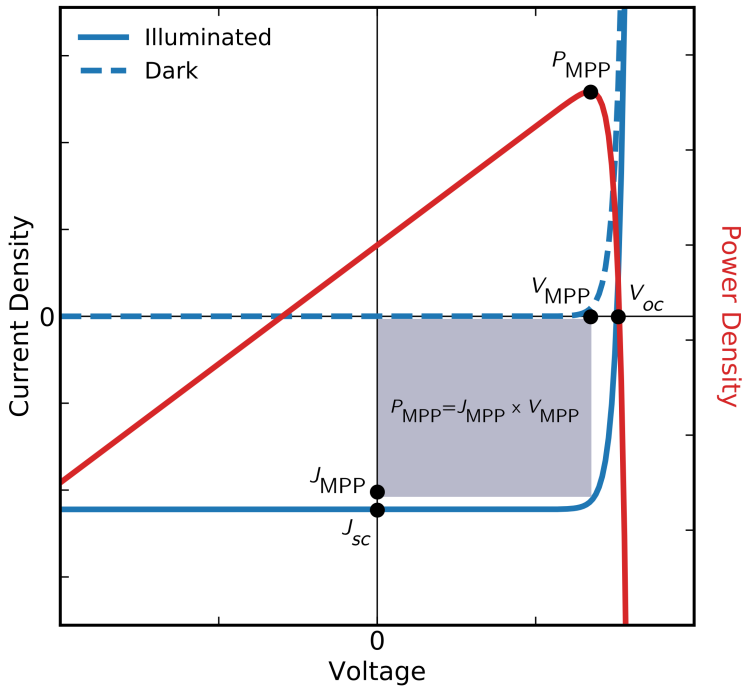


Figure 2.11: Example $J-V$ curve modelled using the Shockley diode equation (equation 2.8) under illumination (solid blue line) and in the dark (dashed blue line). The power density is calculated as $P = JV$, and is shown in red. The short-circuit current density (J_{sc}), open-circuit voltage (V_{oc}), and the $J-V$ characteristics at the maximum power point (J_{MPP}, V_{MPP}, P_{MPP}) are labelled. Redrawn and adapted after reference [33].

Rau's optoelectronic reciprocity theorem [20] links EQE and EL spectra via the black-body spectrum $\phi_{BB}(T, E)$ and a voltage-dependent exponential term as

$$\delta\phi_{em}(E, T, V) = EQE(E) \cdot \phi_{BB}(E, T) \cdot (e^{\frac{qV}{k_B T}} - 1), \tag{2.12}$$

where $\delta\phi_{em}$ describes the excess emission upon charge carrier injection compared to the emission in the dark without applied bias. Equation 2.12 is often used to convert between EL and EQE spectra, e.g. to align the relative EL to the EQE, or extend the sensitivity of EQE measurements into the sub-gap region.

When working with absorption and emission spectra, it is instructive to confirm the validity of reciprocity. Reciprocity relations generally hold well for OSCs [23], [77], but static disorder [78], optical interference [79], or low mobilities [80] might cause reciprocity to be violated. Two ways of testing for reciprocity are (1) converting EL to EQE spectra,

and vice versa, to check for spectral matching, and (2) varying the injection current during EL measurements to confirm that emission peaks do not shift for the chosen experimental conditions [81].

2.3.5 Voltage Losses

Voltage losses are a major contributor to non-ideal performances and are significantly higher for OSCs than other well-performing PV technologies. Voltage losses are either described in terms of energy or voltage and quantify the difference between a reference energy and the measured open-circuit voltage, $q\Delta V = E_{ref} - qV_{oc}$, at Standard Testing Conditions (STC; 100 mW cm^{-2}, 25°C cell temperature, AM1.5g solar spectrum).

In the following, we discuss two common approaches for quantifying voltage losses in OSCs. The detailed balance (DB) method is purely based on thermodynamic principles [20], [21], and is equally applicable to organic and inorganic solar cells. The energetic state (EN) method is also based on detailed balance, but incorporates physical concepts that are unique to OSCs, i.e. by explicitly considering charge transfer states.

2.3.5.1 Reference Energies

As explained earlier, the description of bandgaps is more complicated for OSCs than for inorganic semiconductors since optical gaps and charge transport gaps are not the same (see Figure 2.6. The optical gap, which is representative of the absorption edge, is commonly used as the reference energy for voltage loss analysis. The issue with this approach is that there is no clearly defined single energy value for optical gaps in OSCs, or any other real solar cell [82].

To circumvent this issue, a variety of approaches have been applied in literature to determine optical gaps. A short overview of two common approaches is presented in the following paragraphs. Any chosen approach needs to strike a balance between being physically meaningful, fit for purpose, easy to use, and reproducible. While it would be advantageous to apply one common methodology across literature, in reality, different studies employ different techniques and results are not always immediately comparable.

As part of the voltage loss analysis in the DB picture, E_{ref} is commonly determined via the EQE [82], [83], [21], since EQE spectra are device relevant and often reported in literature. When E_{ref} is determined via the inflection point of the EQE absorption onset, the reference energy is understood as a "photovoltaic bandgap" (E_g^{PV}) referring to a device rather than material property [21]. While the inflection point approach carries an uncertainty of about 10 meV, errors can, for instance, be reduced by averaging over multiple samples [21].

In the EN picture, the optical gap used as E_{ref} is defined as the lowest absorbing singlet energy (E_{S_1}) [83]. E_{S_1} can be determined by fitting the EQE using Gaussian functions as described in more detail in Chapter 3. Alternatively, E_{S_1} can be determined by fitting absorption or emission spectra of films based on neat (unblended) materials, or determined as the intersection point between absorption and emission spectra [83]. However, this approach requires careful consideration of any spectral shifts between blended and neat films that might arise from polarization and electrostatic effects of different chemical and morphological environments of the molecules. Significant spectral shifts make the determination of E_{S_1} from neat films unsuitable.

2.3.5.2 Radiative Limit

The radiative saturation current density (J_0^{rad}) and the short-circuit current density (J_{sc}) can be calculated via integration of the EQE as

$$J_0^{rad} = q \int_0^{\infty} EQE \cdot \phi_{BB} dE, \tag{2.13}$$

$$J_{sc} = q \int_0^{\infty} EQE \cdot \phi_{AM1.5} dE, \tag{2.14}$$

where $\phi_{AM1.5}$ is the AM 1.5g solar spectrum at 100 mW cm^{-2}. Compared to the J_{sc} determined via $J-V$ measurements, equation 2.14 often leads to deviations that can be rationalized considering that most EQE measurements are relative rather than absolute. As a result, imperfect optical alignment, low charge carrier densities when measuring without bias illumination, and uncertainties in the photovoltaic active area can explain the deviations.

Following from equations 2.13 and 2.14, the radiative upper limit of the open-circuit voltage (V_{oc}^{rad}), assuming that the EQE is not a step-function but only radiative recombination occurs, can be calculated as

$$V_{oc}^{rad} = \frac{k_B T}{q} \ln\left(\frac{J_{sc}}{J_0^{rad}}\right). \tag{2.15}$$

V_{oc}^{rad} is central to both the detailed balance and the energetic state picture, and does not rely on consensus definitions or fitting approaches like E_{ref}. The only requirement is that all quantities in the integral are measured with sufficient dynamic range. The boundaries of the integral, which in theory should be $0 - \infty$ eV, are in practice limited by the experimental range and noise floor of the measurement setup. As demonstrated in reference [2], the low energy tail of the EQE is often extended beyond the limit of the measurement setup, e.g. through linear or Gaussian fits, and V_{oc}^{rad} is plotted as a function of integration bounds. This allows to estimate the integral bounds for which V_{oc}^{rad} starts to saturate.

The derivation of equation 2.15 is based on the superposition principle and the assumption that at V_{oc}, where the total extracted current is zero, the photocurrent density $J_{ph}(V_{oc}) = J_{ph}(0) \equiv J_{sc}$. As discussed in Section 2.3.3, since the photocurrent of OSCs is voltage-dependent, this assumption is not quite true. However, since an accurate determination of the voltage-dependence of J_{ph} is challenging [77], J_{sc} is often used as a decent approximation.

The difference between the measured V_{oc} and V_{oc}^{rad} arises from non-radiative voltage losses (ΔV_{oc}^{nr}) typically caused by phonons and vibration-mediated electronic transitions [17], [84]. Non-radiative voltage losses relate to the LED quantum efficiency (Q_{LED}), i.e. the inverse ratio of the number of injected charge carriers that are converted into photons, via another reciprocity theorem [20], [85], [86],

$$\Delta V_{oc}^{nr} = V_{oc}^{rad} - V_{oc} = \frac{k_B T}{q} \ln(Q_{LED}^{-1}) = \frac{k_B T}{q} \ln\left(\frac{J_0}{J_0^{rad}}\right). \tag{2.16}$$

Again, the quantification of ΔV_{oc}^{nr} agrees between the DB and EN picture.

2.3.5.3 Voltage Losses - Detailed Balance Picture

In the DB picture [20], [21] the voltage losses are split as follows [87], [88],

$$\begin{aligned}\Delta V^{DB} &= E_{ref}/q - V_{oc} \\ &= (E_g^{PV}/q - V_{oc}^{SQ}) + (V_{oc}^{SQ} - V_{oc}^{J_{sc}}) + (V_{oc}^{J_{sc}} - V_{oc}^{rad}) + (V_{oc}^{rad} - V_{oc}) \\ &= \Delta V_{oc}^{SQ} + \Delta V_{oc}^{J_{sc}} + \Delta V_{oc}^{rad} + \Delta V_{oc}^{nr},\end{aligned} \tag{2.17}$$

where ΔV_{oc}^{SQ} captures the losses compared to the Shockley-Queisser limit [89], $\Delta V_{oc}^{J_{sc}}$ is the loss due to an imperfect J_{sc}, ΔV_{oc}^{rad} and ΔV_{oc}^{nr} describe radiative and non-radiative losses respectively. In the following, we explain the origin of each loss term in equation 2.17.

The first loss term, $\Delta V_{oc}^{SQ} = E_g^{PV}/q - V_{oc}^{SQ}$ is calculated as the difference between the reference energy (i.e. the photovoltaic bandgap introduced earlier) and the V_{oc} in the Shockley-Queisser limit [89], [87] (calculated with E_g^{PV} as the bandgap). ΔV_{oc}^{SQ} is non-zero even for ideal solar cells due to unavoidable radiative recombination in the absorbing material. This loss term is approximately proportional to the bandgap and varies between $250 - 300$ mV for $E_g^{PV} = 1.2 - 1.3$ eV.

The second loss term, $\Delta V_{oc}^{J_{sc}} = V_{oc}^{SQ} - V_{oc}^{J_{sc}}$, arises from the difference in the measured J_{sc} and the short-circuit current density in the Shockley-Queisser limit,

$$\Delta V_{oc}^{J_{sc}} = \frac{k_B T}{q} \ln\left(\frac{J_{sc}^{SQ}}{J_{sc}}\right). \tag{2.18}$$

The logarithmic relationship results in comparably low voltage losses of 17.5 mV and 5.6 mV for a 50% and 20% decrease in J_{sc} compared to the Shockley-Queisser limit, with the latter roughly corresponding to the value of today's highest performing OSCs [61]. Reduced photocurrents arise from losses in charge carrier collection or incomplete absorption. The latter manifests in gradual absorption onsets or an EQE below unity.

ΔV_{oc}^{rad} in equation 2.17 capture additional radiative losses beyond those covered by ΔV_{oc}^{SQ}, and arise from broad absorption tails. For inorganic solar cells, this is mainly caused by disorder resulting in an exponentially decaying tail in the density of states of the sub-gap

region. For OSCs, the energetic difference between CT and singlet states is a dominant contributor to radiative losses [24], and depending on the CT state properties these losses can vary between 10s mV to 100s mV [90].

Finally, $\Delta V_{oc}^{nr} = V_{oc}^{rad} - V_{oc}$ accounts for the remaining losses. Non-radiative losses in OSCs are usually on the order of $200 - 500$ mV [91], with some efficient NFA-based blends achieving losses as low as 150 mV [92]. While the exact mechanisms of non-radiative recombination are still debated, ΔV_{oc}^{nr} is generally attributed to high energy phonons and vibration-mediated energy losses [17], [93]. For fullerene-based OSCs, ΔV_{oc}^{nr} was found to inversely scale with the CT state energy as described by the energy gap law [17], [94], i.e. systems with larger E_{CT} generally show lower ΔV_{oc}^{nr}. This observation was rationalized considering that systems with low E_{CT} show an increased wave function overlap with higher order vibrational modes of the ground state, increasing the probability of non-radiative recombination [17]. Interestingly, many NFA-based blends do not follow the energy gap law [92].

2.3.5.4 Voltage Losses - Energetic State Picture

In the EN picture [83], voltage losses are calculated with respect to the energetic states present in OSCs, i.e. singlet and CT states,

$$\begin{aligned} \Delta V^{EN} &= E_{S_1}/q - V_{oc} \\ &= (E_{S_1} - E_{CT})/q + (E_{CT}/q - V_{oc}^{rad}) + (V_{oc}^{rad} - V_{oc}) \\ &= \Delta V_{oc}^{CT} + \Delta V_{oc}^{rad,CT} + \Delta V_{oc}^{nr}. \end{aligned} \tag{2.19}$$

Here, E_{S_1} is reference energy as described earlier. V_{oc}^{rad} and thus ΔV_{oc}^{nr} are defined identically to the DB analysis. The radiative losses, on the other hand, are defined differently in the two approaches and cannot be directly compared. Figure 2.12 shows a schematic of the relevant energy levels and voltage losses in both frameworks. ΔV_{oc}^{rad} in the DB picture is generally larger than $\Delta V_{oc}^{rad,CT}$ in the EN picture since some loss contributions are already captured by ΔV_{oc}^{CT}.

ΔV_{oc}^{CT} emphasizes the importance of the CT state energy for determining the V_{oc} of OSCs and is sometimes referred to as the energetic offset or driving force for exciton separation,

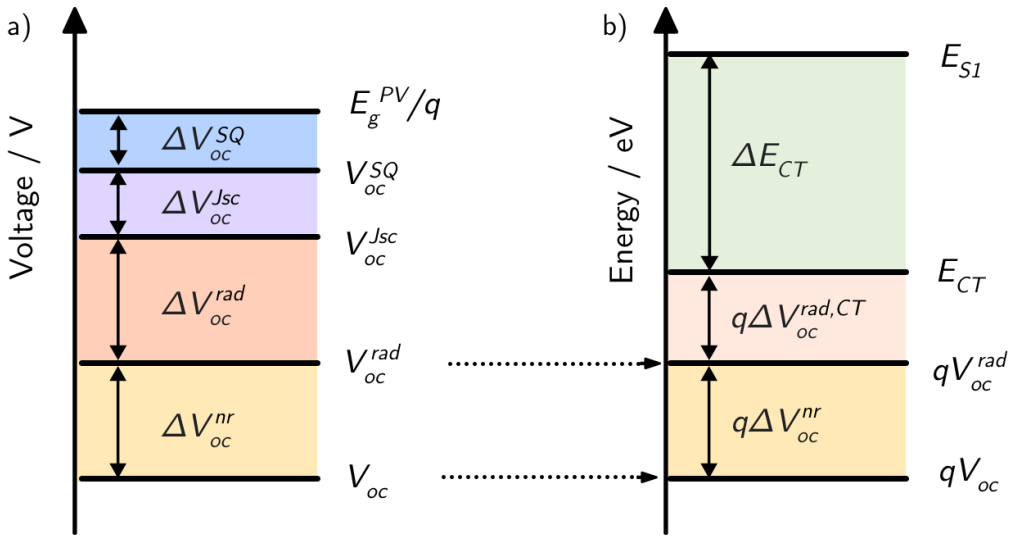


Figure 2.12: Schematic of relevant energy levels and voltage losses in a) the detailed balance (DB), and b) the energetic state (EN) picture. In the DB picture, voltage losses are calculated with respect to the "photovoltaic band gap" (E_g^{PV}). This energy is reduced by ΔV_{oc}^{SQ} compared to the Shockley-Queisser limit (V_{oc}^{SQ}), which defines the theoretical upper limit of V_{oc}. ΔV_{oc}^{Jsc} denotes losses from an imperfect short-circuit current density due to non-unity EQE, and ΔV_{oc}^{rad} and ΔV_{oc}^{nr} describe radiative and non-radiative losses. In the EN picture, the singlet energy E_{S_1} is used as a reference energy that is related to the CT state energy E_{CT} by ΔE_{CT}. Radiative losses $\Delta V_{oc}^{rad,CT}$ are defined differently from the DB picture. Non-radiative voltage losses are calculated as the difference between the radiative upper limit (V_{oc}^{rad}) and the measured V_{oc} in both frameworks. Reused from Jungbluth et al. [1] with permission under CC BY 4.0.

as described earlier. The relation of ΔV_{oc}^{CT} to the IE and EA of the donor and acceptor molecules in the blends and the resulting impact on device performance is still debated [95], [54], and is a focus of this thesis.

Reducing $\Delta E_{CT} = E_{S_1} - E_{CT}$ increases V_{oc}^{rad} and decreases ΔV_{oc}^{rad} in the DB picture. Major performance improvements of OSCs, for instance the development of NFAs, were motivated by reducing ΔE_{CT} or ΔV_{oc}^{rad}.

While the physics of OSCs is well represented in the EN picture, this method relies on fitting CT state energies from experimental data, which comes with its own intricacies and challenges as explained in Chapters 3 and 5. In addition, it fails to easily show that the maximum attainable voltage will always be lower than the reference limit due to the thermodynamic considerations captured by ΔV_{oc}^{SQ}.

By combining the reciprocity theorem and classical Marcus theory (which is introduced and discussed in Chapter 3), Vandewal et al. derived a new expression for V_{oc}^{rad} in terms of CT state properties [24],

$$V_{oc}^{rad} = \frac{E_{CT}}{q} - \frac{k_B T}{q} \cdot \ln\left(\frac{f q 2\pi (E_{CT} - \lambda)}{J_{sc} h^3 c^2}\right), \tag{2.20}$$

where E_{CT} is the CT state energy, f is an absorption pre-factor dependent on the oscillator strength of the optical transition between the ground and CT state, and λ describes the reorganization energy of the molecule upon charge transfer. Equations like this are very helpful for connecting molecular and blend properties to measurable performance characteristics. For instance, equation 2.20 predicts an almost linear correlation between V_{oc}^{rad} and E_{CT}/q.

Importantly, equation 2.20 was derived under the assumption that all radiative recombination occurs via the CT state, which is reasonable considering the steep decay of the black-body spectrum at high energies. In addition, it is assumed that all EQE and EL spectral features can be described by classical Marcus theory, which only implicitly accounts for static disorder, and disregards the influence of phonon modes and energetic hybridization. Given how relevant CT states are for investigating the causes of voltage losses in OSCs, an in-depth discussion on the accurate analysis of CT state properties, which is the focus of the next chapter, is paramount.

3 | The Physics of Charge Transfer States

Building on the previous chapter, which covered the physics of organic semiconducting molecules and introduced the donor-acceptor heterojunction concept for well-performing OSCs, this chapter focuses on the physics of charge transfer (CT) states that form at the donor:acceptor interface. An accurate determination of CT state properties is not only important for voltage loss analyses, but ultimately paramount for investigating the fundamental working principles of OSCs and determining opportunities for performance improvements. This chapter provides an in-depth overview of the different theoretical frameworks that are traditionally applied to describe CT in OSCs. More specifically, we draw on the work by Marcus [96], [97], [98], [99], [100] and Jortner [101], amongst others [22], [102], [103], to discuss classical, semi-classical, and quantum mechanical models describing Gaussian-distributed CT states. In addition, we discuss recent advances in the development of three-state models that account for the hybridization between ground, CT, and excited singlet states [104], [92], [105], [106]. We provide an in-depth overview of the underlying assumptions and constraints of each model, as well as a guide for when each model is most applicable.

This chapter is based on A. Jungbluth, P. Kaienburg, M. Riede. Charge transfer state characterization and voltage losses of organic solar cells. J. Phys. Mater. ***5*** *024002 (2022) [1]. Text and figures were reproduced or adapted with permission under CC BY 4.0.*

3.1 Marcus Theory

3.1.1 Charge Transfer Events & Transition Rates

Marcus theory was originally developed for chemical reactions in solution but has since been applied to other areas of chemistry and physics to describe CT processes from electron donors to electron acceptors [96], [97], [100]. With this, Marcus theory has proven useful to describe CT processes between organic semiconductors in thin films. Marcus theory relies on the Franck-Condon principle, introduced in Section 2.1.2, which states that CT is faster than the motion of a nucleus, and that electronic transitions favorably occur between vibrational energy states with wave function overlap. In addition, it assumes energy conservation during the CT process. These assumptions have clear implications on how CT between an initial state and a final state is understood to proceed, which is discussed in detail in this chapter.

From thermodynamic principles, the Gibbs free energy (G) of a system depends on the internal energy (U), the pressure (P), volume (V), temperature (T), and entropy (S) as

$$G = U + PV - TS. \tag{3.1}$$

To describe the change in Gibbs free energy (ΔG) upon CT from an initial state to a final state, the CT process is assumed to be isobaric and that changes in the entropic term can be neglected. As a result, the Gibbs free energy is directly related to the internal energy U. The internal energy can be further approximated as the potential energy of the system of interest. In most cases, organic semiconducting molecules and their atomic bonds are modelled as simple harmonic oscillators. This allows to express the potential energy as having a parabolic dependence on the reaction coordinate, a generalized quantity that describes the position, and the translational and vibrational movement of all atomic nuclei.

Figure 3.1 shows a schematic of free energy curves of the ground, excited, and CT state. As described earlier, classical Marcus theory assumes that transitions between states are isoenergetic (only horizontal transitions on the free energy diagram are allowed), and that charge transfer is faster than the movement of nuclei (only vertical transitions are allowed).

The only instance where both conditions are simultaneously met is at the intersection points of the free energy parabolas, marked by red circles in Figure 3.1.

For a localized exciton to undergo CT from the lowest vibronic excited state (D^*/A) to the CT state (D^+/A^-), an energetic barrier (ΔG^*) between the free energy curves needs to be overcome. Note that the same logic applies for electron or hole transfer if donor or acceptor molecules are excited. Upon CT, the free energy of the system is lowered, and the reaction coordinate is changed, resulting in molecular reorganization realized through molecular deformation or a change of atomic positions, bond lengths, and angles. Marcus derived the height of the potential energy barrier, corresponding to the energetic difference between the minimum energy of the CT state and the intersection point of the excited and CT state parabolas, as

$$\Delta G^* = \frac{(\Delta G_0 + \lambda)^2}{4\lambda}, \tag{3.2}$$

where ΔG_0 describes the energetic difference between the minima of the free energy curves of the initial and final state, and λ describes the reorganization energy. The reorganization energy is determined as the excess energy of one state at the minimum energy nuclear coordinate of another state. We would like to note that Marcus theory is generally discussed in the context of charge transfer from the excited state to the CT state. For simplicity, Figure 3.1 also visualizes this transition. However, when measuring CT state absorption or emission, we are usually interested in the direct transition between the ground and CT state. In this case, the same logic applies, with ΔG_0 describing the energetic difference and λ denoting the molecular reorganization between the ground and CT state.

According to Boltzmann statistics, the transition rate of a reaction with an activation energy ΔG from an initial state i to a final state j is proportional to

$$k_{i \to j} \propto e^{(-\frac{\Delta G}{k_B T})}, \tag{3.3}$$

where k_B is the Boltzmann constant, and T is the temperature. As discussed in Section 2.1.2, Fermi's golden rule describes the transition rate between the initial and final state as

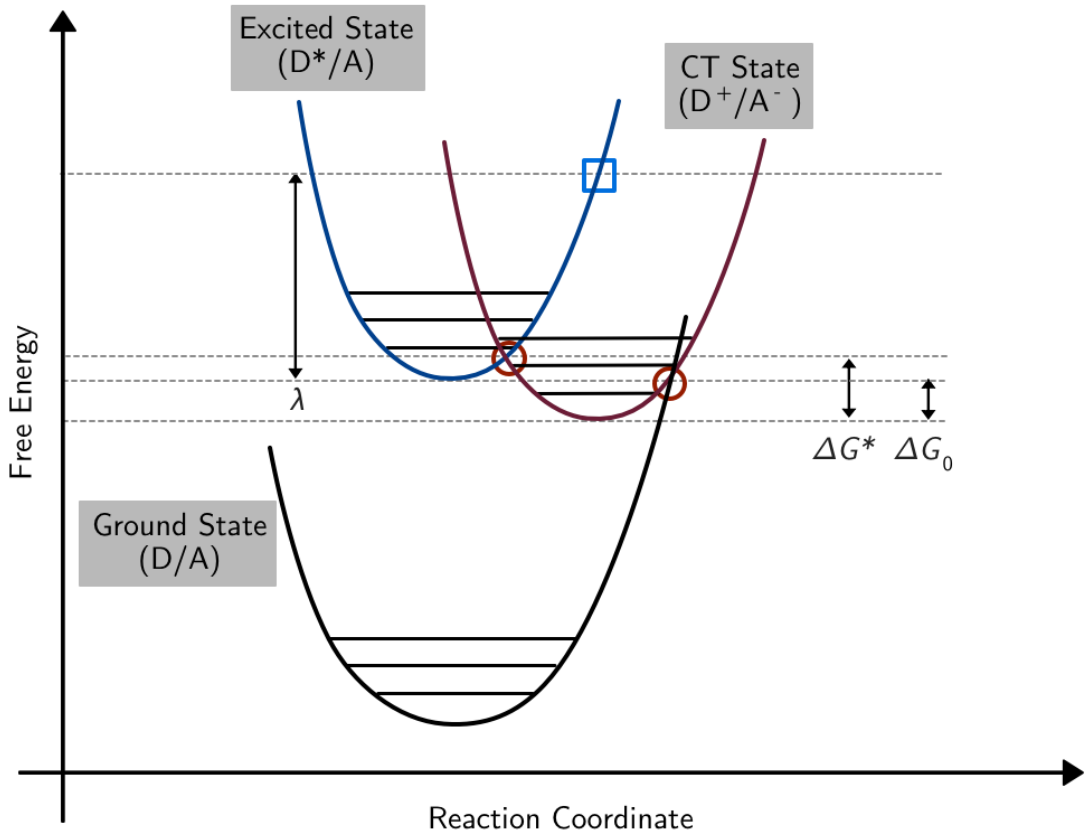


Figure 3.1: Schematic of parabolic free energy curves of the ground, excited, and CT state as a function of reaction coordinate. The horizontal lines indicate vibrational energy states whose quantized nature is only accounted for in an extension of Marcus theory. The potential energy barrier between the excited and the CT state is given by ΔG^*, and the difference between the minima of the free energy curves is given by ΔG_0. For clearer illustration, this figure shows CT from the excited state to the CT state. However, the same logic applies to direct transitions between the ground and CT state. The reorganization energy λ describes the amount of energy a molecule minimizes when undergoing CT. λ is determined as the difference in free energy between the initial state at its energetic minimum, and the energy the system would have if it was still in the initial state but at the reaction coordinate of the energetic minimum of the final state (highlighted as blue square). The red circles show the intersection points between the free energy curves of the excited and CT state (left) and the ground and CT state (right) where isoenergetic transitions at the same reaction coordinate are possible. Reused from Jungbluth et al. [1] with permission under CC BY 4.0, and originally adapted with permission from Clarke et al. [107], Copyright 2010 American Chemical Society.

$$k_{i\to j} = \frac{2\pi}{\hbar}|\langle\Psi_j|H'|\Psi_i\rangle|^2\rho, \tag{3.4}$$

where $\Psi_{i,j}$ denotes the eigenstates of the initial or final state, H' is the Hamiltonian describing the interaction between states, and ρ is the density of final states. The matrix element of perturbation ($\langle\Psi_j|H'|\Psi_i\rangle$) can be separated into electronic and vibrational contributions, which depend on the electronic coupling term (I_{ij}) and the Franck-Condon factor (FC) of the vibrational transition,

$$k_{i\to j} = \frac{2\pi}{\hbar}|I_{ij}|^2 \cdot FC. \tag{3.5}$$

In addition, we can relate equation 3.3 to the density of final states and connect the height of the potential energy barrier, as derived via Marcus theory, to the activation energy of an optoelectronic transition. This results in an equation relating the transition rate to the reorganization energy and the energetic difference between an initial and final state [18], [108],

$$k_{i\to j} = \frac{|I_{ij}|^2}{\hbar}\sqrt{\frac{\pi}{\lambda k_B T}}e^{-(\frac{(\Delta G+\lambda)^2}{4\lambda k_B T})}, \tag{3.6}$$

with

$$FC = \frac{1}{\sqrt{4\pi\lambda k_B T}}e^{-(\frac{(\Delta G+\lambda)^2}{4\lambda k_B T})}. \tag{3.7}$$

Equation 3.6 assumes that the thermal energy is significantly larger than the phonon energy ($k_B T >> \hbar\omega$), meaning that the quantum nature of molecular vibrations does not need to be considered explicitly [101]. Even though some work argues that this assumption is satisfied above 100 K for molecules typically used in OSCs [102], other accounts suggest that the quantum nature of phonons needs to be explicitly accounted for [101], [102], [109].

Figure 3.2 shows calculations of the transition rate as a function of the energetic offset (ΔG_0) and reorganization energy (λ) and applying Marcus theory (equation 3.6). Note that this

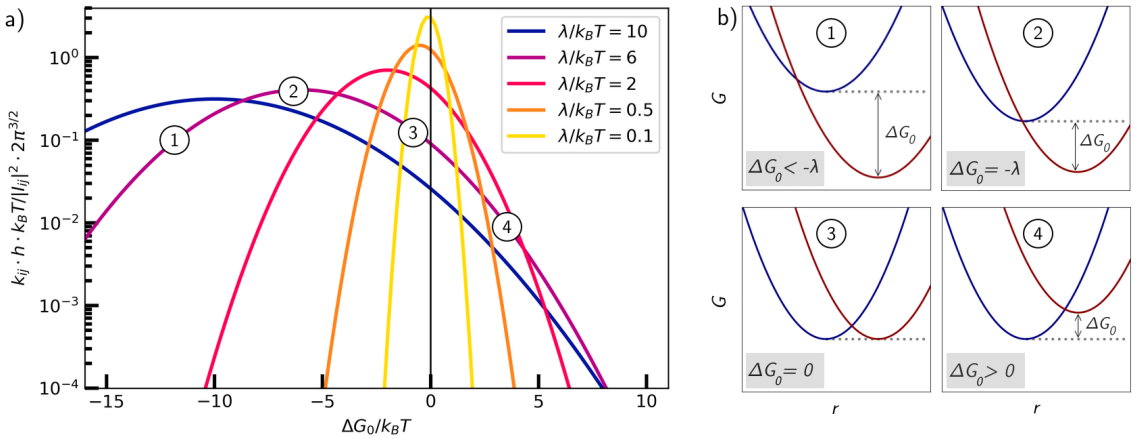


Figure 3.2: a) Transition rates as a function of energetic offset (ΔG_0) and reorganization energy (λ) between the relaxed initial and final state. Transition rates are reduced for uphill processes ($\Delta G_0 > 0$) and in the Marcus inverted regime (MIR; $\Delta G_0 > -\lambda$). b) Schematics of potential energy curves of initial states (blue) and final states (red) for different energetic offsets. Case 1 describes the MIR. The most efficient charge transfer is achieved for case 2. The numbers in a) show where the four cases might fall on the transfer rate vs. ΔG_0 curve. Reused from Jungbluth et al. [1] with permission under CC BY 4.0, and originally adapted with permission from Tress [18], Copyright 2014 Springer Nature.

discussion primarily focuses on thermally activated transitions that are relevant for charge transfer and exciton dissociation, rather than the direct absorption/emission of CT states. As intuitively expected, if the energetic minimum of the final state is higher than of the initial state ($\Delta G_0 > 0$, panel 4 in Figure 3.2b) the transition rate severely decreases. Surprisingly, Marcus theory predicts the same for systems with large energetic offsets ($\Delta G_0 << 0$, panel 1 in Figure 3.2b). This regime where transition rates decrease with increasing energetic offset is called the Marcus inverted region (MIR) [97], [96], [100], [98], [99].

The MIR arises from the requirement of isoenergetic charge transfer and can be rationalized considering that transitions need to occur at a reaction coordinate smaller than the equilibrium coordinate of either the initial or final state. The MIR has been challenging to verify experimentally [110], though recent work showed the impact of the interfacial driving force on CT processes in thin-film polymer blends [102], [111], quantified the reorganization energy for photoinduced electron transfer in the MIR of a carbon nanotube heterojunction [112], and investigated charge transport in transistors based on thin film small molecules [110] and molecular junctions based on self-assembled monolayers [113].

The highest transition rate occurs for systems where $\Delta G_0 = \lambda$ (case 3 in Figure 3.2b) and

when potential energy parabolas intersect at the equilibrium reaction coordinate of the initial state. Larger λ reduce the differential dependence on the activation energy.

3.1.2 Determination of CT State Properties

CT states between electron donors and acceptors were shown to be the lowest energy absorbing and emitting states in organic semiconductor blends [22], [114], [23], [24], [115]. This implies that absorption and emission can occur directly between the ground and the CT state. With this, ΔG_0 in equation 3.2 is dependent on the energy of the CT state. According to Vandewal et al. the absorption cross-section (σ_{CT}) can be described by Marcus theory as

$$\sigma_{CT}(E)E = \frac{f_{CT}}{\sqrt{4\pi\lambda_{CT}k_BT}} e^{\left(-\frac{(E_{CT}+\lambda_{CT}-E)^2}{4\lambda_{CT}k_BT}\right)}, \tag{3.8}$$

where E_{CT} is the CT state energy, λ_{CT} is the reorganization energy between the ground and CT state, capturing broadening from both intra- and inter-molecular vibrations, f_{CT} is the oscillator strength describing the optical dipole coupling between the two states, and E is the photon energy.

As briefly discussed earlier, the reorganization energy describes the amount of energy the donor-acceptor complex can reduce by undergoing charge transfer and molecular reorganization. In the final state, a minimum energy is reached for different positional, translational, vibrational, or torsional properties of the molecules. As such, the reorganization energy is more than just a fit parameter, but a fundamental property of the donor-acceptor complex. The reorganization energy between the ground and the CT state is, in some cases, e.g. for rigid molecules like C_{60}, similar to the reorganization energy between the excited state and the CT state [102], [116], [117].

If CT states are measured through sensitive absorption techniques, for example through EQE measurements (discussed in more detail later), the CT state absorption cross-section needs to be linked to the EQE. The EQE can be expressed as the product of the absorption rate (η_a), and the internal quantum efficiency (IQE). Neglecting interference effects (the validity of this assumption is discussed in detail later), and assuming weak absorption with

well-reflecting back electrodes, the EQE can be approximated as

$$EQE(E) = \eta_a(E) \cdot IQE(E) \approx 2d \cdot \alpha(E) \cdot IQE(E), \tag{3.9}$$

where d is the absorber layer thickness, and α is the absorption coefficient [24]. The absorption coefficient in the spectral region of CT absorption equals the product of the absorption cross-section and the number of CT complexes, $\sigma_{CT}N_{CT}$. With this, the EQE can be expressed as

$$EQE(E) = \frac{f}{E\sqrt{4\pi\lambda_{CT}k_BT}} e^{\left(-\frac{(E_{CT}+\lambda_{CT}-E)^2}{4\lambda_{CT}k_BT}\right)}, \tag{3.10}$$

with f as an absorption pre-factor that is dependent on the oscillator strength, $f = 2d\eta_a N_{CT} f_{CT}$. Assuming reciprocity between absorption and emission [20], [84], [118], a similar expression to equation 3.10 can be derived for the EL,

$$EL(E) = \frac{E \cdot f'}{\sqrt{4\pi\lambda_{CT}k_BT}} e^{\left(-\frac{(E_{CT}-\lambda_{CT}-E)^2}{4\lambda_{CT}k_BT}\right)}. \tag{3.11}$$

If the singlet and CT state absorption are spectrally resolved in the EQE, equation 3.10 can be used to determine the CT state energy, reorganization energy, and absorption pre-factor by fitting a Gaussian linewidth to the low energy EQE tail. Similarly, EL spectra can be fit with equation 3.11. In an alternative approach, EL and EQE measurements are combined to determine the CT state energy. For this, the EQE and EL spectra are reduced to remove the dependence on energy in the exponential pre-factor.

$$EQE(E) \cdot E = EQE_R(E) = \frac{f}{\sqrt{4\pi\lambda_{CT}k_BT}} e^{\left(-\frac{(E_{CT}+\lambda_{CT}-E)^2}{4\lambda_{CT}k_BT}\right)}, \tag{3.12}$$

$$\frac{EL(E)}{E} = EL_R(E) = \frac{f'}{\sqrt{4\pi\lambda_{CT}k_BT}} e^{\left(-\frac{(E_{CT}-\lambda_{CT}-E)^2}{4\lambda_{CT}k_BT}\right)}. \tag{3.13}$$

The EL spectrum is then aligned to the same height as the (absolute) EQE such that $f = f'$, and the CT state energy is determined as the intersection point between the two spectra [24].

3.1.3 Static & Dynamic Disorder

Classical Marcus theory as discussed until this point describes absorption and emission of a single absorber with a single value for E_{CT}, and models the observed vibrational broadening in terms of the reorganization energy λ [51]. However, disordered films like the photovoltaic active layers of OSCs are not expected to show one single CT state energy. Instead, the statistical spread of molecular packing in disordered thin films leads to microstructural disorder at the D:A interface. This microstructural disorder translates into interfacial energetic disorder and an inhomogeneously broadened distribution of CT states [109], [51], [103], [119]. Inhomogeneous broadening means that D:A interfaces in a disordered thin film might show different interfacial E_{CT}, but that the collection of all E_{CT} remains Gaussian distributed. Further evidence for the existence of a distribution of CT states comes from the fact that equations 3.10 and 3.11 predict a strong spectral narrowing at decreasing temperature which has not been observed experimentally.

Burke et al. first described the impact of microstructural and energetic disorder by disentangling dynamic (i.e. temperature dependent) and static (i.e. temperature independent) contributions [51]. They showed that equations 3.10 and 3.11 can be used to model CT state absorption and emission if the experimentally determined CT state energy E_{CT}^{exp} and reorganization energy λ_{CT}^{exp} are understood to already incorporate static and dynamic disorder contributions,

$$E_{CT}^{exp} = E_{CT} - \frac{\sigma_{CT}^2}{2k_BT}, \tag{3.14}$$

$$\lambda_{CT}^{exp} = \lambda_{CT} + \frac{\sigma_{CT}^2}{2k_BT}, \tag{3.15}$$

where σ_{CT} describes the static disorder, and $2\lambda_{CT}k_BT$ is the dynamic disorder [51]. The possible impact of static disorder on spectral broadening and device performance is still heavily debated in literature and likely depends on the material system under investigation. Burke et al. showed that static disorder contributions between $60 - 100$ meV adequately describe their studied selection of polymer:PCBM solar cells, a result that has also been

confirmed elsewhere [109]. In comparison, other studies argue that static disorder in OSCs is insignificant for determining the spectral linewidth of OSCs [103], [119], [120]. A detailed discussion on alternative sources of spectral broadening follows later.

Nonetheless, equations 3.14 and 3.15 highlight the difficulty of correctly separating experimental quantities from fundamental properties. For the equations presented in this thesis, unless specified otherwise, E_{CT} and λ_{CT} refer to the experimentally determined values that incorporate disorder contributions.

3.1.4 Limitations of Classical Marcus Theory

3.1.4.1 Interference Effects

One of the assumptions that leads to the derivation of equations 3.10 and 3.11 is that inferences effects in the thin active layers of OSCs can be neglected. This, however, is not guaranteed to be a true assumption. The influence of microcavity effects and out-coupling on the emission spectra of organic LEDs is documented in detail [121], [122], [123], [124], [125], [126]. In the context of OSCs, optical simulations are commonly used to understand interference effects and tune device stacks to improve in-coupling of incident light for increased charge generation [127], [128], [129]. In addition, microcavities are used to increase device performances by enhancing the EQE [130], [131], [132], [133], [134], or specifically enhance CT state absorption to realize organic infrared photodetectors with improved sensitivity [135], [136].

According to List et al. [137], most optical studies of OSCs focus on optimizing donor and acceptor molecule absorption and thus increasing the EQE, but little work has been done to understand the corresponding effect of microcavities on emission spectra of CT state emission. In reference [137], the authors fabricate a range of OSCs, changing the reflective electrodes and varying active layer thicknesses, to show that interference effects play a significant role in determining the spectral shape of the EL. Without correction, applying equation 3.11 to fit the relevant CT state parameters leads, in most circumstances, to incorrect results.

Building on the work by List et al., Armin et al. investigate the effects of interference on both the low energy tail of the EQE, the high energy tail of the EL, and the intersection between the two [79]. Their work confirms that interference effects influence both the spectral shape of the emission spectrum and the measured EQE. The determination of E_{CT}, λ_{CT}, and the absorption pre-factor f therefore leads to different results, depending on whether the EQE or the EL are fit. These discrepancies arise from the fact that EL and EQE are device or "external" quantities, while CT state properties are material or "internal" quantities. Simple models that relate the two are not always appropriate. The results of Armin et al. do not challenge the validity of the detailed balance principle, but highlight that interference effects can break reciprocity if mode coupling and microcavities are experienced differently in emission and absorption processes [79].

EL spectra are more severely affected by interference effects since microcavities can lead to multi-modality (multiple peaks) in the spectra [79]. To increase the accuracy of CT state fitting, emission and absorption spectra therefore need to be corrected for interference effects. A process to correct EL spectra is presented in reference [137]. To correct the EQE, knowledge of the absorption coefficient of the active layer blend is required. This is a straightforward task above the optical gap, where the complex reflective index can be determined using transmission, reflection, or spectroscopic ellipsometry measurements [138]. Since absorption in the sub-gap region is orders of magnitude lower than above the optical gap, precise measurements of the complex refractive index below the optical gap are very challenging.

Reference [79] draws on the work of Kaiser et al. [138] to correctly determine the absorption coefficient in the sub-gap region. In their presented approach, the authors use the complex refractive index to model absorption above the optical gap via the transfer matrix approach. The results are subsequently combined with highly sensitive sub-gap EQE measurements to determine optical constants in the low energy region [138]. The code to perform these numerical calculations is publicly available in the Supplementary Materials of reference [138].

As expected, interference effects strongly depend on device architectures and active layer thicknesses. Armin et al. further show that the fit results of uncorrected EQE spectra only match those of corrected absorption spectra when active layer thickness are thin (i.e. $\approx$ 100 nm) [79]. This is good news for evaporated small molecule OSCs, where active layer

thicknesses are ≤ 100 nm, but further highlights the need to correct for interference effects when active layers are thicker, as is the case for many solution-processed polymer solar cells.

3.1.4.2 Low Offset Systems

If the CT state is not spectrally resolved in the EQE [139], [140], [141], standard EQE fitting approaches may be inadequate. This is the case for systems with low energetic offset between CT and singlet states [142], [106], [57], most of which are based on NFAs [139], [140], [141], [143], [144], though a few examples of low energetic offsets have also been reported for donor:fullerene blends [83], [145].

Material systems that do not show distinct sub-gap absorption features are generally classified as being "low offset" or "low driving force" meaning that CT and singlet states are close in energy. To determine the CT state energy of low offset systems, it was suggested to combine absorption and emission measurements [24], [83] and take E_{CT} as the intersection point of the reduced EQE and EL spectra (equations 3.12 and 3.13). As discussed earlier, this requires that interference effects do not obstruct the use of EL data for CT fitting, and that reciprocity between EL and EQE measurements is given. The critical point in determining the intersection point is to align the height of absorption and emission spectra.

For cases where CT state absorption is clearly resolved in an EQE spectrum, the EL is aligned to match the height of the (fitted) CT state peak in the EQE (e.g. Figure 3b in reference [83]). Without a clearly defined CT state peak, consistently aligning the EL to the height of the CT state absorption becomes substantially more challenging. Often, the EL is aligned to the first resolvable peak in the absorption spectrum (e.g. Figure 3e in reference [83]), even if it cannot be assigned clearly to the CT state.

In the following, we demonstrate why this approach is insufficient, possibly leading to > 50 meV errors of E_{CT}. In addition to assuming that a lack of sub-gap absorption features arises from a low energetic offset between CT and singlet states, aligning EL spectra to the first strongly absorbing peak implies that the oscillator strength of the $S_0 \rightarrow$ CT state transition is similar to that of the $S_0 \rightarrow S_1$ transition. However, direct transitions into the CT state are substantially weaker than transitions between ground and singlet states [83], [24], [146].

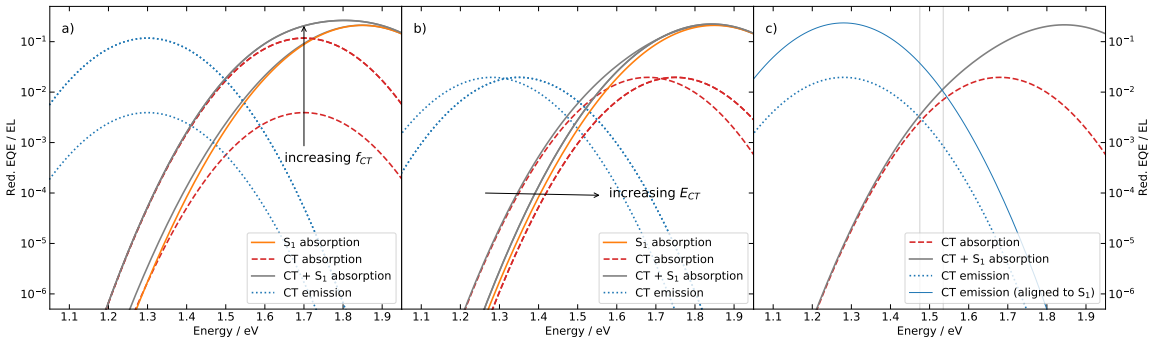


Figure 3.3: Schematics of simulated EQE and EL spectra for varying CT state properties and using equations 3.12 and 3.13. All modelling parameters are chosen such that the CT state (red dashed line) is not spectrally resolvable from the S_1 peak (orange solid line), as is the case for low driving force systems. The blue dotted lines show the CT state emission spectra. a) The CT oscillator strength is increased from $0.001 - 0.030$ eV^2, with $E_{S_1} = 1.60$ eV, $E_{CT} = 1.50$ eV, $\lambda_{CT} = 0.20$ eV. b) The CT state energy is increased from $1.48 - 1.55$ eV, with $E_{S_1} = 1.60$ eV, $f_{CT} = 0.005$ eV^2, $\lambda_{CT} = 0.20$ eV. c) Example of how aligning the EL to the height of the S_1 peak leads to an intersection point that is higher in energy (right vertical line) than if the EL is aligned to the correct height of the CT state absorption peak (left vertical line). Reused from Jungbluth et al. [1] with permission under CC BY 4.0.

Figure 3.3 shows schematics of simulated EQE spectra and EL spectra modelled with varying CT state properties. The absorption behavior of the CT state (red dashed line) and singlet (orange solid line) are modelled as Gaussians according to standard Marcus theory and using equation 3.12. Grey solid lines show the sum of the CT and singlet state absorption contributions, assuming that the two transitions can be treated independently. In an EQE experiment, this sum would be measured. The blue dotted lines show CT state emission spectra, modelled with the same parameters and using equation 3.13. All modelling parameters are chosen such that the CT state is not resolvable from the S_1 peak.

Figure 3.3a shows the effect of varying the absorption pre-factor f in equation 3.12, which, assuming λ_{CT} and E_{CT} stay constant, can be directly equated to changes in the CT state oscillator strength f_{CT}. On the other hand, Figure 3.3b shows the effect of increasing E_{CT} and reducing the energetic gap between the CT and singlet state. The exact modelling parameters are reported in the figure caption. These examples show that various parametrizations of CT and singlet states yield similar EQE spectra without spectrally resolved CT state absorption shoulders. It is thus not appropriate to simply assume that the CT oscillator strength is equal to the singlet oscillator strength whenever no clear CT shoulder is visible.

Importantly, for the intersection point to recover the value of E_{CT} that is used as a model input, the height of the emission peak needs to match that of the CT state absorption. If the emission spectra are instead aligned to match the first resolvable peak, the extracted CT state energy may carry a large error. In the example in Figure 3.3c, an error of 50 meV arises in the determination of the intersection point. When the alignment of the EL is done correctly, the intersection point of the EL with the (fitted) CT state absorption must be considered rather than the full EQE that would be determined in an experiment, since the latter also contains contributions from absorption of the singlet state.

3.2 Marcus-Levich-Jortner Theory

3.2.1 Phonon Modes & Transition Rates

Whether Marcus theory is fundamentally applicable to describe CT processes in organic semiconductors is still heavily debated in literature [102], [109], [103]. Moving beyond the limitations discussed in the previous paragraphs, several arguments [101] have been brought forward to justify why classical Marcus theory, neglecting any quantum physical effects, does not always describe charge transfer in organic molecular solids accurately. Some of the proposed extensions to Marcus theory are discussed in the following sections.

Classical Marcus theory as presented in equation 3.6 assumes that the energy of internal ($\hbar\omega_i$) and external ($\hbar\omega_e$) vibrational (phonon) modes is substantially smaller than the thermal energy of the surrounding (i.e. $\hbar\omega_i + \hbar\omega_e = \hbar\omega << k_B T$) [101]. Under this assumption, thermal energy is sufficient to reach higher vibrational energy states to facilitate charge transfer, and the quantum nature of phonons does not need to be considered explicitly. However, it has been argued that in organic thin films, especially in the Marcus inverted regime and at low temperatures, transitions are not just governed by thermal activation but quantum tunnelling between an initial and a final state becomes significant [102], [147], [148].

Internal phonon modes describe vibrations within one molecule (intra-molecular) and are indicated as horizontal levels in the potential energy curves of energetic states (refer back to Figure 3.1). Intra-molecular vibrations are on the order of $50 - 300$ meV [109], and are

often dominated by the high frequency C−H and C−C bond vibrations of around $150 - 180$ meV [109], [103], [119], [19], [149]. In comparison, external phonon modes describe inter-molecular processes, i.e. vibrations between molecules and their surroundings, and are usually classified as low frequency with $1 - 10$ meV [101], [109], [103], [19].

With this, external phonon modes are smaller than k_BT below ~ 120 K (where the thermal energy is 10 meV), but internal phonon modes are generally larger than k_BT, rendering the assumption that $\hbar\omega_i << k_BT$ untrue. The relative magnitude of intra-molecular phonon modes compared to thermal energy at room temperature suggests that classical Marcus theory falls short in this regime. Therefore, external phonon modes can, in the first instance, be treated classically at room temperature but high frequency internal phonon modes need to be treated quantum mechanically. This leads to an extension of equation 3.6, known as the Marcus-Levich-Jortner (MLJ) equation [101],

$$k_{l\rightarrow m} = \frac{|I_{lm}|^2}{\hbar}\sqrt{\frac{\pi}{\lambda_e k_B T}}\sum_{n=0}^{\infty}\frac{e^{-S_i}S_i^n}{n!}e^{(-\frac{(\Delta G_0+\lambda_e+n\hbar\omega_i)^2}{4\lambda_e k_B T})}. \tag{3.16}$$

Here, a transition from an initial state l to a final state m is described by the electronic coupling term $|I_{lm}|^2$, the driving force ΔG_0, and the reorganization energy (λ_e) associated with the external phonon modes. In addition, contributions of internal phonon modes are indicated by the subscript i. Equation 3.16 is, in the first instance, dependent on the dominant high frequency mode with energy $\hbar\omega_i$. This phonon contribution is summed up for all phonon quanta $n = 0 - \infty$. In analogy to equation 3.7, the quantum mechanical Franck-Condon weighted density of states is therefore given by

$$FC = \frac{1}{\sqrt{4\pi\lambda_e k_B T}}\sum_{n=0}^{\infty}\frac{e^{-S_i}S_i^n}{n!}e^{(-\frac{(\Delta G_0+\lambda_e+n\hbar\omega_i)^2}{4\lambda_e k_B T})}. \tag{3.17}$$

As introduced in Section 2.1.2, S_i is the Huang-Rhys parameter, a dimensionless factor that depends on changes in the equilibrium reaction coordinate when a system undergoes a transition from one state to another. The Huang-Rhys parameter depends on the coupling strength of a transition and is related to the reorganization energy λ as

$$S_i = \frac{\Delta Q^2 m\omega_i}{2\hbar} = \frac{\lambda}{\hbar\omega_i}, \tag{3.18}$$

where $\hbar\omega_i$ is the energy associated with the vibrational mode i, ΔQ is the change in the equilibrium reaction coordinate upon CT, and $m\omega$ is the force constant of the system. As described earlier, for rigid molecules, where the $0-0$ transition is the dominant feature in absorption or emission measurements, the Huang-Rhys factor is on the order of $S_i \leq 1$ [109]. With larger Huang-Rhys factors, the maxima of the $0-0$ transition are eventually no longer resonant, leading to a large Stokes shift between absorption and emission. Low frequency inter-molecular modes are generally described by lager Huang-Rhys factors, leading to phonon wings with a Gaussian line shape as discussed in more detail in reference [109].

Classical Marcus theory as described in equation 3.6 requires knowledge of the electronic coupling term (and therefore the oscillator strength), which can be fit from spectroscopic data [150] or determined via quantum mechanical calculations [151], [152], [153], for example using density functional theory (DFT) [154]. Otherwise, equation 3.6 is primarily dependent on E_{CT} and $\lambda_C T$. In comparison, equation 3.16 requires knowledge of dominant vibrational modes to determine $\hbar\omega$ and thereby the Huang-Rhys factor S_i. Experimentally, vibrational modes can be probed via Raman spectroscopy or determined via DFT calculations [149].

3.2.2 CT State Properties in the MLJ Framework

Following from equation 3.16, the EQE in the MLJ picture can be described by

$$EQE(E) = \frac{f}{E \cdot \sqrt{4\lambda_{CT} k_B T}} \sum_{n=0}^{\infty} \frac{e^{-S_i} S_i^n}{n!} e^{\left(-\frac{(E_{CT}+\lambda_{CT}+n\hbar\omega_i - E)^2}{4\lambda_{CT} k_B T}\right)}. \tag{3.19}$$

Importantly, applying the reciprocity relation yields an expression for the EL which is no longer mirror symmetric to the EQE [103].

$$EL(E) = \frac{E \cdot f'}{\sqrt{4\lambda_{CT} k_B T}} e^{\left(-\frac{E_{CT}}{k_B T}\right)} \sum_{n=0}^{\infty} \frac{e^{-S_i} S_i^n}{n!} e^{\left(-\frac{n\hbar\omega_i}{k_B T}\right)} e^{\left(-\frac{(E_{CT}-\lambda_{CT}+n\hbar\omega_i - E)^2}{4\lambda_{CT} k_B T}\right)}. \tag{3.20}$$

The positive vibrational contribution in the exponential ($+n\hbar\omega_i$) removes the mirror symmetric behaviour of absorption and emission spectra that was predicted by classical Marcus theory. In addition, the emission is now damped by the $e^{(-\frac{E_{CT}}{k_BT})}$ and $e^{(-\frac{n\hbar\omega_i}{k_BT})}$ pre-factors, as discussed in [103].

Following the approach presented by Burke et al. [51], equations 3.19 and 3.20 can be extended to a disordered MLJ model [109], [103],

$$EQE(E) = \frac{f}{E \cdot \sqrt{4\lambda_{CT} k_B T + 2\sigma_{CT}^2}} \sum_{n=0}^{\infty} \frac{e^{-S_i} S_i^n}{n!} e^{(-\frac{(E_{CT}+\lambda_{CT}+n\hbar\omega_i - E)^2}{4\lambda_{CT} k_B T + 2\sigma_{CT}^2})}, \tag{3.21}$$

$$\begin{aligned} EL(E) = & \frac{E \cdot f'}{\sqrt{4\lambda_{CT} k_B T + 2\sigma_{CT}^2}} e^{(-\frac{E_{CT}}{k_BT} + \frac{\sigma_{CT}^2}{2(k_BT)^2})} \\ & \times \sum_{n=0}^{\infty} \frac{e^{-S_i} S_i^n}{n!} e^{(-\frac{n\hbar\omega_i}{k_BT})} e^{(-\frac{(E_{CT}-\lambda_{CT}+n\hbar\omega_i - E)^2}{4\lambda_{CT} k_B T + 2\sigma_{CT}^2})}. \end{aligned} \tag{3.22}$$

As before, the broken mirror symmetry between the EL and EQE is apparent.

3.2.3 Multiple Phonon Modes

As mentioned earlier, the underlying assumption to treat vibrational modes classically is that the energy of the phonon mode is smaller than k_BT. For external phonon modes with energies $1 - 10$ meV [101], [109], [103], [19], this requirement is satisfied at temperatures relevant for the operation of OSCs. However, at low enough temperatures, this simplification breaks down and external phonon modes also need to be considered explicitly. This is discussed in detail in the works of Kahle et al. [109] and Göhler et al. [103]. The Franck-Condon weighted density of states is then proportional to the sum over the product of multiple phonon modes and their corresponding vibrational overtones,

$$FC \propto \sum_m \prod_i \frac{e^{-S_i} S_i^{m_i}}{m_i!}. \tag{3.23}$$

In the case where only the highest energy intra- and inter-molecular modes need to be considered, the EQE and EL become

$$EQE(E) = \frac{f}{E \cdot \sqrt{4\lambda_{CT} k_B T + 2\sigma_{CT}^2}} \times \sum_{n=0}^{\infty} \sum_{m=0}^{\infty} \frac{e^{-S_0} S_0^n}{n!} \frac{e^{-S_1} S_1^m}{m!} e^{\left(-\frac{(E_{CT}+\lambda_{CT}+n\hbar\omega_0+m\hbar\omega_1-E)^2}{4\lambda_{CT} k_B T + 2\sigma_{CT}^2}\right)}, \tag{3.24}$$

$$EL(E) = \frac{E \cdot f'}{\sqrt{4\lambda_{CT} k_B T + 2\sigma_{CT}^2}} e^{\left(-\frac{E_{CT}}{k_B T} + \frac{\sigma_{CT}^2}{2(k_B T)^2}\right)} e^{\left(-\frac{(n\hbar\omega_0 + m\hbar\omega_1)}{k_B T}\right)} \times \sum_{n=0}^{\infty} \sum_{m=0}^{\infty} \frac{e^{-S_0} S_0^n}{n!} \frac{e^{-S_1} S_1^m}{m!} e^{\left(-\frac{(E_{CT}-\lambda_{CT}+n\hbar\omega_0+m\hbar\omega_1-\frac{\sigma_{CT}^2}{k_B T}-E)^2}{4\lambda_{CT} k_B T + 2\sigma_{CT}^2}\right)}. \tag{3.25}$$

3.3 Sources of Spectral Broadening

As an intermediate summary, we now discuss how the different CT state models introduced until this point are applied to explain linewidth broadening of CT state absorption and emission. Current understanding in literature is that spectral broadening can be of homogeneous (i.e. affecting all molecules the same), or inhomogeneous nature (i.e. affecting molecules unevenly, but overall leading to a Gaussian linewidth of the collective absorption or emission) [17]. Static disorder based on a statistical distribution of molecular packing causes inhomogeneous broadening, while vibrational contributions arising from dynamic disorder affect all molecules homogeneously [109], [51], [103].

However, a lack of agreement still exists in literature on which mechanisms are dominant contributors to spectral linewidth broadening, and how this relates to molecular properties and device performance. Energetic disorder affects charge carrier generation and recombination mechanisms, therefore directly impacting device parameters like the V_{oc} [119]. Similarly, high frequency modes link to non-radiative recombination and lead to voltage losses [17]. Understanding the origin of energetic disorder and the impact of vibrational modes are amongst the most important research questions in the field of OPV. Addressing these research questions will help to estimate performance limits more accurately and improve our understanding on how dominant loss mechanisms can be overcome.

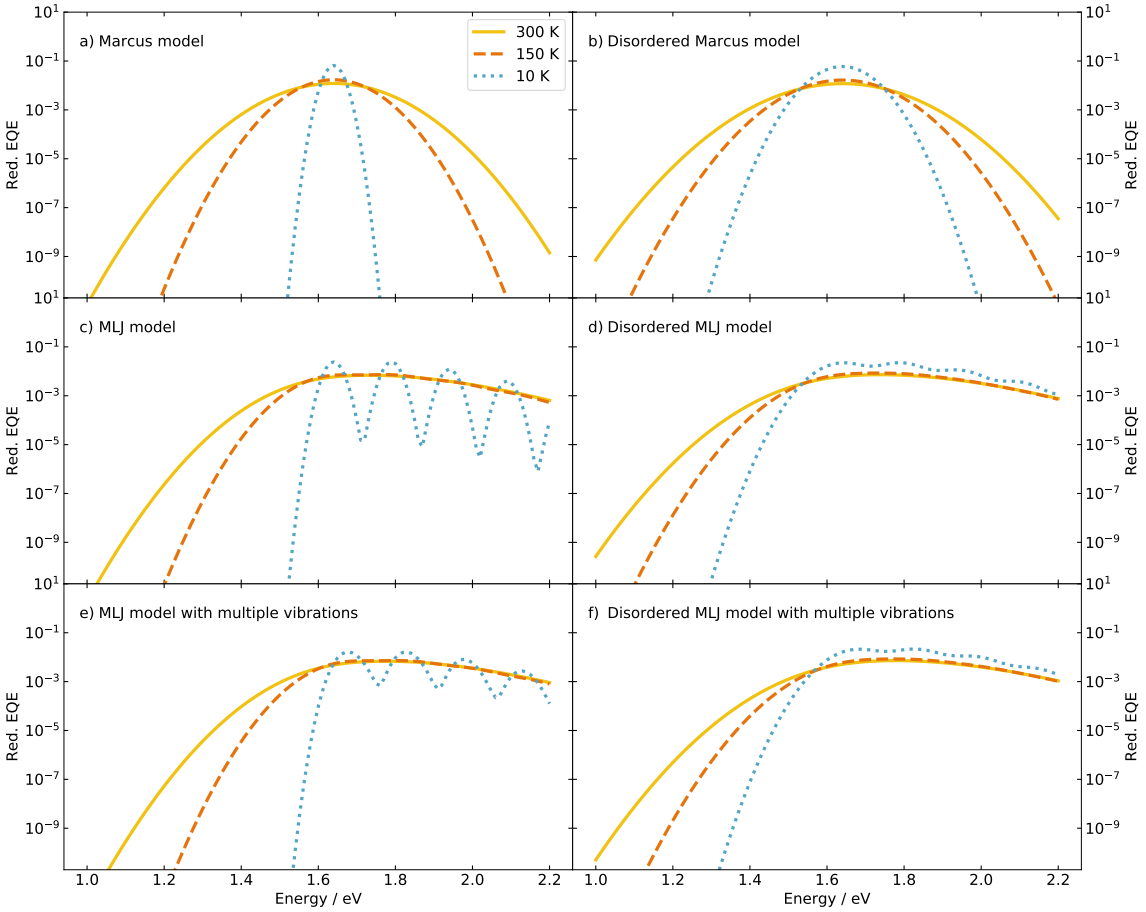


Figure 3.4: Simulated low energy EQE tails based on a-b) the Marcus model (equation 3.10), c-d) the MLJ model considering only high frequency vibrations (equations 3.19 and 3.21), and e-f) the MLJ model considering high and low frequency vibrations (equation 3.24). The left column shows models without static disorder, the right column assumes $\sigma_{CT} = 50$ meV. The modelling parameters are chosen as $E_{CT} = 1.45$ eV, $\lambda_{CT} = 190$ meV, $f = 0.003$ eV^2, $S_i = 1$, $\hbar\omega_i = 150$ meV, $S_{\text{low}} = 4$, $\hbar_{\text{low}} = 10$ meV, where the subscript "i" describes intra-molecular, high frequency vibrations, and the subscript "low" marks inter-molecular, low frequency vibrations. All equations are reduced to remove the dependence on energy. Reused from Jungbluth et al. [1] with permission under CC BY 4.0.

In the following, we compare the temperature-dependence of the different CT state models, and summarize current understanding on which model is most appropriate in different contexts. Figure 3.4 shows modelled low energy EQE tails using the CT models discussed earlier. The modelling parameters are chosen to reflect values published in literature for polymer or small molecule OSCs (e.g. [109], [119]) and are listed in the figure caption.

As discussed by Tvingstedt et al. [119], the classical Marcus model excluding static disorder predicts vanishingly small CT rates and absorption linewidths with decreasing temperatures.

This can be clearly observed in Figure 3.4a. In addition, the Gaussian variance of the spectral linewidth is predicted to be linearly dependent on temperature in the classical Marcus model, which has never been experimentally confirmed [119].

As can be seen in Figure 3.4b, the inclusion of static disorder reduces the dependence of the linewidth on temperature and leads to spectral broadening. However, the main differences between assuming zero static disorder (Figure 3.4 left column) and static disorder of 50 meV (Figure 3.4 right column) are only visible at very low temperatures and much less dominant for the other temperatures shown.

Including a quantum mechanical treatment of vibrational modes (Figure 3.4c-f) removes the mirror symmetry of the spectrum. Without static disorder, the vibrational overtones lead to strong periodic peaks in the high energy region at low temperatures, which have, to the best of our knowledge, not yet been observed experimentally. These peaks are still visible when inter- and intra-molecular modes are treated quantum mechanically, shown in Figure 3.4e, though their periodic amplitude is reduced. Including static disorder in either model substantially dampens the impact of the periodic overtones.

The work by Kahle et al. investigates how well a Franck-Condon fit, including static disorder and a quantum mechanical treatment of high and low frequency modes similar to the discorded MLJ model with multiple vibrations, describes the temperature dependent EQE and PL spectra of the MeLPP:PCBM system [109]. Their Franck-Condon fit is compared to the MLJ model treating only high frequency modes quantum mechanically. They find that both models describe the system equally well, as long as static disorder is considered [109]. In addition, they determine a static disorder contribution of 67 meV to be appropriate, matching previously reported values of $60 - 100$ meV for polymer systems [51].

Tvingstedt et al. agree that a Franck-Condon description based on high and low frequency modes is appropriate. However, they do not find experimental evidence to justify that a substantial contribution to the linewidth comes from static disorder [119]. Similar results are also shown in the theoretical work of Panhans et al. [155] and the experimental work of Göhler et al. who argue that the extended Marcus-Levich-Jortner model, accounting for low and high frequency vibrations but assuming no static disorder, adequately describes absorption and emission spectra of dilute small molecule blends [103].

In contrast, the recent work by Yan et al. criticises that the material systems studied by Tvingstedt et al. and Göhler et al., i.e. dilute donor:fullerene systems, have previously been studied precisely because morphological disorder is minimised [156]. Polymer-based solar cells show a range of disorder contributions, e.g. large conformational and torsional disorder [157], electronic anisotropy, and possible phase aggregation, that are not present in dilute small molecule blends [156].

In multiple accounts, static disorder is found to have a strong impact on CT state properties and recombination losses for polymer-based solar cells [157]. In addition, it is argued that the sphere-like nature of fullerene acceptors promotes distortion and bending of donor molecules, increasing both dynamic and static disorder. In comparison, NFAs with rigid backbones cause less disorder [157], which might be another reason for their improved performance in OSCs.

In conclusion, future studies of static and dynamic disorder should investigate both small molecule and polymer-based systems. In addition to measuring the temperature-dependence of absorption and emission, experimental and theoretical studies of the interfacial microstructure and phase aggregation are crucial to providing a more complete picture of the possible impact of static disorder on CT state properties [156].

3.4 Three-State Models

The CT state models introduced until this point all assume that absorption and emission occur via two states, i.e. the ground and CT state. However, several recent publications argue for the use of a three-state approach accounting not only for coupling between the ground and CT state, but also incorporating contributions of electronic and vibrational coupling with excited singlet (also called local excited; LE) states when CT and singlet states are close in energy. In the following sections, we discuss the impact of this energetic hybridization on potential energy curves and introduce a selection of recently published three-state models.

3.4.1 Diabatic vs. Adiabatic States

Electronic transfer processes can be described via diabatic or adiabatic states [105]. Diabatic states are defined as pristine states without hybridization, while adiabatic states are characterized by hybridization between the ground, singlet, and CT state. Figure 3.5 shows a schematic of the potential energy curves of diabatic and adiabatic states. In the context of a donor-acceptor interface, a diabatic CT state corresponds to a Coulomb-bound electron-hole pair between the D^+ cation and the A^- anion. A diabatic LE state consists of an exciton fully localized on either the donor or acceptor molecule.

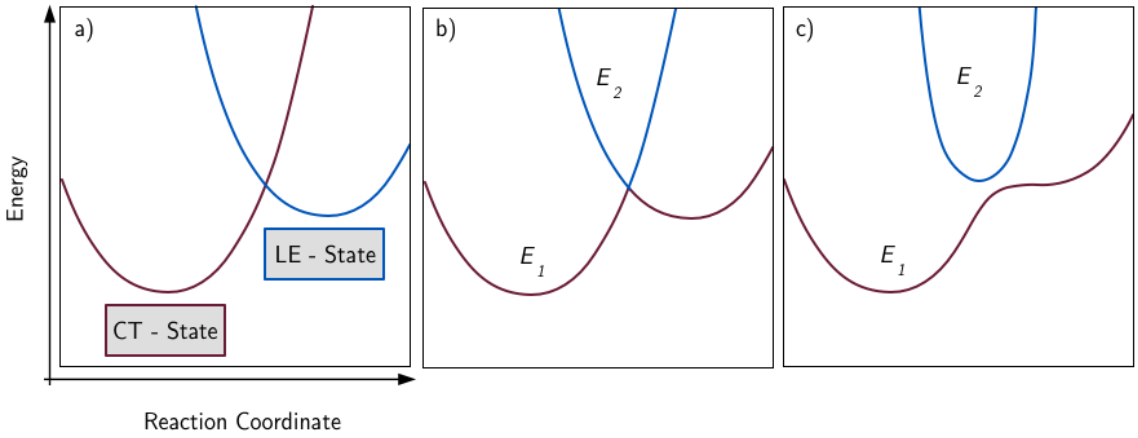


Figure 3.5: Schematic diagrams of potential energy curves. a) Diabatic state without hybridization between the CT and LE singlet state. In comparison, adiabatic states with b) small, and c) large electronic coupling are characterized by hybridization between the two states. Reused from Jungbluth et al. [1] with permission under CC BY 4.0, and originally adapted with permission from Tress [18], Copyright 2014 Springer Nature.

3.4.2 CT State Modeling using Three-State Approaches

To the best of our knowledge, the work by Chen et al. [92], [104], currently provides the most detailed discussion of three-state approaches to simulate CT absorption and fit experimental data. Their work presents a model to account for both the electronic coupling (hybridization) between ground and CT states, in addition to the coupling between CT and singlet states (equations 11-13 in [104]). They show through simulations that molecular packing at the D:A interface greatly impacts the spectral shape of CT state absorption and affects the results

of CT state fitting. This has also been experimentally and theoretically confirmed elsewhere [158], [159], [160], [161].

Increased hybridization between energetic states leads to an increase in the absorption intensity of the CT state, caused by an intensity borrowing mechanism. Compared to Chen et al.'s three-state approach, a standard two-state model consistently overestimates λ_{CT}, underestimates E_{CT}, and incorrectly attributes contributions of the S_1 to CT state absorption. This leads to an overestimation of the hybridization between CT and S_1 states [104].

Interestingly, when comparing Chen et al.'s three-state approach to the MLJ model introduced earlier, they find better agreement across their studied systems than if a simple two-state model, not accounting for vibrations, is applied. This suggests that while a three-state model might describe the physics of organic D:A systems most accurately, a big improvement in fitting accuracy is achieved by explicitly considering high frequency vibrational modes. Nonetheless, the work of Chen et al. highlights the need for accessible models accounting for energetic hybridization that can be easily implemented across research groups.

3.5 Discussion of Advanced CT State Models

To finish our discussion of CT state models, we comment on the most suitable applications for each approach, as well as the necessary trade-off between physical accuracy and complexity. The simplest and hence most common approach relies on fitting the classical two-state Marcus model to absorption/emission data. However, as explained in detail in the previous sections, classical Marcus theory has certain shortcomings that might warrant the use of more complex models.

The first addition to classical Marcus theory is the explicit consideration of static and quantized dynamic disorder. Even though the exact impact of static disorder on linewidth broadening is still debated [103], [119], [156], static disorder of polymer blends is likely significant, given the many torsional and conformational degrees of freedom of the molecules.

The need to explicitly consider the quantum nature of vibrational modes arises when the energy of phonons is no longer smaller than the thermal energy ($\hbar\omega_i << k_BT$). For high fre-

quency, intra-molecular vibrational modes caused by C−C or C−H bond vibrations greater than 100 meV [52], [101], [102], [89], [61], [90], as is in principle always the case for organic semiconducting molecules, the semi-classical MLJ model, which considers intra-molecular modes quantum mechanically, is the most appropriate.

An experimental challenge of the MLJ model, however, is that instead of fitting three free parameters, as is the case for classical Marcus theory were E_{CT}, λ_{CT}, and f are fit, the vibrational modes ($\hbar\omega_i$) or the Huang-Rhys parameter (S_i) are needed as model inputs to reduce the number of free fit parameters. These can be determined experimentally using Raman spectroscopy, which not every research group has access to, or computationally via DFT simulations [149], [154]. An estimation of these parameters based on previously published results might suffice, but could introduce small errors across material systems.

A further explicit consideration of the quantum mechanical nature of low frequency, inter-molecular modes will in most instances not be necessary, unless material systems are compared at very low temperatures (i.e. < 120 K). Studies at these low temperatures would help to disentangle inter- and intra-molecular effects that are convoluted at higher temperatures, but are usually not required for the simulation of device operating conditions.

While DFT calculations can easily determine internal vibrational modes, the complex interactions between individual molecules and their surrounding environments are extremely challenging if not impossible to determine computationally. As such, an explicit consideration of both internal and external phonon modes would require the fitting or input of seven parameters (E_{CT}, λ_{CT}, f, $S_0/\hbar\omega_0$, $S_1/\hbar\omega_1$) which might be challenging to implement or overparameterize the data.

The biggest advance of our understanding of different material systems is likely achieved by employing a three-state model over the two-state approaches of Marcus or MLJ theory. The three-state approach, which considers energetic hybridization between ground, singlet, and CT states, is not just limited to low energetic offset systems based on NFAs, but has previously also been applied to fullerene-based blends [106], [104].

To evaluate how much information is gained from applying a three-state approach, donor-acceptor systems need to be classified into three categories: (1) systems with large energetic

offset between E_{S_1} and E_{CT} and no hybridization between energy states, (2) systems with large energetic offset and partial hybridization, and (3) systems with small energetic offset and partial to strong hybridization. Here, EQE and EL spectra are crucial for assessing which category a material system falls into. The less spectrally resolved the CT state is from the singlet peak, the more hybridization will play a role.

However, three-state models are more challenging to implement than fitting simple Gaussian functions to absorption and emission spectra. Rather than fitting one analytical equation, the models presented in literature [92], [106] require complex numerical evaluations of Hamiltonians and calculations of a system's eigenstates. Even if the simulation code is made publicly available, current approaches require specialist knowledge to fit spectra accurately.

An accurate determination of hybridization of energetic states is, however, not only crucial for correct determination of CT state properties, but is immensely important for understanding dominant sources of voltage losses, and whether an intensity borrowing mechanism between energetic states reduces radiative and non-radiative voltage losses. With the availability of simple and easily accessible three-state approaches, we would be able to gain this experimental understanding across different classes of materials.

The next logical step in the further development of three-state models is the inclusion of static disorder and electronic delocalization, which were shown to impact CT absorption [102], [109], [51], [162]. On this point, however, care should be taken to develop models that are physically representative, rather than models with enough free parameters to fit any spectrum with high confidence.

To connect our discussion of CT state properties back to voltage losses, we revisit equation 2.20. Equations like this are extremely helpful for the design of novel molecules, since they highlight which inter- and intra-molecular properties should be modified to achieve better device performance. For example, the expression in the logarithm of equation 2.20 is larger than one and predicts a decrease of ΔV_{oc}^{rad} with decreasing oscillator strength of the CT transition. This suggests that decreasing f_{CT} increase V_{oc} and thereby the overall PCE. However, this logic is incomplete, since it does not consider the effect of the oscillator strength on non-radiative recombination.

Equation 2.20 assumes that all relevant EQE or EL spectral features can be modelled using classical Marcus theory and excluding disorder. As discussed above, MLJ theory or three-state models more accurately describe CT state absorption and emission. Benduhn et al. therefore derive a model applying MLJ theory and yielding a refined expression for V_{oc}^{rad} and non-radiative recombination losses [17]. The latter is found to inversely depend on E_{CT}, also known as the energy gap law for OSCs. The reason behind this dependence is a decreasing wave function overlap with lower energetic offsets between CT and singlet states, reducing non-radiative loss pathways.

This model is further refined by Azzouzi et al. [93], who present an illustrative overview of how different CT states properties affect V_{oc}^{rad} and ΔV_{oc}^{nr}. For example, they confirm that an increase in the CT state oscillator strength leads to a decreased V_{oc}^{rad}. Simultaneously, non-radiative recombination decreases, thereby keeping the experimentally determined V_{oc} approximately constant. Their model predicts the largest voltage loss improvements with decreasing λ_{CT}, increasing E_{CT}, and decreasing energetic gap between E_{S_1} and E_{CT}.

Eisner et al. [106] investigate the effect of energetic hybridization, i.e. following a three-state approach, on radiative and non-radiative voltage losses by studying a range of donor-acceptor blends with varying energy levels, including fullerenes and NFAs. They find that for certain blends with moderate to low energetic offsets, hybridization between the singlet and CT state becomes significant. With an increasing CT state energy, non-radiative recombination via the CT state is reduced according to the energy gap law [17].

However, the observed voltage loss trends of systems with low energetic offsets can not be explained by changes in E_{CT} alone [106]. Instead, it is suggested that non-radiative recombination in low offset systems is not just determined by the emission properties of the CT state, but also by those of the S_1 [163], [106], [164], [165], [166], [167]. Through an intensity borrowing mechanisms, highly luminescent S_1 states can increase the luminescence of the CT state, thereby reducing non-radiative recombination. This led Eisner et al. to define an effective oscillator strength of the ground to CT state transition for systems that show hybridization between energetic states,

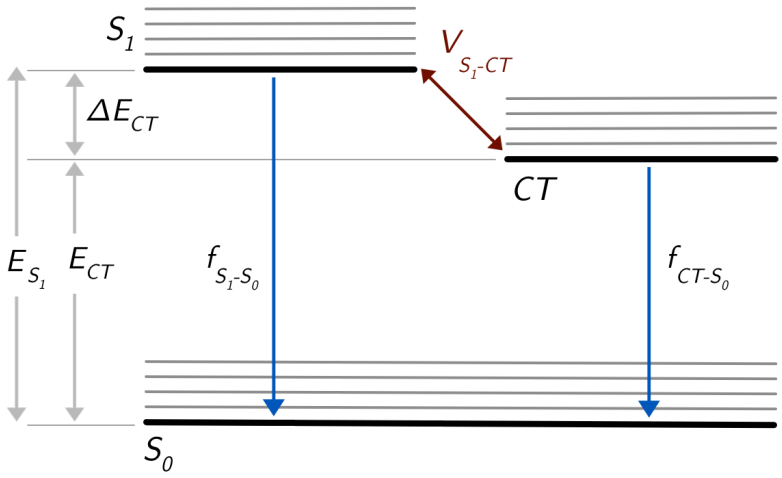


Figure 3.6: Schematic of the three-state approach accounting for hybridization between the ground state (S_0), singlet excited state (S_1), and CT state. V_{S_1-CT} describes the coupling between the lowest singlet state and CT state. The oscillator strengths of the $S_1 - S_0$ and $CT - S_0$ transitions are described by $f_{S_1-S_0}$ and $f_{CT} - S_0$ respectively. Reused from Jungbluth et al. [1] with permission under CC BY 4.0, and originally adapted with permission from Eisner et al. [106], Copyright 2019 American Chemical Society.

$$f^*_{CT-S_0} = f_{CT-S_0} + \frac{f_{S_1-S_0} V^2_{S_1-CT}}{\Delta E^2_{CT}} + \frac{(f_{S_1-S_0})^2 (f_{CT-S_0})^2 V_{S_1-CT}}{\Delta E_{CT}}, \tag{3.26}$$

where f_{CT-S_0} ($f_{S_1-S_0}$) describes the oscillator strength of ground to CT state (singlet state) transitions in the absence of energetic hybridization, and V_{S_1-CT} is the coupling strength between singlet and CT state. A schematic of the corresponding processes is shown in Figure 3.6. Despite the decreasing non-radiative recombination for low offset systems, the work by Eisner et al. confirms that the total recombination rate increases with higher electronic coupling, suggesting a limit for how far voltage losses in OSCs can be reduced.

Further opportunities for voltage loss improvements are presented, for example, by Panhans et al. who simulate the impact of electronic and electron-phonon coupling on the absorption linewidth and radiative losses of low donor small molecule OSCs [155]. They expand the three-state approach to account for hybridization between CT states (CT−CT coupling), and between singlet and CT states (LE−CT coupling). They find that a dominant contribution to voltage losses arises from electron-phonon coupling, like zero-point vibrations, that might also be present at 0 K. In comparison to Azzouzi et al. [93], their work suggests that

electronic coupling could increase the steepness of the low-energy absorption tail, thereby reducing radiative voltage losses. A very recent publication, again by Chen et al. [92], demonstrates further success of a three-state model and the importance of hybridization. The authors provide a unified framework for non-radiative voltage losses and demonstrate that fullerene-based blends behave as predicted by the energy gap law, while the behaviour of many low-loss NFA-based systems deviates from the energy gap law.

4 | Materials & Methods

This chapter provides a detailed overview of the experimental methods applied in this thesis. First, the molecular structures and chemical names of the chosen molecules are presented. Next, sample fabrication based on vacuum thermal deposition is explained, and an exemplary device architecture is shown. Finally, the different experimental and computational techniques used to study thin film samples and full devices are detailed.

4.1 Materials

Figure 4.1 shows the molecular structure of the materials used in this thesis. All samples made in Oxford by the author of this thesis are fabricated via vacuum thermal deposition of small molecule donors and C_{60} as the electron acceptor. The acronyms, chemical names, and supplier information of the evaporated materials can be found in Table 4.1. All materials are used as received. The small molecules are bought purified via sublimation. Table 4.1 also summarizes the densities of the molecules used during the evaporation process. ZnPc and all its fluorinated derivatives are assumed to have the same density of 1.55 g/cm^3 [37]. Solar cells based on PM6, PTQ10, and Y6 are provided by Dr. Pascal Kaienburg and are solution-processed at North Carolina State University by Dr. Kan Ding. The devices are included in the discussion of Chapter 8, but are not the focus of this thesis. Hence, the molecules are included for completeness in Figure 4.1 but not discussed further.

Table 4.1: Acronyms, chemical names, densities, and supplier details for the materials used in this work. All materials are deposited via vacuum thermal deposition.

Acronym	**Chemical Name**	**Density / g/cm^3**	**Supplier**
α-6T	α-Sexithiophene	1.40	Lumtec
BPhen	4,7-Diphenyl-1,10-phenanthroline	1.20	Lumtec
C_{60}		1.65	CreaPhys
CuPc	Copper phthalocyanine	1.60	Lumtec
DCV5T	DCV5T Me 3,4	1.33	Synthon Chemicals
F_{16}ZnPc	Zinc-hexadecafluoro-phthalocyanine	1.55	Lumtec
F_8ZnPc	Zinc-octafluoro-phthalocyanine	1.55	Lumtec
F_4ZnPc	Zinc-tetrafluoro-phthalocyanine	1.55	Lumtec
MoO_3	Molybdenum trioxide	4.69	Lumtec
Rubrene	5,6,11,12-Tetraphenylnaphthacene	1.18	Lumtec
TAPC	1,1-Bis[(di-4-tolylamino) phenyl]cyclohexane	1.12	Lumtec
ZnPc	Zinc phthalocyanine	1.55	Lumtec
Al	Aluminium		Lesker

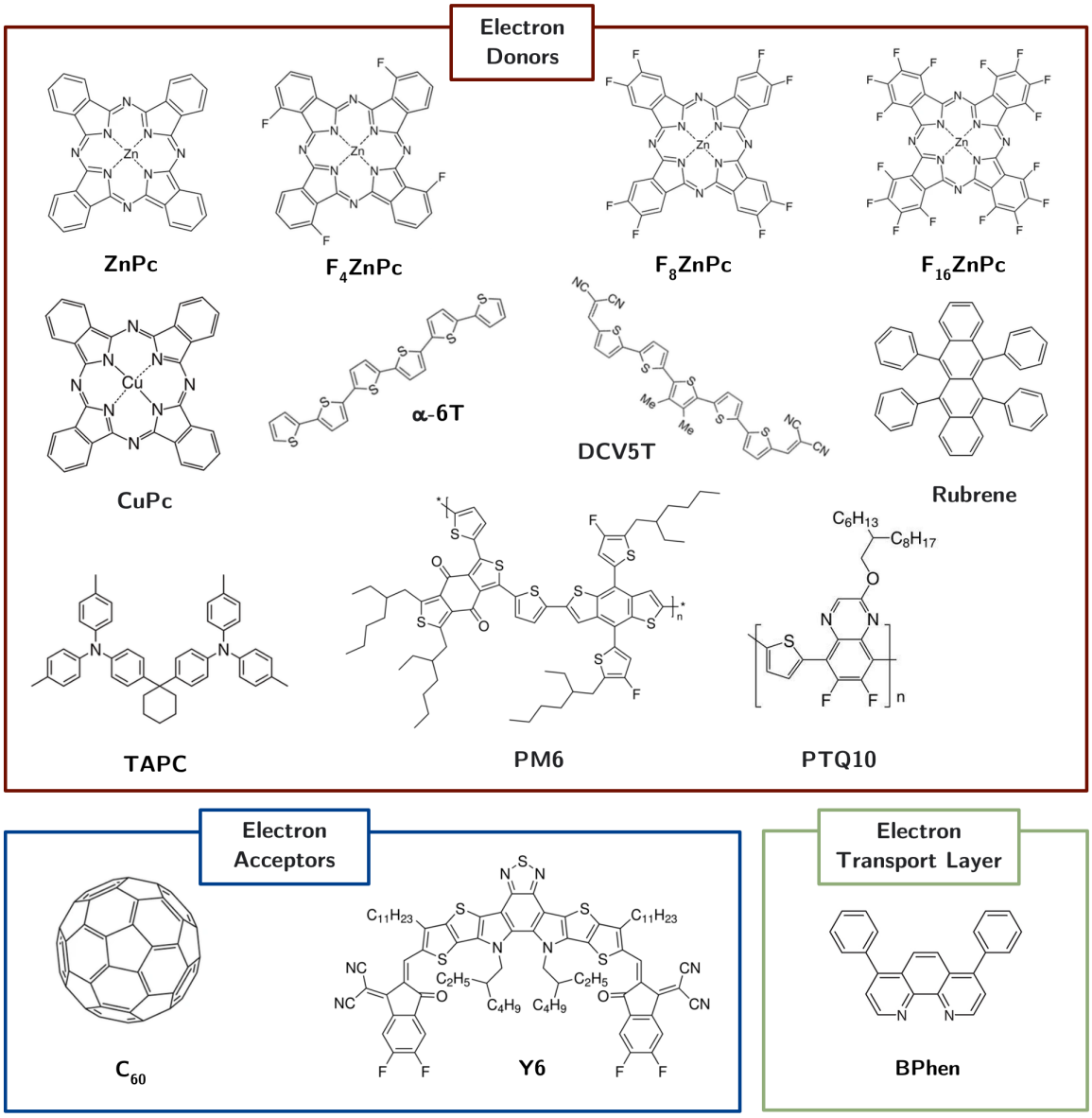


Figure 4.1: Molecular structure of the electron donors, acceptors, and transport materials used in this work. All chemical names are listed in Table 4.1.

4.2 Sample Fabrication

4.2.1 Vacuum Thermal Deposition

Thin film samples and full solar cell are fabricated through vacuum thermal deposition in the Evaporation CHamber Oxford (ECHO)[1]. Figure 4.2 shows a schematic of co-depositing two molecular species using ECHO. Prior to deposition, all substrates are cleaned via ultrasonic baths in a Hellmanex solution, de-ionized water, acetone, and isopropanol. Each sonication step lasts for 10 mins and is performed at a bath temperature of $55°$C. Afterwards, the substrates are treated with an O_2 plasma for 10 mins before being loaded into the evaporation chamber. For full device stacks, pre-patterened substrates of indium tin oxide (ITO)-coated glass[2] are used. Thin film samples are fabricated on plain glass[3] or fused quartz[4]. Powders of the molecules are placed inside ceramic crucibles and loaded into the chamber in air. Using roughing[5] and turbomolecular[6] pumps, a base pressure of $10^{-6} - 10^{-7}$ mbar is reached. The ceramic crucibles, which are located approximately 50 cm below the substrates, are heated by tungsten coils and enclosed in water-cooled copper shields. The crucibles are gradually heated until the materials sublime. A substrate shutter prevents premature deposition of the molecules on the substrates. The deposition rates are measured via quartz crystal microbalances (QCMs), and are varied between $0.01 - 0.40$ Å/s in this work. Once the desired deposition rates are reached, the substrate shutter is opened and molecules condense onto the substrates. All substrates are held at room temperature for the work presented in this thesis. The deposition area is controlled via the use of shadow masks. The evaporation rates and thicknesses are displayed on the screen of the deposition controller[7]. Based on the manufacturer's specifications, the displayed deposition rates carry an error of $\pm 5\%$. After deposition, the substrates are transferred into a N_2-filled glovebox without air exposure, and encapsulated[8] for testing.

[1] CreaPhys GmbH, EVAP300
[2] Thin Film Devices Inc., 20 Ohms/sq
[3] Thin Film Devices Inc., Eagle XG
[4] Knight Optical Ltd, Type WHQ
[5] Pfeiffer GmbH, ACP15
[6] Pfeiffer GmbH, HiPace 700
[7] Inficon, SQC-310
[8] Voltera, V-One PCB Printer

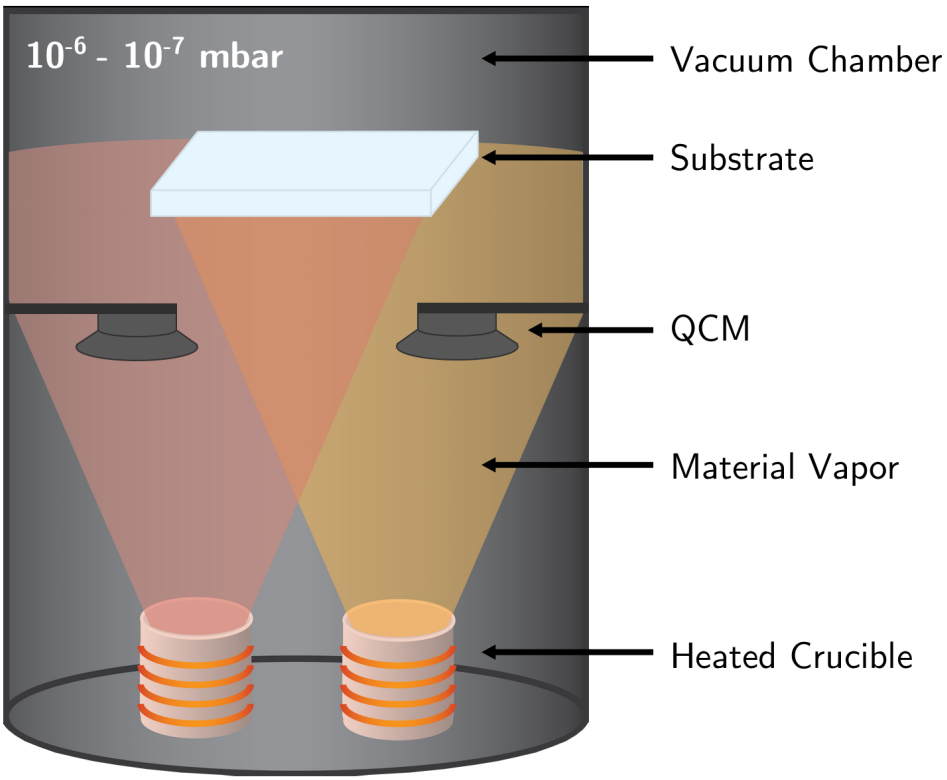


Figure 4.2: Schematic of the Evaporation CHamber Oxford (ECHO). The vacuum deposition chamber is put under vacuum (base pressure $10^{-6} - 10^{-7}$ mbar). Ceramic crucibles filled with material powder are heated until the materials sublime. By measuring and regulating the evaporation rate using crystal quartz microbalances (QCMs), the mixing ratio of different molecules can be tuned. The molecules condense onto the substrate, and film thicknesses are controlled with nanometer precision. By adding shadow masks (not pictured), the deposition area can be controlled. Once the desired thickness is reached, a shutter (also not pictured) is inserted to protect the substrate from further deposition.

4.2.2 Device Architectures

Figure 4.3 shows a schematic of the typical device stacks fabricated for this thesis. The layer thicknesses are not drawn to scale. Apart from the active layer composition, all solar cells deposited via vacuum thermal evaporation are fabricated with nominally identical device architectures, and through subsequent evaporation of MoO_3 (3 nm, $0.05 - 0.10$ Å/s), D:C_{60} (50 nm, varying rates and mixing ratios), BPhen (8 nm, $0.1 - 0.2$ Å/s), and Al ($\sim$ 100 nm, $1 - 2$ Å/s). For thin film samples, only the 50 nm thick active layer is deposited onto the substrates. The D:A mixing ratio in this thesis is either given in terms molar (mol.%) or weight (wt.%) content. The conversion between both quantities follows

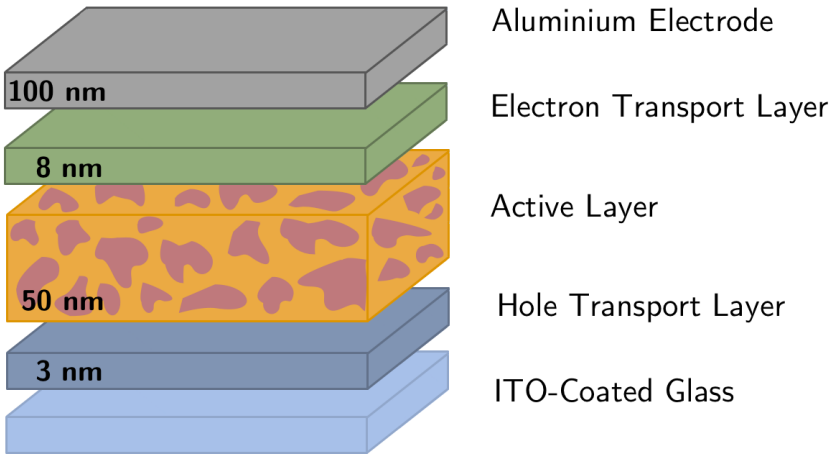


Figure 4.3: Schematic of the device stack used in this work. The thicknesses of the different layers were kept nominally identical across all fabricated devices.

$$\mathrm{WR} = \frac{M_D \cdot \mathrm{MR}}{(M_D \cdot \mathrm{MR}) + (M_A \cdot (1 - \mathrm{MR}))}, \tag{4.1}$$

where WR describes the desired weight ratio, MR is the molar ratio, and M_D and M_A are the molar masses of the donor and acceptor molecules respectively.

Converting between molar and volume fraction (vol.%) follows,

$$\mathrm{VR} = \frac{M_D \cdot \mathrm{MR}/\rho_D}{(M_D \cdot \mathrm{MR}/\rho_D) + (M_A \cdot (1 - \mathrm{MR})/\rho_A)}, \tag{4.2}$$

where VR is the volume ratio, and ρ_D and ρ_A describe the densities of the donor and acceptor molecules. Assuming the desired deposition rate of the acceptor is set as R_A, the corresponding rate of the donor (R_D) can be calculated as

$$R_D = R_A \cdot \frac{\mathrm{VR}}{(1 - \mathrm{VR})}. \tag{4.3}$$

4.3 Thin Film Characterization

4.3.1 Absorption Measurements

Absorption measurements of thin film samples on quartz are carried out using a UV-Vis-NIR photo-spectrometer[9]. Sample measurements are performed in transmission (T) mode and after collection of a light and dark baseline. The light baseline is performed by measuring the transmission of a clean quartz substrate. The thin film absorption (A) is calculated from the baseline corrected transmission as $A \approx 1 - T$, and neglecting any photon reflection.

4.3.2 Spectroscopic Ellipsometry

Spectroscopic ellipsometry measurements are carried out by Dr. Sameer Vajjala Kesava and Irfan Habib using a spectroscopic ellipsometer[10] at $55°$, $65°$, and $75°$ angles of incidence. Measurements are performed on neat films and D:A blends. From the measurements of Ψ and Δ, the optical constants, i.e. the refractive index n and extinction coefficient κ, are determined via optical modelling[11]. Optical modelling is also carried out by Dr. Sameer Vajjala Kesava and Irfan Habib.

4.3.3 Electron Paramagnetic Resonance Spectroscopy

Electron paramagnetic resonance (EPR) spectroscopy studies unpaired electron spins via the Zeeman effect. In the presence of an external magnetic field (B_0), the magnetic moment of an unpaired electron aligns parallel ($m_s = -1/2$) or anti-parallel ($m_s = +1/2$) to the magnetic field. Each magnetic state has a unique energy, and the energetic difference between $m_s = \pm 1/2$ is given as

$$\Delta E = g\mu_b B_0 = h\nu, \tag{4.4}$$

[9] Perkin-Elmer, Lambda 1050
[10] J. A. Woollam, RC2 Spectroscopic Ellipsometer
[11] J. A. Woollam, CompleteEASE software

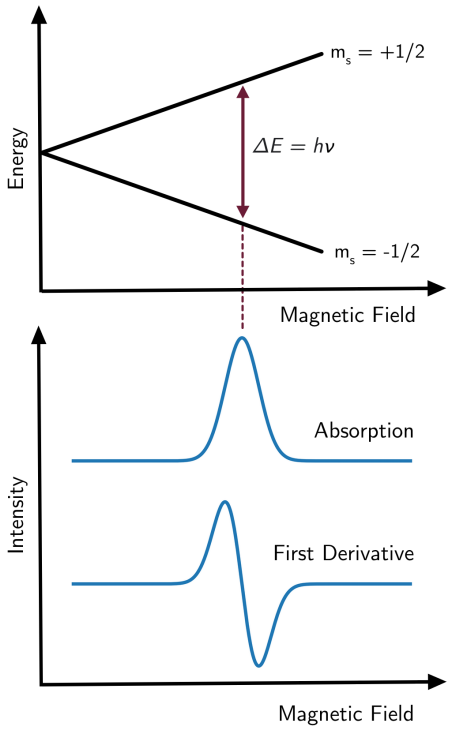


Figure 4.4: Zeeman splitting and the corresponding absorption spectrum for an $S = 1/2$ paramagnetic species. The first derivative of the EPR spectrum is shown in the bottom graph.

where g describes the electron g-factor and μ_b is the Bohr magneton. This energetic splitting can be probed via light absorption, and usually falls in the microwave region. Photons are absorbed if their energy is equal to the energetic splitting caused by the Zeeman effect. For EPR spectra, the first derivative of the absorption spectrum is typically reported (Figure 4.4).

To prepare the EPR samples, thin films are evaporated onto microscope cover glass. The cover glass is cut to a width of 3 mm with a diamond-tipped glass cutter and placed into quartz EPR tubes. The tubes are sealed using bi-component resin[12] inside a nitrogen-filled glovebox to avoid air exposure.

The EPR measurements and analysis are performed by Dr. Alberto Privitera. Time-resolved EPR (trEPR) spectra are recorded on a spectrometer[13] equipped with a cryostat[14] to control the sample temperature. The laser pulses for trEPR are collimated into the cryostat and resonator windows using a multi-mode optical fibre[15]. The pulses are set to 7 ns and 2 mJ

[12] Devcon, 5-Minute Epoxy
[13] Bruker, Elexsys E680 X-Band Spectrometer
[14] Oxford Instruments, CF9350 Cryostat
[15] Thorlabs, FT600UMT

energy at a wavelength of 532 nm and are produced by an optical parametric oscillator[16] and a Nd:YAG pulsed laser[17] operating at 20 Hz and 355 nm. The trEPR spectra are recorded using a transient recorder[18] with timing synchronized by a delay generator[19]. The overall response time of the instrument is approximately 200 ns. The measured spectra are analysed through spectral simulations using open-source MATLAB code[20]. Best-fit simulations are used to determine zero-field splitting (ZFS) parameters, triplet population sublevels, and the relative contribution between inter-system crossing and back charge transfer triplets.

4.3.4 Grazing Incidence Wide Angle X-Ray Scattering

Grazing Incidence Wide Angle X-Ray Scattering (GIWAXS) probes the structural arrangement in thin films on molecular length scales. Atomic and molecular planes diffract incident light and if constructive interference occurs, bright spots appear on the detector. The angle of diffraction relates to the spacing between planes, while the direction of diffraction is given by the orientation of the planes. The magnitude of the scattering vector (q) is given by

$$q = \frac{4\pi}{\lambda} \sin\theta, \tag{4.5}$$

where λ is the wavelength of the incident X-rays, and θ is the scattering angle. In the resulting 2D image, scattering along the q_z direction indicates diffraction from planes parallel to the substrate, and scattering along the q_{xy} direction indicates diffraction from planes perpendicular to the substrate.

The GIWAXS measurements presented in this thesis are partially carried out at the Surface and Interface Diffraction beamline (I07) at the Diamond Light Source (DLS)[21]. The distance between the sample and the detector[22] is calibrated using silver behenate (AgBeh) and was determined as 664.8 mm.

[16] GWU, VersaScan, Optical Parametric Oscillator
[17] Newport/Spectra Physics Lab, Quanta Ray, Nd:YAG Pulsed Laser
[18] Bruker, SpecJet II
[19] Stanford Research Systems, DG645
[20] EasySpin Toolbox [168]
[21] 20 keV (0.62 Å) Beam Energy
[22] Pilatus 2M Area Detector

Other GIWAXS measurements, i.e. those presented in Chapter 8, are carried out at the European Synchrotron Radiation Facility (ESRF) at BM28 (XMAS/THE UK CRG). The same beam energy and detector type are used as for the DLS measurements. A flight tube with Kapton windows is used to reduce air scattering, and the sample-to-detector distance was measured as 421.6 mm using AgBeh.

Images are converted to 2D reciprocal space using specialized software[23] with an applied polarisation and solid angle correction [169]. The reciprocal space maps shown in this thesis are plotted using a logarithmic colour scale with limits that are chosen to facilitate the readers' understanding of scattering features.

Peak positions and the FWHM are determined from radial profiles of the reciprocal space maps, where each peak's intensity I is fitted using a Lorentzian with a 1$^{\text{st}}$ degree polynomial background.

$$I = I_L \cdot \frac{\Gamma^2}{(q - q_0)^2 + \Gamma^2} + a \cdot q + b, \tag{4.6}$$

Here, q_0 describes the peak center, Γ describes the width, and a, b, and I_L are constants. An adapted Scherrer equation [170],

$$D_{hkl} = \frac{2\pi K}{\Delta q_{hkl}}, \tag{4.7}$$

is used to determine the d-spacing (D_{hkl}), where $\Delta q_{hkl} = \text{FWHM} = 2\Gamma$. K is chosen to be 1.047, corresponding to spherical grains [171]. We note that this is a simplification for ease of comparison and that our Scherrer analysis does not take other sources of peak broadening (due to the detector, beam source, etc.) into account. As such, the results of the Scherrer analysis should only be treated as a relative comparison of grain sizes across samples in our studies. The GIWAXS measurements and analysis presented in this thesis are performed by Dr. Thomas Derrien and Andreas E. Lauritzen.

[23] DAWN Software Package

4.4 Device Characterization

4.4.1 Current Density-Voltage Measurements

The $J-V$ characteristics of solar cells are measured under simulated AM1.5g light with 100 mW/cm^2 intensity using a solar simulator[24] and a sourcemeter[25]. The light source is calibrated using an NREL-certified KG5 filtered silicon reference diode. The active area of the OSCs is not masked, but is constrained to 0.08 cm^2 by the pattern of the ITO substrate and the resulting overlap between ITO, the active layer, and the aluminium electrodes. The exact voltage range is adapted depending on device performance. However, measurements are generally performed via forward and backward sweeps between -1.5 V to $+1.5$ V and with 0.02 V steps. All samples are measured under light and dark conditions.

4.4.2 Mismatch Correction

Since the spectrum of AM1.5g light is challenging to replicate and generally does not match the spectrum of the light source used for $J-V$ measurements, mismatch correction needs to be performed. In addition, variations in the EQE of different devices under testing (DUT) need to be considered to report comparable photocurrents and power conversion efficiencies.

To correctly report the photocurrent of the DUT at AM1.5g ($J_{\mathrm{DUT},AM1.5g}$), the measured photocurrent under solar simulator illumination ($J_{\mathrm{DUT},sim}$) is scaled as

$$J_{\mathrm{DUT},AM1.5g} = J_{\mathrm{DUT},sim} \cdot \frac{\text{Intensity Correction Factor}}{\text{Spectral Correction Factor}}. \tag{4.8}$$

The intensity correction is performed using a calibrated silicon reference diode[26] and the spectral correction is performed by measuring the EQE of the DUT. In addition, the spectrum of the incident solar simulator light (ϕ_{sim}) is measured and compared to the spectrum at AM1.5g ($\phi_{AM1.5g}$). Then, the photocurrent is corrected using the mismatch factor M,

[24] Abet Technologies, Sun 2000 Class AAB
[25] Keithley, 2400 Source Measure Unit
[26] NREL-certified KG5 filtered silicon diode

$$J_{\text{DUT},AM1.5g} = \frac{J_{\text{DUT},sim}}{M} \cdot \frac{J_{\text{ref},AM1.5g}}{J_{\text{ref},sim}}, \tag{4.9}$$

$$M = \frac{\int EQE_{\text{DUT}}\phi_{sim}}{\int EQE_{\text{DUT}}\phi_{AM1.5g}} \cdot \frac{\int EQE_{\text{ref}}\phi_{AM1.5g}}{\int EQE_{\text{ref}}\phi_{sim}}. \tag{4.10}$$

In practice, the photocurrent of the reference diode under AM1.5g illumination is often divided by M, and the intensity of the solar simulator is tuned until $J_{\text{ref},sim} = \frac{J_{\text{ref},AM1.5g}}{M}$. Then, the measured photocurrent of the DUT should match the photocurrent under AM1.5g.

4.4.3 External Quantum Efficiency Measurements

4.4.3.1 Room Temperature Measurements

Sensitive external quantum efficiency measurements are performed using a custom-built setup employing a monochromator[27], preamplifier[28], and Lock-In amplifier[29] for signal readout. A detailed description of the experimental setup and the custom Python code written to perform measurements is included in Chapter 5. Increased sensitivity of the measurement is achieved through spectral filters[30].

4.4.3.2 Temperature-Dependent Measurements

Temperature-dependent EQE measurements are performed using a cryostat[31] and the same custom-built EQE setup. The samples are loaded onto the temperature stage in air, and electrical connections are established via thin metal pins. The cryostat is connected to the temperature controller, liquid nitrogen pump[32], and a liquid nitrogen-filled dewar. To remove water and oxygen inside the cryostat, the temperature stage is flushed with nitrogen for $5-10$ mins before measurement. Subsequently, the cryostat is placed onto a custom-built holder

[27] Princeton Instruments, Spectra-Pro HRS300, Triple Grating Imaging Spectrograph
[28] Zürich Instruments, HF2TA Current Amplifier
[29] Zürich Instruments, HF2LI Lock-In Amplifier
[30] Thorlabs, Premium-coated edge pass and long pass filters
[31] Linkam, LTS420
[32] Linkam, LNP95

and aligned in the EQE setup. A thin plastic tube with warm nitrogen air is pointed onto the quartz window to avoid condensation during measurement. The temperature is set using a windows program[33] provided by the supplier, and measurements are taken using the same custom Python program used for standard EQE measurements. While the temperature range of the cryostat spans -196°C to $+420$°C, most measurements presented in this thesis are taken between -125°C and $+80$°C.

4.5 Computational Methods

4.5.1 Transfer Matrix Modelling

Transfer matrix modelling (TMM) is performed using the methodology and code published in reference [127]. TMM is a method developed for modelling the propagation of electromagnetic waves through layered stacks. The complex behavior of transmission and reflection of incident light across multiple layers is treated as a superposition of forward and backward traveling waves that are related via transmission and propagation matrices. For solar cell research, TMM is useful for understanding the spectral dependence of interference patterns in a device stack. In addition, the short-circuit current density, assuming complete charge carrier collection (100% IQE), can be calculated. The complex refractive index ($\tilde{n} = n + i\kappa$) is used as input to the TMM code. The $\tilde{n}$ of the materials used in this work is either taken from literature (e.g. reference [127]), or measured experimentally using the spectroscopic ellipsometry setup detailed earlier.

4.5.2 Density Functional Theory

Density functional theory (DFT) is a computational technique used for solving many body Schrödinger equations to determine molecular structures, energy levels, and other material properties. The DFT calculations and analysis presented in this thesis are performed by Dr. Veaceslav Coropceanu and Dr. Eunkyung Cho from the University of Arizona. The

[33] Linkam, LINK program

electronic structure of molecules is determined using the screened range-separated hybrid functional LC-ωhPBE with 20% Hartree-Fock exchange and using the 6-31G** basis set. A dispersion correction is included for all calculations. The properties of excited states are obtained at the time-dependent DFT (TDDFT) level within the Tamm-Dancoff approximation (TDA-TDDFT) [172]. All DFT/TDDFT calculations are performed using the Gaussian 16 program [173], [174].

5 | Sensitive External Quantum Efficiency Measurements & Analysis

This chapter summarizes the technical details of the sensitive external quantum efficiency ($sEQE$) setup that was custom-built for this thesis. Compared to standard setups, which are often limited to a dynamic range of $2-3$ orders of magnitude in measuring the EQE, this $sEQE$ setup can cover 7 orders of magnitude and measures the weak spectral signatures of charge transfer state absorption. In addition to describing how the additional sensitivity is achieved, this chapter details the custom Python code written to (1) control the $sEQE$ setup, and (2) analyse the properties of charge transfer state absorption from $sEQE$ spectra. A detailed comparison of different $sEQE$ fitting approaches is provided, and the fitting methodology used in this thesis is introduced.

Parts of this chapter are based on A. Jungbluth, P. Kaienburg, M. Riede. Charge transfer state characterization and voltage losses of organic solar cells. J. Phys. Mater. ***5*** *024002 (2022) [1]. Text and figures were reproduced or adapted with permission under CC BY 4.0.*

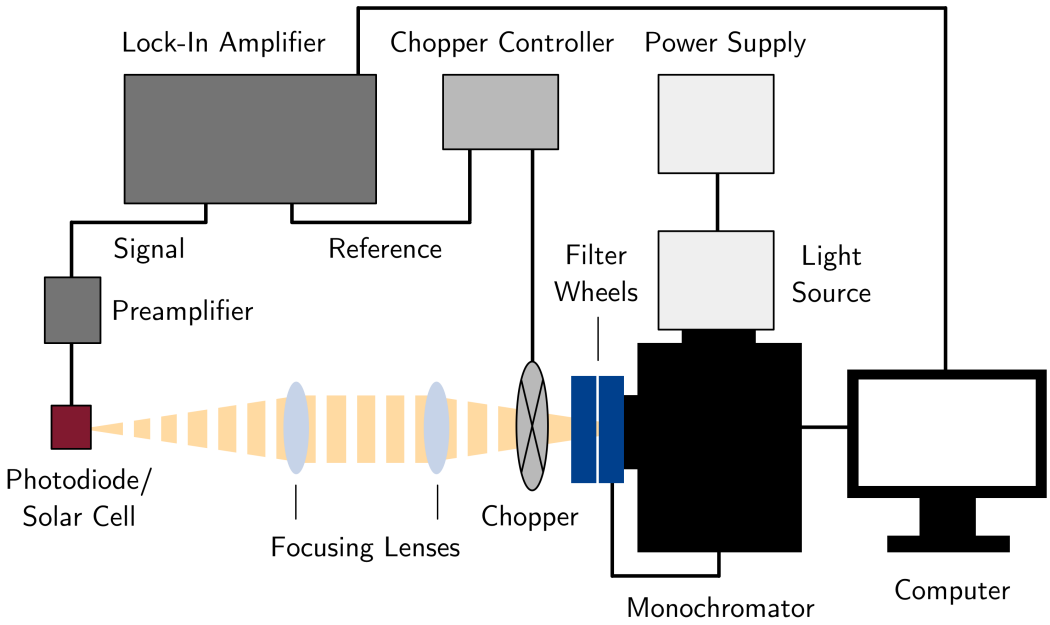


Figure 5.1: Schematic of the custom-built $sEQE$ setup used in this work. White light from a tungsten-halogen light source is directed into a monochromator and split by wavelength. The monochromatic light is subsequently modulated by a chopper wheel and focused onto the device under testing (i.e. a solar cell or reference photodiode). When measuring OSCs, the devices are either loaded into a standard sample holder for room temperature measurements, or connected inside a cryostat[1] to perform temperature-dependent $sEQE$ measurements. The resulting photocurrent is pre-amplified and converted to a voltage, before being analysed further by a Lock-In amplifier.

5.1 Measurement Setup

The sensitive external quantum efficiency ($sEQE$) setup used in this work was custom-built and programmed by the author of this thesis, following literature on similar setups (e.g. [33]). In the following paragraphs, the working principles of the setup are detailed, including how the increased sensitivity is achieved. We also introduce the open-source Python program written to control the setup and take $sEQE$ measurements.

Figure 5.1 shows a schematic, and Figure A.1 in the Appendix shows a photo of the $sEQE$ setup. White light from a tungsten-halogen light source[2] is directed into a monochromator[3] and diffracted by wavelength. The monochromator used in this setup has three spectral

[1] Linkam, LTS420
[2] Princeton Instruments, TS-428, 250 W tungsten-halogen light source
[3] Princeton Instruments, Spectra-Pro HRS300, Triple Grating Imaging Spectrograph

gratings[4] and is capable of achieving sub-nanometer spectral resolution. Each grating has a different blaze wavelength for which the diffraction of light is most efficient. The optimal grating switching points[5] are determined as the crossing points of the diffraction curves of each grating and are preset in the $sEQE$ control software. The monochromator exit slit width, which controls the spectral resolution and light intensity, is set to 1.5 mm. While higher spectral resolution is technically possible, all measurements presented in this thesis are performed in 5 nm wavelength steps.

Upon exiting the monochromator, the diffracted light is send through two filter wheels with preinstalled spectral filters. This is to ensure that stray room light or higher order dispersions of the diffracted light are removed. The first filter wheel[6] contains three premium hard-coated edge pass filters[7] that cover a wide spectral range. The filter switching positions[8] are determined from the transmission data supplied with the filters and are preset in the control program. Transitions between filters should occur in spectral regions where both filters show equally good transmission to avoid artifacts in the measured spectra. The second filter wheel[9] contains five long-pass filters[10] that remove additional light at long wavelengths. While the first filter wheel is used for all measurements, the second filter wheel is only used for high sensitivity measurements of the sub-gap tail. Consequently, depending on the absorption onset of the studied systems, the filters in the second filter wheel can be exchanged.

The diffracted light is modulated by a chopper wheel[11] set to run between $260 - 300$ Hz. The chopper frequency is limited by the response speed of the device under testing (DUT), which is on the order of 10s of nanoseconds for organic photodetectors [175], [176], [177], and should avoid frequencies of indoor lighting (e.g. $100 - 120$ Hz for incandescent light bulbs). The modulated light is focused onto the DUT, i.e. a solar cell or reference photodiode, via an iris[12] and focusing lenses[13]. To perform room temperature measurements, the solar cells are

[4] Princeton Instruments, 300/750/1600 nm blaze wavelength and 600 g/mm each
[5] Grating 1: $350 - 535$ nm, Grating 2: $535 - 1150$ nm, Grating 3: $1150 - 1800$ nm
[6] Princeton Instruments, FA2448 Filter Wheel
[7] Thorlabs, FESH0700, FESH1000, FELH0950
[8] Filter 1: $410 - 650$ nm, Filter 2: $650 - 985$ nm, Filter 3: $985 - 1000$ nm
[9] Thorlabs, FW102C Motorized Filter Wheel
[10] Thorlabs, FGL665, FGL715, FGL780, FGL850, FGL1000
[11] Stanford Research Systems, SR540, Optical Chopper
[12] Thorlabs, ID20/M Mounted Standard Iris
[13] Thorlabs, LB1904 Bi-Convex Lense

placed in a custom-built sample holder, designed and fabricated by Dr. Greyson Christoforo. To measure temperature-dependent $sEQE$ spectra, the samples are mounted in a cryostat[14].

The current that arises from light absorption of the DUT is first fed into a preamplifier[15] to be amplified and converted from current to voltage. Afterwards, the signal is analysed using a Lock-In amplifier[16]. Lock-In amplifiers are able to isolate signals with known frequencies from all other frequency components, which makes the detection of weak signals in noisy environments possible. The reference frequency for demodulation is provided by the chopper controller, and even small fluctuations on the modulation frequency are detected.

To convert the measured signal into EQE, the power of the incident light needs to be determined. By measuring the photocurrent of a calibrated reference photodiode with known spectral response (usually provided by the supplier), the power of incident light can be calculated. Compared to standard EQE setups, which often only use a silicon reference photodiode, sensitive setups measure long spectral ranges that often require a combination of photodiodes. In this setup, a silicon reference photodiode[17] is used to cover the $350 - 1100$ nm spectral range, and an indium gallium arsenide (InGaAs) reference photodiode[18] is used between $800 - 1800$ nm. The spectral overlap ($800 - 1100$ nm) between the reference diodes facilitates optimal switching between measurements.

As a final comment, correct measurements of the EQE depend on careful alignment of the light beam. In order to ensure that the same number of photons are shown onto the reference photodiodes and samples, active areas can either be masked, or underexposed. The latter is done in this setup, and the circular illumination spot size (≤ 3.1 mm^2) is controlled via the monochromator exit slit width and the adjustable iris. Importantly, measurement conditions need to be kept consistent between sample and reference measurements, and the same illumination spot size, wavelength intervals, and spectral filters should be employed.

In summary, increased sensitivity of EQE measurements across 7 orders of magnitude is achieved by using (1) pre- and Lock-In amplifiers with known reference signals, (2) spectral

[14] Linkam, LTS420
[15] Zürich Instruments, HF2TA Current Amplifier
[16] Zürich Instruments, HF2LI Lock-In Amplifier
[17] Thorlabs, FDS100-CAL
[18] Thorlabs, FGA21-CAL

filters to remove higher order dispersions, and (3) a combination of reference photodiodes with wide spectral range. Although not extensively tested for this setup, measurement sensitivities are also affected by electrical noise of the equipment, thermal noise of the DUT, and photon noise of the input or bias light sources [178]. While measurements are currently performed without bias illumination, future work could expand the current setup to include bias light sources with low photon noise. By optimizing all components of the setup, and increasing the integration time of the measurements, in principle, EQE signals as low as 10^{-10} could be detected [178].

5.2 Measurement Control Software

The Python software controlling the $sEQE$ setup is open-source and publicly available on GitHub[19]. Figure 5.2 shows a screenshot of the graphical user interface (GUI) of the program. The main functionalities are highlighted and numbered, and will be explained in more detail in the following sections.

On the first page of the GUI, the monochromator and Lock-In settings can be adjusted. Panel 1 in Figure 5.2 allows to manually set the spectral filter, grating, and wavelength. The latter is important for generating visible illumination spots for sample alignment. In panel 2, the amplification factor of the preamplifier and the time constant of the Lock-In amplifier is set. The latter determines the integration time (in seconds) of the measurement. Each measurement is repeated five times and averaged before returning a measurement value. For the measurements presented in this thesis, the amplification factor is dynamically adjusted depending on the photocurrent of the DUT. While most measurements are performed with the default time constant of 0.1 s, samples with low signal-to-noise ratio are measured with $0.3 - 0.5$ s time constants. As briefly outlined earlier, the switching points of the diffraction gratings and standard spectral filters are pre-determined and set in panel 3. All measurements in this thesis are performed with the default settings.

[19]The code can be accessed at https://github.com/annajungbluth/sEQE-Control-Software.

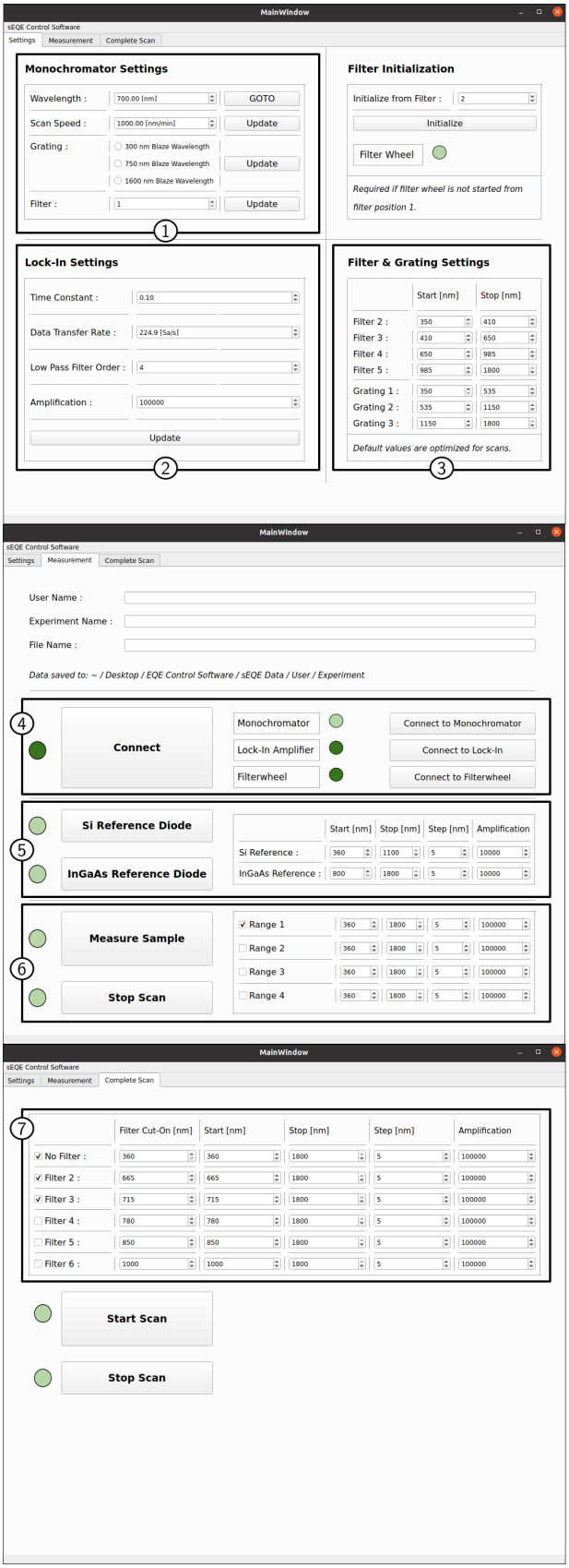


Figure 5.2: The graphical user interface of the Python program controlling the $sEQE$ setup. The main functionalities are numbered and detailed in the main text.

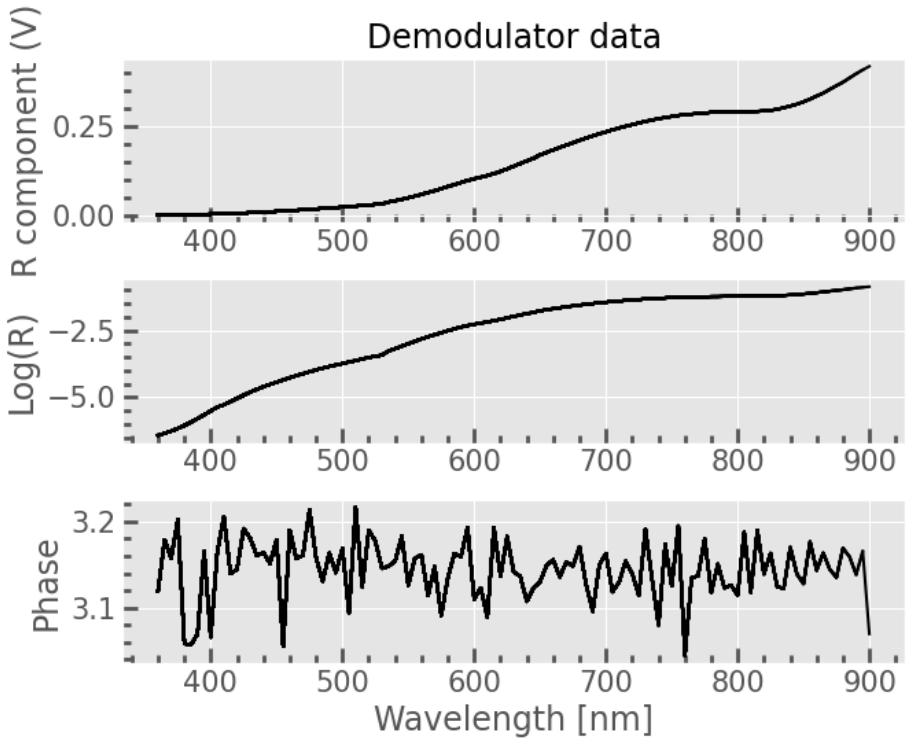


Figure 5.3: Example measurement output of the custom-built $sEQE$ setup. The signal (R) is measured in terms of voltage, and later converted into EQE. The last panel captures the phase, i.e. the time offset between the reference and the measured signal.

On the second page of the GUI, connections to the individual components are established (panel 4). If the connection is successful, the indicators next to the connection buttons turn dark green. Panels 5 and 6 allow to perform basic measurements of samples and reference diodes by setting the measurement wavelength range, wavelength steps, and amplification factor. Figure 5.3 shows an example scan of a silicon photodiode measurement. Each measurement output is plotted in terms of voltage, and converted into EQE at a later stage.

Finally, using panel 7 on the last page, advanced measurements of the sub-gap absorption features are set up. For each filter checkbox that is clicked, measurements using the corresponding spectral filter (installed in the second filter wheel) are performed. The measurement output of each scan is saved in comma-separated values (CSV) file format. Each file contains 6 data columns, namely the wavelength, measured photocurrent, measured voltage signal, Lock-In frequency, amplification factor, and phase.

5.3 Charge Transfer State Analysis

Having introduced the working mechanisms of the $sEQE$ setup used in this thesis, we next turn to discussing how the resulting data is analysed to fit CT state properties. The following paragraphs detail the custom Python program written to compile $sEQE$ spectra and fit CT states using some of the theoretical frameworks introduced in Chapter 3. The fitting methodology applied in this thesis is introduced using a simple example and expanded for fitting both CT state and singlet peaks.

5.3.1 Analysis Program

Figure 5.4 shows a screenshot of the graphical user interface of the $sEQE$ analysis program used in this work. The code is open-source and publicly available on GitHub[20], and was written from scratch by the author of this thesis. Initially, the analysis program was written to simply convert the measurement output to EQE, but it quickly grew into a complex piece of software capable of fitting CT states in a myriad of ways. The most relevant functionalities are numbered in Figure 5.4 and are discussed in the following paragraphs.

The first functionality of the program, labelled as panel 1 in Figure 5.4, aims to convert the measurement output of the $sEQE$ setup into the external quantum efficiency. To do this, matching reference scans and sample data are imported. The EQE is calculated as $\frac{\text{current/electron charge}}{\text{total power/photon energy}}$, i.e. by dividing the measured sample current by the incident power at a specific wavelength and correcting the units to result in a unit-less quantity.

As explained earlier, measurements of the sample and reference diodes are performed using spectral filters to achieve higher sensitivities in the sub-gap absorption regions. The final $sEQE$ spectra are compiled by stitching different measurements together (Figure 5.5), and by identifying optimal switching points in the regions of overlap. Consequently, panel 1 on page 1 of the analysis program is repeated six times to allow combining and plotting different measurements. Panel 2 plots the compiled $sEQE$ spectra as a function of wavelength or energy, and normalizes the spectra to a chosen wavelength.

[20]The code can be accessed at https://github.com/annajungbluth/sEQE-Analysis-Software.

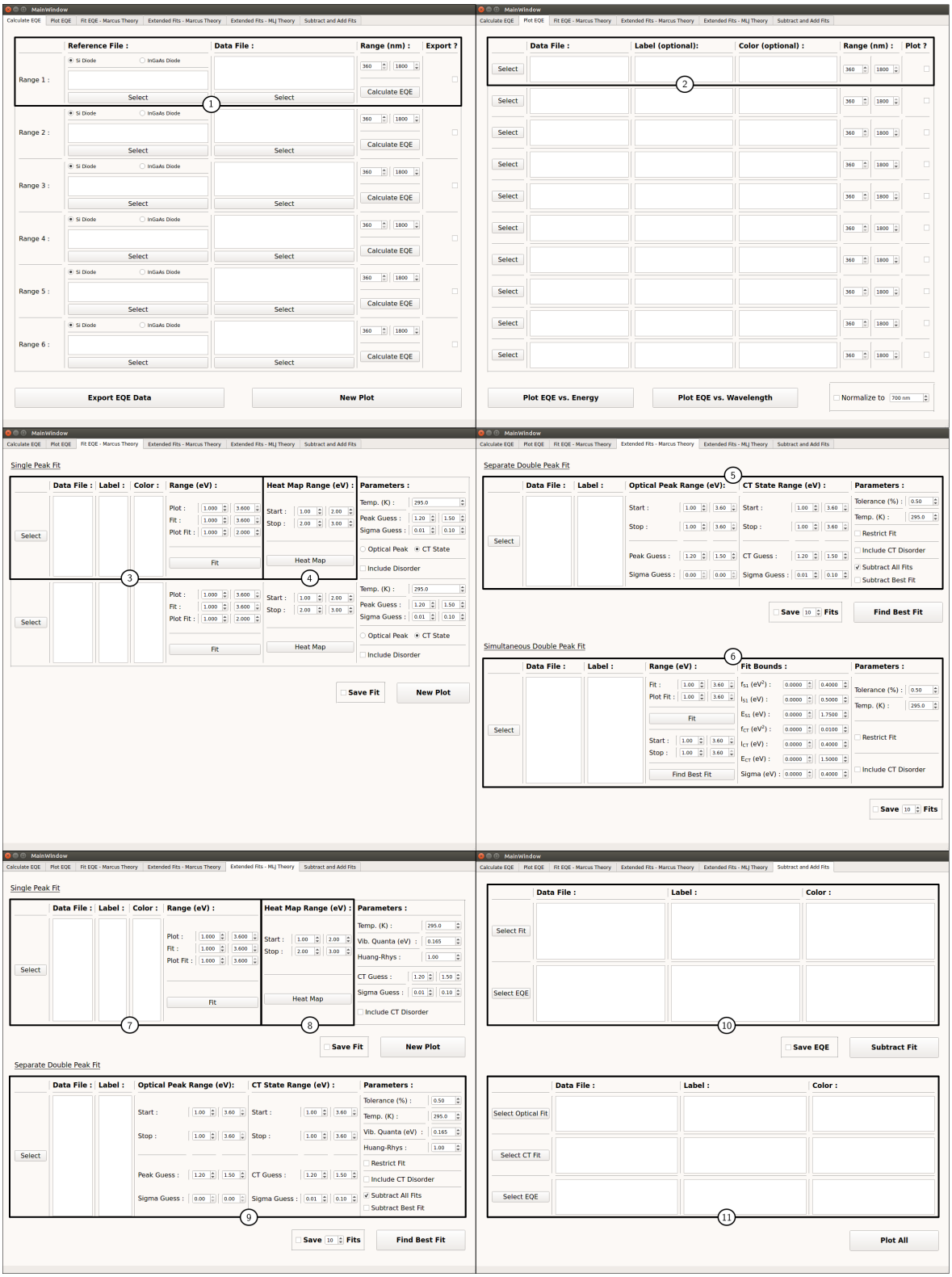


Figure 5.4: The graphical user interface of the $sEQE$ analysis program. The main functionalities are numbered and detailed in the main text.

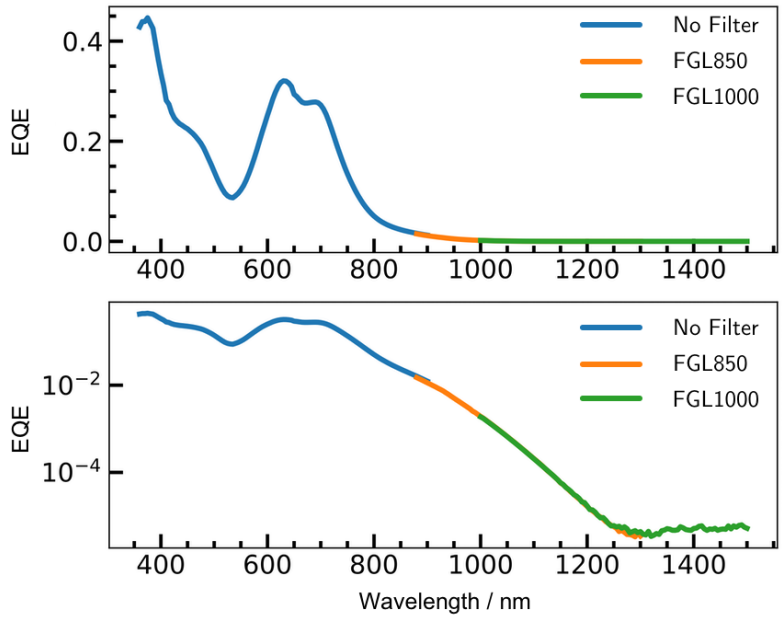


Figure 5.5: Example $sEQE$ spectra measured with different spectral filters. To save the final $sEQE$ spectrum, the individual scans are stitched together.

5.3.2 Fit Example

In the simplest case, functions like classical Marcus theory (equation 3.10) are fit to the $sEQE$ of blends with discernible CT state peaks. CT fitting becomes more complicated the more complex the fitting function or if the CT state is not resolvable from the singlet absorption. In these cases, care must be taken to avoid overfitting the data, and to return fit values that are physically meaningful. In addition, objective metrics are needed to evaluate the quality of a fit, and fit values should always be reported with uncertainties. In the following, we present a fitting methodology that builds on the approach presented by Benduhn [33], which, to our knowledge, best outlines how to quantify uncertainties for CT state fitting.

Our fitting implementation relies on curve fit algorithms from Python's scipy and lmfit packages. These algorithms can accommodate initial guesses and constraints of the fit parameters. Small variations in the initial guesses usually converge to the same results if the fit functions are stable and enough data is given as input. Based on our experience, the fit results are less affected by the initial guesses but more so by the data range that is fit. Depending on the amount of data that is passed into the curve fit algorithms, different solutions can be found. This can lead to large errors when reporting CT state parameters.

As a result, following the methodology of reference [33], we consistently vary the data range that is fit. By specifying a range of start and stop energies, we perform a grid search to find the best fit, i.e. the fit with the highest R^2, and plot the results in a heat map. While we choose the R^2 as a quality metric, other metrics evaluating the goodness of fit can also be used, as long as they are clearly documented and kept consistent throughout extended analyses.

Figure 5.6 shows an example of fitting classical Marcus theory (equation 3.10) to the sub-gap absorption feature of ZnPc:C_{60}. Figure 5.6a shows the best CT state fit determined via the highest R^2 and using panel 3 in the analysis program. The light grey areas highlight the range of start and stop energies that were used to generate the heat map shown in Figure 5.6b. The heat map shows the fit results of E_{CT} and spans 305 fit ranges. Using panel 4 in the analysis program, similar heat maps can be generated for the other fit parameters (i.e. λ_{CT} and f). The same fits can be performed using MLJ theory (equation 3.19) using panels 7 and 8 shown in Figure 5.4. Uncertainties on the fit results can be determined as the errors on single fits, or using the averages and standard deviations across multiple fit ranges.

For the fit results presented in this thesis, the uncertainties of room temperature measurements are generally calculated as the fit uncertainties on the best fit, unless specified otherwise. For temperature-dependent $sEQE$ measurements, used to study disorder in Chapter 8, uncertainties are calculated as the standard deviation across the $5 - 10$ best fits (depending on how many successful fits can be achieved). This is because the inclusion of disorder increases the number of free parameters in the Gaussian fitting function, which occasionally leads to deviations in the convergence of fit results when different fit ranges are considers. By calculating the average and standard deviation across multiple fits, these deviations are appropriately considered.

5.3.3 Fitting Singlet & CT State Absorption

To increase the accuracy of CT state fitting, equation 3.10 can also be applied to describe the absorption (and charge separation) contribution of the S_1 state in $sEQE$ spectra [179], [180]. Equation 3.10 is then adapted as

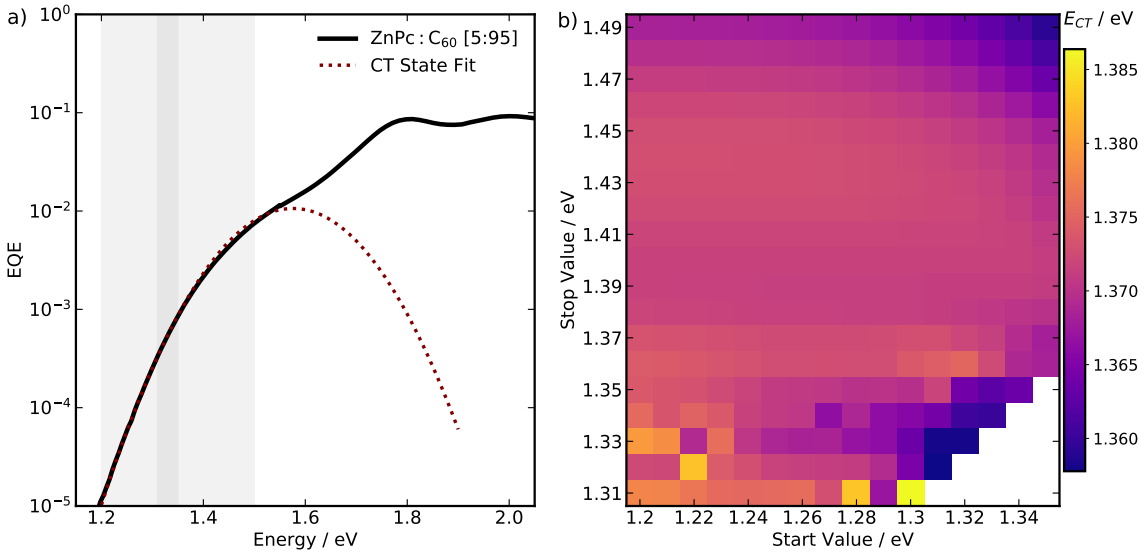


Figure 5.6: a) Example Gaussian CT state fit and b) heat map of E_{CT} for dilute ZnPc:C_{60}. The light grey shaded areas in a) highlight the range of start and stop energies used for the heat map fitting. The dark grey shaded area indicates $E_{\text{stop}} < E_{\text{start}}$ and corresponds to the empty squares in b). Adapted from Jungbluth et al. [1] with permission under CC BY 4.0.

$$EQE(E) = \frac{f}{E\sqrt{4\pi\lambda_{S_1}k_BT}} e^{\left(-\frac{(E_{S_1}+\lambda_{S_1}-E)^2}{4\lambda_{S_1}k_BT}\right)}, \tag{5.1}$$

where f_{S_1} is now related to the $S_0 \rightarrow S_1$ oscillator strength, λ_{S_1} describes the corresponding reorganization energy, and E_{S_1} is the singlet energy [179].

The extended EQE tail is then described as $EQE = EQE_{CT} + EQE_{S_1}$. This assumes that CT and singlet states can be treated independently, and that no hybridization between the states exists. Whether this assumption holds true is dependent on the material system, and whether E_{S_1} and E_{CT} are in energetic resonance and show sufficient wave function overlap. Without a defined CT state shoulder, some energetic hybridization is likely present. In this case, fitting each absorption contribution independently likely leads to attributing some of the CT absorption to the S_1 peak, thereby underestimating the "true" E_{CT} and f_{CT}. In this case, the $sEQE$ spectra would measure S_1-CT mixed states, and the fit results would describe "effective" CT state parameters.

Nonetheless, under the assumption of no energetic hybridization, equation 5.1 can be used to fit singlet peaks in the $sEQE$. Here, two different approaches can be applied. The first

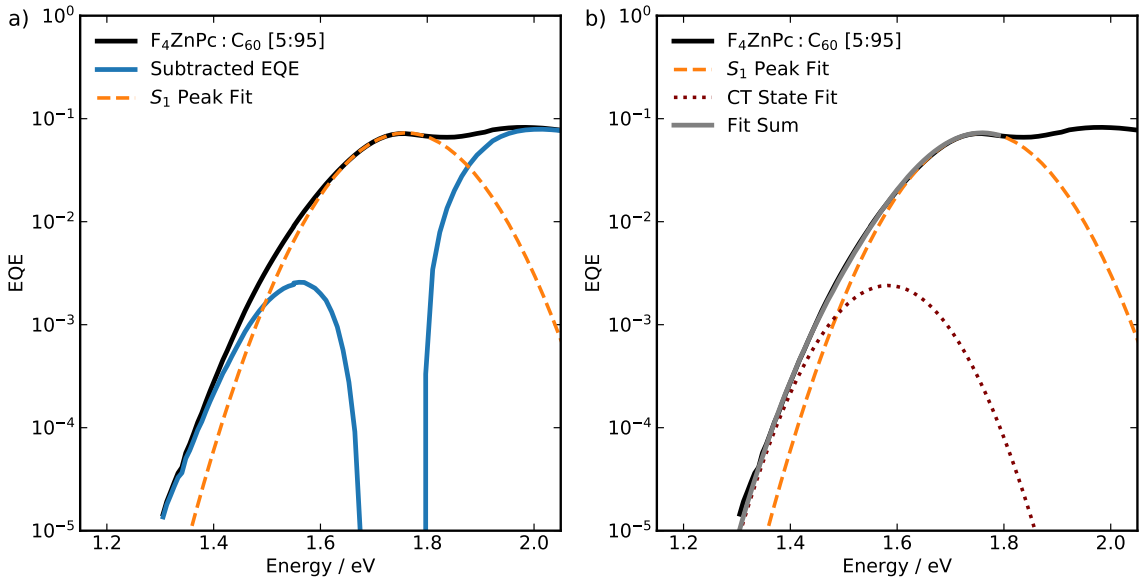


Figure 5.7: Example of a Gaussian fitting approach accounting for singlet and CT state absorption for systems without clearly resolvable sub-gap features. a) The singlet peak is fit using classical Marcus theory (orange dashed line) and subsequently subtracted from the $sEQE$ (blue solid line). The remaining sub-gap peak is fit as the CT state. b) Best fit result of singlet (orange dashed line) and CT state (red dotted line) fitting. The grey solid line shows the sum of the singlet and CT state absorption contribution. The best fit was chosen as the highest R^2 fit out of > 20 fit ranges. Adapted from Jungbluth et al. [1] with permission under CC BY 4.0.

approach involves fitting the S_1 absorption, and subsequently subtracting it from the $sEQE$. The remaining tail is then attributed to CT state absorption [179], [180]. Figure 5.7 demonstrates this fitting approach for $F_4ZnPc:C_{60}$, a system without clearly resolvable CT state absorption. When subtracting the S_1 fit, a distinctly Gaussian absorption feature remains that is fit as the CT state. In the analysis program shown in Figure 5.4, this approach of separate double peak fitting is performed using panel 5 for Marcus theory, and panel 9 for MLJ theory. Importantly, fit results should now be evaluated based on how well the fit sum (grey line in Figure 5.7b) describes the shape of the $sEQE$ tail, rather than evaluating the goodness of fit based on one absorption contribution alone.

The second approach for incorporating S_1 absorption is to simultaneous fit the sum of two Gaussians to describe CT state and S_1 absorption (panel 6 in Figure 5.4). Simultaneous fitting of functions to describe complex spectra is a standard tool in spectroscopic analysis (e.g. [109]). While this approach still considers singlet and CT state absorption to occur

independently, it reduces the risk of wrongfully attributing CT state absorption to that of the singlet. The experimental challenge of simultaneous double peak fitting is that each fit now relies on 6 free parameters, i.e. E_{S_1}, λ_{S_1}, f_{S_1}, E_{CT}, λ_{CT}, and f_{CT}. Occasionally, the algorithms converge to results that are nonphysical or where half the fit parameters are set to zero. To circumvent this limitation, panel 6 allows to set constraints on each fit parameter.

As a side note, simultaneous double peak fitting is currently only implemented for Marcus theory, though future versions of the analysis program can easily expand this fitting approach to MLJ theory. The explicit inclusion of static disorder, however, is already implemented for all fitting approaches described in the previous paragraphs. To finish our discussion of the Python analysis program, we note that panels 10 and 11 in Figure 5.4 allow to manually subtract and add fits, automatically showing plots of the corresponding $sEQE$ spectra.

5.3.4 Fit Approach Comparison

Figure 5.8 shows a comparison of the three different fit approaches discussed in the previous paragraphs, i.e. approach 1 - fitting just the CT state, approach 2 - separately fitting the S_1 and CT state peaks by subtracting the S_1 from the $sEQE$, and approach 3 - simultaneously fitting the S_1 and CT state absorption contribution. All fits were performed using classical Marcus theory and excluding disorder 3.10. Approach 1 is shown in the first column of Figure 5.8, approach 2 in the second column, and approach 3 in the third column. The S_1 peak fits in Figure 5.8a/d are included for completeness and were not considered during fitting. The top row (a-c) shows fits of ZnPc:C_{60} with a discernible CT state shoulder, and the bottom row (d-f) shows fits of F_4ZnPc:C_{60} without a clear distinction between CT state and singlet absorption. The corresponding fit results are shown in Tables 5.1 and 5.2 respectively.

Visually comparing the fits of each material system, we observe strong differences depending on which fit approach is chosen. The simplest approach, fitting just the CT state contribution, leads to CT state fits that look visually correct, but underestimate (overestimate) the $sEQE$ tail of ZnPc:C_{60} (F_4ZnPc:C_{60}) when combined with a representative S_1 absorption contribution.

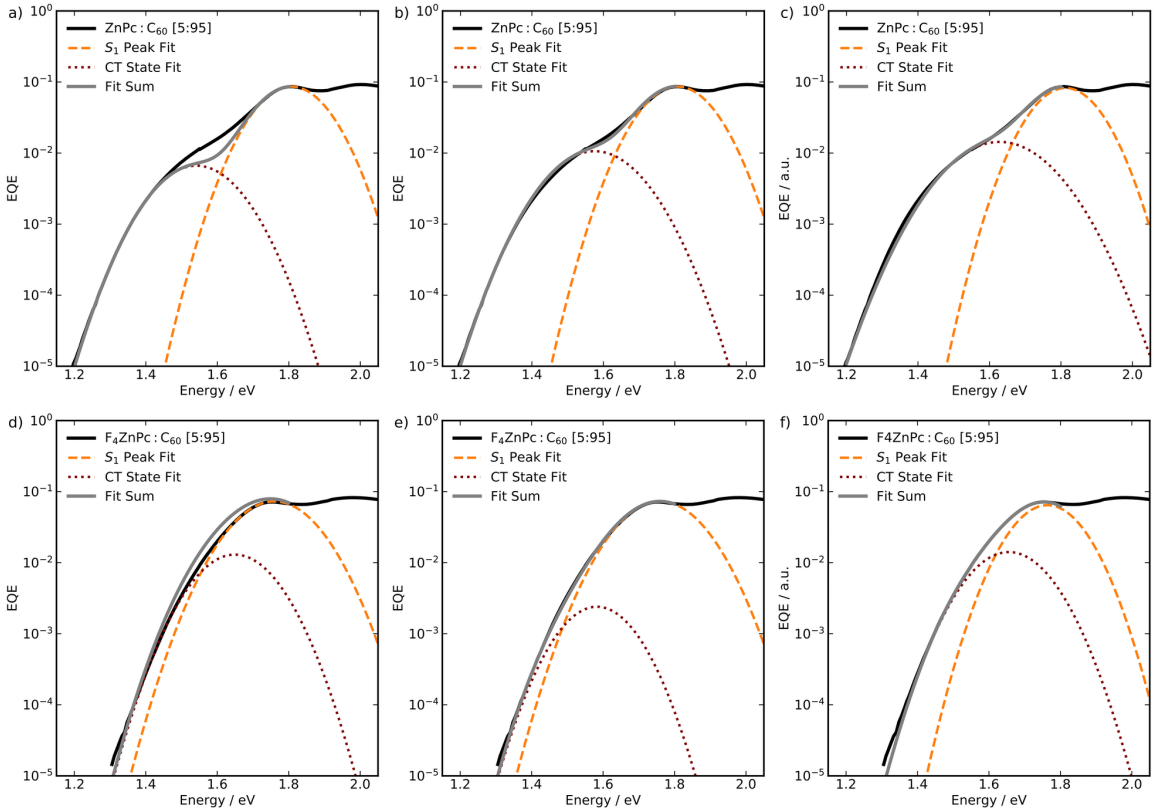


Figure 5.8: Comparison of different Gaussian fit approaches for a-c) dilute ZnPc:C_{60}, which shows a distinct CT absorption peak, and d-f) dilute F_4ZnPc:C_{60}, without sub-gap absorption features. The first column (a&d) shows the simplest case where just the CT state peak is fit. The S_1 peak fit is added for completeness but was not considered during fitting. The second column (b&e) shows the fit result of fitting the S_1 peak first, and subsequently subtracting it from the data to fit the CT state absorption contribution. The third column (c&f) shows the result of simultaneously fitting two Gaussian functions to the low energy $sEQE$ tail.

Table 5.1: Fit result comparison of the three approaches introduced in the main text for dilute ZnPc:C_{60} with clearly resolved sub-gap absorption features. Approach 1 refers to fitting the CT state independently, approach 2 to fitting and subtracting the singlet peak before fitting the CT state, and approach 3 refers to a simultaneous Gaussian fitting of the singlet and CT state peaks. The uncertainties are calculated as the fit uncertainties. The percent deviation is calculated from the ratio of the standard deviation and the average across all values x i.e. $\sigma_x/\bar{x} \times 100$.

	Approach 1	**Approach 2**	**Approach 3**	**Deviation**
E_{S_1} / eV	-	1.68 ± 0.00	1.70 ± 0.01	1 %
λ_{S_1} / eV	-	0.136 ± 0.000	0.121 ± 0.004	8 %
f_{S_1} / eV^2	-	0.0325 ± 0.0000	0.0294 ± 0.0008	7 %
E_{CT} / eV	1.37 ± 0.01	1.38 ± 0.01	1.39 ± 0.01	1 %
λ_{CT} / eV	0.175 ± 0.068	0.199 ± 0.015	0.250 ± 0.018	18 %
f_{CT} / eV^2	0.0042 ± 0.0053	0.0042 ± 0.0014	0.0066 ± 0.0005	28 %

Table 5.2: Fit result comparison of the three approaches introduced in the main text for dilute F_4ZnPc:C_{60} without clearly resolved sub-gap absorption features. Approach 1 refers to fitting the CT state independently, approach 2 to fitting and subtracting the singlet peak before fitting the CT state, and approach 3 refers to a simultaneous Gaussian fitting of the singlet and CT state peaks. The uncertainties are calculated as the fit uncertainties. The percent deviation is calculated from the ratio of the standard deviation and the average across all values x i.e. $\sigma_x/\bar{x} \times 100$.

	Approach 1	**Approach 2**	**Approach 3**	**Deviation**
E_{S_1} / eV	-	1.59 ± 0.00	1.64 ± 0.01	2 %
λ_{S_1} / eV	-	0.179 ± 0.000	0.128 ± 0.004	23 %
f_{S_1} / eV^2	-	0.0307 ± 0.0000	0.0230 ± 0.0015	20 %
E_{CT} / eV	1.48 ± 0.04	1.45 ± 0.01	1.50 ± 0.01	2 %
λ_{CT} / eV	0.119 ± 0.065	0.136 ± 0.030	0.159 ± 0.013	15 %
f_{CT} / eV^2	0.0033 ± 0.0027	0.0008 ± 0.0005	0.0053 ± 0.0014	72 %

Comparing the results of separate and simultaneous double peak fitting (approaches 2 and 3), we notice broader (higher λ_{CT}) and taller (higher f_{CT}) CT state peaks for the simultaneous double peak fitting approach. As briefly mentioned earlier, fitting S_1 and CT state contributions separately might wrongfully attribute CT absorption contributions to that of the singlet state. Comparing the fit results presented in Tables 5.1 and 5.2, the smallest deviations of $1-2\%$ are observed for fitting E_{CT}. Larger deviations are observed for λ_{CT} (up to 18%) and f_{CT} (up to 72%).

As expected, the fit results deviate less for the ZnPc:C_{60} blend given that the absorption features are easier to distinguish than for F_4ZnPc:C_{60}. Nonetheless, our results show that even for systems with clear CT absorption shoulders, the choice of fitting methodology matters and fit results differ across approaches. While E_{CT} is an important parameter, λ_{CT} and f_{CT} have also been shown to be significant for voltage loss analyses [24], [106]. In addition, an accurate determination of all CT state parameters is important for future molecular design.

The standard fitting approach employed in this thesis follows approach 2, i.e. separately fitting singlet and CT state absorption contributions. Despite the limitations described earlier, separate double peak fitting was found to be the most reliable and robust across the large set of material systems. Compared to simultaneous double peak fitting, which experimentally requires tight parameter constraints that need to be adjusted for each material system, separate double peak fitting leads to physically reasonable results without the same constraints.

6 | Charge transfer in dilute organic solar cells based on fluorinated Zinc-Phthalocyanines and C_{60}

Free charge generation in organic solar cells generally proceeds via (1) the formation of charge transfer (CT) excitons after photo-excitation of donor or acceptor molecules, and (2) CT dissociation into the charge separated (CS) state. While the efficiency of CT formation depends on the energetic difference between molecular singlet and CT states, the CT dissociation efficiency is determined by the energetic barrier between the CT and CS state. For a long time, research primarily focused on understanding and improving CT formation as a way to increase photocurrents. In this context, a major focus of research is centered on understanding the minimum energetic difference between local excitation (LE) and CT states that leads to efficient charge transfer [90], [106], [54], [181]. Recent studies of well-performing non-fullerene acceptors demonstrate that changing the energetics at the donor-acceptor interface not only impacts CT formation, but also affects the CT dissociation efficiency [181]. In this chapter, we investigate how charge transfer and exciton dissociation processes depend on interfacial molecular energetic offsets and electronic coupling in fullerene-based blends. We fabricate devices based on dilute donor content blends of ZnPc or its fluorinated derivatives and C_{60}. Fluorination of ZnPc simultaneously shifts the molecular orbitals away from the vacuum level, which increases the CT state energy at the donor-acceptor interface with C_{60} [182], [41]. Through density functional theory (DFT) calculations and time-resolved electron paramagnetic resonance (trEPR) measurements, we draw a comprehensive picture of how LE, CT, and CS energy levels and the energetic transitions between states change upon fluorination of ZnPc. We find that upon fluorination of ZnPc, not only CT formation, but also CT dissociation decreases, resulting in a strong decrease in the measured photocurrents of the blends.

A manuscript based on the data presented in this chapter is in preparation and will be submitted by A. Jungbluth, E. Cho, A. Privitera, P. Kaienburg, A. E. Lauritzen, T. Derrien, S. V. Kesava, I. Habib, J. L. Brédas, V. Coropceanu, and M. Riede.

6.1 Introduction

The power conversion efficiency (PCE) of organic solar cells (OSCs) is primarily limited by large energy losses of 100s meV that reduce the open-circuit voltage (V_{oc}) compared to the optical gap (E_{opt}) of the light-absorbing molecules [1], [90]. These energy losses arise from radiative and non-radiative recombination, often facilitated via the charge transfer (CT) state that forms at the donor-acceptor interface [83]. In addition to a reduced open-circuit voltage, free charge generation, which generally proceeds via (1) the formation of CT excitons after photo-excitation of donor or acceptor molecules and (2) the dissociation of CT excitons into the charge separated (CS) state, is often also limited. While the efficiency of CT formation depends on the energetic difference between the molecular optical gap and the CT state energy ($\Delta E_{CT} = E_{opt} - E_{CT}$), the efficiency of CT dissociation depends on the energetic barrier between the CT and CS state ($\Delta E_{CS} = E_{CT} - E_{CS}$).

For a long time, research primarily focused on improving CT formation as a way to increase free charge generation. Based on studies of fullerenes, which were the standard acceptor molecules in the OSC research field for decades, it was believed that ΔE_{CT} of 100s meV were needed for efficient charge transfer, resulting in an apparent trade-off between high V_{oc} and high photocurrents [183], [57]. Understanding the minimum ΔE_{CT} that leads to efficient free charge generation is still a major focus of research [90], [106], [54], [181].

The emergence of non-fullerene acceptors (NFAs) has brought the tradeoff between voltage and photocurrent into question, as OSCs based on NFA blends achieve efficient free charge generation with very low or vanishing ΔE_{CT} [54], [184], [140], [185]. Recently, OSCs based on NFAs have reached PCEs of up to 19% [186], naming enhanced charge carrier dynamics and energetics, facilitated via strong light absorption, ultra-long exciton lifetimes [95], [187], enhanced morphologies [91], and energetic hybridization between highly emissive local excitations (LE) and CT states [106], [104] as the main reasons for increased performances.

In addition to efficient CT formation, many well-performing NFA systems show no signatures of geminate triplets, suggesting that CT dissociation is efficient and strongly outclasses geminate recombination pathways [65]. While the CT $-$ CS transition has traditionally re-

ceived less attention in literature, recent work demonstrated for polymer:NFA blends that changing the energetics at the donor:acceptor interface not only changes ΔE_{CT}, but also impacts the efficiency of CT dissociation [181]. This challenges the common understanding that donor and acceptor molecular energy levels primarily influence the LE $-$ CT transition, and that ΔE_{CT} and not ΔE_{CS} is the limiting factor for efficient free charge generation.

Following from these initial insights into the charge separation mechanisms of NFAs, the question remains why low energetic offsets work for NFAs but generally do not work for fullerenes. Beyond a scholarly interest in fullerene acceptors, they are highly relevant for upscaling industrial production, since their cost and synthetic complexity are lower than those of NFAs.

In this chapter, we investigate how charge transfer and exciton dissociation processes depend on interfacial molecular energetic offsets and electronic coupling in fullerene-based blends. More specifically, we study model systems of dilute bulk heterojunctions (donor:acceptor ratio of 5:95 wt.%) of zinc-phthalocyanines (ZnPc) or its fluorinated derivates (F_4ZnPc, F_8ZnPc, F_{16}ZnPc) as donors and C_{60} as the electron acceptor. At dilute donor content, donor aggregation is largely suppressed, leading to comparable morphologies across donor choices and allowing to disentangle microstructural and energetic effects [3].

Through density functional theory (DFT) calculations and time-resolved electron paramagnetic resonance (trEPR) measurements, we draw a comprehensive picture of how LE, CT, and CS energy levels and the energetic transitions between states change upon fluorination of ZnPc. We show that for ZnPc:C_{60}, which shows a large LE $-$ CT offset, both CT formation and CT dissociation are efficient. For smaller offsets, as observed for F_4ZnPc:C_{60} and F_8ZnPc:C_{60}, CT formation remains efficient, but CT dissociation slows down. We find that the measured photocurrent, which is high for F_4ZnPc and low for F_8ZnPc, is primarily determined by how much CT dissociation decreases in efficiency. Finally, F_{16}ZnPc:C_{60}, which shows the lowest LE $-$ CT offset, shows reduced photocurrents that are attributed to both limited CT formation and CT dissociation.

6.2 Materials & Devices

To investigate the impact of interfacial energetic offsets on charge transfer and separation, we study the performance of dilute OSCs based on F_xZnPc (x=0, 4, 8, 16) and C_{60}. Fluorination of ZnPc gradually shifts the HOMO and LUMO away from the vacuum level, keeping the molecular singlet energy (E_{S_1}) roughly constant [188], [189], [41], [190]. This shift in donor molecular orbitals is accompanied by a corresponding shift in the interfacial CT state energy in F_xZnPc:C_{60} bulk heterojunctions (BHJs) [182].

For small molecule vacuum thermal evaporated OSCs, low donor contents (in our case with donor:acceptor ratios of 5:95 wt.%) were shown to produce well-performing devices with reduced recombination losses [49], [52], [191], [192], [193]. In addition, microstructural characterization of the dilute blends highlights the lack of crystalline C_{60} features, which is caused by interspersed donor molecules that effectively disrupt C_{60} packing (see Figure B.1 in the Appendix) [3], [4], [194]. This leads to comparable morphologies and makes dilute F_xZnPc:C_{60} blends an ideal model system to study the impact of gradually shifted donor energy levels on device performance in terms of voltage losses and photocurrent.

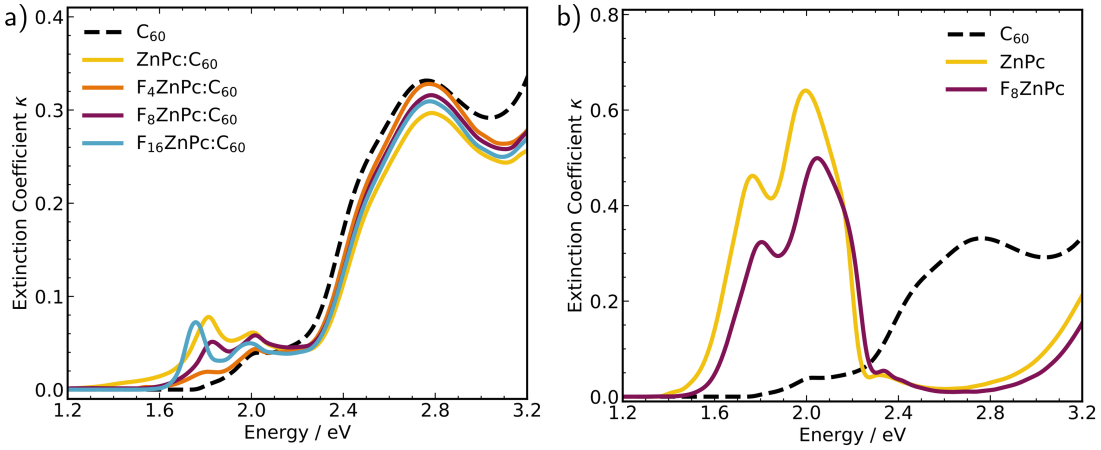


Figure 6.1: Extinction coefficient (κ) measured via spectroscopic ellipsometry for thin films on quartz of a) dilute F_xZnPc:C_{60} and b) neat ZnPc, F_8ZnPc, and C_{60}. The absorbance of the dilute blends strongly follows that of neat C_{60}, with only minor changes between 1.6 – 2.2 eV caused by the characteristic absorption doublet of F_xZnPc [189], [188]. Compared to the absorption profile of ZnPc, the slight red shift (blue shift) of the absorption peaks of F_4ZnPc and F_{16}ZnPc (F_8ZnPc) is ascribed to changes in the transition dipole alignment and intermolecular coupling upon fluorination [189]. The ellipsometry measurements and analysis were performed by Irfan Habib and Dr. Sameer V. Kesava.

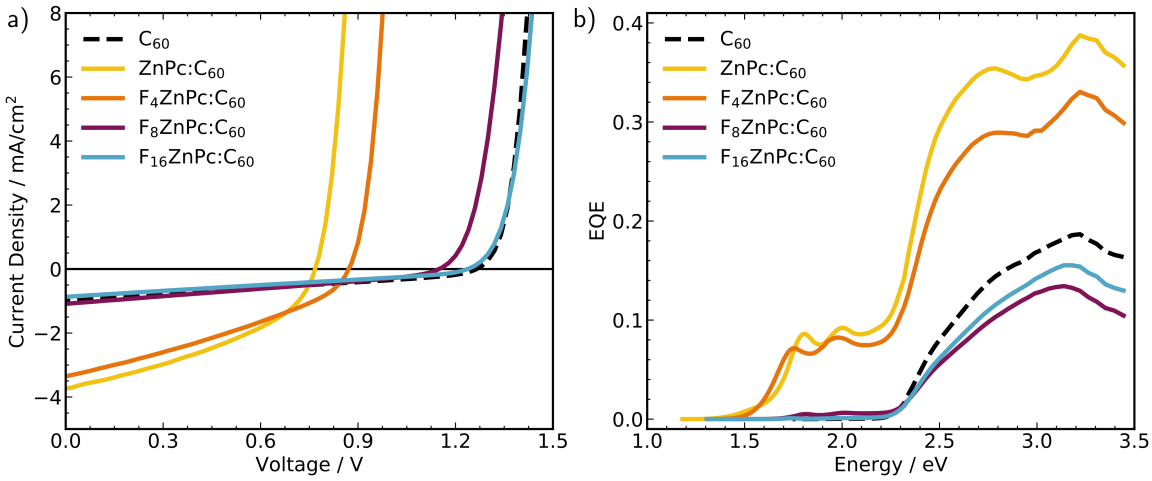


Figure 6.2: a) Current density-voltage ($J-V$) characteristics under simulated 1 Sun illumination and b) external quantum efficiency (EQE) of the best performing (highest PCE) dilute F_xZnPc:C_{60} blends at room temperature. The performance of a neat C_{60} reference device is shown for comparison. The $J-V$ data was not mismatch corrected. However, due to the strong similarities in the donor absorption profiles (Figure 6.1), mismatch correction would result in similar scaling for all samples and preserve the observed performance trends.

6.3 Device Performance

Figure 6.2a shows the current density-voltage ($J-V$) characteristics of the best performing (highest PCE) devices from batches of nominally identical samples. An overview of the performance trends is shown in Table C.1 in the Appendix. Upon fluorination, the V_{oc} increases from 0.76 ± 0.01 V (ZnPc) to 1.21 ± 0.02 V (F_{16}ZnPc). This trend agrees with literature reports on the performance of intermixed 1:1 blends of F_xZnPc:C_{60} [190], [182] and F_xZnPc/C_{60} bilayer OSCs [189]. The improvement in V_{oc} results from the fluorination-induced shift of the donor HOMO energies that increase E_{CT} and reduce the energetic offset between the CT state and the F_xZnPc singlet. This change is accompanied by a decrease in J_{sc} from 3.6 ± 0.2 mA/cm^2 (ZnPc) to 0.8 ± 0.1 mA/cm^2 (F_{16}ZnPc). Interestingly, the J_{sc} of the F_8ZnPc and F_{16}ZnPc blends is comparable to that of neat C_{60}.

The J_{sc} is governed by the active layer absorbance, exciton separation efficiency, and charge collection efficiency. With increasing donor fluorination, active layer absorbance, as observed via the extinction coefficient of the blends, remains largely unchanged (Figure 6.1a). With nominally identical device stacks and active layer thicknesses of 50 nm, changes in the

charge collection efficiency, potentially reflected in a small relative decrease in fill factor between the dilute ZnPc and F_{16}ZnPc blends (Table C.1), are not enough to explain the $\sim 80\%$ drop in J_{sc} with increasing fluorination. Instead, the J_{sc} is primarily limited by poor exciton separation caused by the reduced energetic offset at the donor-acceptor interface. Consequently, while the V_{oc} of our fullerene-based blends behaves much like that of low-offset NFAs, we do not observe the appreciable photocurrents that low-offset NFAs show.

In agreement with the $J-V$ behavior, the external quantum efficiency (EQE) of the dilute blends show an improvement in free charge generation for ZnPc and F_4ZnPc compared to neat C_{60} (Figure 6.2b). Free charge generation in the dilute F_8ZnPc and F_{16}ZnPc blends, however, is severely limited, as observed by the reduced EQE. Both C_{60} and F_xZnPc contribute to photon absorption, with neat F_xZnPc strongly absorbing between $1.6-2.2$ eV (Figure 6.1b). While C_{60} absorption in this spectral region is symmetry-forbidden and therefore weak [195], C_{60} absorbs strongly above 2.2 eV. This suggests that excitons generated in C_{60} dissociate via hole transfer, and excitons generated in F_xZnPc dissociate via electron transfer - as is commonly observed in fullerene-based BHJs.

Comparing the EQE and absorbance profiles of the dilute blends, efficient free charge generation in the donor absorption region is only observed for the ZnPc and F_4ZnPc blends (Figure 6.2b and Figure 6.3). The characteristic F_xZnPc doublet is barely visible for F_8ZnPc and cannot be resolved in the linear EQE of F_{16}ZnPc. This suggests that the contribution of donor absorption and subsequent electron transfer to C_{60} to the total photocurrent in these blends is low. In addition, the EQE of the F_8ZnPc and F_{16}ZnPc blends in the C_{60} absorption region is roughly equal to that of the neat C_{60} device. This, combined with the overall reduction in the EQE when going from F_4ZnPc to higher donor fluorinations, suggests that the F_8ZnPc:C_{60} and F_{16}ZnPc:C_{60} interfaces barely contribute to the splitting of singlet excitons.

Instead, we hypothesize that most excitons are split via intermolecular CT states across C_{60} molecules [195], which explains the observed "C_{60}-like" $J-V$ behavior of the F_8ZnPc and F_{16}ZnPc blends. This allows us to formally categorize ZnPc/F_4ZnPc as systems with efficient charge separation but $V_{oc} < 1$ V, and F_8ZnPc/F_{16}ZnPc as systems with $V_{oc} > 1$ V but limited photocurrents.

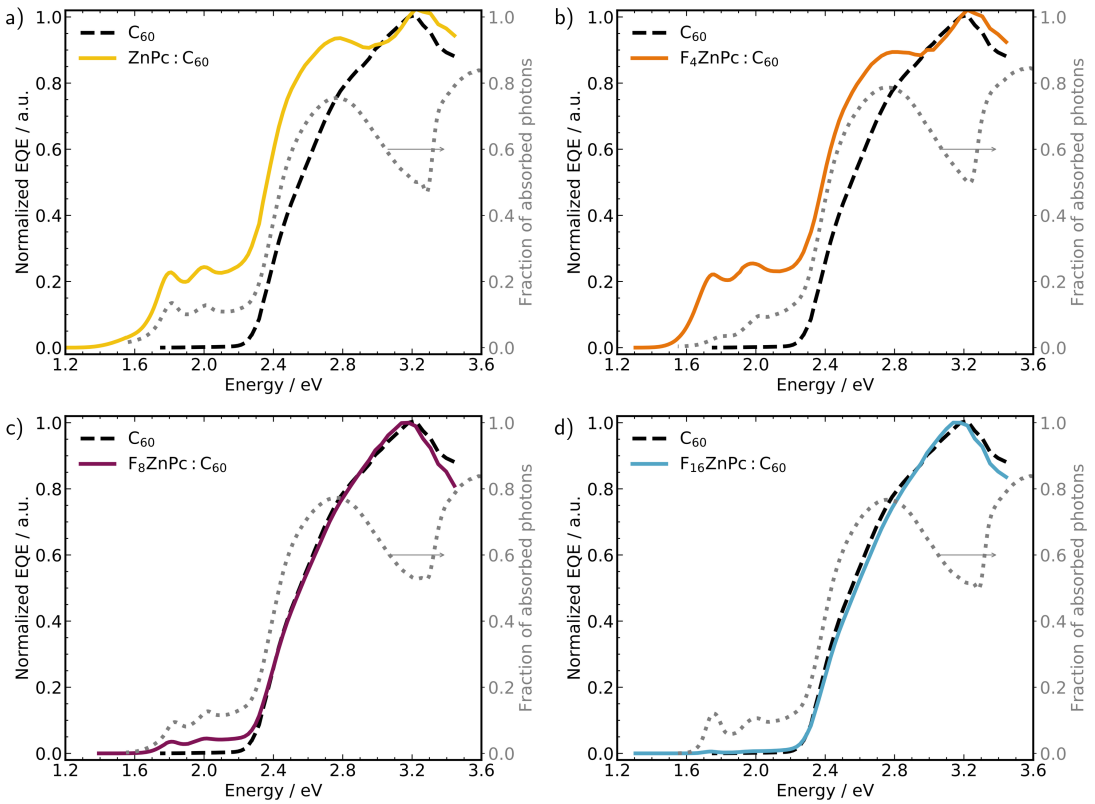


Figure 6.3: Comparison of photon absorption (right axis) and charge generation (left axis) for dilute donor blends of a) ZnPc, b) F_4ZnPc, c) F_8ZnPc, and d) F_{16}ZnPc and C_{60}. The complex refractive index of the blends was measured via spectroscopic ellipsometry, and the fraction of absorbed photons calculated using the transfer matrix approach [127]. This is compared to the external quantum efficiency (EQE) at room temperature of full devices with the respective blends as active layers. All material systems show photon absorption between $1.5 - 2.2$ eV, but only the ZnPc and F_4ZnPc blends show efficient free charge generation in this spectral region.

6.4 Energy Levels

To contextualize the device performances of the fluorinated blends and connect them to molecular and CT state energy levels, we performed density functional theory (DFT) calculations and modelled the CT absorption band in the sensitive EQE spectra of the blends. All DFT calculations and energy level analyses were performed by Dr. Veaceslav Coropceanu and Dr. Eunkyung Cho at the University of Arizona. Using time-dependent DFT (TDDFT) based on the screened range-separated hybrid (SRSH) functional LC-ωhPBE and 6-31G** basis set, the excited state properties of LE and CT state singlet and triplet energies were determined (see Tables B.1, B.2, B.3, and B.4 in the Appendix).

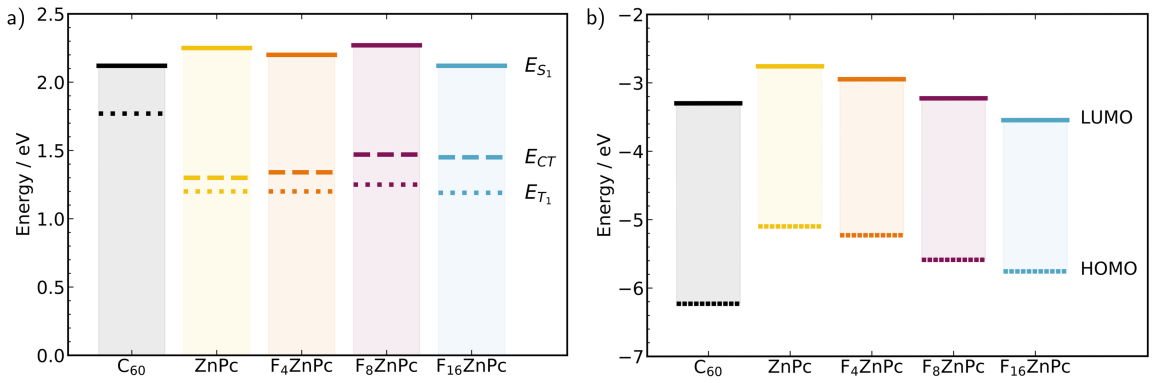


Figure 6.4: a) DFT calculations of the lowest energy LE singlet (E_{S_1}), triplet (E_{T_1}), and CT states (E_{CT}) of isolated F_xZnPc:C_{60} complexes. b) DFT estimates of the HOMO and LUMO energies of F_xZnPc and C_{60} molecules embedded into a dielectric medium with $\epsilon = 4$. The calculated energy levels for the isolated complexes are likely larger than what would be observed in thin films. The DFT calculations were performed by Dr. Veaceslav Coropceanu and Dr. Eunkyung Cho.

Table 6.1: DFT calculations of the lowest energy LE singlet (E_{S_1}), triplet (E_{T_1}), and CT states (E_{CT}) of isolated F_xZnPc:C_{60} complexes for $\epsilon = 4$. The donor energy levels are labelled with the subscript D. All calculated energy levels are included in Tables B.1, B.2, B.3, and B.4 in the Appendix, and are plotted in Figure 6.4. The DFT calculations were performed by Dr. Veaceslav Coropceanu and Dr. Eunkyung Cho.

State / eV	**ZnPc:C_{60}**	**F_4ZnPc:C_{60}**	**F_8ZnPc:C_{60}**	**F_{16}ZnPc:C_{60}**
$E_{S_1,C_{60}}$	2.12	2.12	2.12	2.13
$E_{T_1,C_{60}}$	1.77	1.77	1.77	1.77
$E_{S_1,D}$	2.25	2.20	2.27	2.12
$E_{T_1,D}$	1.20	1.20	1.25	1.19
E_{CT}	1.30	1.34	1.47	1.45

In line with experimental measurements [188], [189], [41], [190], our DFT calculations show that fluorination of ZnPc only has a modest effect on E_{S_1}, with a 0.1 eV decrease when going from ZnPc to F_{16}ZnPc. In addition, the lowest excited state in neat C_{60} films is found to be about 1.7 eV, which is attributed to structural defects (C_{60} dimerization for instance) [196].

Based on the DFT results, we next discuss the energetic evolution of the singlet CT state upon fluorination. As seen in Figure 6.4 (and Table 6.1), the CT state energy of the four complexes can be grouped in two pairs, i.e. ZnPc:C_{60} with F_4ZnPc:C_{60}, and F_8ZnPc:C_{60} with F_{16}ZnPc:C_{60}, since the energy difference of E_{CT} within each pair is smaller than between pairs. This pairing matches the identical pairing observed for the device performances.

Table 6.2: Calculated energies of the charge separated (CS) and charge transfer (CT) state of isolated F_xZnPc:C_{60} complexes for $\epsilon = 4$, and using equations 6.1 and 6.2. E_{CT} describes the energy of the singlet CT state, with the triplet CT state differing by only a few meV. The DFT calculations were performed by Dr. Veaceslav Coropceanu and Dr. Eunkyung Cho.

State / eV	**ZnPc:C_{60}**	**F_4ZnPc:C_{60}**	**F_8ZnPc:C_{60}**	**F_{16}ZnPc:C_{60}**
E_{CS}	1.80	1.93	2.29	2.46
E_{CT}	1.30	1.43	1.79	1.96

According to the TDDFT results obtained for $\epsilon = 4$ (roughly the static dielectric constant of a neat C_{60} film), the CT state energies upon fluorination span a range of 1.30 eV (ZnPc:C_{60}) to 1.45 eV (F_{16}ZnPc:C_{60}). We note, however, that the intermolecular distances between F_xZnPc and C_{60} obtained from the geometry optimization of the isolated complexes using DFT are most likely smaller than that those in the blends with low donor content where the donor can interact with several C_{60} molecules. As a result, the TDDFT derived CT state energies are likely an underestimate due to the overestimation of the electrostatic effect. To get an alternative estimation, we represent the CT state energy as the sum of the energy of the charge separated state (E_{CS}) and the hole-electron electrostatic interaction energy (E_{el})

$$E_{CT} = E_{CS} + E_{el}. \tag{6.1}$$

Estimating E_{CS} via the energies of the frontier molecular orbitals of the donors (D) and acceptor (A), we obtain

$$E_{CT} = [E_{\mathrm{LUMO}}(\mathrm{C_{60}}) - E_{\mathrm{HOMO}}(\mathrm{F_xZnPc})] + E_{el}. \tag{6.2}$$

In donor-acceptor blends, E_{el} is expected to be between -0.3 eV and -0.6 eV [174], [157], [197]. For the calculations presented in this chapter, E_{el} was assumed to be constant for all four blends and equal to -0.50 eV.

The E_{LUMO} and E_{HOMO} values, calculated for C_{60} and F_xZnPc molecules embedded into a dielectric medium with $\epsilon = 4$, are plotted in Figure 6.4b (and recorded in Table B.5 in the Appendix). As found for the CT states, the E_{HOMO} values of the donors can also be grouped

into pairs based on their magnitude. The estimated E_{CS} and E_{CT} values (using equation 6.2) are given in Table 6.2.

From these calculations, E_{CT} was determined as 1.30 eV (1.43 eV) for ZnPc (F_4ZnPc) and 1.79 eV (1.96 eV) for F_8ZnPc (F_{16}ZnPc) respectively. Importantly, E_{CT} of F_8ZnPc:C_{60} and F_{16}ZnPc:C_{60} is found to be in close resonance with the singlet LE states of the donor and acceptor units calculated via TDDFT. This suggests that ΔE_{CT} is low in these systems and CT state formation is discouraged. Thus, we hypothesize that the interfacial CT states in F_8ZnPc:C_{60} and especially F_{16}ZnPc:C_{60} do not provide an effective route for charge transfer, which is qualitative agreement with our observation of low photocurrents in these blends.

We now switch to a discussion of triplet states. The presented DFT calculations indicate that the energy of the lowest triplet state (T_1) in F_xZnPc is about 1.2 eV. This value compares well with the experimental value of 1.13 eV measured for triplet states of ZnPc in solution [182], [198], [199]. The DFT estimate for T_1 in C_{60} is about 1.77 eV which is a slight overestimate compared to the measured value of 1.6 eV for C_{60} in a noble gas matrix [200], or 1.5 eV measured in C_{60} thin films [201]. Nonetheless, both DFT calculations and experimental results confirm that the T_1 of F_xZnPc is the lowest energetic state in the blends, and that it is lower in energy than the T_1 of C_{60}.

Finally, we note here that in agreement with previous studies, the DFT calculations predict that the triplet and singlet CT states in the F_xZnPc:C_{60} blends are quasi-degenerate with an energy splitting that does not exceed more than a few meVs [202], [174]. Therefore, the values presented in Table 6.2 suggest that the triplet CT levels in the ZnPc:C_{60} and F_4ZnPc:C_{60} blends are located between the T_1 of F_xZnPc and C_{60}. In comparison, in the F_8ZnPc:C_{60} and F_{16}ZnPc:C_{60} blends, the triplet CT levels are located above the T_1 levels of both the F_xZnPc and C_{60} molecules. This will become important later when we discuss geminate recombination pathways.

To connect our DFT results to experimental observations, we fit CT state energies by deconvolution of the low-energy tail of the EQE spectrum through Gaussian functions using classical Marcus theory (Figure 6.5) and following the fitting methodology presented in Chapter 5 [1]. In brief, we first fit the lowest singlet state, and then subtract its contribution from the EQE spectrum to fit the remaining sub-gap absorption as the CT state.

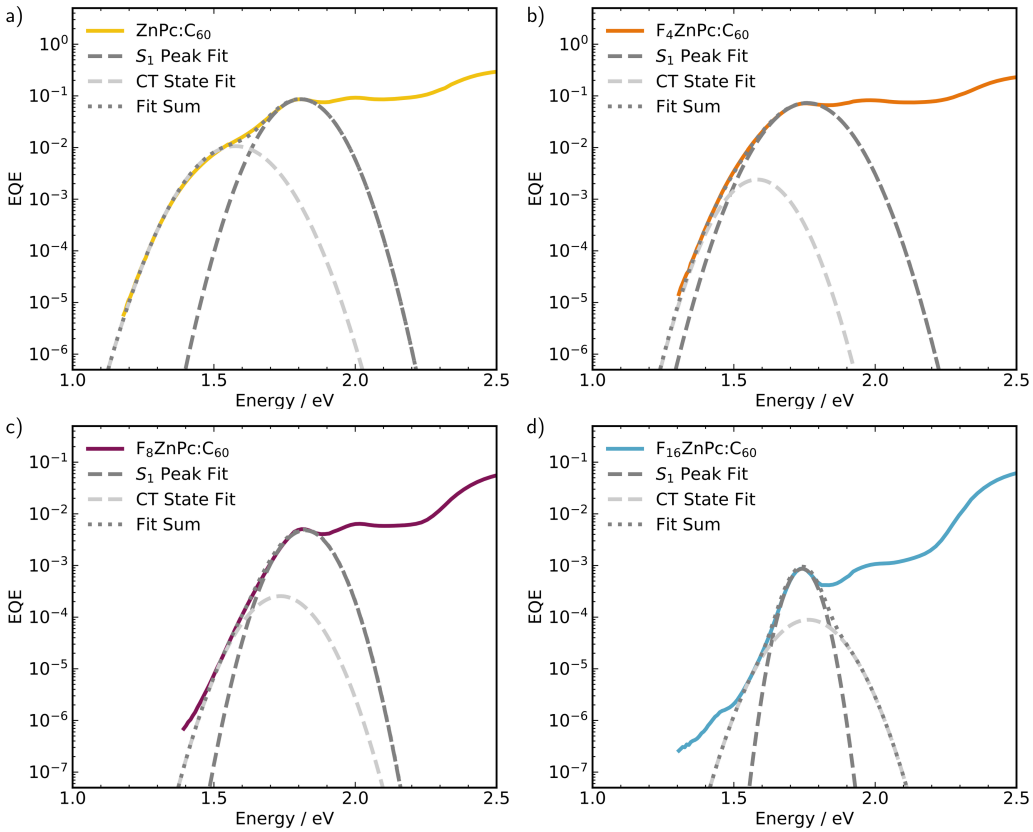


Figure 6.5: Fitting of room temperature EQE spectra of dilute donor blends of a) ZnPc, b) F_4ZnPc, c) F_8ZnPc, and d) F_{16}ZnPc and C_{60}. The light grey (dark grey) dashed lines show the fits of CT (singlet S_1) states. The dotted lines indicate the sum of the fits. Both the S_1 and CT states were fit using the classical Marcus theory, and following the fitting methodology outlined in Chapter 5.

The application of this approach yields singlet E_{CT} values of 1.38 ± 0.01 eV, 1.45 ± 0.01 eV, 1.59 ± 0.01 eV, and 1.61 ± 0.01 eV for ZnPc:C_{60}, F_4ZnPc:C_{60}, F_8ZnPc:C_{60}, and F_{16}ZnPc:C_{60} respectively. Again, these values suggest that triplet CT states in F_8ZnPc:C_{60} and F_{16}ZnPc:C_{60}, in contrast to those of ZnPc:C_{60} and F_4ZnPc:C_{60}, are located above the T_1 level of C_{60}.

Looking at the EQE on a logarithmic scale (Figures 6.5 and 6.6a), only the ZnPc:C_{60} system shows a clearly resolvable peak in the sub-gap region, attributable to CT state absorption. Since the energetic offset between the orbital energy levels of the donor and acceptor molecules decreases with fluorination of ZnPc, the CT state shoulder merges with the LE singlet transitions. This makes a simple spectral band deconvolution approach ambiguous.

Moreover, two-state models (like classical Marcus theory) only accounts for coupling between the CT and ground state (GS). However, it is well recognized that in many instances

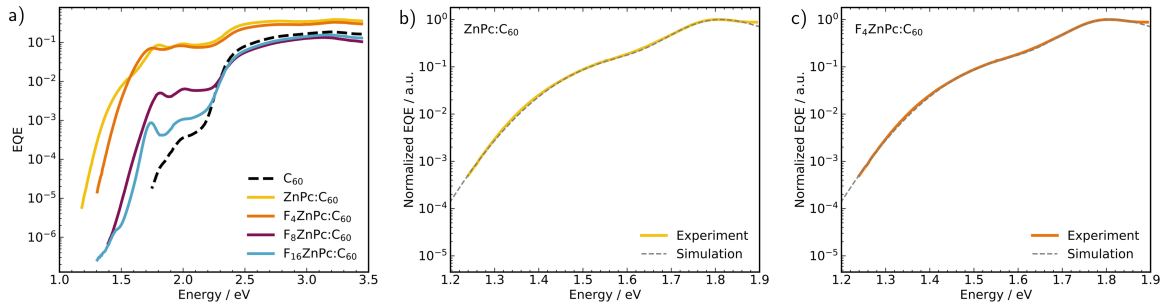


Figure 6.6: a) Sensitive EQE measurements of the dilute blends at room temperature. Only the ZnPc:C_{60} system shows a resolvable CT state absorption shoulder in the sub-gap region. Simulated EQE spectra of b) ZnPc:C_{60} and c) F_4ZnPc:C_{60} blends using a three-state vibronic model (gray dashed lines), as compared to the experimental data (yellow/orange solid lines). The fitting parameters are listed in Table B.7 in the Appendix. The three-state vibronic fits were performed by Dr. Veaceslav Coropceanu and Dr. Eunkyung Cho.

the intensity and the shape of the CT band can strongly depend on the hybridization of the CT state with the local excitation on the donor and/or acceptor molecules [104], [92]. Therefore, we next analyze the low-energy EQE tail in the framework of a three-state dynamic vibronic model [104], [92]. The three-state vibronic fits were performed by Dr. Veaceslav Coropceanu and Dr. Eunkyung Cho.

The simulations of the CT absorption bands of the ZnPc and F_4ZnPc systems show that a very good fit of the EQE band can be obtained when only accounting for the hybridization between CT and LE states (Figures 6.6b and c). In these simulations, the CT energies and the electronic coupling between CT and LE states were considered as fitting parameters (see Table B.7 in the Appendix for details). The derived CT state energy and the energetic difference (ΔE_{CT}) between LE and CT states from the fitting are 1.38 eV and 0.3 eV for ZnPc:C_{60}, and 1.45 eV and 0.2 eV for F_4ZnPc:C_{60}, respectively. These values agree with those predicted above using Marcus theory. In the case of F_8ZnPc:C_{60} and F_{16}ZnPc:C_{60} a reasonable simulation of the low-energy EQE band can only be obtained assuming that the oscillator strength of the $S_0 \rightarrow S_1$ transition in F_8ZnPc and F_{16}ZnPc is about 100 times smaller than that in ZnPc; this assumption is evidently unreasonable.

We note that the classical and dynamic vibronic models used above are designed to interpret the absorption CT bands. Here, in fact, we deal with EQE spectra which not only depend on the absorption but also on the charge-separation efficiency of CT and LE states. Therefore,

if the charge-separation efficiency of the CT and LE states is for instance energy-dependent, then the approaches based on the fitting of EQE spectra to derive electronic structure information might not work properly.

As discussed earlier, while the absorbance of the dilute blends stays roughly constant with increasing donor content (Figure 6.3), the EQE reduces for F_8ZnPc and F_{16}ZnPc, with the starkest decrease observable in the donor absorption region. This results in a lower internal quantum efficiency (IQE) indicative of reduced exciton dissociation in the F_8ZnPc and F_{16}ZnPc blends, and manifests in what would be observed as an extremely low oscillator strength in the EQE when fitting the three-state vibronic model.

To conclude, fitting the low-energy EQE bands via a three-state vibronic model reveals that in line with DFT calculations (see Table B.6 in the Appendix), there is a strong hybridization between CT and LE states of ZnPc/F_4ZnPc that defines the shape of the EQE band tail. A strong hybridization between CT and LE states is also predicted by DFT calculations for F_8ZnPc and F_{16}ZnPc.

Nonetheless, fitting the low-energy EQE bands with the two-state Marcus model and the three-state vibronic model reveals that both methods agree on the value of E_{CT} for ZnPc:C_{60} and F_4ZnPc:C_{60}, and predict that the CT level is energetically located below the T_1 of C_{60} in these blends. In the absence of three-state fits of F_8ZnPc:C_{60} and F_{16}ZnPc:C_{60}, combining DFT calculations and two-state Marcus theory suggests that ΔE_{CS}, i.e. the energetic difference between the CT and CS state, increases with increasing donor fluorination. This observation is in agreement with previously published work [41], which measured increasing ΔE_{CS} with increasing fluorination of ZnPc [41].

6.5 Charge Separation & Recombination

Having discussed the dependence of the interfacial energetic offset and E_{CT} on donor fluorination, we now relate these findings to charge separation and recombination processes in our blends. For this, we performed time-resolved electron paramagnetic resonance (trEPR) measurements. In this context, trEPR is an ideal technique to investigate the dynamics of

charge species containing unpaired electron spins, e.g. in CT and triplet states, by probing their unique spectral signatures [203], [204]. With this, trEPR allows us to study geminate recombination, i.e. recombination of electron-hole pairs that were created by the same photon. All trEPR measurements and analysis presented in this chapter were performed by Dr. Alberto Privitera.

As a matter of clarity, although non-geminate recombination can usually not be observed through trEPR, the presence of geminate recombination suggests that non-geminate pathways are also present [205]. However, our main interest in this work is to study the process of free charge generation to explain the variations in J_{sc} as a function of donor fluorination. For this, understanding the competition of CT formation (LE $-$ CT transition) and CT dissociation (CT $-$ CS transition) with different recombination pathways is key. This competition can be studied qualitatively with EPR.

We carried out trEPR at 80 K by using 532 nm laser excitation (exciting both F_xZnPc and C_{60}) on the dilute blends (Figure 6.7), and, for comparison, on the neat donors (Figure B.2 in the Appendix). All spectra show two main species: (1) a spectrally narrow signal centered around 345 mT, assigned to photogenerated free charges [65], [206], and (2) a broad signal ranging from about 320 to 370 mT which can be attributed to triplet states, generated either via back electron transfer (BET) or inter-system crossing (ISC) [3].

ISC from LE singlet to triplet states competes with CT formation and BET from CT states to donor or acceptor triplets competes with CT dissociation. In addition to the formation of triplets and subsequent relaxation to the GS, charges can also directly recombine from LE singlet or CT states. However, the focus of this work is not necessarily on understanding triplet formation as recombination pathways. Instead, observing a strong BET signal implies that CT dissociation is slow, allowing triplets to form. This can be used as a qualitative indication of inefficient CT dissociation.

Looking at the spectra in Figure 6.7, the observed low intensities of the signal of photogenerated free charges in the blends can be rationalized considering quick recombination of free charges (faster than 100s ns, which is the time resolution of our trEPR setup) [3], [207].

As for the triplet signal, we recall that trEPR spectroscopy not only provides information on

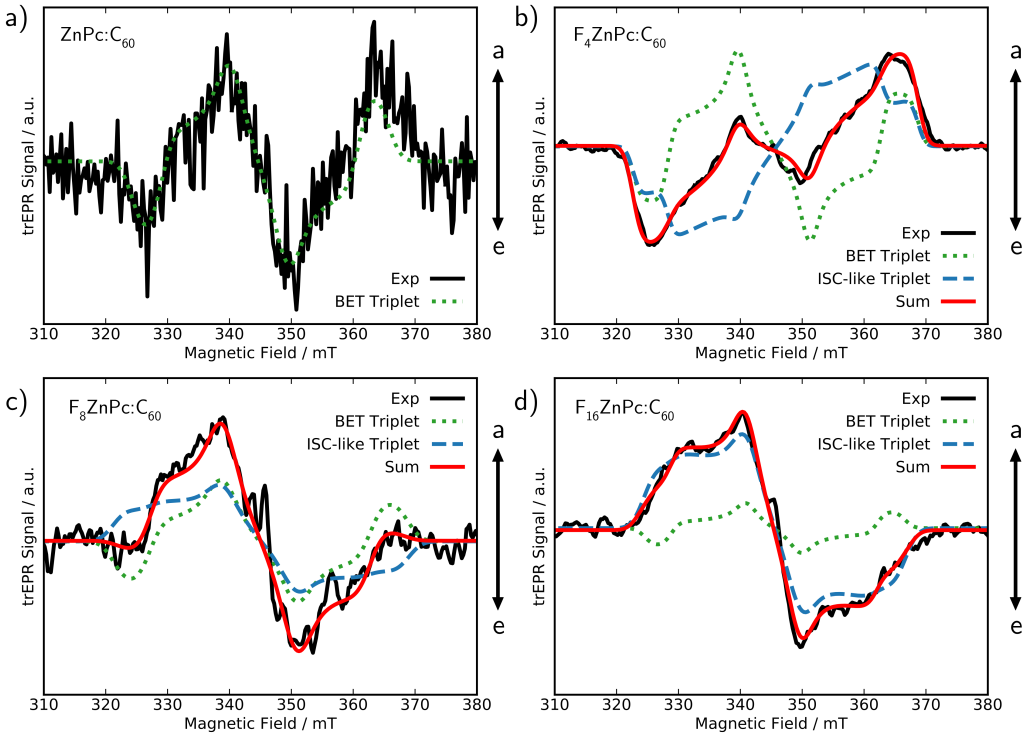


Figure 6.7: Time-resolved EPR spectra at 80 K of the dilute a) ZnPc, b) F_4ZnPc, c) F_8ZnPc, and d) F_{16}ZnPc blends with C_{60}. Black line: trEPR spectra of the dilute blends recorded at 1 μs (integration window $0.8 - 1.2$ μs) after a 532 nm laser pulse. Absorption (a) is up, and emission (e) is down. The narrow signal centered around 345 mT correspond to photogenerated free charges, and the broad peaks between $320 - 370$ mT correspond to triplet states. Red line: best-fit spectral simulations of donor triplets obtained as the sum of two contributions: (1) inter-system crossing (ISC)-like contribution (blue dashed line), and (2) geminate back electron transfer (BET) to a low lying T_1 triplet state (dotted green line). The values of the best-fit simulations are reported in Table 6.3. The trEPR measurements and analysis were performed by Dr. Alberto Privitera.

T_1 localization in the blend, but also on the T_1 formation pathways through the characteristic polarization patterns resulting from non-Boltzmann population of the triplet sublevels [65], [208]. The main results obtained from the best-fit simulations of the trEPR spectra are reported in Table 6.3. The complete list of fit results is included in the Appendix in Table B.8 for the neat films and Table B.9 for the dilute blends. Schematics of the charge transition pathways are shown in Figure 6.8 and are discussed below.

In the trEPR spectrum of the neat ZnPc film (Figure B.2 in the Appendix), a strong T_1 signal attributable to an efficient $S_1 \rightarrow T_1$ ISC process is observed. Conversely, in the dilute ZnPc blend, the same T_1 signal is mostly quenched, suggesting that ISC from an excited singlet

state is hindered by almost immediate CT formation and exciton dissociation [3].

The best-fit simulations reveal that the ZnPc T_1 in the dilute blend is populated via geminate recombination (i.e. via BET from the CT state to the ZnPc T_1 state). However, this BET contribution is very weak compared to the other blends, as indicated by the low signal-to-noise ratio in Figure 6.7a. This suggests that geminate BET in ZnPc:C_{60} occurs with low probability due to efficient CT dissociation. Efficient CT formation and dissociation rationalize the high photocurrents observed in the dilute ZnPc:C_{60} OSCs (Figure 6.2).

The T_1 zero-field splitting (ZFS) parameters in the dilute ZnPc blend, $\mathrm{D} = 583$ MHz and $\mathrm{E} = 107$ MHz, are comparable, but slightly larger than those obtained for the neat ZnPc film, suggesting that the T_1 in the blend is localized on the ZnPc molecule. In addition, no evidence of the C_{60} triplet is observed. Compared to the neat film, where ZnPc triplets can easily delocalize across neighboring molecules, the larger D value for the ZnPc triplets in the dilute blends can be assigned to tighter exciton localization on isolated ZnPc molecules.

We hypothesize that triplets generated via ISC on the C_{60} molecules in the ZnPc blend undergo charge transfer to the CT triplet states (as depicted in Figure 6.8a) [3]. Due to the hyperfine interactions, CT triplets are easily converted into singlets and are not expected to deteriorate device performance [65]. This means that in dilute ZnPc:C_{60}, a part of the photocurrent can arise from the dissociation of C_{60} triplet excitons via the $T_{1,C_{60}} \rightarrow$ CT $\rightarrow$ CS pathway [202]. The same pathway is energetically also possible in the F_4ZnPc blend. However, due to the close energetic matching between the T_1 of C_{60} and the CT state of F_4ZnPc:C_{60}, this pathway is hypothesized to occur with lower probability than in the ZnPc:C_{60} blend.

Table 6.3: A subset of the best-fit values obtained for the trEPR analysis of the dilute F_xZnPc:C_{60} blends. The complete list of fit values is included in Table B.9 in the Appendix. For each film, the zero-field splitting (ZFS) parameters are reported in absolute value units of MHz. The last column details the relative weight of ISC and BET triplets. The trEPR measurements and analysis were performed by Dr. Alberto Privitera.

	Triplet Species	**[D E] / MHz**	**weight$_{ISC}$:weight$_{BET}$**
ZnPc:C_{60}	BET	[583 107]	0:1
F_4ZnPc:C_{60}	ISC+BET	[646 108]	0.46:0.54
F_8ZnPc:C_{60}	ISC+BET	[670 112]	0.48:0.52
F_{16}ZnPc:C_{60}	ISC+BET	[592 115]	0.79:0.21

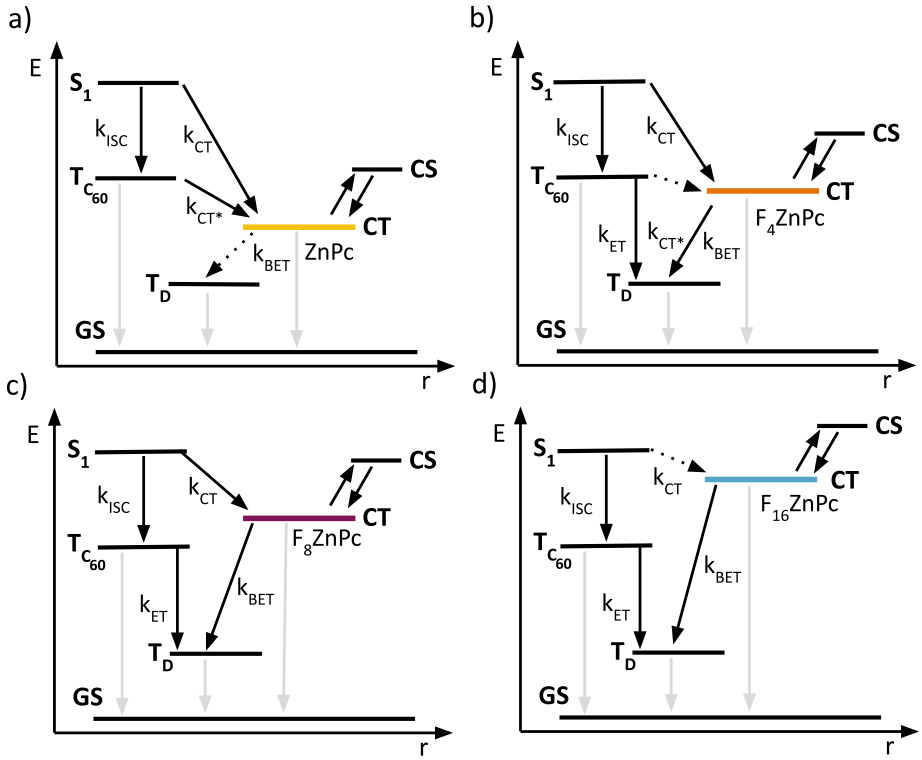


Figure 6.8: Schematic representations of charge transfer (CT), inter-system crossing (ISC), back electron transfer (BET), and energy transfer (ET) processes observed via trEPR shown for dilute a) ZnPc, b) F_4ZnPc, c) F_8ZnPc, and d) F_{16}ZnPc blends with C_{60}. The dotted lines signal pathways that we observe with lower probability. The indicated CT state comprises of almost degenerate singlet and triplet CT states. While the schematics focus on photon absorption of C_{60}, LE of the donor molecules lead to similar pathways (minus the ET process). The light grey arrows indicate recombination of excited states to the ground state (GS).

Further investigating the T_1 population pathways in all fluorinated blends, two main contributions to T_1 formation are observed. The first resembles the ISC contribution observed in the neat films but with different T_1 sublevel populations (for simplicity, we label this process as an "ISC-like" contribution), and the second is due to geminate BET. Again, the T_1 ZFS parameters in the dilute F_xZnPc blends are comparable but slightly larger than those of the neat F_xZnPc films, highlighting that triplets are located on the donor molecules.

Regarding the T_1 formation pathways, the ISC-like contribution can arise from triplet-triplet energy transfer from C_{60} to F_xZnPc, as previously observed in literature [3]. This is rationalized by two main considerations. Firstly, excited singlet states on the donor molecules undergo CT more efficiently than ISC, since all donors are surrounded by C_{60} molecules in the dilute blends. Secondly, we observe a change in the spin-populations of the ISC-

like triplet in the dilute blends with respect to the neat films, which suggests a different T_1 populating mechanism. Conversely, the geminate BET contribution can be rationalized considering that the T_1 state of F_xZnPc is the lowest energetic state in the system, and lower in energy than the CT state, as discussed earlier. As a result, faster BET to the donor triplet than CT dissociation into the CS state can occur.

In the case of the dilute F_{16}ZnPc:C_{60} blend, the trEPR data indicate only a weak signature of triplet formation via BET. Instead, the F_{16}ZnPc triplets are mainly populated via the ISC-like contribution of triplet-triplet energy transfer. This observation can be rationalized considering the close energetic matching of the singlet and CT state in this blend, discouraging CT formation (Figure 6.8d).

Finally, we turn to investigating the behavior of F_4ZnPc:C_{60} and F_8ZnPc:C_{60} more closely. Notably, in the F_4ZnPc and F_8ZnPc blends, the C_{60} and CT triplets are much closer in energy than in the other two blends, which rationalizes the comparable contributions of CT and C_{60} triplet excitons to the donor T_1 population. However, despite ISC and BET occurring in similar proportions in both blends, the photocurrents (observed via the $J-V$ and EQE measurements presented in Figure 6.2) decrease substantially with increasing donor fluorination. We hypothesize that the stark difference in J_{sc} in these blends primarily arises from an increased CT dissociation barrier ΔE_{CS}, reducing the efficiency of CT state dissociation. Consequently, we attribute ΔE_{CS} and not ΔE_{CT} to be the limiting factor for free charge generation in the F_8ZnPc blend.

6.6 Conclusions

In summary, we studied dilute donor content blends of F_xZnPc (x=0, 4, 8, 16) and C_{60} as a model system to investigate the effect of interfacial energetic offsets on charge transfer, geminate recombination, and device performance. In agreement with previously published work [189], [41], [190], we find that the fluorination-induced shift of the donor HOMO/LUMO leads to an increase in the interfacial CT state energy and a corresponding increase in V_{oc}. This change is accompanied by a rapid decrease in J_{sc} for the F_8ZnPc and F_{16}ZnPc blends, due to severely reduced exciton separation as shown via $J-V$, EQE, and trEPR.

Our experimental data and theoretical results show that the observed trends in device performance upon fluorination of ZnPc can be related to the change in the relative positions of the energy levels of CT and LE excitons. In addition, the energy of the CS state needs to be considered to obtain a full picture of the charge dynamics in the blends.

In comparison to neat C_{60}, where free charges are predominately formed via dissociation of high-energy C_{60} states, in the dilute F_xZnPc blends, free charge generation depends on the formation and dissociation of CT excitons at donor:acceptor interfaces. Through trEPR measurements, we find that charge generation in the dilute donor blends can occur via the dissociation of singlet donor excitons (i), and the dissociation of the singlet (ii) and triplet (iii) C_{60} excitons. The latter only occurs if the CT state is energetically accessible (i.e. $E_{T_1,\mathrm{C_{60}}} > E_{CT}$), and the dissociation of CT excitons is faster than geminate recombination. Our data suggest that all three pathways, (i)-(iii), contribute to photocurrents in OSCs based on the ZnPc and F_4ZnPc blends. However, the relative contribution of successfully splitting C_{60} triplets to the measured photocurrent is expected to be small, and not enough to explain the stark differences in J_{sc} when comparing the ZnPc/F_4ZnPc and F_8ZnPc/F_{16}ZnPc blends.

Informed by DFT calculations and experimental determinations of ΔE_{CT}, and from studying triplet formation processes that compete with CT formation and CT dissociation, we conclude that: (1) For ZnPc:C_{60}, which shows a large LE $-$ CT offset, CT formation and CT dissociation are efficient. (2) For smaller LE $-$ CT offsets, observed for F_4ZnPc:C_{60} and F_8ZnPc:C_{60}, CT formation remains relatively efficient, but CT dissociation slows down as observed via the increasing contribution of BET. This may yield two different outcomes; either CT dissociation remains efficient as indicated by the high photocurrent observed for F_4ZnPc:C_{60}, or CT dissociation becomes inefficient as indicated by the low photocurrents generated via the F_8ZnPc:C_{60} interface. In the latter case, we hypothesize that CT $-$ GS recombination prevails over the CT $-$ CS transition. (3) In the case of F_{16}ZnPc:C_{60}, both CT formation and CT dissociation are limited, as observed via the rising contribution of ISC.

To conclude, our work challenges the standard picture of free charge generation which primarily focuses on optimizing the LE to CT state transition to achieve efficient exciton separation. Instead, our results emphasize the importance of decoupling the impact of ΔE_{CT} and ΔE_{CS} in experimental data and developing design rules that minimize ΔE_{CS} in OSCs.

7 | The impact of donor concentration on the performance of organic solar cells based on fluorinated Zinc-Phthalocyanines and C_{60}

The performance of organic solar cells is strongly governed by the properties of the light-absorbing layer. In particular, the energetics at the donor (D):acceptor (A) interface dictate the properties of charge transfer (CT) states and limit the open-circuit voltage [24]. Molecular energy levels in thin films are affected by electrostatic effects that vary with D:A mixing ratio and impact molecular optical gaps and the energetic landscape at the D:A interface. For the latter, charge-quadrupole interactions play a significant role [41], [40], though their exact impact on CT state properties and exciton separation is not yet understood. In this chapter, we investigate the role of D:A mixing ratios on the performance of bulk heterojunctions based on ZnPc or its fluorinated derivatives and C_{60}. For each donor molecule, we systematically vary the donor content from neat C_{60} to neat F_xZnPc ($x = 0, 4, 8, 16$) and study device performances and CT state properties. We find that device performances are strongly dependent on D:C_{60} mixing ratios for all materials and show that the changing polarization environments affect the optical gaps and CT state energies of the D:C_{60} blends. In addition, we observe that charge-quadrupole induced electrostatic shifts decrease the CT dissociation efficiency in the F_8ZnPc and F_{16}ZnPc blends with increasing donor content. This rationalized the low observed photocurrents, as well as the strong dependence of free charge generation on D:C_{60} mixing in these blends.

A manuscript based on the data presented in this chapter is in preparation and will be published by A. Jungbluth, P. Kaienburg, and M. Riede.

7.1 Introduction

The performance of organic solar cells (OSCs) is dependent on molecular design, device architectures, and fabrication conditions, with a large parameter space still open for exploration. Compared to other solar cell technologies, e.g. perovskites, which are mainly limited by energy losses between material layers [209], OSCs are currently limited by recombination in the bulk and at D:A interfaces. The energetics at the D:A interface determine the CT state energy and limit V_{oc} [210], [23], [24]. In addition, the energetic offset between molecular singlet and CT state energies ($\Delta E_{CT} = E_{S_1} - E_{CT}$), often termed the "driving force" for charge transfer, impacts the charge separation efficiency of fullerene-based blends and with that the generation of free charges [102], [180]. Consequently, studying interfacial energetics is paramount for understanding, predicting, and improving OSC device performances.

E_{CT} is linked to the ionization energy (IE) of the donor and the electron affinity (EA) of the acceptor. IE and EA of molecules in organic thin films are impacted by polarization effects and change with D:A mixing ratios, molecular orientation, dielectric constants, and microstructure [193], [211], [48], [212], [213], [214]. In addition, electrostatic effects caused by charge-quadrupole interactions between neighboring molecules shift molecular energy levels [215], [216], [166], [35], [217], [34], [40], and impact E_{CT} [41] and exciton dissociation [36], [218].

However, disentangling the impact of these different polarization and electrostatic effects on molecular energy levels and E_{CT} is a challenging task and the focus of this chapter. Importantly, charge-quadrupole interactions scale with D:A mixing ratios, as was shown for blends of ZnPc and its fluorinated derivatives, which allows to linearly tune interfacial energy levels [41], [40], [219]. In this chapter, we investigate the impact of D:A mixing ratios on interfacial CT state energies and device performance. We study BHJs of zinc phthalocyanine (ZnPc) or its fluorinated derivatives (F_4ZnPc, F_8ZnPc, and F_{16}ZnPc) as donors and C_{60} as the acceptor. We systematically vary the donor content from neat C_{60} to neat F_xZnPc, and measure device performances via $J-V$ and EQE measurements at room temperature.

Fluorination of isolated ZnPc molecules simultaneously shifts the molecular orbital energies (i.e. the HOMO and LUMO) away from the vacuum level [190], [189]. In organic thin

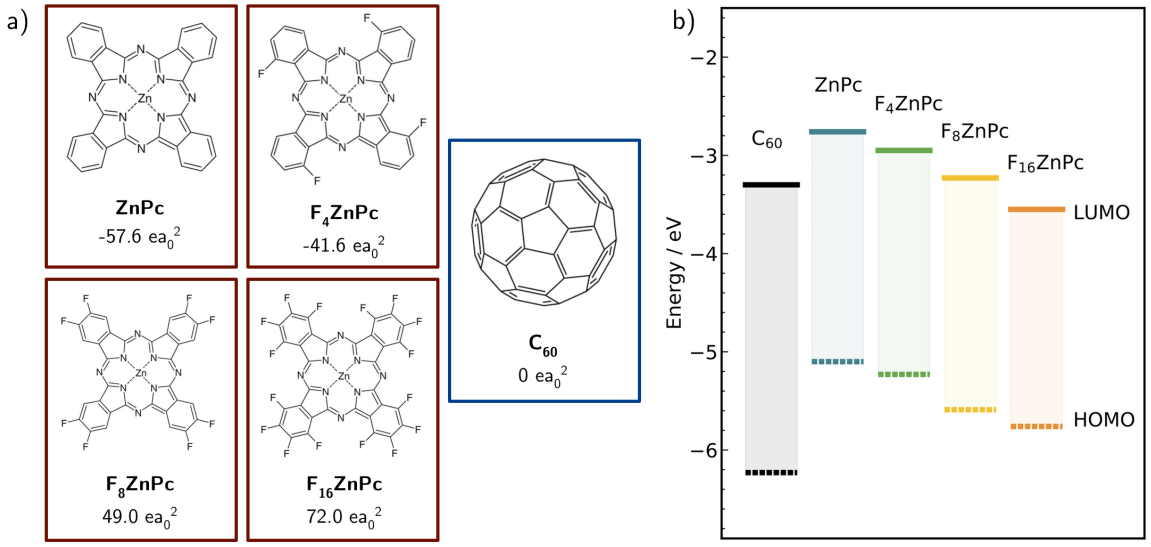


Figure 7.1: a) Molecular structure and quadrupole moments [41] of the donor (red outline) and acceptor (blue outline) molecules. b) Overview of the shifting molecular orbitals as a function of donor fluorination. The F_4ZnPc used in this study consists of a mixture of isomers. Figure a) was reproduced and adapted from reference [41] with permission under CC BY 4.0. The HOMO and LUMO levels were calculated by Dr. Veaceslav Coropceanu and Dr. Eunkyung Cho and and were previously included as Figure 6.4 in Chapter 6.

films, this results in a corresponding shift of the donor IE and EA, which increases the interfacial CT state energy (and reduces ΔE_{CT}) in blends with C_{60}. For the F_xZnPc donor molecules, fluorination also increases the molecular quadrupole moments. This makes the F_xZnPc donor series an ideal model system to investigate the impact of interfacial energetic offsets and quadrupole moment-induced energy level shifts on device performance. This chapter builds on the results presented in Chapter 6, and increases the complexity of the studied material systems by investigating both the role of fluorination, and D:C_{60} mixing.

7.2 Materials & Devices

The molecular structure and quadrupole moments (Q) of the donor and acceptor molecules used in this study are shown in Figure 7.1a. The quadrupole moments are taken from reference [41] and were determined by Schwarze et al. via DFT calculations. Importantly, these values represent the quadrupole component perpendicular to the molecular plane (Q_π), since Q_π dominates Q for planar molecules like F_xZnPc that favor arrangements in a $\pi - \pi$

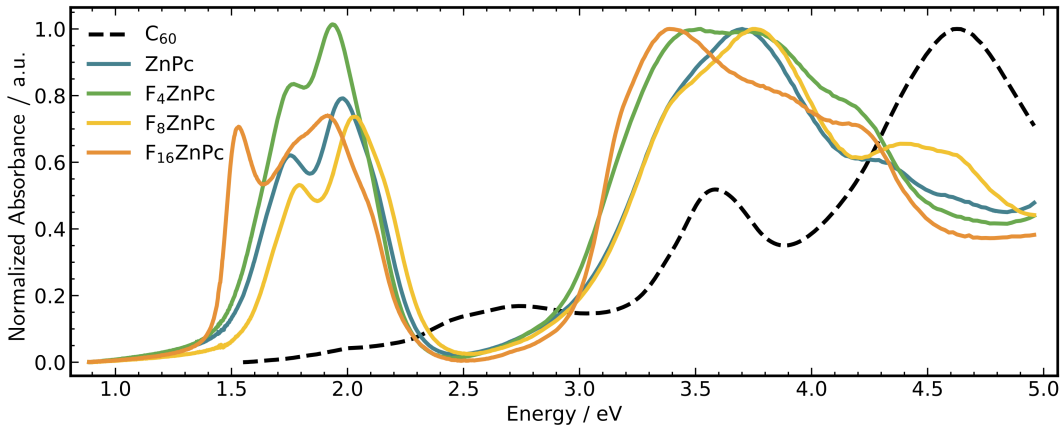


Figure 7.2: Normalized absorbance of neat F_xZnPc and neat C_{60} thin films. All films consist of 50 nm thick layers deposited via vacuum thermal deposition on quartz substrates. The spectra are normalized to the absorbance peaks between $3-5$ eV, and were determined via UV-Vis-NIR measurements in transmission mode as outlined in Chapter 4.

stacking geometry [41], [220], [221]. Based on these quadrupole moments, we can separate our donors into 2 categories; i.e. molecules with negative Q_π (ZnPc, F_4ZnPc) or positive Q_π (F_8ZnPc, F_{16}ZnPc). The quadrupole moment of C_{60} is zero.

Fluorination of ZnPc molecules simultaneously shifts the HOMO and LUMO away from the vacuum level, keeping the optical gap of the molecules roughly constant [190], [189] (see Figure 7.1b). The latter is confirmed by absorbance measurements of the neat films (Figure 7.2), which show visually similar absorption onsets for all donor molecules. F_xZnPc absorption is dominated by characteristic double peaks at around 1.7 eV and 2.0 eV, in addition to strong absorption past 3.0 eV. The slight red-shift in the absorption peaks of F_4ZnPc, and the blue-shift of F_8ZnPc compared to ZnPc is ascribed to changes in the transition dipole alignment and intermolecular coupling upon fluorination [189]. In addition to the absorption doublet, F_{16}ZnPc also shows a strong peak around 1.5 eV which is not present in the other ZnPc derivatives. For neat films of C_{60}, absorption below 2.2 eV is weak and mainly attributed to intermolecular CT absorption and localized Frenkel absorption [4]. The peak at 1.9 eV in neat C_{60} corresponds to the symmetry-forbidden $S_0 \rightarrow S_1$ transition [195].

To disentangle the impact of fluorination- and quadrupole moment-induced effects on device performance, we study OSCs based on F_xZnPc:C_{60} blends as model systems. We systematically vary the D:C_{60} mixing ratio between ZnPc or its fluorinated derivatives and C_{60}, studying dilute, intermixed, and neat blends. More specifically, we fabricate devices with 0,

5, 25, 50, 75, 95, and 100 wt.% donor loading. A photo of the studied samples is included as Figure C.1 in the Appendix and a detailed description of the fabrication processes and experimental arrangements can be found in Chapter 4. All samples were fabricated via vacuum thermal evaporation, co-depositing donor and acceptor molecules in the desired weight ratio. Apart from the active layer blend composition, all samples were fabricated with nominally identical device architectures and through subsequent evaporation of MoOx (3 nm, $0.05-0.1$ Å/s), F_xZnPc:C_{60} (50 nm, combined rate of 0.4 Å/s), BPhen (8 nm, $0.1 - 0.2$ Å/s), and Al (100 nm, $1 - 2$ Å/s). The substrates were held at room temperature during deposition.

7.3 Device Performance

7.3.1 Comparison across D:C_{60} Mixing Ratios

In the following sections, we first discuss how the D:C_{60} mixing ratio impacts the device performance of each D:C_{60} system by showing $J-V$ and EQE spectra for OSCs with varying donor content. We then compare the performance trends across donor molecules and as a function of fluorination. Figure 7.3 shows the current density-voltage ($J-V$) and external quantum efficiency (EQE) characteristics of the best performing (highest PCE) devices for all F_xZnPc:C_{60} blends. The first, second, third, and fourth row show the spectra of the ZnPc, F_4ZnPc, F_8ZnPc, and F_{16}ZnPc blends with C_{60} respectively. The D:C_{60} mixing ratios are given in square brackets, and line colors darken with increasing donor content. Performance statistics were calculated for multiple devices (see Appendix Table C.1). Although the data presented in Figure 7.3 and Table C.1 is reported as measured, spectral mismatch correction only marginally shifts the short-circuit current density (J_{sc}) and preserves all observed performance trends (Figure C.2).

While devices based on neat C_{60} show a high open-circuit voltage (V_{oc}), active layer absorbance in the neat film is limited and exciton separation is poor, leading to a low J_{sc}. Adding even small amounts of ZnPc drastically improves the photocurrent (Figure 7.3a). This increase in J_{sc} between neat C_{60} and dilute ZnPc:C_{60} largely stems from improved exciton separation at the D:C_{60} interface, as was previously discussed in Chapter 6.

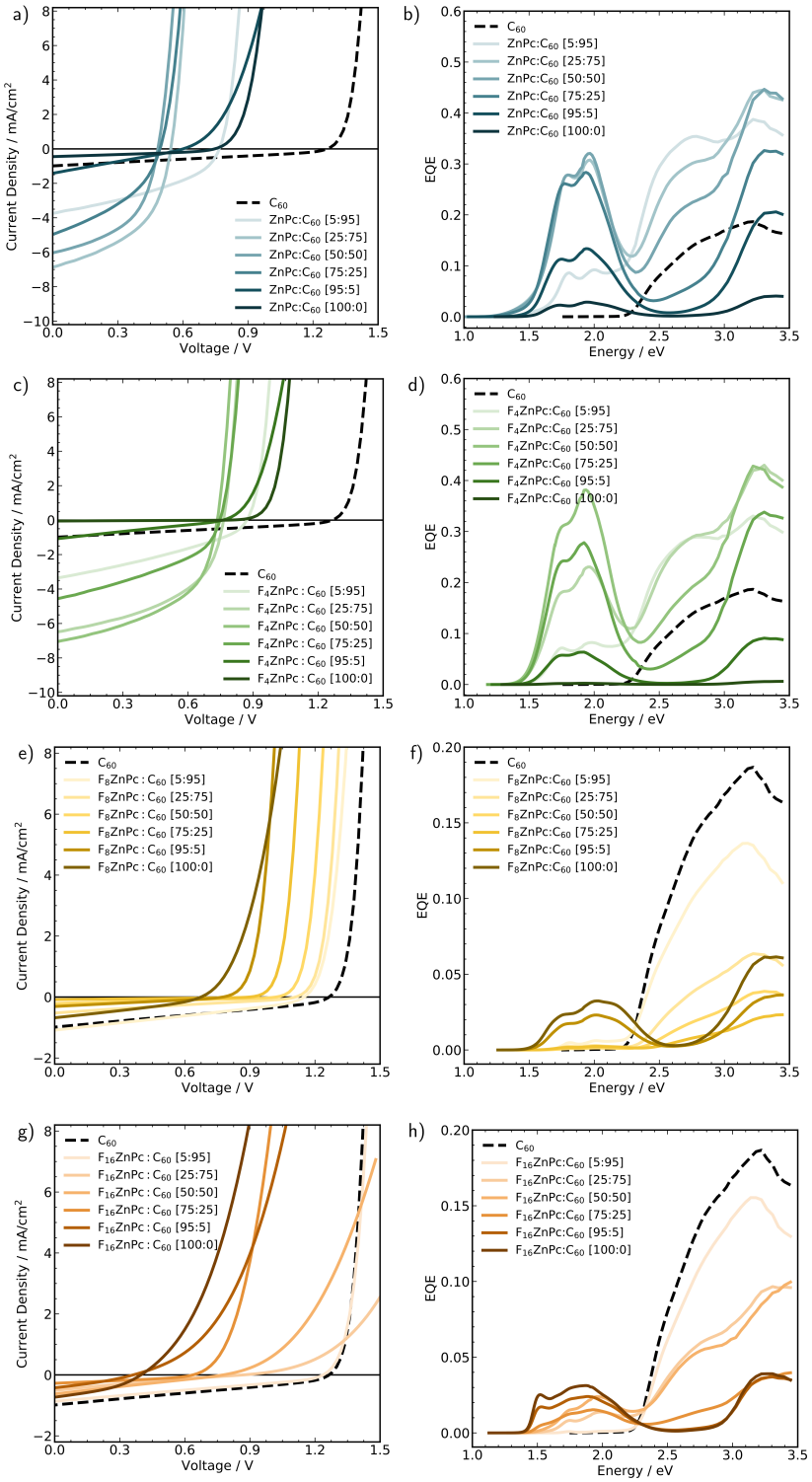


Figure 7.3: a,c,e,g) $J-V$ characteristics under simulated 1 Sun illumination and b,d,f,h) EQE of the best performing (highest PCE) F_xZnPc:C_{60} devices measured at room temperature. The first, second, third, and fourth row show the spectra of ZnPc, F_4ZnPc, F_8ZnPc, and F_{16}ZnPc blends with C_{60} respectively. The donor:acceptor ratios are given in weight percent in square brackets, and the line colors darken with increasing donor content. A summary of the $J-V$ performance metrics can be found in Figure 7.4. The data was plotted as measured, though spectral mismatch correction only marginally shifts the J_{sc} of each blend.

The same improvement in J_{sc} is observed for dilute F_4ZnPc:C_{60} (Figure 7.3c). The increase in J_{sc} is accompanied by a decrease in V_{oc} for the dilute ZnPc and dilute F_4ZnPc blends compared to neat C_{60}. ZnPc and F_4ZnPc both contribute to photon absorption, as indicated by the emergence of the characteristic double peak between $1.5-2.5$ eV in the EQE (Figure 7.3b and d). This suggests that charge transfer occurs via hole transfer for excitons generated on C_{60}, and via electron transfer for excitons generated on F_xZnPc - as is often observed in fullerene-based BHJs.

The highest J_{sc} of the ZnPc concentration series is achieved for ZnPc:C_{60} [25:75], which shows strong free charge generation in both the donor and acceptor absorption regions. With the addition of more ZnPc, free charge generation between $2.2-3.0$ eV, where mainly C_{60} absorbs, quickly decreases. In addition, the V_{oc} settles to around 0.5 V, in agreement with literature [193], and stays roughly constant between $25-75$ wt.% donor content.

While the J_{sc} of the F_4ZnPc blends are comparable to those of the corresponding ZnPc blends, the V_{oc} is generally $0.1-0.2$ V larger. This observation, discussed for dilute F_xZnPc:C_{60} in Chapter 6, can be rationalized considering that donor fluorination shifts molecular energy levels and reduces the energetic offset at the D:C_{60} interface (see Figure 7.1b). This leads to an increase in E_{CT} (discussed later) and a corresponding increase in V_{oc}.

Compared to the dilute donor blends, which result in well-performing devices, the dilute acceptor blends (ZnPc:C_{60} [95:5] and F_4ZnPc:C_{60} [95:5]) show a lower V_{oc} and photocurrent. Neat ZnPc and neat F_4ZnPc also show a low J_{sc}, which can be attributed to poor exciton separation. In addition, charge collection in the neat donors is worse than in neat C_{60}.

Compared to ZnPc and F_4ZnPc, which show comparable performance trends across the donor concentration series, F_8ZnPc (Figure 7.3e-f) and F_{16}ZnPc (Figure 7.3g-h) display clear differences in performance. Firstly, a gradual decrease in V_{oc} from dilute F_8ZnPc:C_{60} (dilute F_{16}ZnPc:C_{60}) to neat F_8ZnPc (neat F_{16}ZnPc) is observed. In addition, the photocurrents of all F_8ZnPc and F_{16}ZnPc blends are smaller than those of the neat materials, indicating that free charge generation at the D:C_{60} interface is inefficient.

While the dilute F_8ZnPc:C_{60} blends show a comparable J_{sc} to that of neat C_{60}, free charge generation drastically decreases with increasing F_8ZnPc content (Figure 7.3e). The lowest

photocurrents are reached for F_8ZnPc:C_{60} [75:25]. For this sample, free charge generation across the entire spectrum is low, as indicated by the reduced EQE of this blend in Figure 7.3f. In fact, only the 95 wt.% and 100 wt.% F_8ZnPc samples show significant free charge generation in the donor absorption region.

The characteristic absorption doublet, which was clearly visible in all ZnPc and F_4ZnPc blends, is unresolvable for most F_8ZnPc:C_{60} blends. This is surprising, given that the absorption profile of F_8ZnPc is very similar to that of the other ZnPc derivatives (Figure 7.2). However, this observation can be rationalized considering the fluorination-induced shift of the molecular energy levels (Figure 7.1b), which suggests that the energetic difference at the F_8ZnPc:C_{60} interface (i.e. the driving force for charge transfer between the donor and the acceptor) decreases. In addition, following from the results presented in Chapter 6, we know that the efficiency of CT dissociation is also strongly affected by the degree of ZnPc fluorination. This hypothesis is validated considering that the highest photocurrents are achieved for the neat materials and the dilute blends, where even without efficient exciton splitting at the D:C_{60} interface, excitons can be separated in the majority donor or acceptor regions. The latter also explains the observed "C_{60}-like" behavior of the $J-V$ and EQE characteristics of the dilute F_8ZnPc blend.

Dilute F_{16}ZnPc:C_{60} also displays a $J-V$ behavior that is similar to neat C_{60}, indicating that for this sample the D:C_{60} interface is not significant for exciton separation. Interestingly, while the F_{16}ZnPc absorption doublet is not visible in the EQE of the dilute donor blend, it becomes clearly visible with 25 wt.% donor content. This suggests that with more donor loading, F_{16}ZnPc not only absorbs photons but also contributes to the splitting of excitons.

7.3.2 Comparison across Donor Molecules

Having introduced how the $J-V$ and EQE characteristics change with D:C_{60} mixing ratio, we now turn to comparing the performance trends across donor molecules. Figure 7.4 summarizes the trends in V_{oc}, J_{sc}, and fill factor (FF) as a function of donor molecule and donor content. The data plotted in Figure 7.4, including the number of devices measured to calculate performance statistics, can be found in Table C.1 in the Appendix.

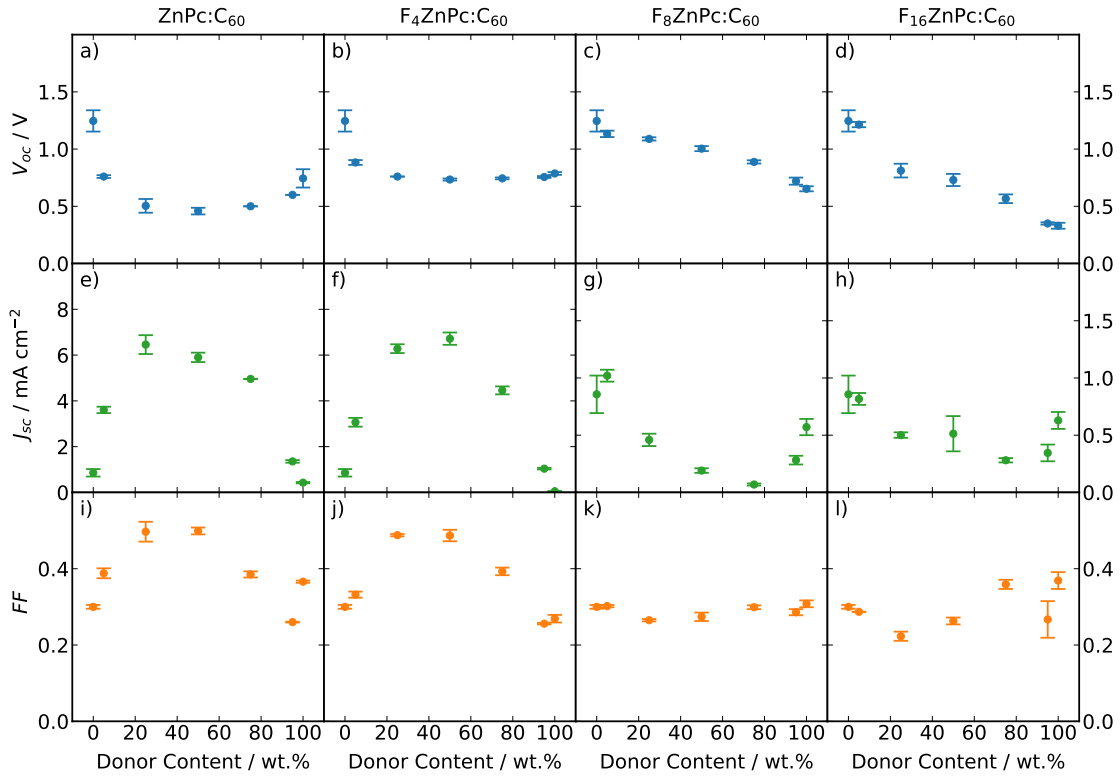


Figure 7.4: $J-V$ characteristics (V_{oc}, top row; J_{sc}, middle row; FF, bottom row) as a function of donor fluorination and D:C_{60} mixing ratio. All measurements were performed under simulated 1 Sun illumination and at room temperature. The data is plotted as measured, and is included in Table C.1 in the Appendix. Spectral mismatch correction only marginally shifts the J_{sc} and preserves all observed performance trends (see Figure C.2 for comparison). Note that the J_{sc} of the ZnPc and F_4ZnPc blends is plotted between $0-10$ mA/cm^2, while the J_{sc} of the F_8ZnPc and F_{16}ZnPc blends is plotted between $0-2$ mA/cm^2.

Summarizing the performance trends, we observe that the V_{oc} of the ZnPc concentration series follows a U-shape (Figure 7.4a). The V_{oc} first decreases with increasing donor content from neat C_{60} to the intermixed blend, and subsequently increases from the intermixed blend to neat ZnPc. Later in this chapter, we show that this change in V_{oc} can largely be explained by corresponding changes in the optical gap and CT state energies of the ZnPc:C_{60} blends. In comparison, the opposite trend is observed for the J_{sc} (Figure 7.4e) and FF (Figure 7.4i), with both parameters peaking for the 25 wt.% and 50 wt.% donor blends. This agrees with previous work, which documented the same trends in V_{oc}, J_{sc}, and FF for changing ZnPc:C_{60} mixing ratios [193], [222].

The F_4ZnPc system (Figure 7.4, second column) follows the same performance trends as ZnPc, though the change in V_{oc} is less pronounced. In comparison, F_8ZnPc (Figure 7.4, third

column) and F_{16}ZnPc (Figure 7.4, fourth column) display a different behavior. Firstly, the V_{oc} no longer follows a U-shape but gradually decreases from the V_{oc} of neat C_{60} to the V_{oc} of neat F_8ZnPc/F_{16}ZnPc. In addition, the FF stays roughly constant (at around 0.3) across the concentration series. The biggest change is observed for the J_{sc}, which now displays a U-shaped behavior and the opposite trend as for ZnPc and F_4ZnPc. To our knowledge, this is the first time that performance trends with changing D:C_{60} ratios were reported for the fluorinated ZnPc derivatives.

The origins of these performance trends are complex and rely on a variety of electrostatic and microstructural effects. For the scope of this study, we are primarily interested in the electrostatic effects that influence molecular energy levels and impact the energetics at the D:C_{60} interface. Since the V_{oc} is limited by interfacial CT state energies [23], [24], it is of particular interest in this work. In addition, interfacial energetics affect exciton separation, which in turn affects the J_{sc} [45], [223], [224], [102].

More specifically, the J_{sc} is governed by the active layer absorbance, exciton separation efficiency, and charge carrier collection efficiency. The observed trends in J_{sc}, whereby ZnPc/F_4ZnPc display high photocurrents that peak for the intermixed D:C_{60} blends, and F_8ZnPc/F_{16}ZnPc display low photocurrents that reach a minimum for the intermixed blends, cannot be explained by absorption changes alone. Figure 7.5 shows transfer matrix calculations of the J_{sc} of ZnPc:C_{60} and F_8ZnPc:C_{60} blends assuming 100% internal quantum efficiency and ideal charge collection. Based on the strong similarities in the donor absorption profiles, shown in Figure 7.2 and discussed earlier, the photocurrents of the ZnPc and F_8ZnPc blends are expected to be of similar magnitude and follow the same trend across the donor concentration series. Even though only ZnPc and F_8ZnPc are shown in Figure 7.5, the same behavior is expected for the F_4ZnPc and F_{16}ZnPc blends.

While the ZnPc:C_{60} system shows lower photocurrents than predicted from transfer matrix modelling, the general trend of rising and falling J_{sc} with increasing donor content is preserved. The same is true for F_4ZnPc:C_{60}. The F_8ZnPc and F_{16}ZnPc blends, on the other hand, not only show a severely reduced J_{sc}, but also display the opposite trend in photocurrent with increasing donor content than predicted by transfer matrix modelling. This means that free charge generation is not limited by absorption of the active layer in these blends.

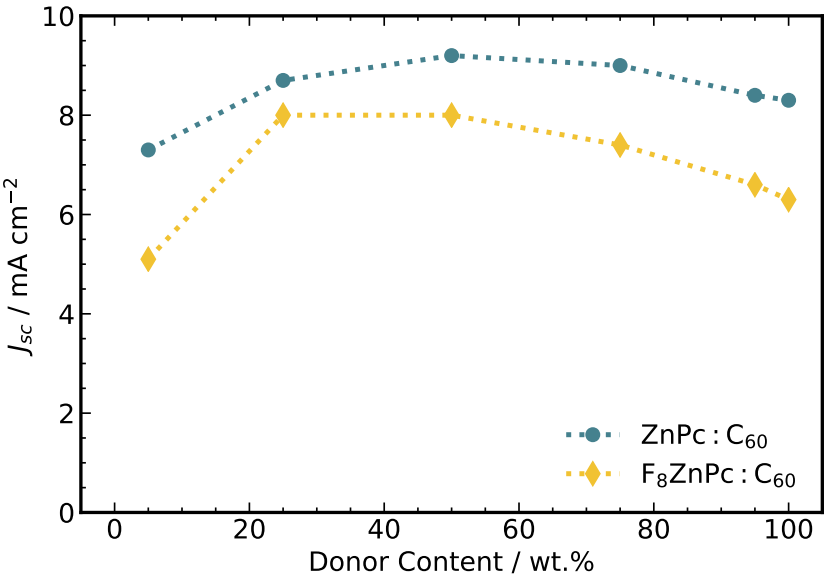


Figure 7.5: Transfer matrix modelling of the short-circuit current density (J_{sc}), assuming that all absorbed photons lead to free charges and that charge collection is ideal. The optical constants of the blends were approximated as proportional combinations of the optical constants of neat donor and neat C_{60} films.

In addition, with nominally identical device stacks and roughly constant fill factors of 0.3 across the donor concentration series, charge collection is expected to remain constant and cannot explain the observed trends in photocurrent of the F_8ZnPc and F_{16}ZnPc blends.

Consequently, exciton separation, which encompasses both CT formation and CT dissociation, is hypothesized to determine the observed performance trends, in particular the photocurrents of F_8ZnPc and F_{16}ZnPc. To provide a qualitative and quantitative analysis of exciton separation, in addition to studying the dependence of the V_{oc} on donor concentration, we next turn to investigating how the CT state energies (and the driving forces for CT formation) change with donor fluorination and D:C_{60} mixing ratio.

7.4 CT State Analysis

E_{CT} provides the most device relevant information on interfacial energy levels, since electrostatic effects that impact the molecular orbital energies will also impact E_{CT}. Figure 7.6 shows the logarithmic EQE of all material systems. Only the ZnPc blends show a clearly

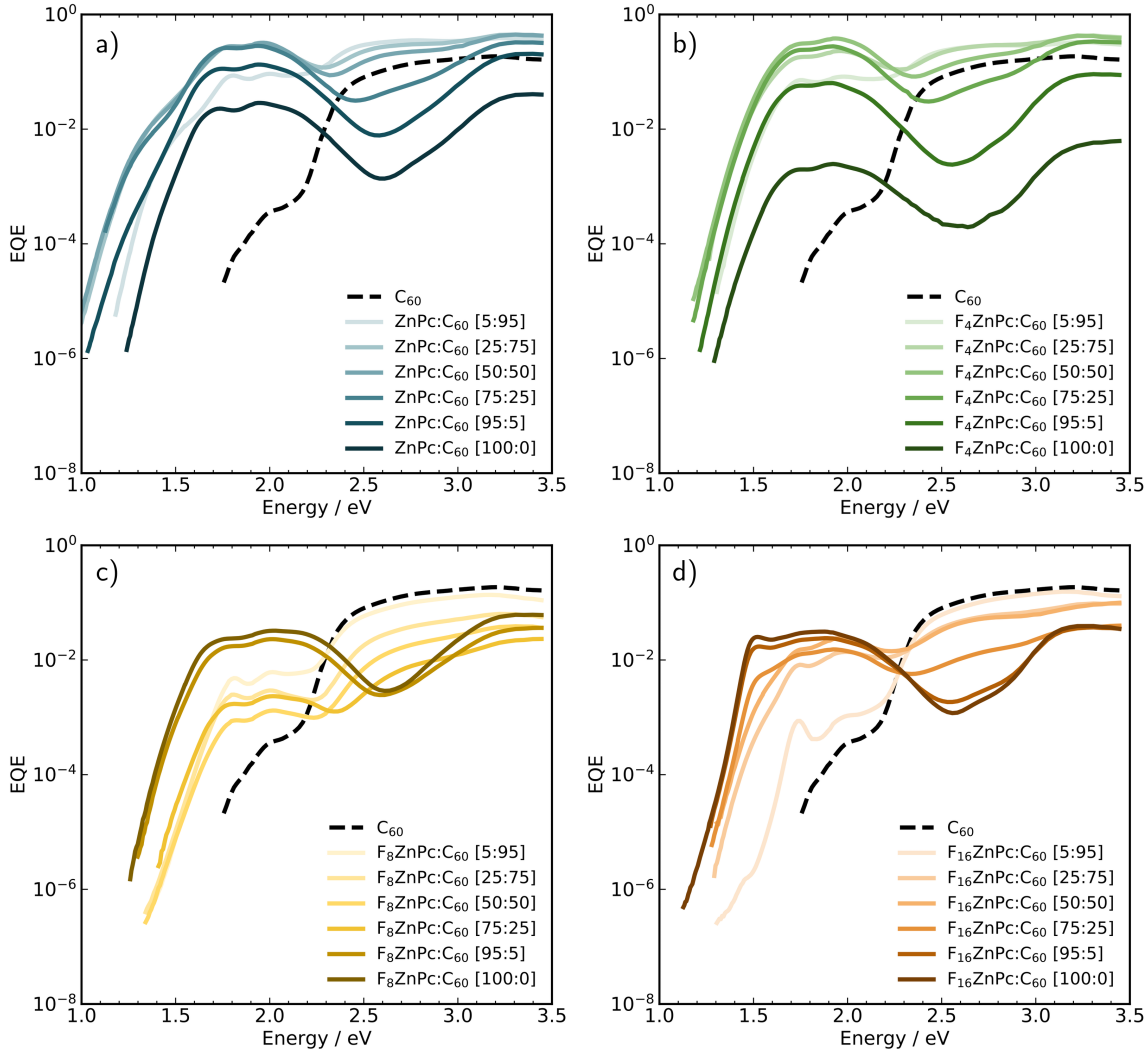


Figure 7.6: EQE on a logarithmic scale for the a) ZnPc, b) F_4ZnPc, c) F_8ZnPc and d) F_{16}ZnPc systems. Only the ZnPc blends show a clearly distinguishable CT state shoulder.

distinguishable CT state absorption shoulder (Figure 7.6a). To determine the CT state energies, we follow the approach presented in Chapter 5 and fit the tail of the sensitively measured EQE using Marcus theory. Figure 7.7 shows two example fits. Importantly, we fit both the singlet S_1 peak and the CT state to ensure that the entire EQE tail is fit appropriately. This approach is especially important for D:A systems where the S_1 and CT state are not clearly resolvable (Figure 7.7b) [1].

Figure 7.8 shows the CT state energies as a function of D:C_{60} mixing ratio and donor fluorination. With ZnPc as the donor molecule, the trend in E_{CT} follows the same U-shape as observed for the V_{oc}, which matches previous literature reports [193]. Between the low

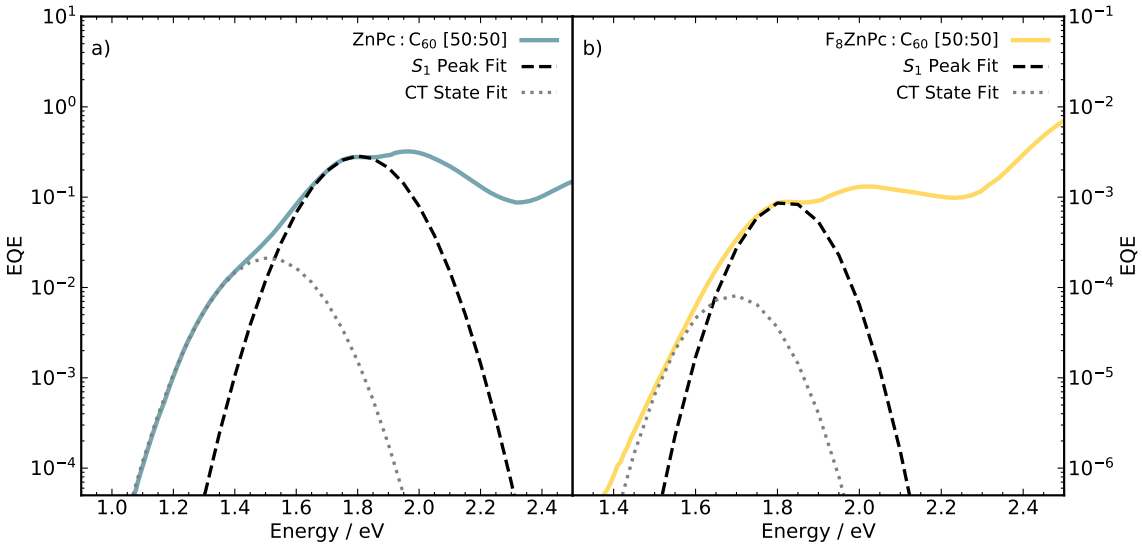


Figure 7.7: EQE fitting of a) ZnPc:C_{60} [50:50] and b) F_8ZnPc:C_{60} [50:50]. The singlet (S_1) peak is fit first and subtracted from the data. The remaining EQE tail is then fit as the charge transfer (CT) state using classical Marcus theory as outlined in Chapter 5.

donor and the 50:50 blends, E_{CT} decreases by around 0.17 ± 0.01 eV. The same U-shaped behavior, although much less pronounced, is also observed for F_4ZnPc. In this case, the largest difference in E_{CT} of 0.09 ± 0.01 eV is observed between the dilute donor and the 75:25 F_4ZnPc:C_{60} blends.

Compared to ZnPc, the F_4ZnPc blends have a larger E_{CT}, which agrees with the higher V_{oc} observed for this material system. E_{CT} is further increased for the F_8ZnPc and F_{16}ZnPc blends. Interestingly, F_8ZnPc shows the largest E_{CT} of all studied blends between 25:75 and 95:5 D:C_{60} mixing ratios (see Figure 7.8). This also matches the V_{oc} measurements presented earlier. Further investigating the behavior of F_8ZnPc, we observe that E_{CT} is gradually decreasing, rather than following the U-shaped behavior reported for ZnPc and F_4ZnPc. Between the dilute donor blend and neat F_8ZnPc, E_{CT} decreases by 0.17 ± 0.01 eV. A similar behavior is observed for F_{16}ZnPc, where E_{CT} decreases by 0.21 ± 0.01 eV across the donor concentration series. Figure 7.8 shows that the fitted E_{CT} of all neat donor devices settles to around 1.40 eV. This suggests that fluorination not only preserves the optical gap of the donors, but that the inter-molecular CT state energy stays constant too.

In the following, we investigate why E_{CT} changes with D:C_{60} mixing ratio, and explore how induced dipoles and quadrupolar electrostatic effects can explain our observations. Com-

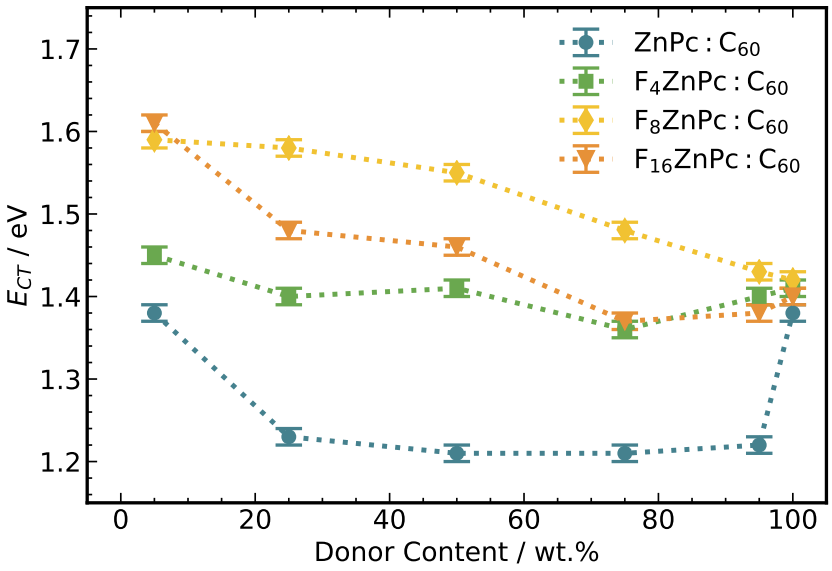


Figure 7.8: Charge transfer state energies (E_{CT}) as a function of D:C_{60} mixing ratio and donor fluorination. E_{CT} was fit from the EQE using Marcus theory. The uncertainty on E_{CT} was determined as the fit uncertainty on the best fit and does not encompass deviations across samples. The data plotted is included in Table C.1 in the Appendix.

pared to molecules in a gas phase, dipole-dependent electrostatic inductions of neighboring molecules in thin films cause polarization effects that increase EA and decrease IE. As a results, the energetic difference between the EA and IE of molecules in thin films is smaller than for isolated molecules (see Figure 2.6 in Chapter 2). This translates to reduced singlet energies and corresponding absorption red-shifts for molecular solids compared to the individual molecules. In comparison, quadrupolar electrostatic effects shift the IE and EA equally [216], [166], [35], [34]. This keeps the molecular optical gap constant, but results in energetic shifts at the D:C_{60} interface that change E_{CT}.

Consequently, as a first step, we need to disentangle the contribution of D:C_{60} mixing on the singlet energies of the individual molecules in the blends, followed by understanding how their relative positions affect the interfacial CT state energy. To address the first point, we refer to previous work employing Ultraviolet Photoelectron Spectroscopy (UPS) and Inverse Photoemission Spectroscopy (IPES) on blends of ZnPc:C_{60} that measured changing $\mathrm{IE}-\mathrm{EA}$ gaps for both ZnPc and C_{60} with increasing ZnPc content [193]. Absorption measurements on the same films, however, did not confirm that the optical gaps of the molecules change [193]. For absorbance spectra of ZnPc:C_{60} blends between 1:6 and 6:1 mixing ratio, the

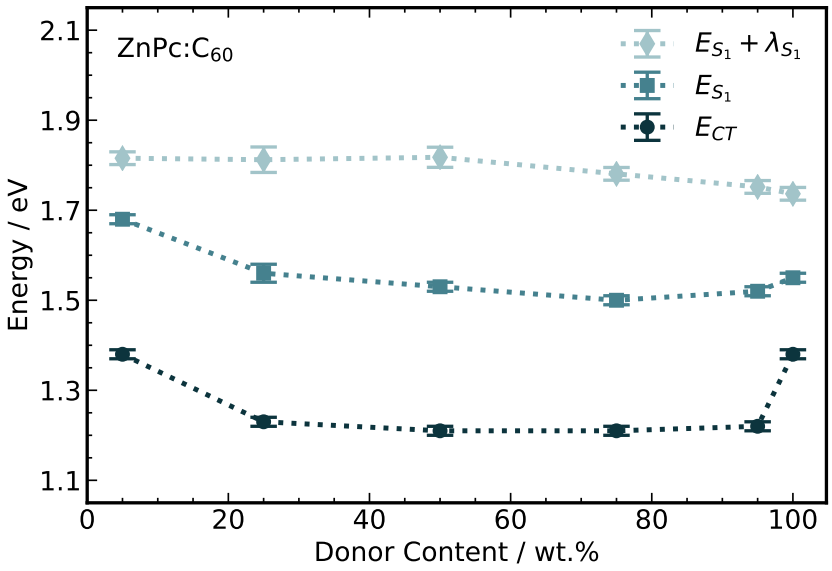


Figure 7.9: CT state energy (E_{CT}) and donor singlet energy (E_{S1}) as a function of ZnPc:C_{60} mixing ratio. E_{CT} and E_{S1} were both fit from the EQE using classical Marcus theory as outlined in Chapter 5. For comparison, the sum of E_{S1} and the reorganization energy (λ_{S_1}) of the $S_0 \rightarrow S_1$ transition is shown.

authors measured a peak shift of the ZnPc absorption doublet of 0.018 eV, which they argue does not explain the observed trends in E_{CT} or V_{oc}. In the following, we challenge this observation and demonstrate that changes in the optical gap can in fact be measured in absorption, or better EQE, spectra.

Given that the singlet energies of the donor molecules are smaller than the singlet of C_{60}, the donor singlets approximately describe the optical gaps of the D:C_{60} blends. Looking back at the donor S_1 peak in the EQE of the ZnPc:C_{60} blends (Figure 7.3b), the singlet peak remains visually constant across the donor concentration series. In fact, between the dilute donor and the 50:50 blend, which display a decrease in E_{CT} by 0.17 ± 0.01 eV, the S_1 peak position remains unchanged. We first observe a red-shift of the peak by around 0.03 eV between the 50 wt.% and 75 wt.% donor blend, and a total shift by 0.07 eV between the dilute donor blend and neat ZnPc.

At first, this suggests that the optical gaps of the ZnPc:C_{60} blends do not change with donor content, as argued by Tietze et al. [193]. However, rather than simply investigating the peak position, the broadness of the peaks needs to be considered as well. Figure 7.9 shows the donor singlet and CT state energies as determined via the EQE fitting process outlined

earlier. When fitting E_{S1} from the EQE, the U-shaped trend of E_{CT} is reproduced. In comparison, the peak position, which is given as the sum of E_{S1} and the reorganization energy λ_{S_1} of the $S_0 \rightarrow S_1$ transition, only shifts by around 0.07 eV as described earlier. This suggests that changes in the optical gap are compensated by an increasing peak broadness. We note that the experimental reorganization energy determined via fitting of the EQE encompasses contributions from both internal (i.e. within a molecule) and external (i.e. between molecules and their local surrounding) reorganization. We hypothesize that the increased peak broadness measured via λ_{S_1} stems from an increased contribution of the external reorganization energy when transitioning from the dilute donor to the intermixed D:C_{60} blend.

Following from the results presented in Figure 7.9, rather than comparing the position of the absorption peaks to E_{CT}, we instead consider the fitted E_{S1} to draw conclusions on the changing CT state energies. In the case of ZnPc, the 0.17 ± 0.01 eV decrease in E_{CT} between the dilute donor and the 50:50 blend is well explained by a 0.15 ± 0.01 eV decrease in E_{S1}. The same conclusions can be drawn for the fluorinated donors (see Figures C.3, C.4, C.5 in the Appendix). More specifically, the 0.09 ± 0.01 eV decrease in E_{CT} observed between the dilute donor and intermixed F_4ZnPc:C_{60} blend can be attributed to a 0.08 ± 0.02 eV decrease in E_{S1}. The same is true for F_8ZnPc and F_{16}ZnPc, where E_{S1} decreases by 0.16 ± 0.01 eV and 0.23 ± 0.01 eV respectively across the concentration series. These results suggest that the dependence of E_{CT} on donor content largely stems from polarization effects that equally change the optical gaps of the material blends.

7.5 Voltage Losses

Having discussed the dependence of singlet and CT state energies on donor content, we now turn to assessing the voltage losses of our material systems. For this, we split our voltage losses according to the energetic state picture detailed in Chapter 2. In the energetic state picture, E_{S1} is used as the reference energy. The difference between E_{S1} and E_{CT} (ΔE_{CT}) describes the driving force for charge transfer from Frenkel to CT excitons [102], [224]. The radiative energy limit of the V_{oc} (qV_{oc}^{rad}) is calculated using equation 2.15 and via integration of the EQE. To ensure that qV_{oc}^{rad} is not restricted by the detection limit of our EQE setup

[2], we extrapolate the EQE to 0.5 eV via the CT state fits. Using qV_{oc}^{rad}, we determine radiative ($q\Delta V_{oc}^{rad}$) and non-radiative ($q\Delta V_{oc}^{nr}$) voltage losses.

Figure 7.10 compares energy levels and voltage losses as a function of donor fluorination and D:C_{60} mixing ratio. Comparing ΔE_{CT} across donor molecules, we observe decreasing ΔE_{CT} with donor fluorination, as expected from the fluorination-induced shifts of the donor energy levels (Figure 7.1b). Following from the detailed analysis of singlet and CT state energies in the previous sections, ΔE_{CT} stays roughly constant across D:C_{60} mixing ratios for each donor molecule. Since the efficiency of CT formation strongly depends on the energetic offset between molecular singlet and CT state energies, a constant ΔE_{CT} suggests that the efficiency of CT formation stays constant with increasing donor content.

The radiative losses of all samples fall between $170-260$ meV and within range of literature reports [83], [17]. The ZnPc blends show the highest $q\Delta V_{oc}^{rad}$ of, on average, 240 meV. This is expected given the broad CT state shoulder in the EQE of these systems (Figure 7.6a) [83]. The non-radiative losses of our samples fall between $250-790$ meV and are on average twice as large as the radiative losses. Across all material systems, the qualitative comparison between $q\Delta V_{oc}^{nr}$ and E_{CT} is in agreement with the energy gap law, which predicts that non-radiative losses decrease for increasing CT state energies [17]. Interestingly, while the non-radiative losses of the ZnPc and F_4ZnPc systems remain roughly constant with D:C_{60} mixing ratio, non-radiative losses strongly increase for higher donor ratios of F_8ZnPc (Figure 7.3f) and F_{16}ZnPc (Figure 7.3h).

The non-radiative losses we determined agree with reports published for other fullerene-based systems, but are significantly higher than for many non-fullerene (NFA) based blends [91], which show voltage losses $\leq$ 200 meV with negligible driving forces [95], [106], [225]. In comparison, F_{16}ZnPc, which shows the lowest driving forces of our material systems, also shows the largest non-radiative losses. For the dilute F_{16}ZnPc:C_{60} blends studied in Chapter 6, increased non-radiative recombination was rationalized considering that both CT formation and CT dissociation are inefficient. While the same is likely true for all F_{16}ZnPc:C_{60} blends, further studies are needed to explain the four-fold increase in $q\Delta V_{oc}^{nr}$ with increasing F_{16}ZnPc content.

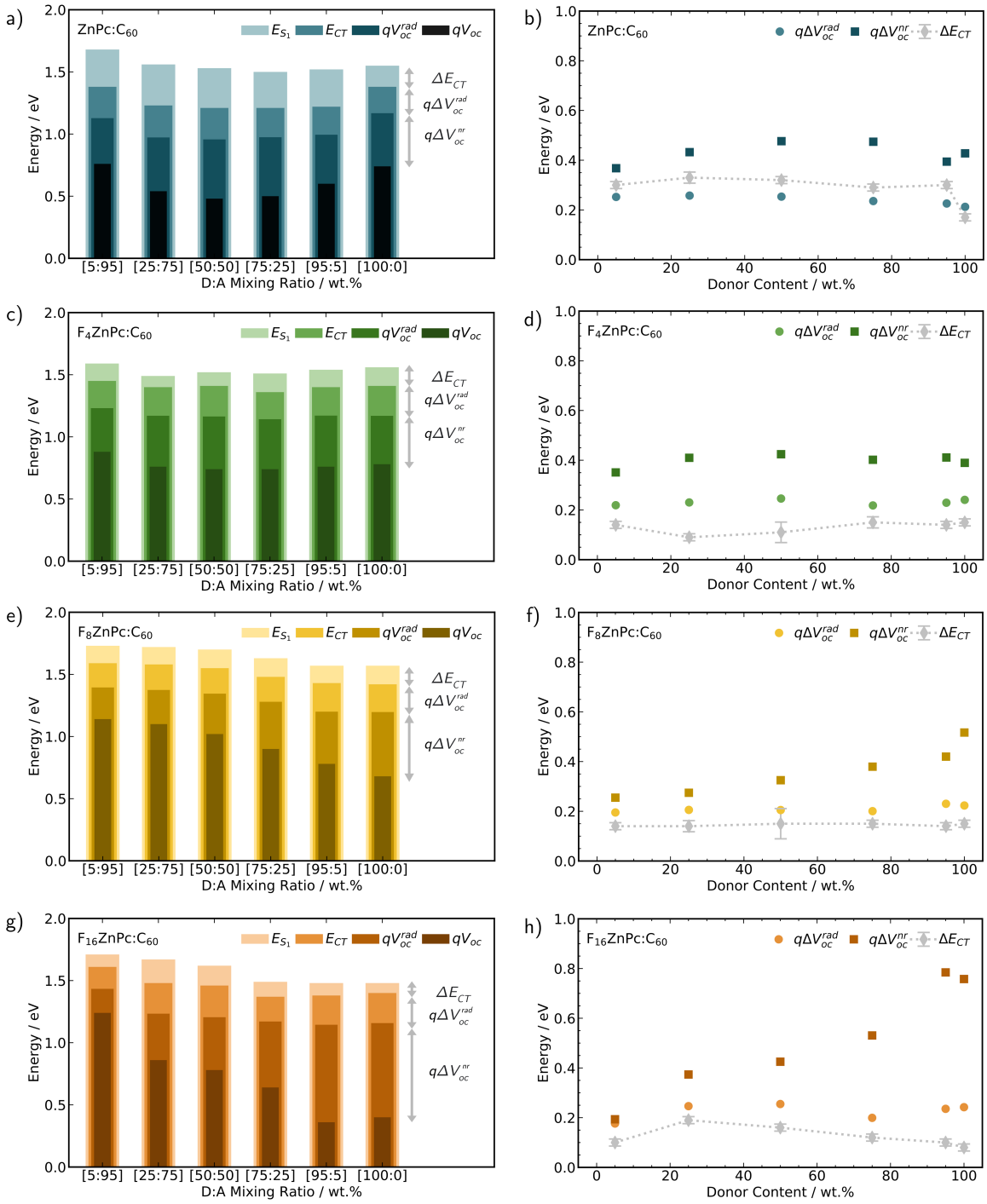


Figure 7.10: Overview of energy levels (a, c, e, g) and voltage losses (b, d, f, h) of the F_xZnPc:C_{60} concentration series. The singlet (E_{S1}) and charge transfer state (E_{CT}) energies were fit from the EQE at room temperature via classical Marcus theory. The radiative limit ($q\Delta V_{oc}^{rad}$) was calculated using the EQE, and qV_{oc} was determined through $J-V$ measurements.

7.6 Discussion

Having presented the photovoltaic performance of all material systems in detail, we now expand our discussion on the different electrostatic effects impacting molecular and blend energy levels in our studied material systems. Through Marcus theory fitting of the EQE, we showed that changing polarization environments with increasing donor content shift E_{S_1} and E_{CT} by roughly the same amount for all donor molecules. While the changes in the donor E_{S1} largely explain the observed trends of E_{CT} and V_{oc}, our work does not draw any conclusions on possible changes to the E_{S1} of C_{60}. Since the singlet absorption of C_{60} is not spectrally resolved from the absorption of ZnPc, fitting E_{S_1} from EQE spectra is impractical. However, the UPS and IPES measurements carried out by Tietze et al. reveal that the $\mathrm{IE} - \mathrm{EA}$ gap of C_{60} equally depends on the D:C_{60} mixing ratio [193]. This suggests that knowledge of the donor E_{S1} only provides a part of the puzzle. This is especially important considering that C_{60} contributes to photon absorption and CT formation, especially in the low donor content blends.

In comparison to dipole-induced polarization effects, which shift the IE and EA towards each other by unequal amounts (see Figure 2.6), charge-quadrupole interactions [40], [34], [41] cause equal shifts of a molecule's IE and EA [166], [216], [35]. Schwarze et al. found that the sign of the quadrupole moment determines the direction of the energetic shift [41], with negative quadrupole moments (e.g. $Q_{\pi,\mathrm{ZnPc}} = -57.6\ \mathrm{ea_0}^2$ and $Q_{\pi,\mathrm{F_4ZnPc}} = -41.6\ \mathrm{ea_0}^2$; Figure 7.11a) shifting IE towards the vacuum level, and positive quadrupole moments (e.g. $Q_{\pi,\mathrm{F_8ZnPc}} = 49.0\ \mathrm{ea_0}^2$ and $Q_{\pi,\mathrm{F_{16}ZnPc}} = 72.0\ \mathrm{ea_0}^2$; Figure 7.11c) shifting IE away from the vacuum level. As indicated in Figures 7.11b and d, the electrostatic shifts of the donor IE and EA are stronger in the bulk than at the interface, since $Q_{\pi,\mathrm{C_{60}}} = 0$.

As a result, E_{CT} and E_{CS}, the energy of the charge separated (CS) state, are reduced for negative quadrupole moments (Figure 7.11b), with a larger relative change in E_{CS} [41]. This reduces the exciton dissociation barrier (ΔE_{CS}), which depends on the energetic difference between E_{CT} and E_{CS} [226]. With increasing $Q_{\pi,D}$ of the ZnPc derivatives, Schwarze et al. found ΔE_{CS} to increase, leading to less efficient exciton dissociation [41], that manifests in reduced photocurrents.

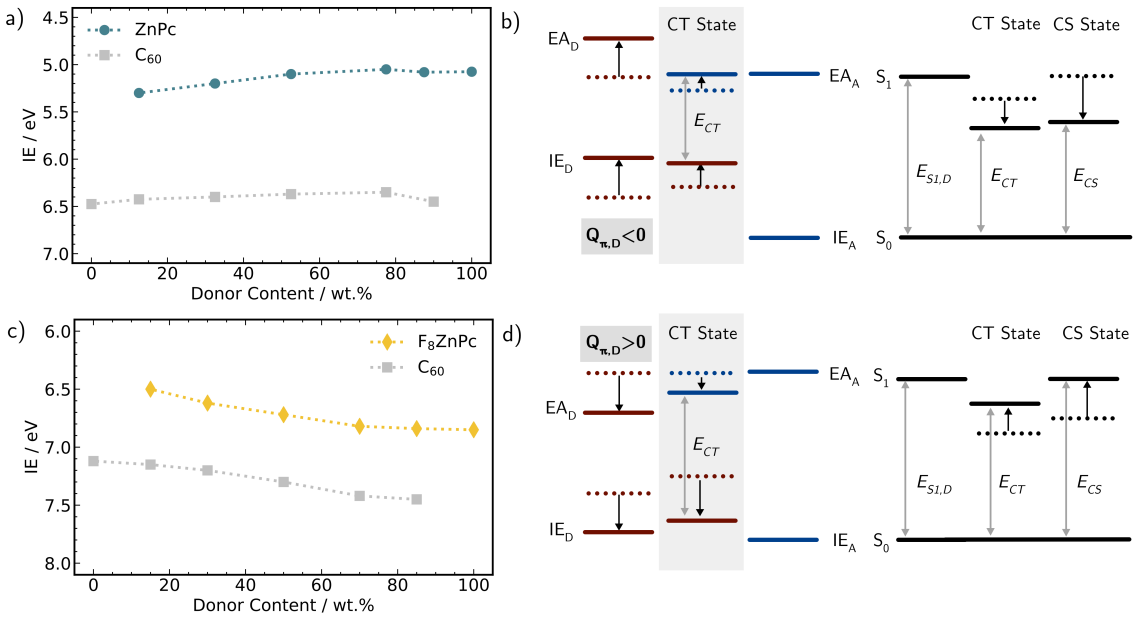


Figure 7.11: Impact of the donor quadrupole moments ($Q_{\pi,D}$) on molecular energy levels for a-b) ZnPc ($Q_{\pi,D} < 0$), and c-d) F_8ZnPc ($Q_{\pi,D} > 0$). The ionization energies (IE) and electron affinities (EA) of ZnPc (F_8ZnPc) and C_{60} shift towards (away from) the vacuum level with increasing donor content. Figures b) and d) show simplified schematics of the donor and acceptor energy levels at the interface (grey shading), and in the bulk. The arrows indicate how the energy levels shift with $Q_{\pi,D} \neq 0$. The data in a) was reproduced with permission from Tietze et al. [193]. The data in c), and the schematics in b) and d) were reproduced and adapted from Schwarze et al. [41] with permission under CC BY 4.0.

Connecting this knowledge to our studied material systems, if exciton separation was equally efficient across all F_xZnPc:C_{60} blends, we would expect to measure roughly the same photocurrents (and the same dependence of J_{sc} on donor concentration) for all donor molecules, as discussed in detail in section 7.3.2. However, this is evidently not the case, suggesting that exciton separation, i.e. CT formation facilitated via ΔE_{CT} or CT dissociation facilitated via ΔE_{CS}, change with donor fluorination and donor concentration.

Based on the results presented in Chapter 6, where we studied CT formation and CT dissociation for dilute donor blends of F_xZnPc:C_{60}, the dilute blends were classified in the following way: (1) ZnPc:C_{60} and F_4ZnPc:C_{60} showed efficient CT formation and CT dissociation, (2) F_8ZnPc:C_{60} showed efficient CT formation but inefficient CT dissociation, and (3) F_{16}ZnPc:C_{60} showed inefficient CT formation and CT dissociation. In the absence of direct measurements of the charge dynamics of F_xZnPc:C_{60} blends with higher donor content, we assume that the same classification applies across the donor concentration series. This

assumption is validated, at least for CT formation, considering that EQE fitting of the singlet and CT state energies reveals that ΔE_{CT} stays constant across the donor concentration series, suggesting that the efficiency of CT formation is invariant to F_xZnPc:C_{60} mixing.

Consequently, we hypothesize that the concentration dependence of the photocurrent in the F_8ZnPc:C_{60} and F_{16}ZnPc:C_{60} blends (Figures 7.4g and h), specifically the drop in J_{sc} for the intermixed blends, can be explained by an increased CT dissociation barrier caused by charge-quadrupole interactions with the positive quadrupole moments of F_8ZnPc/F_{16}ZnPc. Privitera et al. showed that the energy profile for charge separation is strongly dependent on film composition and morphologies [40], and Schwarze et al. showed that the effect of charge-quadruple induced electrostatic shifts is stronger in the bulk than at the interface with C_{60}. As a result, we hypothesize that at dilute concentrations, the impact of charge-quadrupole interactions is small, since donor aggregation is suppressed and all donor molecules are well inter-dispersed in the C_{60} matrix [183], [4]. With increasing F_8ZnPc/F_{16}ZnPc content, the effect of charge-quadrupole interactions is expected to increase since more D:C_{60} interfaces are formed. This effect saturates for the intermixed D:C_{60} blends, or when donor and acceptor aggregation limit the number of new interfaces. In the case of ZnPc:C_{60} and F_4ZnPc:C_{60}, the opposite effect of reduced CT dissociation barriers with increasing donor content possibly contributes to the high photocurrents observed for the intermixed blends, although CT dissociation is already efficient at low donor contents.

7.7 Conclusions

In conclusion, in this chapter, we study device performance characteristics as a function of donor fluorination and D:A mixing ratio for blends of ZnPc, F_4ZnPc, F_8ZnPc, or F_{16}ZnPc and C_{60}. Through $J-V$ and sensitive EQE measurements at room temperature, we observe that the photocurrents and V_{oc} change with D:C_{60} mixing ratios for all donor blends. We also establish a pairing of ZnPc/F_4ZnPc, and F_8ZnPc/F_{16}ZnPc based on the similarities of the observed performance characteristics.

The performance trends are rationalized considering different electrostatic effects that shift the position of the molecular energy levels in the films. Our work demonstrates that invalu-

able insights on the energetic landscape and driving forces in the active layers can be gained when both singlet and CT state peaks are fit in the EQE. From the EQE fit results, we determine that donor singlet energies are strongly impacted by changing polarization environments with increasing D:C_{60} mixing ratios. The trends in E_{CT} follow those of E_{S1} for all F_xZnPc:C_{60} blends, suggesting that polarization effects are the dominant electrostatic effects impacting the CT state energies of our material systems.

Charge-quadruple interactions, on the other hand, strongly influence the energetic landscape via changes in the CT dissociation efficiency. In the case of F_8ZnPc and F_{16}ZnPc, which have a positive quadrupole moment, CT dissociation is found to strongly depend on D:C_{60} mixing, with the lowest CT dissociation efficiencies observed for the intermixed blends. This is rationalized considering that charge-quadrupole interactions are strongly dependent on film morphology. In the case of ZnPc and F_4ZnPc, which have a negative quadrupole moment, CT dissociation is found to be efficient for all D:C_{60} mixing ratios.

Our work emphasizes the importance of understanding and improving the CT $\rightarrow$ CS transition to increase photocurrents in OSCs. Our results also highlight that future molecular design should not only focus on tuning molecular energy levels and absorption profiles, but also synthesize donor-acceptor pairs with favorable quadrupole moments to aid charge separation. Schwarze et al. demonstrated that the correlation of J_{sc} with Q_π is not unique to the fluorinated ZnPc derivatives, but equally applies to other donor and non-fullerene acceptor blends [41]. As a result, we hypothesize that if a molecule with the same energy levels and absorption profile as F_8ZnPc but opposite quadrupole moment could be engineered, we would observe the opposite trend in J_{sc} with D:C_{60} mixing.

With the advent of well-performing non-fullerene acceptors, which generally have a non-zero Q_π, higher J_{sc} were documented for donor-acceptor pairs with smaller (i.e. higher magnitude and negative) $Q_{\pi,D} - Q_{\pi,A}$ [41]. This highlights that promising donor-acceptor pairs should not only be selected based on complimentary absorption profiles and balanced charge carrier mobilities, but that donor and acceptor quadrupole moments need to be considered as well.

8 | The impact of static and dynamic disorder on the performance of organic solar cells based on dilute and intermixed donor:acceptor blends

The origin of the spectral linewidth of charge transfer (CT) state absorption and emission is still heavily debated in literature. While spectral broadening is generally attributed to energetic disorder, disagreement exists on whether the main contributions to energetic disorder are of temperature-dependent (dynamic) or temperature independent (static) nature [156], [119], [103], [155]. While dynamic disorder arises from temperature activated vibrations, static disorder is caused by statistical distributions of molecular orientation and packing geometries of the donor (D) and acceptor (A) molecules in organic thin films. While some studies determined static disorder contributions of $50 - 150$ *meV, other work argued that dynamic disorder dominates the spectral linewidth and that static disorder in organic solar cells is negligible [119], [103], [155]. In this chapter, we revisit the debate on which factors impact the spectral linewidth and investigate the temperature dependence of CT state absorption for a range of D:C_{60} systems. More specifically, we study the performance of TAPC,* α*-6T, CuPc, Rubrene, and DCV5T blends with* C_{60}*. To disentangle the contributions of molecular properties and morphology, we fabricate devices with low donor, intermixed D:A, and low acceptor content using vacuum thermal evaporation. We find that static disorder is non-negligible across all systems and often dominates the spectral linewidth. In addition, we measure increased static disorder for donors that favor aggregation and show that donor aggregation impacts the measured CT state properties. Finally, we compare our fullerene systems to well-performing blends of non-fullerene acceptors (NFAs), PM6:Y6 and PTQ10:Y6, to draw conclusions on their increased device performance.*

A manuscript based on the data presented in this chapter is in preparation and will be published by A. Jungbluth, P. Kaienburg, A. E. Lauritzen, M. Zhu, O. Gough, I. Habib, F. Otieno, and M.Riede.

8.1 Introduction

Over the last decades, the role of charge transfer (CT) states, which form at the interface between donor (D) and acceptor (A) molecules, on device performance has been studied in detail [23], [24], [120], [17]. Free charge generation is generally understood to proceed via the formation and dissociation of CT excitons. With that, CT states are highly relevant for the generation of photocurrents. In addition, CT states limit the open-circuit voltage (V_{oc}) and strongly impact radiative and non-radiative recombination [23], [24], [17].

However, the origin of the linewidth of CT state absorption and emission remains one of the most debated research questions in the field [119], [156]. Usually, broad spectral tails and large Stokes shifts between absorption and emission spectra are indicative of energetic disorder that negatively impacts charge transport, recombination, and V_{oc} [119].

Contributions to energetic disorder can be classified into temperature-dependent (i.e. dynamic; σ_D), or temperature independent (i.e. static; σ_S) disorder (see Figure 8.1.) Dynamic disorder, which arises from molecular vibrations, is agreed to be significant for OSC device performance [103], [119]. However, the origin, magnitude, and impact of static disorder in organic thin films is still heavily debated [156].

CT states are often modelled as single energy levels [24], even though the statistical distribution of molecular conformations, orientations, and packing geometries (Figure 8.1a) likely leads to distributions of CT state energies (E_{CT}). Burke et al. first disentangled the different disorder contributions by explicitly considering a Gaussian distribution of E_{CT} [51]. Their work showed that the experimentally determined CT state properties, like E_{CT}^{exp} and the reorganization energy λ_{CT}^{exp}, effectively account for static disorder as

$$E_{CT}^{exp} = E_{CT} - \frac{\sigma_S^2}{2k_BT}, \tag{8.1}$$

$$\lambda_{CT}^{exp} = \lambda_{CT} + \frac{\sigma_S^2}{2k_BT}, \tag{8.2}$$

where T denotes temperature, k_B is the Boltzmann constant, and E_{CT} and λ_{CT} describe the

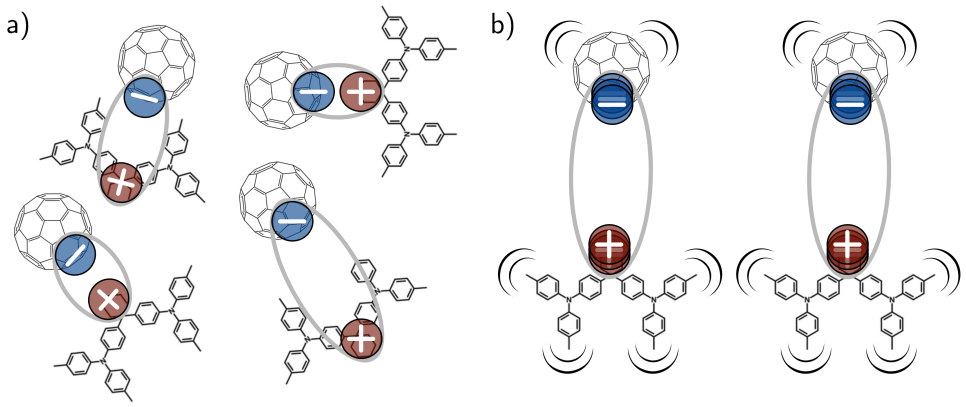


Figure 8.1: Schematic of a) static disorder, and b) dynamic disorder for the model TAPC:C_{60} system. While static disorder is temperature independent, and is related to molecular orientation and packing geometries, dynamic disorder is facilitated by temperature activated molecular vibrations. The schematics were reproduced from reference [119] with permission under CC BY 4.0.

corrected CT state energy and reorganization energy excluding static disorder. These equations are immensely helpful to connect experimental observations to molecular properties, and give way to probe static and dynamic disorder from experimental characterization of CT states. Following from equation 8.2, dynamic disorder is defined as $\sigma_D^2(T) = 2\lambda_{CT} k_B T$. The total disorder ($\sigma_T(T)$) is then calculated as the sum of the different disorder contributions.

$$\sigma_T^2(T) = \sigma_S^2 + \sigma_D^2(T) \tag{8.3}$$

However, an accurate determination of energetic disorder is not only important for accurate reporting of E_{CT} and λ_{CT}, but also informs on device performances and voltage losses. Figure 8.2 shows modelled EQE spectra for systems with a) low static and b) low dynamic disorder. Here, the CT state was modelled using Marcus theory (equation 3.10) including static disorder. The singlet energy (E_{S_1}) and E_{CT} were assumed to be constant, and the changes in the low-energy EQE tail exclusively arise from changes in the static and dynamic disorder contributions. As expected, if dynamic disorder dominates, the spectral linewidth of the CT absorption peak is strongly temperature-dependent. In addition, the increasing width of the CT absorption band for increasing static disorder leads to a lower radiative limit of the V_{oc} (qV_{oc}^{rad}) and larger radiative recombination ($q\Delta V_{oc}^{rad}$). The same trends have been observed for non-radiative losses [156].

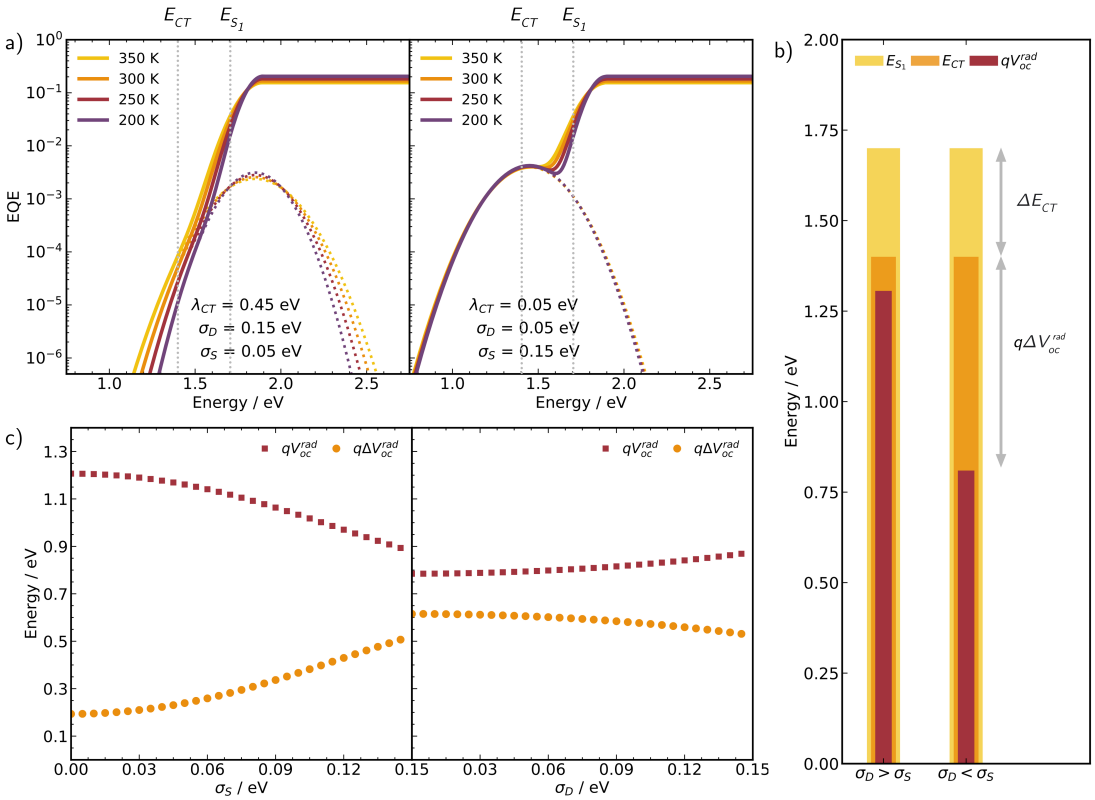


Figure 8.2: a) Simulated external quantum efficiency (EQE) spectra for low static (σ_S; left graph) and low dynamic disorder (σ_D; right graph). The CT state was modelled using classical Marcus theory (equation 3.10) including static disorder and assuming $T = 300$ K. The singlet (S_1) and CT state were modelled with $E_{S_1} = 1.70$ eV, $f_{S_1} = 0.08$ eV^2, $\lambda_{S_1} = 0.2$ eV, $E_{CT} = 1.40$ eV, $f_{CT} = 0.001$ eV^2, $\lambda_{CT} = 0.05 - 0.45$ eV. These values fall within the ranges usually reported for OSCs, and match the fitting results presented later in this chapter. The values for σ_D and σ_S were chosen such that the total disorder, i.e. the amount of CT state broadening, is constant in both examples. The grey dotted vertical lines indicate the values of E_{S_1} and E_{CT} used in the modelling. For each set of CT state parameters, the colored dotted lines show the resulting Gaussian linewidth using equation 3.10. b) Voltage losses at room temperature calculated for the same model systems shown in a). c) Dependence of qV_{oc}^{rad} and $q\Delta V_{oc}^{rad}$ on static disorder (left graph), assuming $\lambda_{CT} = 0.45$ eV and $\sigma_D = 0.15$ eV, and dynamic disorder (right graph), assuming $\sigma_S = 0.15$ eV.

While some work found negligible σ_S, suggesting that dynamic disorder is more important than static disorder in OSCs [119], [103], [155], other work observed the opposite [51], [109], [227], [156] and reported σ_S of $\sim 50-150$ meV. Across these reports, discrepancies in the studied systems (i.e. small molecule vs. polymer), fabrication conditions (i.e. vacuum vs. solution-processed), molecular properties, and blend morphologies might partially explain the disagreements. Nonetheless, the ongoing discussion highlights that a clear understanding on which molecular and blend properties define energetic disorder is still lacking.

In this chapter, we elucidate some of the dominant factors impacting static and dynamic disorder, and relate this understanding to device performance. More specifically, we investigate the impact of molecular properties and D:A mixing ratios on the emergence of energetic disorder. We choose five common small molecule donors that span a broad range of molecular properties and electronic qualities (see Figure 8.3), and fabricate devices with C_{60} as the acceptor. To disentangle the contributions of molecular properties and morphology, we study blends with low donor, intermixed D:C_{60}, and low acceptor content. At low donor content (usually < 10 %), the donor molecules are fully dispersed in the C_{60} matrix, and donor aggregation is suppressed [49], [4], [3]. This creates comparable morphologies across donor choices. At higher donor content, donor aggregation becomes significant. We observe that donors that favor polycrystalline aggregation show larger static disorder than donors that favor amorphous film growth. In addition, we see a strong experimental correlation between qV_{oc}^{rad} and disorder that applies to both fullerene and non-fullerene acceptor (NFA) systems.

8.2 Materials & Devices

Figure 8.3a shows the molecular structure of the donor and acceptor molecules used in this study. Five donors, namely TAPC, α-6T, CuPc, Rubrene, and DCV5T, were chosen to investigate disorder across a broad range of molecular properties. To evaluate the suitability of the different donors, we follow the methodology outlined in reference [2] and conduct a meta-analysis of published and measured OSC device performances. As part of our meta-analysis, we study the electronic quality (Q) [228] and the Scharber efficiency (η_{Sch}) [210] for the different D:C_{60} blends (Figure 8.3b).

The electronic quality captures the competition between charge transport and recombination and was defined as $Q = \mu^2/\beta^{0.8}$ by Kaienburg et al. [2], where μ is the mobility and β is the bimolecular recombination coefficient. As discussed in reference [228], Q is a blend specific quantity that is calculated directly from device performance characteristics (i.e. the short-circuit current density (J_{sc}), fill factor (FF), V_{oc}, and the active layer thickness). η_{Sch}, on the other hand, combines information on voltage losses, and energy level matching between the AM1.5g solar spectrum and the blend's optical gap (E_{opt}). The latter is determined via

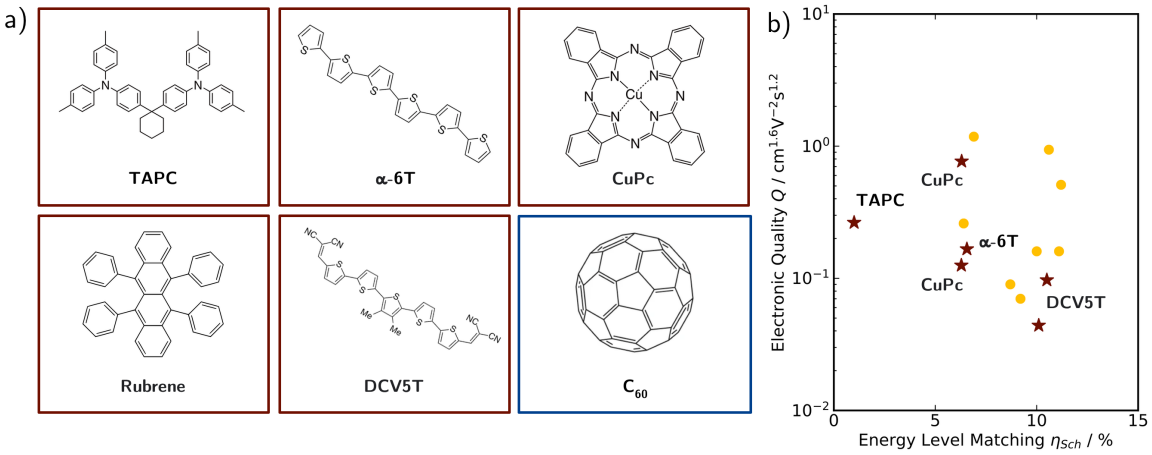


Figure 8.3: a) Molecular structure of the donor (D; red outline) and acceptor (A; blue outline) molecules of this study. b) Electronic quality (Q) [228] vs. Scharber efficiency (η_{Sch}) [210] for different D:C_{60} blends. The donor blends used in this study are labelled and highlighted as red stars. The data plotted in b) is included in Table D.1 in the Appendix and was either calculated by Dr. Pascal Kaienburg for this work or reproduced from Kaienburg et al. [2] with permission under CC BY 4.0.

the inflection point of the external quantum efficiency (EQE) [21]. Both Q and η_{Sch} were calculated by Dr. Pascal Kaienburg for this work or reproduced from Kaienburg et al. [2].

Looking at Figure 8.3b, we see that our chosen donor molecules span a broad range of Q and η_{Sch}. More specifically, TAPC:C_{60} shows very low energy level matching but a reasonably high electronic quality. DCV5T:C_{60}, on the other hand, shows a high η_{Sch} but the lowest Q. The other donor blends in Figure 8.3b are intermediate systems that roughly fall between the two extremes. In addition, the chosen molecules qualitatively span a range of interesting molecular and microstructural properties. For instance, while TAPC tends to grow amorphously [4], α-6T easily aggregates [120] and is highly crystalline [229]. In addition, Rubrene is classified as a stiff molecule with a lower reorganization energy than donors like TAPC or α-6T [120]. Low reorganization energies result in low dynamic disorder and less spectral broadening if static disorder is also low.

To investigate the impact of molecular properties on static and dynamic disorder, we study OSCs based on dilute and intermixed D:C_{60} blends. More specifically, we fabricate devices with 5, 50, and 95 mol.% donor content. A photo of all studied samples is included as Figure D.1 in the Appendix. Studying both dilute donor and dilute acceptor blends helps reveal how disorder is impacted by the molecular properties and aggregation of the majority species. As

discussed in Chapter 4, all samples were fabricated via vacuum thermal evaporation and co-deposition of the donor and acceptor molecules. Apart from the active layer, all samples were fabricated with nominally identical device architectures and through subsequent evaporation of MoOx (3 nm, $0.05 - 0.1$ Å/s), D:C_{60} (50 nm, combined rate of 0.4 Å/s), BPhen (8 nm, $0.1 - 0.2$ Å/s), and Al (100 nm, $1 - 2$ Å/s).

8.3 Device Performance

Before discussing disorder, we first consider the device performances at room temperature. Figure 8.4 shows the current density-voltage ($J - V$) and EQE characteristics of the best performing (highest power conversion efficiency; PCE) devices for all D:C_{60} blends. For each material system, the D:C_{60} mixing ratios are given in square brackets, and the line colors darken with increasing donor content. Performance statistics are calculated for multiple devices and are reported in Table D.2 in the Appendix.

Since we are mainly interested in qualitative trends across D:C_{60} mixing ratios, the $J - V$ data presented in this chapter is reported as measured. Spectral mismatch correction only marginally shifts the J_{sc} of all blends and preserves all performance trends (Figure D.4). The stark differences in D:C_{60} mixing ratios, i.e. comparing dilute and intermixed blends, cause larger differences in device performance than attributable to absorption changes alone.

Looking at the $J-V$ performance of TAPC:C_{60} (Figure 8.4a), we observe strong differences in the V_{oc} and J_{sc} with increasing donor content. Both the V_{oc} and the J_{sc} peak for the dilute donor blend. These results match those presented by Zhang et al. who first reported improved device performances for TAPC:C_{60} blends with low donor content [49]. The V_{oc} first decreases for the intermixed TAPC:C_{60} blend, and then increases for the dilute acceptor system. This behavior can be rationalized considering that voltage losses were found to scale with D:A interfacial areas [52]. In addition, we would like to note the low J_{sc} of the intermixed and dilute acceptor blends. Since TAPC is a transparent donor, photons are mainly absorbed by C_{60} and CT occurs via hole transfer [4]. The J_{sc} of the TAPC:C_{60} system is therefore primarily limited by poor photon absorption of C_{60} in the visible and infrared region [52].

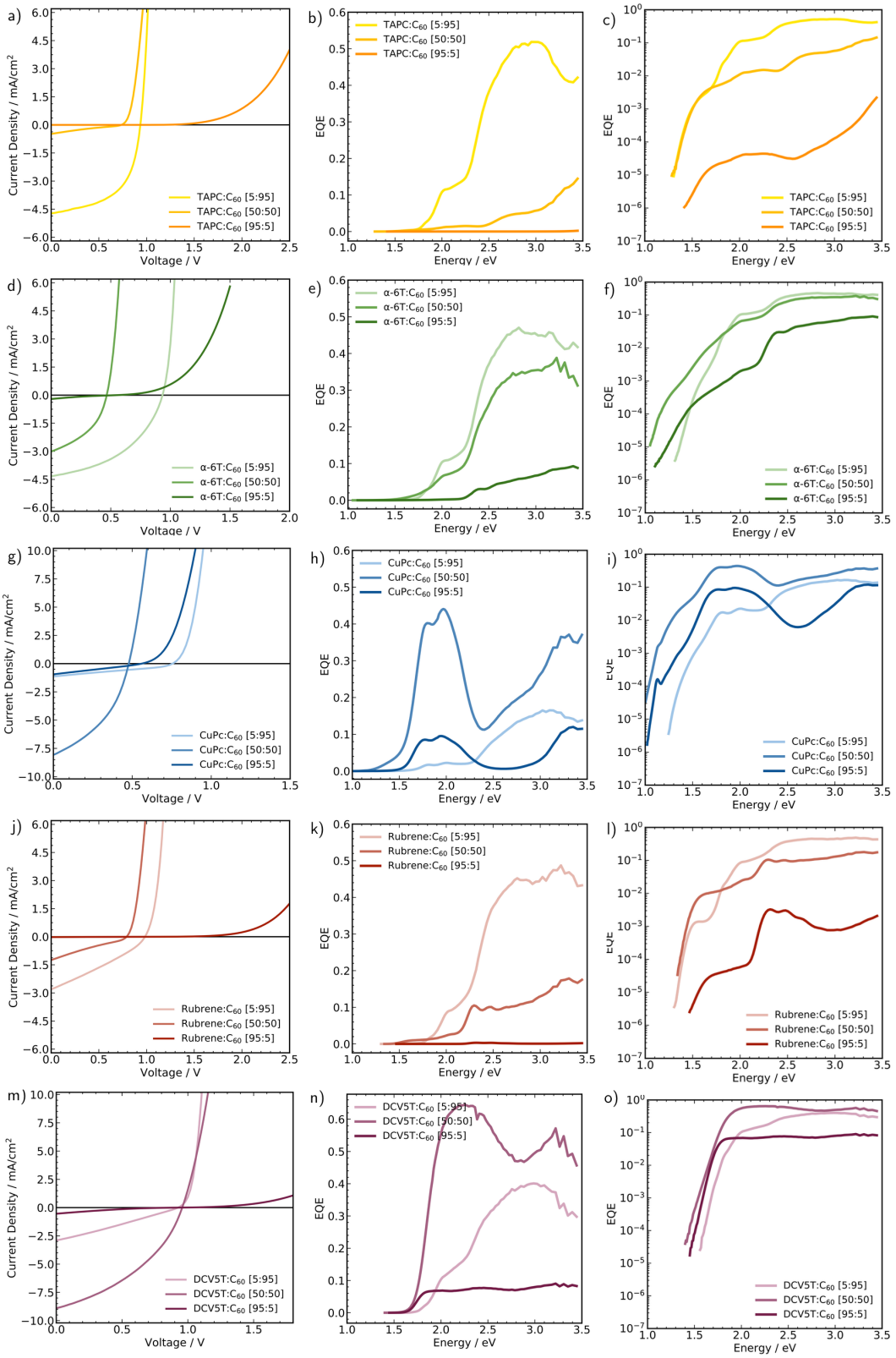


Figure 8.4: $J-V$ characteristics under simulated 1 Sun illumination and EQE of the best performing (highest PCE) blends based on C_{60} and a-c) TAPC, d-f) α-6T, g-i) CuPc, j-l) Rubrene, and m-o) DCV5T. The donor:acceptor ratio is given in molar percent in square brackets. The $J-V$ data is plotted as measured.

The low photocurrents of the intermixed and dilute acceptor TAPC:C_{60} blends can also be seen in the low EQE (Figure 8.4b-c). Investigating the EQE further, we note that the position of the CT state peak does not change with increasing TAPC content. This is in good agreement with previous work that observed a constant E_{CT} of 1.45 eV until 50 wt.% TAPC content, followed by only a small increase to around 1.50 eV at higher donor content [120].

Looking at the other material systems, we observe that most D:C_{60} blends show the highest V_{oc} and J_{sc} for low donor contents. Only CuPc and DCV5T show significantly higher photocurrents for the intermixed blends. Especially the dilute donor CuPc blend stands out for its low photocurrent.

Compared to TAPC, all other donor molecules absorb in the visible spectrum (see Figure D.5 in the Appendix) [2], [230], [182]. However, the device performances and especially the photocurrents of the dilute acceptor blends are poor across the board. While this observation can in part be explained by the extinction coefficients of the donors, photocurrents are also affected by the exciton separation efficiency, and the charge collection efficiency. The latter can be studied via the fill factor and depends, for instance, on the active layer thickness, charge carrier mobilities and lifetimes [228]. We note that the dilute acceptor blends show the lowest FF across all D:C_{60} mixing ratios, suggesting poor charge collection. With nominally identical active layer thicknesses, we hypothesize that low or unbalanced charge carrier mobilities are in part to blame for the poor device performances [231].

Looking back at the EQE spectra on a logarithmic scale in Figure 8.4, we observe that all material systems apart from DCV5T show a clearly resolvable CT absorption peak. Rubrene, just like TAPC, shows a constant CT absorption onset for the dilute donor and intermixed blends. In comparison, α-6T, CuPc, and DCV5T show high energy absorption onsets for the low donor systems, and low energy onsets for the intermixed blends. This indicates shifting E_{CT} with increasing donor content for these material systems, possibly caused by electrostatic energy level shifts and changing polarization environments upon donor aggregation [48], [41], further discussed in the following sections.

8.4 GIWAXS Analysis

We performed Grazing Incidence Wide Angle X-Ray Scattering (GIWAXS) meausuremens to determine the presence of ordered molecular regions (crystallites) in the dilute donor, intermixed donor:acceptor, dilute acceptor, and for reference neat donor films. While GIWAXS allows to probe the morphology and microstructure of the bulk, it is not sensitive to ordering at the donor:acceptor interface specifically, which is the main focus of this work. However, since the ordering of the bulk inherently influences interfaces properties, GIWAXS provides useful information on donor and acceptor aggregation, which can be connected to the CT state properties measured via fitting of EQE spectra. The GIWAXS measurements presented in this chapter were carried out by Andreas E. Lauritzen, Olivia Gough, and Irfan Habib, and the GIWAXS analysis was carried out by Andreas E. Lauritzen.

Figures D.2 and D.3 in the Appendix show the 2D scattering maps of the dilute donor, intermixed donor:acceptor, dilute acceptor, and neat donor films. The presence of ordered regions in the bulk is indicated by Bragg rings or peaks in the scattering maps [232]. In our GIWAXS analysis, the films are classified by the number of scattering peaks, i.e. no Bragg scattering peaks, only first order scattering peaks, or having second order (or higher) scattering peaks. Higher order peaks are generally indicative of more ordered film growth. We note, however, that the presence of Bragg peaks is also affected by the volume fraction and size of the crystalline domains, as well as the molecular disorder and lattice parameter fluctuations between crystallites [233]. We also note that depending on the material system, the scattering peaks or rings can be more or less well defined. Distinguishing the scattering features from the diffuse signal of, for instance, the substrate background is not always straightforward [233].

Table 8.1: Summary of acceptor aggregation features, measured via GIWAXS, as a function of donor molecule and content. The numbers indicate the order of the C_{60} Bragg scattering peaks. The GIWAXS measurements were carried out by Andreas E. Lauritzen, Olivia Gough, and Irfan Habib, and the GIWAXS analysis was carried out by Andreas E. Lauritzen.

Donor Content / mol.%	**TAPC**	**α-6T**	**CuPc**	**Rubrene**	**DCV5T**
5	1	2+	0	1	2+
50	0	0	0	0	2+
95	0	0	0	0	0
100	0	0	0	0	0

Table 8.2: Summary of donor aggregation features, measured via GIWAXS, as a function of donor molecule and content. The numbers indicate the order of the donor Bragg scattering peaks. The asterisk labels features that were only observed faintly. The GIWAXS measurements were carried out by Andreas E. Lauritzen, Olivia Gough, and Irfan Habib, and the GIWAXS analysis was carried out by Andreas E. Lauritzen.

Donor Content / mol.%	**TAPC**	**α-6T**	**CuPc**	**Rubrene**	**DCV5T**
5	0	0	0	0	0
50	0	0	1*	0	1*
95	0	2+	1	0	1
100	0	2+	2+	1	1

Table 8.1 summarizes the order of the acceptor aggregation features, and Table 8.2 summarizes the order of the donor aggregation features determined from the analysis of the 2D scattering maps. Starting with the pure donor films, second or higher order donor features are present in α-6T and CuPc. First order peaks are observed for Rubrene and DCV5T, and no visible features are observed for TAPC. This matches previous studies of TAPC, which was found to grow amorphous thin films [234], [4]. For the dilute acceptor blends (95:5 mol.% donor:acceptor mixing ratio), second or higher order features are only present for α-6T. DCV5T and CuPc show first order donor features, while no signatures of donor features are found for TAPC and Rubrene. At these high donor concentrations, no C_{60} aggregation features can be observed in any of the donor:C_{60} blends.

Looking at the intermixed blends (50:50 mol.% donor:acceptor mixing ratio) only CuPc and DCV5T show faint first order donor scattering peaks. In both cases, the faint peaks are ordered along the out-of-plane direction. Acceptor features are only present for DCV5T, where second order Bragg rings can be detected. Finally, for the dilute donor blends (5:95 mol.% donor:acceptor mixing ratio), none of the films show donor aggregation features, confirming that the donor molecules are well inter-dispersed in the C_{60} matrix, and that donor aggregation is suppressed. α-6T and DCV5T both display second order acceptor features, meaning that the ordered C_{60} matrix is least disrupted for these two donor molecules. TAPC and Rubrene both display first order acceptor features, and no acceptor features can be observed for the dilute CuPc blend.

Summarizing the main results of our GIWAXS analysis, we find that both TAPC and Rubrene form amorphous blends at all donor concentrations. The lack of C_{60} scattering features indi-

cates that the C_{60} matrix is effectively disrupted, even when only small amounts of the donor molecules are added. Connecting this observation to the device characteristics presented earlier, we find that the lack of donor/acceptor aggregation matches our observation of constant E_{CT} in the TAPC and Rubrene blends. While Rubrene can also be grown into single crystals [235], [236], previous work confirms that Rubrene, deposited via vacuum thermal deposition, forms amorphous layers [48]. We note, however, that fabrication conditions, such as the temperature of the substrate, likely influence the crystallinity of the active layer. The samples fabricated for this work were all deposited onto substrates held at room temperature.

In comparison, both α-6T and CuPc show strong features of donor aggregation at high donor content. While the DCV5T:C_{60} blends show only faint signals of donor aggregation, the C_{60} scattering features are well preserved for the low donor and intermixed donor:acceptor blends. As a result, we hypothesize that donor/acceptor aggregation in these three blends, α-6T:C_{60}, CuPc:C_{60}, and DCV5T:C_{60}, can cause electrostatic shifts that contribute to the observed dependence of the absorption onset (and E_{CT}) on D:A mixing in these blends.

8.5 Disorder Analysis

Having discussed the device performances at room temperature and presented the microstructural characterization of the active layers, we now turn to investigating the role of interfacial disorder for the different D:C_{60} blends. In the following, we first introduce our methodology for determining static and dynamic disorder from the temperature dependence of the EQE. We then investigate the physical accuracy of different CT state models, and determine how the choice of fit model impacts the fit results. Finally, we present the results of our disorder analysis for all D:C_{60} systems.

8.5.1 Determination of Static & Dynamic Disorder

Figure 8.5 shows an example of how energetic disorder is determined for TAPC:C_{60} [5:95]. While both absorption and emission spectra can be used to study disorder, our work focuses on absorption determined via the EQE, and follows the methodology of Benduhn [33].

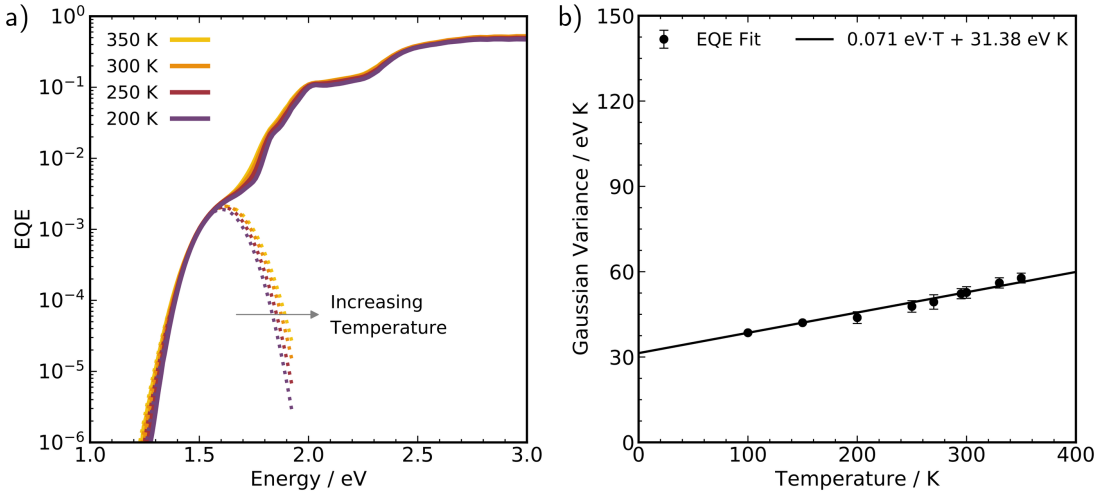


Figure 8.5: a) Temperature dependence of the EQE of TAPC:C_{60} [5:95]. A subset of four temperature measurements is shown. With increasing temperature, the CT state shoulder broadens. The dotted lines show CT state fits based on classical Marcus theory (equation 3.10). b) Measured Gaussian variance as a function of temperature for TAPC:C_{60} [5:95]. The uncertainties on the EQE fit values are determined as the standard deviation across $5-10$ different CT state fits. By linearly fitting the temperature dependence of the Gaussian variance (using equation 8.4), the reorganization energy and static disorder can be determined.

Temperature-dependent measurements of the EQE (Figure 8.5a) show that the width of the CT state absorption band increases with increasing temperature. This indicates that the spectral shape and linewidth of the EQE in part arise from thermally assisted transitions. Referring back to equations 8.1 and 8.2, we can disentangle the contributions of temperature and static interfacial disorder on the spectral linewidth by explicitly fitting both quantities.

As first introduced in Chapter 3, CT models based on Gaussian functions describe the broadness of the Gaussian peaks in the denominator of the exponential. Without considering static disorder explicitly, this denominator equals $2\lambda_{CT}^{exp} k_B T$. Substituting equation 8.2 for λ_{CT}^{exp}, the peak broadness is described by $2\lambda_{CT} k_B T + \sigma_S^2$. This can be minimally rearranged to define the Gaussian variance W as

$$W = \lambda_{CT} T + \frac{\sigma_S^2}{2k_B}. \tag{8.4}$$

Importantly, W linearly relates the temperature to the spectral linewidth, with the reorganization energy being described by the slope, and the static disorder being related to the

y-intercept. Consequently, to determine static and dynamic disorder contributions, we calculate the Gaussian variance from CT state fits of the EQE at different temperatures and determine the linear fit that best describes the relationship of W and T (Figure 8.5b). Following the fit process outlined in Chapter 3, we fit both the singlet (S_1) and CT state peaks for all material blends. The uncertainty on the fit parameters is determined as the standard deviation across $5-10$ different fit ranges.

8.5.2 Marcus vs. MLJ Theory

Having introduced the methodology for determining static and dynamic disorder from the temperature-dependent EQE, we next turn to discussing the physical accuracy of different CT state models. Many reports on disorder in OSCs employ classical Marcus theory (introduced as equation 3.10 in Chapter 3) [120], [33],

$$EQE(E) = \frac{f_{CT}}{E\sqrt{4\lambda_{CT}k_BT + 2\sigma_S^2}} \exp\left(-\frac{E_{CT} + \lambda_{CT} - E)^2}{4\lambda_{CT}k_BT + 2\sigma_S^2}\right), \tag{8.5}$$

where f_{CT} is an absorption pre-factor that relates to the oscillator strength of the optical transition. However, recent work argues that more advanced models, like Marcus-Levich-Jortner (MLJ) theory, are required to describe CT state properties at low temperatures accurately [109], [103], [102], [156], [119]. Classical Marcus theory relies on the assumption that the energy of internal ($\hbar\omega_i$) and external ($\hbar\omega_e$) vibrational modes is much smaller than the thermal energy (k_BT), i.e. $\hbar\omega_i + \hbar\omega_e << k_BT$ [101]. Under this condition, the quantum nature of vibrations does not need to be considered explicitly, and thermal energy is large enough to facilitate charge transfer. For organic molecules in thin films, external vibrations, i.e. vibrations between molecules and their surrounding, are usually on the order of $1-10$ meV [101], [109], [51], [19], and the condition that $\hbar\omega_e << k_BT$ is met until ~ 120 K. However, the energy of internal vibrational modes is often dominated by carbon bond vibrations and falls between $50-300$ meV [109]. This means that $\hbar\omega_i > k_BT$ even at room temperature.

For the work in this chapter, we focus on EQE measurements performed at ≥ 150 K and continue to treat external vibrational modes classically. Internal vibrational modes, on the

other hand, are treated quantum mechanically by employing semi-classical MLJ theory to fit the CT state peaks in the EQE,

$$EQE(E) = \frac{f_{CT}}{E\sqrt{4\lambda_{CT}k_BT + 2\sigma_S^2}} \sum_{n=0}^{\infty} \frac{e^{-S_i}S_i^n}{n!} \exp\left(-\frac{E_{CT} + n\hbar\omega_i + \lambda_{CT} - E)^2}{4\lambda_{CT}k_BT + 2\sigma_S^2}\right). \quad (8.6)$$

S_i in equation 8.6 is the Huang-Rhys parameter, a dimensionless quantity that is defined as $S_i = \lambda_{CT}/\hbar\omega_i$. Note that equation 8.6 was previously introduced as equation 3.21 in Chapter 3. We simplify our calculations by varying n from $0 - 5$. We find that 6 vibrational overtones suffice to converge the fit values, and fitting with more overtones does not improve the results.

Importantly, when fitting the CT peaks using MLJ theory, we pass S_i and $\hbar\omega_i$ as pre-defined parameters and fit E_{CT}, λ_{CT}, f_{CT}, and σ_S. The values of S_i and $\hbar\omega_i$ can be calculated via density functional theory (DFT) or determined experimentally via Raman spectroscopy or Franck-Condon analysis of absorption and emission spectra [237], [238], [239], [240]. To determine S_i and $\hbar\omega_i$ for this work, we performed a literature search of published values. Based on the work by Unger et al. [102] and Tvingsted et al. [119], we chose $S_i = 1$ to describe the high-frequency vibrations. The values of S_i reported in literature generally fall between $S_i = 1 - 4$, depending on the vibrational mode that is being described. Since $\hbar\omega_{C=C} = 180$ meV and $\hbar\omega_{C-C} = 150$ meV [238], we chose $\hbar\omega_i = 165$ meV to model the internal vibrational modes, in agreement with reference [102].

Nonetheless, we briefly turn to discussing how the CT fits and fit results vary with S_i and $\hbar\omega_i$ by performing a sensitivity analysis. Figure 8.6 demonstrates how the MLJ fits of TAPC:C_{60} [5:95] vary with S_i (Figure 8.6a-b), and $\hbar\omega_i$ (Figure 8.6c-d). We observe that while the CT state tail is consistently well described, the Gaussian fits become broader with increasing S_i and eventually overestimate the high energy region of the CT peak (Figure 8.6a). For varying $\hbar\omega_i$, the CT fits remain virtually unchanged (Figure 8.6c). Looking at the fitted values of E_{CT}, we observe constant fit results for all parameters. In the case of the Gaussian variance, we observe a 35% decrease upon increasing S_i from 0.4 to 5.5, and an 8% increase upon increasing $\hbar\omega_i$ from 150 to 200 meV.

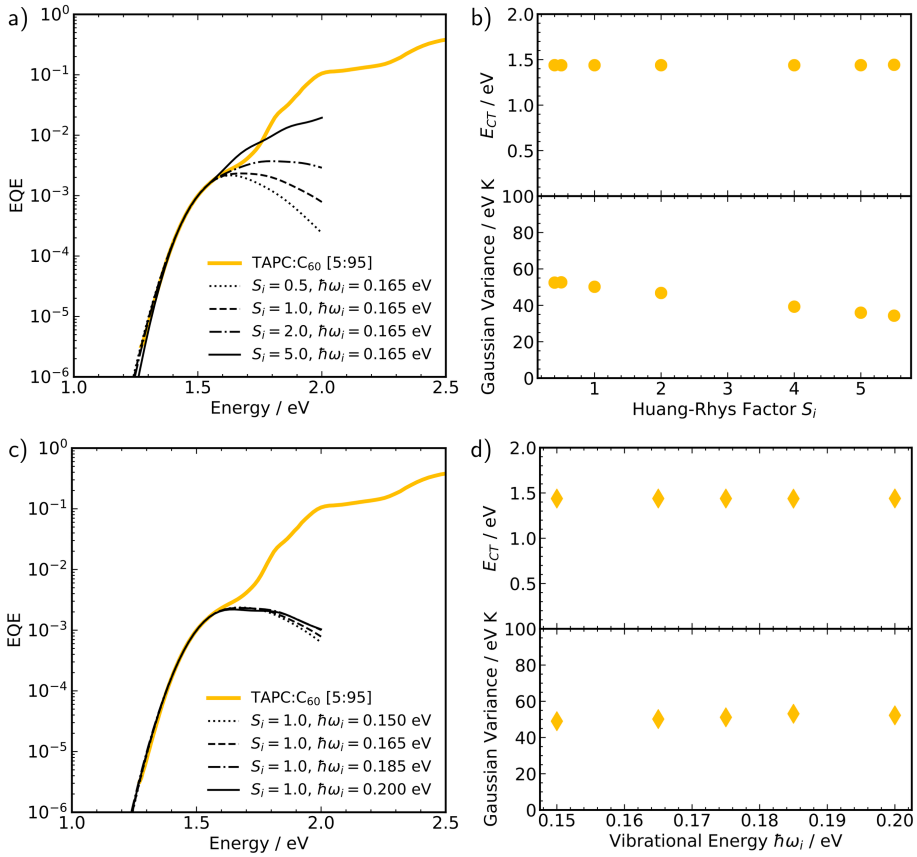


Figure 8.6: Dependence of the a) CT state fits, and b) E_{CT} and Gaussian variance fit results upon varying the Huang-Rhys parameter S_i. Dependence of the c) CT state fits, and d) E_{CT} and Gaussian variance fit results upon varying the energy of the internal vibrational energy $\hbar\omega_i$. All fits were performed for the TAPC:C_{60} [5:95] model system.

In the context of our disorder analysis, an $\pm X\%$ change in the Gaussian variance would scale the fitted reorganization energy λ_{CT} by $1 \pm X$, and therefore the dynamic disorder by $\sqrt{1 \pm X}$. The fitted static disorder would also be scaled by $\sqrt{1 \pm X}$. This means that while deviations in S_i and $\hbar\omega_i$ propagate into small deviations of the fit results, static and dynamic disorder would scale equally and all observed trends would be preserved.

Finally, we return to the debate on Marcus vs. MLJ theory and compare the fit results of both models for all D:C_{60} blends studied in this work. Figure 8.7 shows correlation plots for the fitted a) E_{CT}, b) λ_{CT}, c) f_{CT}, and d) Gaussian variance. While E_{CT} largely agrees between both models, λ_{CT} shows a linear correlation with large amount of scatter. f_{CT} shows a clear relationship of $f_{CT,\mathrm{MLJ}} > f_{CT,\mathrm{Marcus}}$. This arises from the slowly decaying high energy tail of the MLJ Gaussian (see Figure 8.6a), compared to the steeper decrease of the

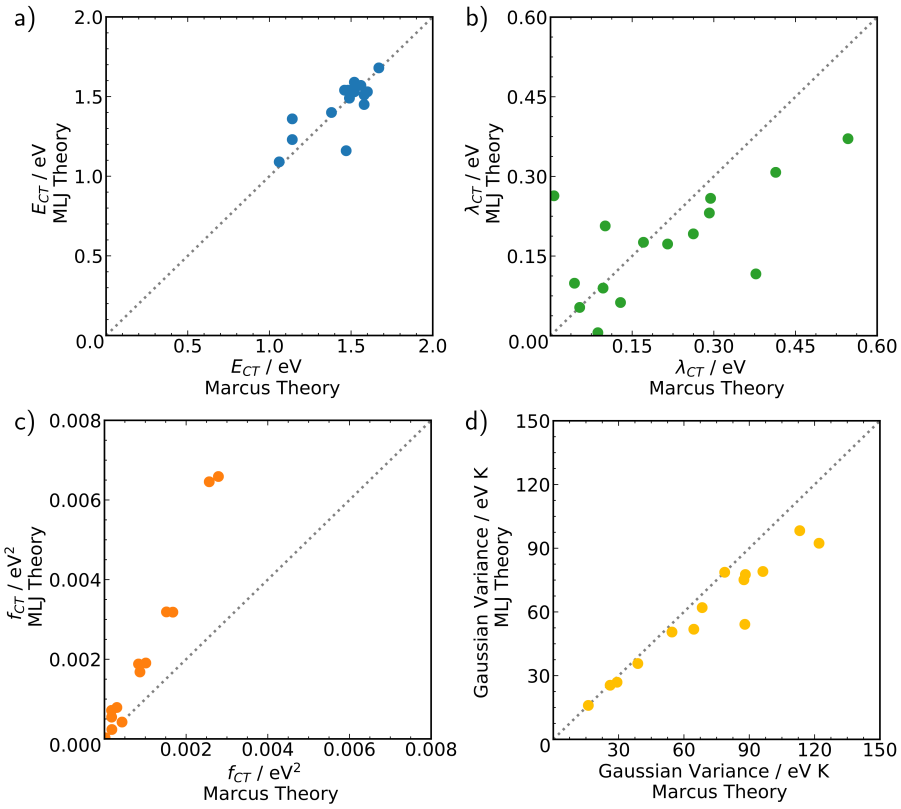


Figure 8.7: Correlation plots of the a) E_{CT}, b) λ_{CT}, c) f_{CT}, and d) Gaussian variance fit results when employing Marcus vs. MLJ theory. The data shown compares the fit results for all D:C_{60} blends studied in this work.

Marcus Gaussian (refer back to Figure 8.5a). Similarly, the Gaussian variance determined via classical Marcus theory overestimates the Gaussian variance determined via semi-classical MLJ theory (using the input parameters discussed earlier). As a result, the static and dynamic disorder determined via Marcus theory will on average be slightly larger than the disorder contributions determined via MLJ theory. With this, the correlation analysis presented in Figure 8.7 presents a helpful guide to compare fit results in literature across fit models.

8.5.3 Material Comparison

We now turn to discussing the results of our disorder analysis. Figure 8.8 shows normalized spectra of the temperature dependence of the low energy EQE tails for all D:C_{60} blends. Each row shows a different donor molecule. The dilute donor, intermixed D:C_{60}, and dilute acceptor blends are shown in the first, second, and third column respectively.

Qualitatively, we observe that some material blends display a stronger linewidth narrowing with decreasing temperature than others. Interestingly, most of the dilute acceptor blends show lower linewidth narrowing than the dilute donor or intermixed systems. However, for certain dilute acceptor blends, like TAPC:C_{60} [95:5] and Rubrene:C_{60} [95:5], the low photocurrents of the devices lead to low signal-to-noise ratios in the EQE which make it difficult to draw qualitative conclusions. Especially for the scans at low temperature, a higher measurement sensitivity would be helpful.

Focusing on the dilute donor and intermixed donor:acceptor blends, most intermixed blends show lower linewidth narrowing than the dilute donor blends. While this initially agrees with the intuitive picture that dilute donor systems are less governed by static disorder [156], we caution the reader to draw premature quantitative conclusions from visual inspection of the EQE spectra alone. Since the spectra in Figure 8.8 were centered on the CT state peak, it is difficult to estimate the broadness of the CT peak in comparison to the rest of the spectrum. Additionally, since the spectra were normalized to the (approximate) peak of the CT state absorption, any changes in the magnitude of the EQE spectra are obscured. Since the magnitude of the EQE (measured via f_{CT}) enters the Gaussian fitting function as an additional fit parameter (and all fit parameters are somewhat dependent on each other), the actual fit results might reveal slightly different trends than expected via visual inspection of the normalized spectra alone.

In addition, the low signal-to-noise ratio of some of the low temperature measurements might visually suggest a lack of linewidth narrowing, but if the EQE was extended, the temperature deviations would become more apparent. An example of this effect can be observed for the 150 K measurement of DCV5T:C_{60} [95:5], which, if it was extended, e.g. via the low energy tail of the Gaussian fit, would display a stronger temperature dependence for this sample.

Nonetheless, the choice of donor clearly impacts both the spectral shape of the CT absorption peak and its temperature dependence, even at low donor content. We next turn to a quantitative evaluation of the disorder contributions and present the obtained fit results.

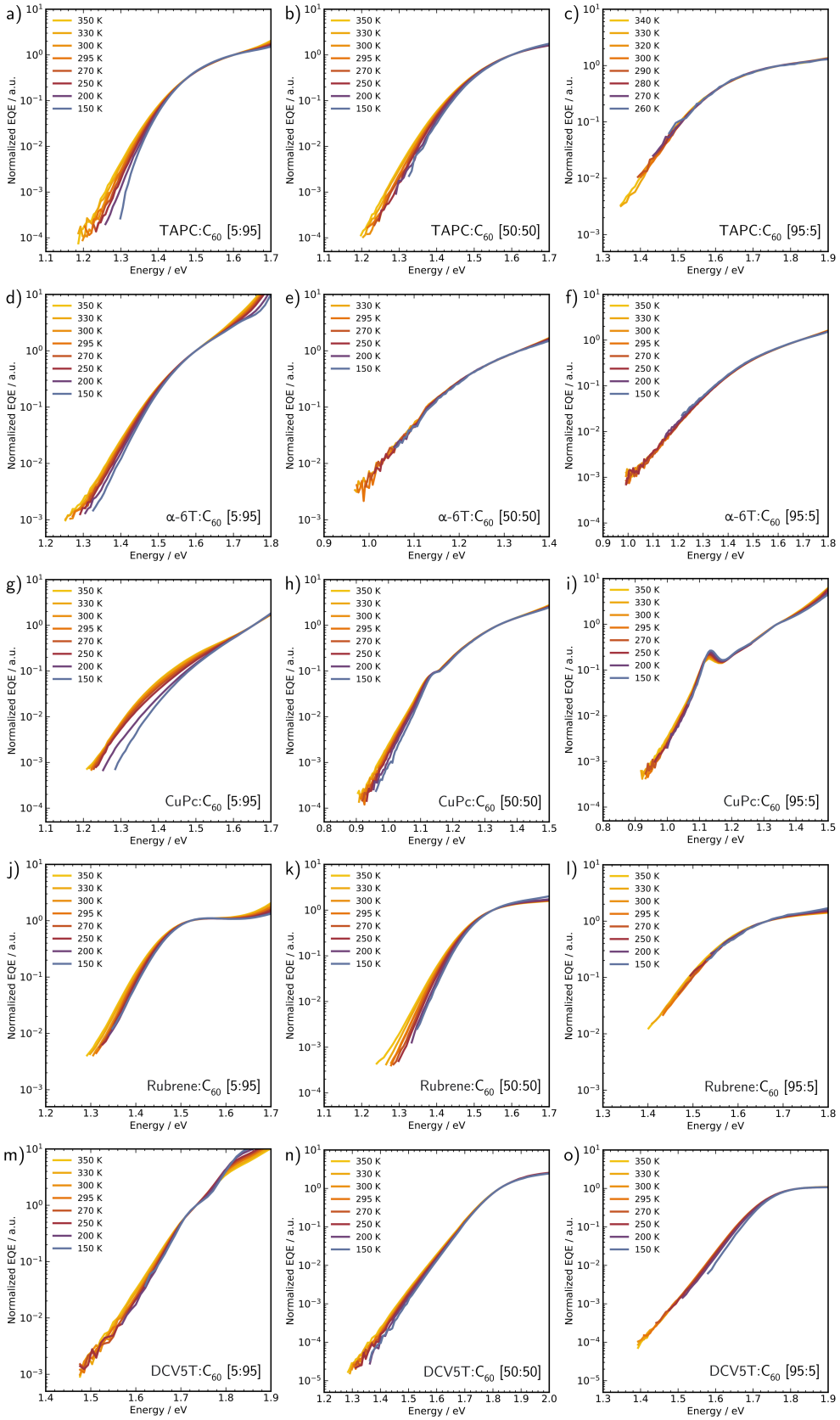


Figure 8.8: Temperature-dependent EQE of a-c) TAPC, d-f) α-6T, g-i) CuPc, j-l) Rubrene, and m-o) DCV5T blends with C_{60}. The spectra were normalized to the (approximate) peak of the CT absorption. The D:C_{60} ratios are given in mol.% in square brackets.

Figure 8.9 shows the temperature dependence of the Gaussian variance for each D:C_{60} system, and Figure 8.10 summarizes how static and dynamic disorder change as a function of donor molecule and D:C_{60} mixing ratio. The dynamic disorder was calculated as $\sigma_D = \sqrt{2\lambda_{CT} k_B T}$, with $T = 300$ K and using the reorganization energy determined via the linear fit analysis of the Gaussian variance. The disorder results, including parameter uncertainties, can be found in Table D.2 in the Appendix.

We note that TAPC (Figure 8.9a) shows a roughly constant reorganization energy across all TAPC:C_{60} mixing ratios. This observation is in agreement with reference [33], which measured similar reorganization energies for dilute donor and intermixed TAPC:C_{60} blends. In addition, Rubrene (Figure 8.9d) also shows a constant reorganization energy for the dilute donor and intermixed systems. All other materials show the lowest reorganization energy for the dilute donor blends. This suggests that with increasing D:C_{60} mixing ratio, donor aggregation for these materials (as studied in section 8.4) affects local CT state properties. The effect of donor aggregation on the position of E_{CT} is further discussed later.

For all material systems, other than TAPC:C_{60}, the largest contribution to the energetic disorder at room temperature stems from static disorder. This is in stark contrast to the results presented by Tvingstedt et al. [119] and Göhler et al [103], which argue that static disorder plays a minor role for the linewidth broadening of small molecule D:C_{60} systems. However, in agreement with our results, other studies also determined static disorder contributions between $50 - 150$ meV for both small molecule and polymer-based blends [33], [102], [109], [51], [156], [227]. In the following paragraphs, we provide a series of suggestions to explain the observed discrepancies across literature reports.

First, we note that Tvingstedt et al. [119] and Göhler et al. [103] use electroluminescence (EL) rather than EQE to study the impact of disorder. Recent work showed that significantly lower static disorder is determined from fitting the EL [33], [103], even with valid reciprocity. The exact reasons for this observation are not clear and require further studies. However, we hypothesize that interference effects, which are experienced differently in absorption and emission as discussed in Chapter 3, could cause spectral shifts and distortions that might contribute to the observed discrepancies. Whether interference effects distort the measured trends across temperature, however, would need to be experimentally tested.

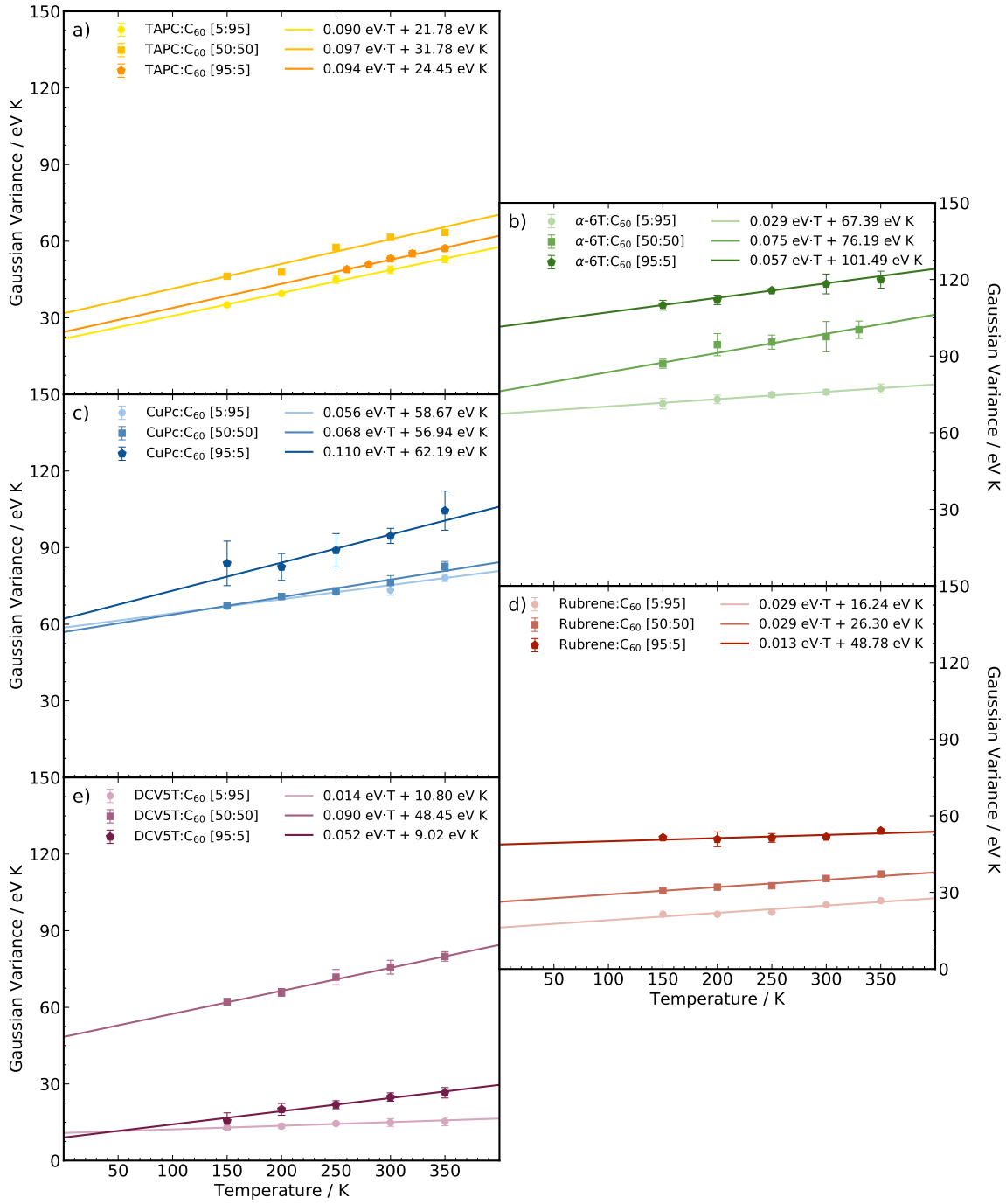


Figure 8.9: Gaussian variance, determined via MLJ theory fitting, as a function of temperature for the a) TAPC, b) α-6T, c) CuPc, d) Rubrene and d) DCV5T blends with C_{60}. The solid lines show linear fits using equation 8.4. Although not shown in the fit labels, uncertainties were determined for all fit values and are included in the discussion in the main text.

In addition, differences in the measurement conditions, and most importantly the mismatch between nominal and real sample temperatures, would also cause discrepancies. To test this hypothesis, the same sample should be placed into the same cryostat for both EQE and

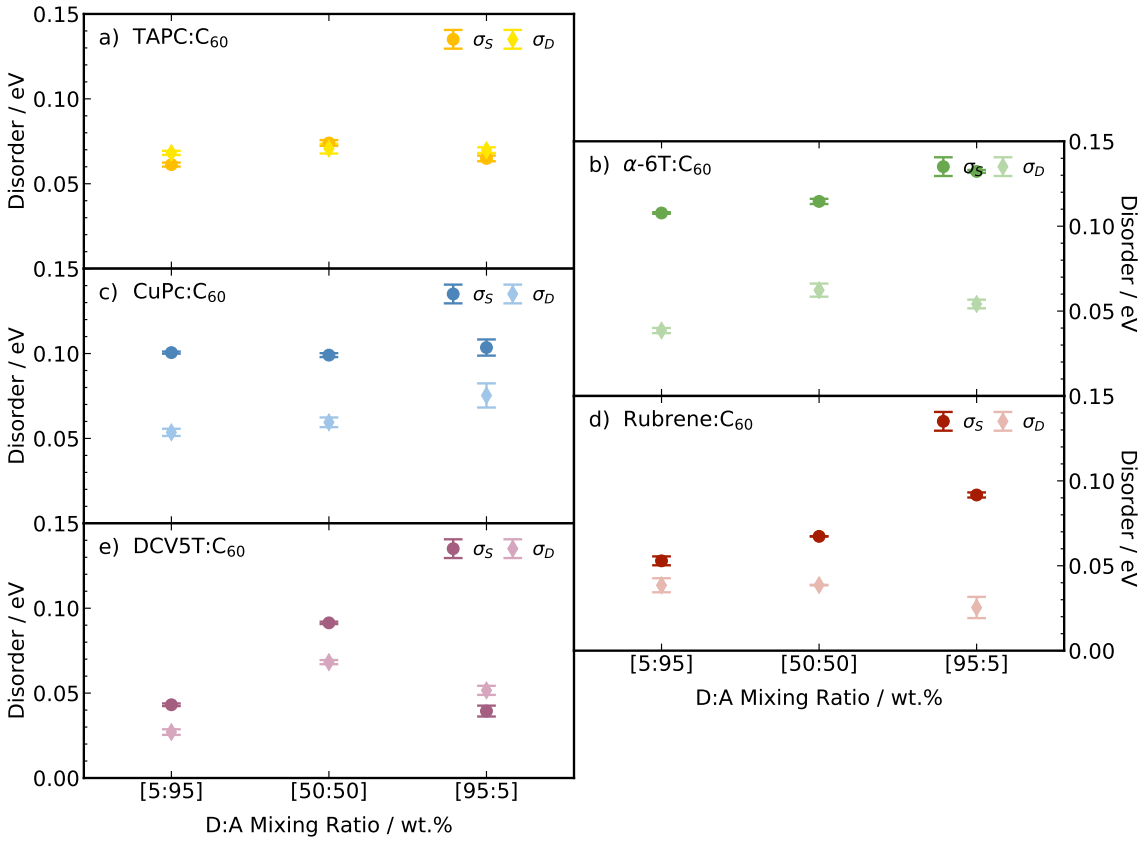


Figure 8.10: Static (σ_S) and dynamic (σ_D) disorder for the a) TAPC, b) α-6T, c) CuPc, d) Rubrene, and e) DCV5T blends with C_{60}. The dynamic disorder was calculated at 300 K.

EL measurements. Importantly, when performing EL measurements, the injection currents should be kept low to avoid Joule heating of the sample [33], [103].

We also note that certain literature reports determined static and dynamic disorder contributions that match the results presented in this thesis, but the conclusions that were drawn strongly differ from our interpretation. For instance, in the work of Benduhn [33], who studied a range of small molecule and polymer OSCs, the relative contribution of dynamic disorder to the total linewidth was found to range between $30 - 85\%$ for most samples, with many material blends showing relative contributions of $\leq 50\%$. Nonetheless, the importance of dynamic disorder (over static disorder) to the total linewidth was emphasized.

Looking back at the results presented in Figure 8.10, our work shows that static disorder is non-negligible across all material systems. While static disorder across D:C_{60} mixing ratios stays roughly constant at $61 - 74$ meV ($99 - 104$ meV) for TAPC (CuPc), σ_S gradually

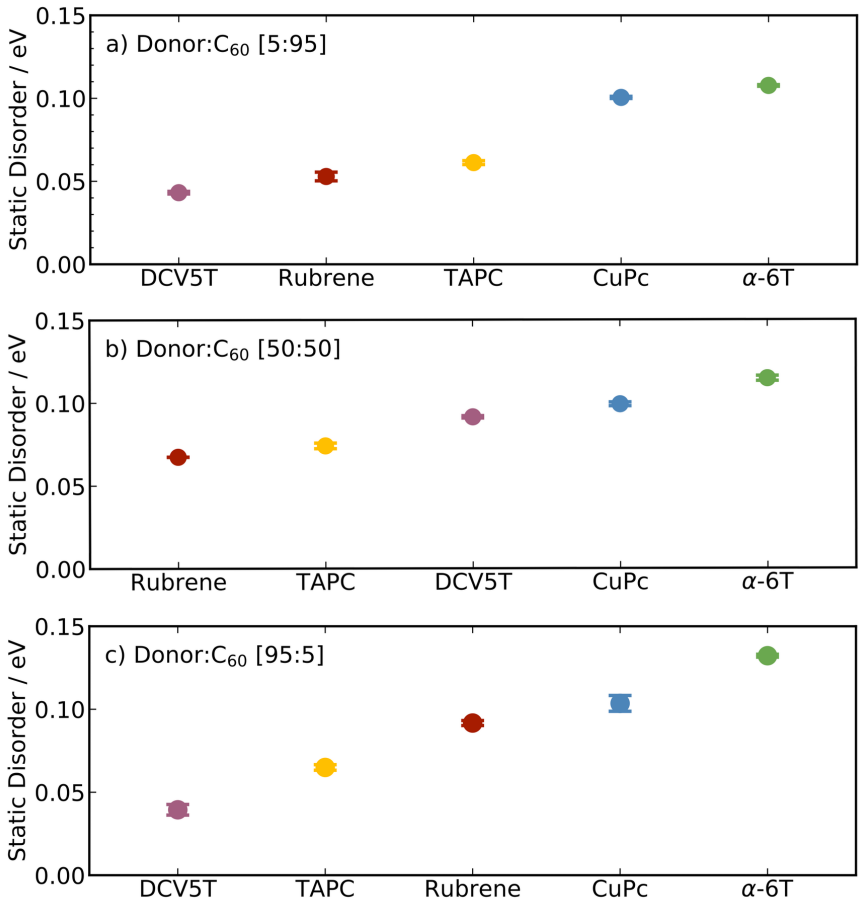


Figure 8.11: Static disorder as a function of donor molecules for a) dilute donor, b) intermixed D:C_{60}, and c) dilute acceptor blends. The static disorder contributions were organized by magnitude to easily spot trends in the ordering of the materials.

increases from $108 - 132$ meV ($53 - 92$ meV) for α-6T (Rubrene). The static disorder of the DCV5T blend peaks for the intermixed D:C_{60} system.

To easily spot trends, Figure 8.11 organizes the static disorder contributions by magnitude. For both dilute donor and dilute acceptor configurations, static disorder varies over a larger range ($\sim 40 - 120$ meV) than for the intermixed blends ($\sim 70 - 120$ meV). Compared to both dilute configurations, the minimum static disorder increases for the intermixed blends, while the maximum static disorder stays roughly constant.

At low donor content, all donors are well inter-dispersed in the C_{60} matrix, as observed via the lack of donor aggregation features in the GIWAXS (see section 8.4). This creates roughly comparable bulk morphologies across D:C_{60} blends [4], [3], [33]. The strong deviations in static disorder at low donor content suggests that the choice of donor molecule, and how

the donors interact with neighboring C_{60} molecules, impacts interfacial disorder. While no donor aggregation features were found for any of the dilute donor blends, second order C_{60} aggregation features were found for α-6T and DCV5T, and first order C_{60} features were found for TAPC and Rubrene (see Table 8.1). Looking at the ordering presented in Figure 8.11, we do not observe any correlation between C_{60} ordering and static disorder.

As discussed in section 8.4, TAPC and Rubrene form amorphous films [4], [48], while α-6T and CuPc easily aggregate at higher donor content [48]. We consistently observe the highest static disorder for the α-6T and CuPc blends, and lower static disorder for TAPC and Rubrene. Interestingly, DCV5T shows the lowest static disorder of all material systems in the dilute donor and dilute acceptor configurations, and an increased disorder for the intermixed blend. The intermixed blend is also the only blend for which DCV5T aggregation is observed. This apparent correlation between donor aggregation and static disorder is agreement with the results presented by Benduhn [33], who also observed larger static disorder for aggregating than for amorphous donors.

We rationalize this observation by considering that donor aggregation, and the formation of locally ordered regions, can introduce substantial disorder at the boundaries between crystalline domains. For α-6T, for instance, it was recently shown that boundaries between domains create electrostatic landscapes that result in strong enough interfacial driving forces for efficient CT formation across α-6T molecules to take place [230]. This paved the way to create α-6T homojunctions with decent device performances. In comparison, the lack of donor aggregation in amorphous thin films creates "homogeneously" disordered layers that do not experience the same strong, localized electrostatic shifts. This conclusion highlights the impact of structural heterogeneity on CT state disorder, as also confirmed elsewhere [156], [241], [242] [243].

8.6 Voltage Losses

In the following, we assess voltage losses according to the energetic state picture discussed in Chapter 2, and by calculating the energetic differences between E_{CT}, qV_{oc}^{rad}, and V_{oc}. As described earlier, we fit the disorder corrected E_{CT} using semi-classical MLJ theory, and

after fitting and subtracting the first singlet peak (with energy E_{S_1}). qV_{oc}^{rad} is determined using equation 2.15 and via integration of the EQE. To ensure that qV_{oc}^{rad} is not restricted by the detection limit of our EQE setup, we extend the EQE to 0.5 eV using the CT fits determined via MLJ theory. Radiative ($q\Delta V_{oc}^{rad}$) and non-radiative ($q\Delta V_{oc}^{nr}$) voltage losses are calculated as the energetic differences between E_{CT}, qV_{oc}^{rad}, and qV_{oc} respectively.

Figure 8.12 compares the energy levels and voltage losses of the different D:C_{60} blends. Note that E_{S_1} is included for completeness. As discussed earlier, the E_{CT} of the TAPC and Rubrene systems stay mostly constant with increasing donor content. In the case of Rubrene, which shows a very broad and level EQE between $\sim 1.5-2$ eV, unambiguously identifying the singlet absorption peak is challenging. As a result, the E_{S_1} shown in Figure 8.12g for the Rubrene blends were plotted as 2.23 eV, i.e. the value of the optical energy gap measured in literature from the absorbance spectrum of Rubrene thin films [244]. Especially in the dilute donor blends, this value is likely an underestimate. The biggest changes in E_{CT} are observed for the α-6T and CuPc blends, which respectively show a 0.42 eV and 0.25 eV decrease in E_{CT} from the dilute donor to the intermixed blends. This is in qualitative agreement with expected energetic shifts upon donor aggregation [33], [48], [41].

The radiative losses of all samples vary between $170-450$ meV and are within the typical ranges reported for OSCs. The non-radiative losses vary between $280-570$ meV for our samples, adding on average the largest contributions to the overall voltage losses. We would like to note that the low $q\Delta V_{oc}^{nr}$ of the Rubrene:C_{60} [95:5] blend is likely an artifact of the low signal-to-noise ratio of the EQE. We hypothesize that this leads to an underestimation of the slope of the CT absorption tail, resulting in a broad EQE tail when extrapolating to 0.5 eV and a lower estimate of qV_{oc}^{rad}. Looking at the voltage loss trends across D:C_{60} mixing ratios, we observe that the intermixed blends generally show the largest $q\Delta V_{oc}^{nr}$ and the lowest $q\Delta V_{oc}^{rad}$. Only the DCV5T:C_{60} system shows the opposite trend.

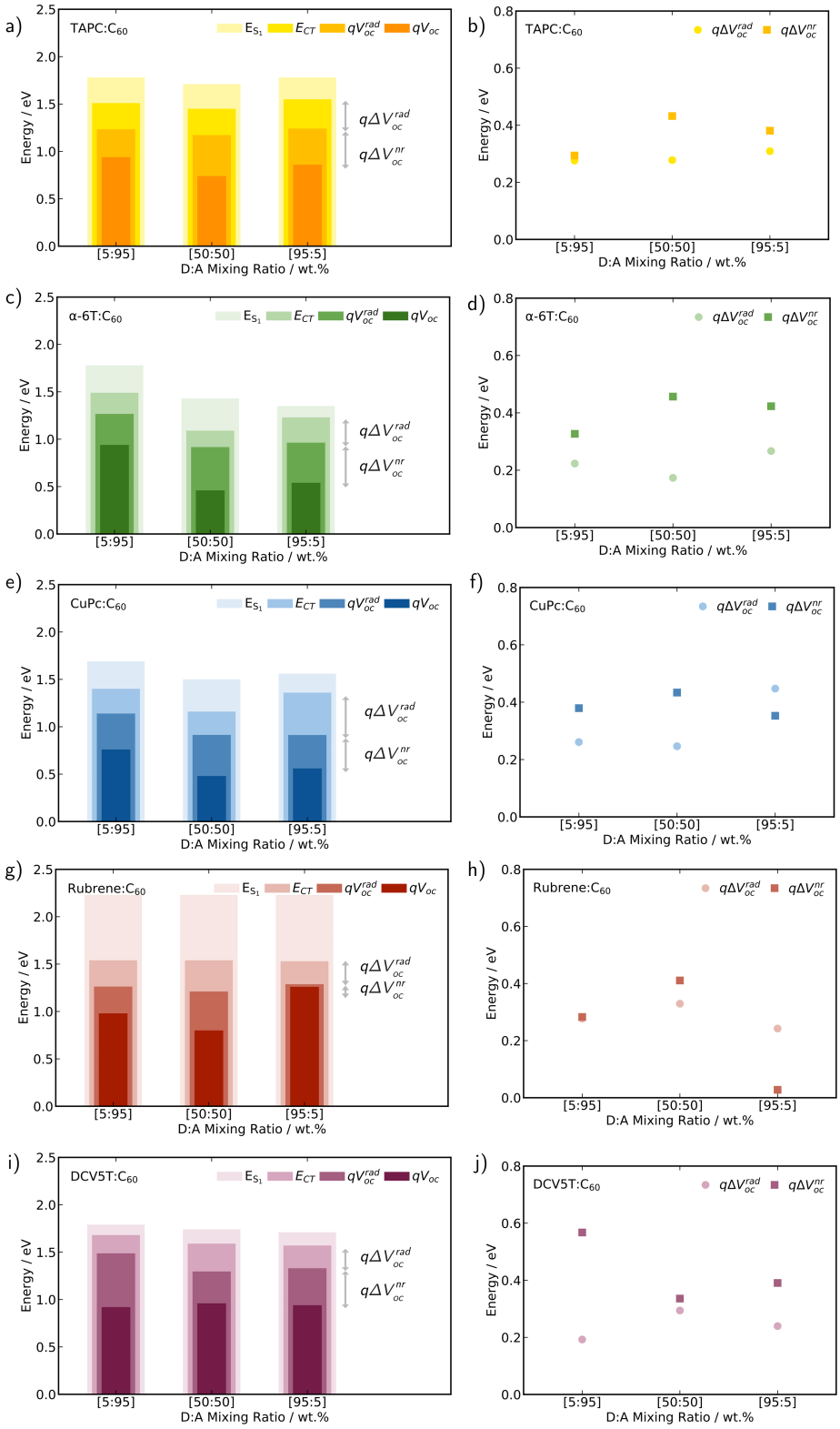


Figure 8.12: Overview of energy levels (a, c, e, g, i) and voltage losses (b, d, f, h, j) of the D:C_{60} blends studied in this work. The charge transfer state (E_{CT}) energy is fit from the EQE at 300 K and following the process outlined in the main text. The radiative limit ($q\Delta V_{oc}^{rad}$) is calculated using the EQE, and qV_{oc} was determined via the $J-V$ measurements presented earlier.

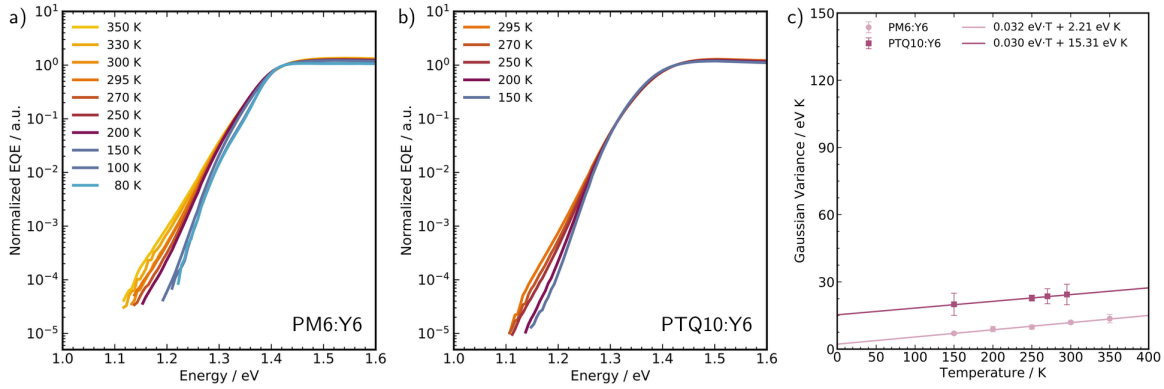


Figure 8.13: Temperature-dependent EQE of a) PM6:Y6, and b) PTQ10:Y6. The spectra were normalized to the (approximate) peak of the CT state absorption. Figure c) shows the Gaussian variance analysis of both polymer:NFA blends on the same scale as used before.

8.7 Discussion

Up until this point, we have mainly considered the impact of donor molecular properties and morphologies on electronic disorder. In the following, we expand our discussion to a general treatment of disorder in fullerene vs. non-fullerene acceptors. Figure 8.13 shows the temperature dependence of the EQE tail and the corresponding Gaussian variance analysis for polymer donors (PM6, PTQ10) blended with the non-fullerene small molecule acceptor Y6. The samples were provided by Dr. Kan Ding from North Carolina State University and were fabricated in a ZnO/polymer:Y6 (120 nm, 1:1 wt.% mixing ratio)/MoOx/Ag architecture and through spin-coating of the active layer in a nitrogen-filled glovebox.

Especially PM6:Y6 has gained significant interest over the last years as a high efficiency, low loss system [245], [65]. Looking at the EQE spectra in Figure 8.13, we observe significant linewidth narrowing of the EQE tails with decreasing temperature. In addition, we note the sharp absorption onsets, indicative of the low energetic difference between the optical gaps and the CT states of theses systems.

CT analysis in the absence of clearly defined absorption peaks is challenging and the correct fitting process for systems with low energetic offsets between E_{S_1} and E_{CT} is still debated [1]. We fit the CT states of the NFA blends following the same process outlined earlier, and by considering both singlet and CT state absorption. We determine the E_{CT} of PM6:Y6 (PTQ10:Y6) to be 1.30 eV (1.26 eV) which closely matches literature reports [246]. Inter-

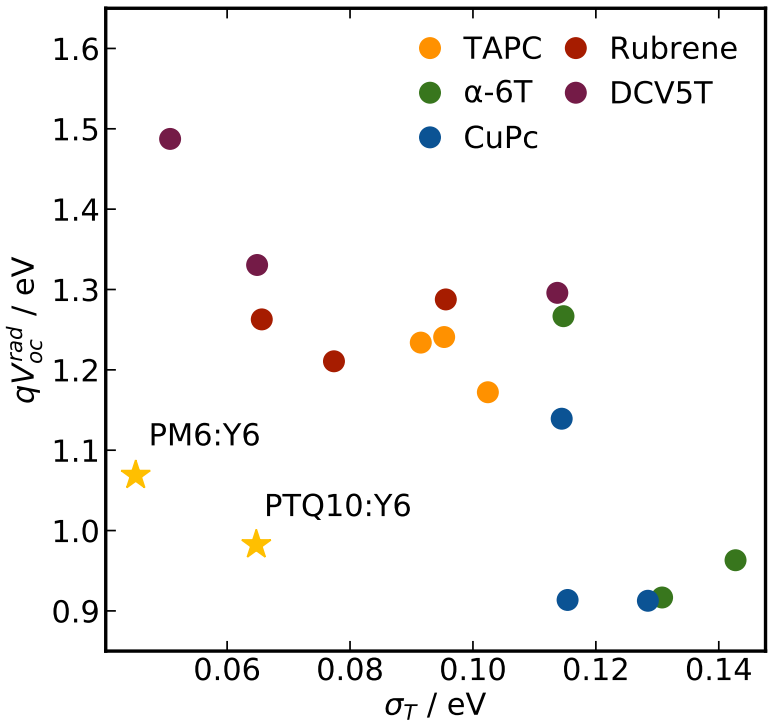


Figure 8.14: Radiative limit (qV_{oc}^{rad}) as a function of total disorder (σ_T) for all D:C_{60} blends studied in this work. Each donor system (encompassing different D:C_{60} mixing ratios) is shown with a different color, and the NFA-based blends are labelled and plotted as stars. The total disorder was calculated as the sum of static disorder and the dynamic disorder contribution at 300 K (equation 8.3).

estingly, in the case of PM6:Y6, the CT state absorption becomes resolvable from the singlet peak at very low temperatures ($80 - 100$ K), further validating our estimate of E_{CT} in this blend. The Gaussian variance analysis reveals low static disorder (20 meV for PM6:Y6 and 50 meV for PTQ10:Y6) and low dynamic disorder at room temperature (40 meV for both NFA blends). This can largely be attributed to the co-planar and rigid backbone of Y6 which limits conformational freedom and suppresses CT state disorder [91], [247].

In comparison, the spherical nature of fullerenes favors aggregation into amorphous clusters and supports the arise of energetic disorder [248], [249]. Theoretical calculations reveal that the relative contribution of the acceptor reorganization energy to the dynamic disorder is larger for fullerenes than NFAs [249]. Even though the operating principles of NFAs are not yet fully understood, low energetic disorder (both static and dynamic) clearly contribute to their improved performance [91], [247].

Figure 8.14 shows qV_{oc}^{rad} as a function of total energetic disorder for all D:C_{60} and NFA systems studied in this chapter. As expected from the model system introduced in section 8.1, qV_{oc}^{rad} follows an inverse relationship with σ_T. The same trend is observed when comparing qV_{oc}^{rad} with static disorder (Figure D.7) or dynamic disorder (Figure D.6) separately. We note, however, that compared to the model system discussed earlier, E_{CT} does not stay constant across our D:C_{60} blends. As a result, Figure 8.14 likely contains contributions from the strong linear dependence of qV_{oc}^{rad} on E_{CT} (see Figure D.8 in the Appendix). While an in-depth discussion of the impact of energetic disorder on non-radiative voltage losses is beyond the scope of this chapter, we want to point the interested reader to a recent publication by Yan et al. who observed decreasing qV_{oc}^{rad} and increasing non-radiative voltage losses with increasing static disorder.

PM6:Y6 shows the lowest energetic disorder of all studied material systems. The lower radiative limit of the NFA blends matches literature reports and translates into a lower $q\Delta V_{oc}^{nr}$ than observed for our D:C_{60} systems [250]. In any case, Figure 8.14 clearly highlights the importance of energetic disorder on the overall device performance. Consequently, future work should focus on reducing both static and dynamic disorder. This could be achieved, for instance, by suppressing the formation of heterogeneous aggregation regions within thin films, and by designing rigid molecules with low reorganization energies and sharp absorption onsets.

8.8 Conclusions

In conclusion, in this chapter, we study static and dynamic disorder for five small molecule donors paired with C_{60}. We fabricate devices with low donor, intermixed D:C_{60}, and low acceptor content to investigate the impact of molecular aggregation.

Through $J-V$ and EQE measurements at room temperature, we observe high photocurrents for the low donor and intermixed D:C_{60} blends. The low acceptor blends show low photocurrents across all material systems that can be explained by limited photon absorption and poor charge collection. As expected, we observe that the V_{oc} scales with D:C_{60} interfacial area, with most material systems showing the lowest V_{oc} for intermixed D:C_{60} blends.

Through temperature-dependent EQE measurements, and subsequent analysis of the CT absorption band via MLJ theory, static and dynamic disorder contributions are quantified for each material blend. In contrast to some recent studies [119], [103], we find an equal, or often slightly larger, contribution of static disorder to the total CT state linewidth, even at low donor content. In addition, increased static disorder is observed for donors that favor aggregation. Donor aggregation also impacts local polarization environments and induces electrostatic shifts that result in changing E_{CT} with D:C_{60} mixing ratio.

Comparing our samples to well-performing NFAs, we observe sharper absorption onsets and lower static and dynamic disorder for the studied NFA blends. Across all samples, we see strong experimental evidence for larger qV_{oc}^{rad} with lower energetic disorder. This highlights the need to reduce both static and dynamic disorder contributions in organic thin films for OPV applications.

9 | Conclusions & Outlook

This thesis investigates the photophysics of charge transfer (CT) states in organic solar cells (OSCs) via sensitive external quantum efficiency ($sEQE$) measurements. CT state properties like the reorganization energy, CT state energy (E_{CT}), and interfacial disorder were determined via experimental fitting of $sEQE$ spectra of OSCs based on small molecule donors (D) and C_{60}. The samples fabricated for this thesis were deposited via vacuum thermal evaporation of MoO_3 (3 nm), D:C_{60} (50 nm, varying mixing ratios), BPhen (8 nm), and Al (~ 100 nm). The determined CT state properties were subsequently related to free charge generation and voltage losses in the studied material systems. To summarize the main takeaways, this thesis expands the current understanding of the field in the following ways:

- Fitting both singlet and CT state absorption peaks in $sEQE$ spectra improves the reliability and reproducibility of CT state fits, especially for low offset systems without discernible CT state shoulders. In addition, an accurate analysis of singlet and CT state properties from $sEQE$ spectra provides important information on the energetic landscape in the active layers.
- The transition from the CT into the charge separated (CS) state was identified as a major bottleneck for free charge generation in low offset systems. This motivates future research of the CS state, specifically to link molecular and blend properties to the efficiency of the CT $\rightarrow$ CS transition. This knowledge would not only inform the design of new molecules with improved performance, but also aid in the search for well-performing donor-acceptor combinations. Engineering molecular quadruple moments, for instance, can provide an effective route to reducing CT dissociation barriers.
- Contrary to what is often stated for evaporated blends of small molecules, static disorder was found to be significant, and often exceed the contribution of dynamic disorder in the CT linewidth. This motivates future studies of interfacial disorder in OSCs, linking bulk and interface morphologies to device performance, and finding ways to reduce disorder to decrease voltage losses. This could be achieved, for instance, by suppressing the formation of heterogeneous aggregation regions, and by designing rigid molecules with low reorganization energies and sharp absorption onsets.

Summarizing each chapter in more detail, Chapter 5 introduced the custom $sEQE$ setup built as part of this thesis. Compared to standard setups, which are usually able to measure signals across $2-3$ orders of magnitude, our $sEQE$ setup is capable of measuring signals across 7 orders of magnitude. This increased sensitivity, which is achieved through the use of a Lock-In amplifier, multiple spectral filters, and through careful optimization of the measurement conditions, allows to resolve the weak photon absorption of CT states which typically result in EQE signals between $10^{-5}-10^{-2}$. The $sEQE$ spectra are analyzed via a custom-created Python analysis program, also introduced in Chapter 5.

Chapter 6 studied dilute donor blends of F_xZnPc ($x = 0, 4, 8, 16$) and C_{60} as model systems to investigate the impact of interfacial energetic offsets on device performance, voltage losses, and the competition between free charge generation and geminate recombination. At dilute donor concentrations ($\sim$ 5 wt.%), the donor molecules are highly dispersed in the C_{60} matrix, leading to comparable morphologies across donor choices and allowing to disentangle microstructural and energetic effects. Our experimental data, coupled with density functional theory (DFT) calculations performed by collaborators, revealed that the trends in device performance upon fluorination of ZnPc can be explained by relative changes in the energetic positions of localized singlet and triplet states, as well as the CT and CS states of the blends. We showed that efficient charge separation can only be observed if CT dissociation into the CS state is faster than geminate recombination. While the reduced interfacial energetic offsets in the F_8ZnPc and F_{16}ZnPc blends lead to reduced CT state formation, CT dissociation was identified as the primary bottleneck, leading to the low photocurrents observed in these blends.

Chapter 7 builds on the results presented in Chapter 6 and studied charge separation and device performance of F_xZnPc:C_{60} blends as a function of donor fluorination and donor:C_{60} mixing ratio (ranging from $0-100$ wt.% donor concentration). Current-density voltage and $sEQE$ measurements showed that the photocurrents strongly dependent on the choice of donor molecule and donor concentration, with the ZnPc and F_4ZnPc, and the F_8ZnPc and F_{16}ZnPc blends displaying similar performance trends. Through fitting of $sEQE$ spectra using Marcus theory, we found that E_{CT} is highest for the dilute donor blends and decreases for intermixed F_xZnPc:C_{60}. This dependence of E_{CT} on donor concentration was explained

by induced polarisation (i.e. dipolar electrostatic effects) that change the donor singlet energies in the blends by the same amount as E_{CT}. As a result, CT dissociation, influenced by the quadrupole moments of the donor molecules, rather than CT formation was suggested to govern the dependence of the photocurrents on donor concentration. More specifically, we hypothesized that the negative (positive) quadrupole moments of ZnPc and F_4ZnPc (F_8ZnPc and F_{16}ZnPc) lead to decreased (increased) dissociation barriers compared to the value expected from the energy levels of the isolated molecules. These results again highlight the importance of the CT $\rightarrow$ CS transition for efficient free charge generation, and suggest that engineering molecular quadrupole moments can provide an effective route to reducing CT dissociation barriers. Further experiments using transient absorption spectroscopy could provide an independent probe of our findings, and quantify the transition rates of charge transfer, exciton dissociation, and recombination.

Finally, Chapter 8 studied energetic disorder for five donor:C_{60} blends (TAPC, α-6T, CuPc, Rubrene, and DCV5T) at 5, 50, and 95 mol.% donor concentration. Through temperature-dependent $sEQE$ measurements between $150-350$ K, and subsequent analysis via Marcus-Levich-Jortner theory, we quantified the contributions of static (i.e. temperature-independent) and dynamic (i.e. temperature-dependent) disorder to the CT linewidth. Contrary to some recent studies, which argued that static disorder in small molecule OSCs is negligible, we determined static disorder contributions of $50-150$ meV for our donor:C_{60} blends, and found that static disorder often exceeds the contributions of dynamic disorder. Relating our device measurements to microstructural characterization of the active layers (performed via GIWAXS by collaborators), we observed larger static disorder for donors that favor aggregation. Future research could validate these results via microstructure simulations, and provide a more quantitative picture of cause and effect. Since energetic disorder increases both radiative and non-radiative losses, our work highlights the need to clarify the connection between molecular and blend properties, both in terms of energetics and microstructure. Here, it is important to elucidate the role of device fabrication conditions on the emergence of energetic disorder, and to identify molecular design strategies that reduce both static and dynamic disorder contributions. The latter can, for instance, be achieved through the design of molecules with rigid backbones.

Adding to the suggestions of the previous paragraphs, we briefly highlight additional recommendations and opportunities for future research. A substantial part of this thesis focused on establishing reliable and reproducible approaches to fit $sEQE$ spectra and estimate CT state properties and their uncertainties. Firstly, in the broader context of research focused on OSCs, experimental fitting of CT state absorption and emission spectra should urgently move away from "visual" alignment and evaluation of fits, as is often done in literature. Instead, fit metrics (e.g. R^2) should be employed to evaluate how well a fit describes the data. Secondly, the quantification of uncertainties, capturing both statistical variations between samples and fit uncertainties, should become a more standard (and required) component of future publications in the field. This would greatly increase the comparability and trustworthiness of fit results across literature reports. The sensitivity analysis presented in this thesis, whereby CT state properties are fit across data ranges, provides a valuable and easy-to-implement approach for estimating fit uncertainties.

Fitting CT state properties accurately is not only important for a correct calculation of voltage losses, but ultimately helps to inform molecular design. Regarding CT state models, the advent of well-performing non-fullerene acceptor (NFA) blends without discernible CT state absorption shoulders highlights the need to further develop accessible three-state models accounting for energetic hybridization between LE, CT, and ground states. Here, simple frameworks that are rooted in physical principles but do not require advanced simulations would be hugely beneficial to clarify the working mechansism of low offset NFAs. In addition, further room for improvement exists for developing three-state models that account for energetic disorder, or four-state models that also include the CS state. Especially if these models easily relate to molecular properties, valuable insight could be gained to direct the development of novel molecules with improved performance. This is especially important for the design of NFAs, which show great potential for increasing the power conversion efficiencies of OSCs beyond 20% for the first time. Here, a further reduction of voltage losses is key for increasing the competitiveness of OSCs with other PV technologies.

Bibliography

[1] A. Jungbluth, P. Kaienburg, and M. Riede, "Charge transfer state characterization and voltage losses of organic solar cells," *Journal of Physics: Materials*, vol. 5, p. 024002, Jan 2022.

[2] P. Kaienburg, A. Jungbluth, I. Habib, S. V. Kesava, M. Nyman, and M. Riede, "Assessing the photovoltaic quality of vacuum-thermal evaporated organic semiconductor blends," *Advanced Materials*, p. 2107584, Dec 2021.

[3] I. Ramirez, A. Privitera, S. Karuthedath, A. Jungbluth, J. Benduhn, A. Sperlich, D. Spoltore, K. Vandewal, F. Laquai, and M. Riede, "The role of spin in the degradation of organic photovoltaics," *Nature Communications*, vol. 12, Jan 2021.

[4] G. J. Moore, M. Causa', J. F. M. Hardigree, S. Karuthedath, I. Ramirez, A. Jungbluth, F. Laquai, M. Riede, and N. Banerji, "Ultrafast charge dynamics in dilute-donor versus highly intermixed TAPC:C60 organic solar cell blends," *The Journal of Physical Chemistry Letters*, vol. 11, pp. 5610–5617, Jun 2020.

[5] P. R. Shukla, J. Skea, R. Slade, A. Al Khourdajie, R. van Diemen, D. McCollum, M. Pathak, S. Some, P. Vyas, R. Fradera, M. Belkacemi, A. Hasija, G. Lisboa, S. Luz and J. Malley, "Climate Change 2022: Mitigation of Climate Change. Contribution of Working Group III to the Sixth Assessment Report of the Intergovernmental Panel on Climate Change," 2022.

[6] M. R. Hannah Ritchie and P. Rosado, "CO2 and Greenhouse Gas Emissions," *Our World in Data*, 2020.

[7] "Paris Agreement," *United Nations Treaty Collection, Chapter XXVII 7. d*, Dec 2015.

[8] L. Hammarström, "Overview: Capturing the sun for energy production," *AMBIO*, vol. 41, pp. 103–107, Mar 2012.

[9] "Photovoltaics Report," *Fraunhofer Institute for Solar Energy Systems*, Feb 2021.

[10] L. C. Andreani, A. Bozzola, P. Kowalczewski, M. Liscidini, and L. Redorici, "Silicon

solar cells: toward the efficiency limits," *Advances in Physics: X*, vol. 4, p. 1548305, Dec 2018.

[11] "World Energy Outlook 2020," *International Energy Agency*, Oct 2020.

[12] "Climate at a Glance: Global Time Series," *NOAA National Centers for Environmental Information*, Jul 2022.

[13] M. Riede, D. Spoltore, and K. Leo, "Organic solar cells - the path to commercial success," *Advanced Energy Materials*, vol. 11, p. 2002653, Nov 2020.

[14] B. Qu and S. R. Forrest, "Continuous roll-to-roll fabrication of organic photovoltaic cells via interconnected high-vacuum and low-pressure organic vapor phase deposition systems," *Applied Physics Letters*, vol. 113, p. 053302, Jul 2018.

[15] R. Abbel, Y. Galagan, and P. Groen, "Roll-to-roll fabrication of solution processed electronics," *Advanced Engineering Materials*, vol. 20, p. 1701190, Apr 2018.

[16] J. Zhang, G. Xu, F. Tao, G. Zeng, M. Zhang, Y. M. Yang, Y. Li, and Y. Li, "Highly efficient semitransparent organic solar cells with color rendering index approaching 100," *Advanced Materials*, vol. 31, p. 1807159, Jan 2019.

[17] J. Benduhn, K. Tvingstedt, F. Piersimoni, S. Ullbrich, Y. Fan, M. Tropiano, K. A. McGarry, O. Zeika, M. Riede, C. J. Douglas, S. Barlow, S. R. Marder, D. Neher, D. Spoltore, and K. Vandewal, "Intrinsic non-radiative voltage losses in fullerene-based organic solar cells," *Nature Energy*, vol. 2, Apr 2017.

[18] W. Tress, "Organic Solar Cells," *Springer International Publishing*, 2014.

[19] A. Köhler and H. Bässler, "Electronic Processes in Organic Semiconductors," *Wiley-VCH Verlag GmbH & Co. KGaA*, May 2015.

[20] U. Rau, "Reciprocity relation between photovoltaic quantum efficiency and electroluminescent emission of solar cells," *Physical Review B*, vol. 76, Aug 2007.

[21] U. Rau, B. Blank, T. C. M. Müller, and T. Kirchartz, "Efficiency potential of photovoltaic materials and devices unveiled by detailed-balance analysis," *Physical Review Applied*, vol. 7, Apr 2017.

[22] K. Vandewal, A. Gadisa, W. D. Oosterbaan, S. Bertho, F. Banishoeib, I. V. Severen, L. Lutsen, T. J. Cleij, D. Vanderzande, and J. V. Manca, "The relation between open-circuit voltage and the onset of photocurrent generation by charge-transfer absorption in polymer:fullerene bulk heterojunction solar cells," *Advanced Functional Materials*, vol. 18, pp. 2064–2070, Jul 2008.

[23] K. Vandewal, K. Tvingstedt, A. Gadisa, O. Inganäs, and J. V. Manca, "On the origin of the open-circuit voltage of polymer-fullerene solar cells," *Nature Materials*, vol. 8, pp. 904–909, Oct 2009.

[24] K. Vandewal, K. Tvingstedt, A. Gadisa, O. Inganäs, and J. V. Manca, "Relating the open-circuit voltage to interface molecular properties of donor:acceptor bulk heterojunction solar cells," *Physical Review B*, vol. 81, Mar 2010.

[25] H. Haken and H. C. Wolf, "Molekülphysik und Quantenchemie," *Springer-Verlag*, 2006.

[26] W. Demtröder, "Experimentalphysik 3," *Springer Berlin Heidelberg*, 2010.

[27] E. Condon, "A theory of intensity distribution in band systems," *Physical Review*, vol. 28, pp. 1182–1201, Dec 1926.

[28] E. U. Condon, "Nuclear motions associated with electron transitions in diatomic molecules," *Physical Review*, vol. 32, pp. 858–872, Dec 1928.

[29] I. R. Gould, D. Noukakis, L. Gomez-Jahn, R. H. Young, J. L. Goodman, and S. Farid, "Radiative and nonradiative electron transfer in contact radical-ion pairs," *Chemical Physics*, vol. 176, pp. 439–456, Oct 1993.

[30] J. A. Bartelt, D. Lam, T. M. Burke, S. M. Sweetnam, and M. D. McGehee, "Charge-carrier mobility requirements for bulk heterojunction solar cells with high fill factor and external quantum efficiency $> 90\%$," *Advanced Energy Materials*, vol. 5, p. 1500577, Jun 2015.

[31] J.-L. Bredas, "Mind the gap!," *Mater. Horiz.*, vol. 1, no. 1, pp. 17–19, 2014.

[32] T. Koopmans, "Über die Zuordnung von Wellenfunktionen und Eigenwerten zu den Einzelnen Elektronen Eines Atoms," *Physica*, vol. 1, pp. 104–113, Jan 1934.

[33] J. Benduhn, *Intermolecular Charge-transfer States in Organic Optoelectronic Devices*. PhD thesis, Technische Universität Dresden, 2019.

[34] M. Schwarze, W. Tress, B. Beyer, F. Gao, R. Scholz, C. Poelking, K. Ortstein, A. A. Günther, D. Kasemann, D. Andrienko, and K. Leo, "Band structure engineering in organic semiconductors," *Science*, vol. 352, pp. 1446–1449, Jun 2016.

[35] H. Yoshida, K. Yamada, J. Tsutsumi, and N. Sato, "Complete description of ionization energy and electron affinity in organic solids: Determining contributions from electronic polarization, energy band dispersion, and molecular orientation," *Physical Review B*, vol. 92, Aug 2015.

[36] C. Poelking and D. Andrienko, "Design rules for organic donor–acceptor heterojunctions: Pathway for charge splitting and detrapping," *Journal of the American Chemical Society*, vol. 137, pp. 6320–6326, May 2015.

[37] R. Warren, *Energy levels in organic semiconductors: tuning and doping*. PhD thesis, University of Oxford, 2020.

[38] G. Maitland, M. Rigby, E. Smith, W. Wakeham, and D. Henderson, "Intermolecular forces: Their origin and determination," *Physics Today*, vol. 36, pp. 57–58, Apr 1983.

[39] N. Sato, K. Seki, and H. Inokuchi, "Polarization energies of organic solids determined by ultraviolet photoelectron spectroscopy," *Journal of the Chemical Society, Faraday Transactions 2*, vol. 77, no. 9, p. 1621, 1981.

[40] A. Privitera, G. Londi, M. Riede, G. D'Avino, and D. Beljonne, "Molecular quadrupole moments promote ground-state charge generation in doped organic semiconductors," *Advanced Functional Materials*, vol. 30, p. 2004600, Sep 2020.

[41] M. Schwarze, K. S. Schellhammer, K. Ortstein, J. Benduhn, C. Gaul, A. Hinderhofer, L. P. Toro, R. Scholz, J. Kublitski, S. Roland, M. Lau, C. Poelking, D. Andrienko, G. Cuniberti, F. Schreiber, D. Neher, K. Vandewal, F. Ortmann, and K. Leo, "Impact of molecular quadrupole moments on the energy levels at organic heterojunctions," *Nature Communications*, vol. 10, June 2019.

[42] P. Bounds and R. Munn, "Polarization energy of a localized charge in a molecular crystal. II. charge-quadrupole energy," *Chemical Physics*, vol. 59, pp. 41–45, Jul 1981.

[43] R. R. Lunt, N. C. Giebink, A. A. Belak, J. B. Benziger, and S. R. Forrest, "Exciton diffusion lengths of organic semiconductor thin films measured by spectrally resolved photoluminescence quenching," *Journal of Applied Physics*, vol. 105, p. 053711, Mar 2009.

[44] J. Meiss, M. Hermenau, W. Tress, C. Schuenemann, F. Selzer, M. Hummert, J. Alex, G. Lackner, K. Leo, and M. Riede, "Tetrapropyl-tetraphenyl-diindenoperylene derivative as a green absorber for high-voltage stable organic solar cells," *Physical Review B*, vol. 83, Apr 2011.

[45] C. W. Tang, "Two-layer organic photovoltaic cell," *Applied Physics Letters*, vol. 48, pp. 183–185, Jan 1986.

[46] Y. Terao, H. Sasabe, and C. Adachi, "Correlation of hole mobility, exciton diffusion length, and solar cell characteristics in phthalocyanine/fullerene organic solar cells," *Applied Physics Letters*, vol. 90, p. 103515, Mar 2007.

[47] R. R. Lunt, J. B. Benziger, and S. R. Forrest, "Relationship between crystalline order and exciton diffusion length in molecular organic semiconductors," *Advanced Materials*, vol. 22, pp. 1233–1236, Mar 2010.

[48] K. R. Graham, G. O. N. Ndjawa, S. M. Conron, R. Munir, K. Vandewal, J. J. Chen, S. Sweetnam, M. E. Thompson, A. Salleo, M. D. McGehee, and A. Amassian, "The roles of structural order and intermolecular interactions in determining ionization energies and charge-transfer state energies in organic semiconductors," *Advanced Energy Materials*, vol. 6, p. 1601211, Aug 2016.

[49] M. Zhang, H. Wang, H. Tian, Y. Geng, and C. W. Tang, "Bulk heterojunction photovoltaic cells with low donor concentration," *Advanced Materials*, vol. 23, pp. 4960–4964, Sep 2011.

[50] L. Ye, H. Hu, M. Ghasemi, T. Wang, B. A. Collins, J.-H. Kim, K. Jiang, J. H. Carpenter, H. Li, Z. Li, T. McAfee, J. Zhao, X. Chen, J. L. Y. Lai, T. Ma, J.-L. Bredas,

H. Yan, and H. Ade, "Quantitative relations between interaction parameter, miscibility and function in organic solar cells," *Nature Materials*, vol. 17, pp. 253–260, Feb 2018.

[51] T. M. Burke, S. Sweetnam, K. Vandewal, and M. D. McGehee, "Beyond Langevin Recombination: How Equilibrium Between Free Carriers and Charge Transfer States Determines the Open-Circuit Voltage of Organic Solar Cells," *Advanced Energy Materials*, vol. 5, p. 1500123, Apr 2015.

[52] K. Vandewal, J. Widmer, T. Heumueller, C. J. Brabec, M. D. McGehee, K. Leo, M. Riede, and A. Salleo, "Increased open-circuit voltage of organic solar cells by reduced donor-acceptor interface area," *Advanced Materials*, vol. 26, pp. 3839–3843, Mar 2014.

[53] D. Spoltore, A. Hofacker, J. Benduhn, S. Ullbrich, M. Nyman, O. Zeika, S. Schellhammer, Y. Fan, I. Ramirez, S. Barlow, M. Riede, S. R. Marder, F. Ortmann, and K. Vandewal, "Hole transport in low-donor-content organic solar cells," *The Journal of Physical Chemistry Letters*, vol. 9, pp. 5496–5501, Sep 2018.

[54] S. Karuthedath, J. Gorenflot, Y. Firdaus, N. Chaturvedi, C. S. P. D. Castro, G. T. Harrison, J. I. Khan, A. Markina, A. H. Balawi, T. A. D. P. na, W. Liu, R.-Z. Liang, A. Sharma, S. H. K. Paleti, W. Zhang, Y. Lin, E. Alarousu, S. Lopatin, D. H. Anjum, P. M. Beaujuge, S. D. Wolf, I. McCulloch, T. D. Anthopoulos, D. Baran, D. Andrienko, and F. Laquai, "Intrinsic efficiency limits in low-bandgap non-fullerene acceptor organic solar cells," *Nature Materials*, vol. 20, pp. 378–384, Oct 2020.

[55] W. Li, S. Zeiske, O. J. Sandberg, D. B. Riley, P. Meredith, and A. Armin, "Organic solar cells with near-unity charge generation yield," *Energy &amp Environmental Science*, vol. 14, no. 12, pp. 6484–6493, 2021.

[56] K. Vandewal, S. Albrecht, E. T. Hoke, K. R. Graham, J. Widmer, J. D. Douglas, M. Schubert, W. R. Mateker, J. T. Bloking, G. F. Burkhard, A. Sellinger, J. M. J. Fréchet, A. Amassian, M. Riede, M. D. McGehee, D. Neher, and A. Salleo, "Efficient charge generation by relaxed charge-transfer states at organic interfaces," *Nature Materials*, vol. 13, pp. 63–68, Nov 2013.

[57] K. Kawashima, Y. Tamai, H. Ohkita, I. Osaka, and K. Takimiya, "High-efficiency polymer solar cells with small photon energy loss," *Nature Communications*, vol. 6, Dec 2015.

[58] W. Li, K. H. Hendriks, A. Furlan, M. M. Wienk, and R. A. J. Janssen, "High quantum efficiencies in polymer solar cells at energy losses below 0.6 eV," *Journal of the American Chemical Society*, vol. 137, pp. 2231–2234, Feb 2015.

[59] X. Ma, J. Wang, J. Gao, Z. Hu, C. Xu, X. Zhang, and F. Zhang, "Achieving 17.4% efficiency of ternary organic photovoltaics with two well-compatible nonfullerene acceptors for minimizing energy loss," *Advanced Energy Materials*, p. 2001404, Jun 2020.

[60] Y. Cui, H. Yao, J. Zhang, K. Xian, T. Zhang, L. Hong, Y. Wang, Y. Xu, K. Ma, C. An, C. He, Z. Wei, F. Gao, and J. Hou, "Single-junction organic photovoltaic cells with approaching 18% efficiency," *Advanced Materials*, vol. 32, p. 1908205, Mar 2020.

[61] Q. Liu, Y. Jiang, K. Jin, J. Qin, J. Xu, W. Li, J. Xiong, J. Liu, Z. Xiao, K. Sun, S. Yang, X. Zhang, and L. Ding, "18% efficiency organic solar cells," *Science Bulletin*, vol. 65, pp. 272–275, Feb 2020.

[62] H. Bässler and A. Köhler, ""Hot or cold": how do charge transfer states at the donor-acceptor interface of an organic solar cell dissociate?," *Physical Chemistry Chemical Physics*, vol. 17, no. 43, pp. 28451–28462, 2015.

[63] C. J. Brabec, G. Zerza, G. Cerullo, S. D. Silvestri, S. Luzzati, J. C. Hummelen, and S. Sariciftci, "Tracing photoinduced electron transfer process in conjugated polymer/fullerene bulk heterojunctions in real time," *Chemical Physics Letters*, vol. 340, pp. 232–236, Jun 2001.

[64] A. Rao, P. C. Y. Chow, S. Gélinas, C. W. Schlenker, C.-Z. Li, H.-L. Yip, A. K.-Y. Jen, D. S. Ginger, and R. H. Friend, "The role of spin in the kinetic control of recombination in organic photovoltaics," *Nature*, vol. 500, pp. 435–439, Aug 2013.

[65] A. J. Gillett, A. Privitera, R. Dilmurat, A. Karki, D. Qian, A. Pershin, G. Londi, W. K. Myers, J. Lee, J. Yuan, S.-J. Ko, M. Riede, F. Gao, G. C. Bazan, A. Rao, T.-Q. Nguyen,

D. Beljonne, and R. H. Friend, "The role of charge recombination to triplet excitons in organic solar cells," *Nature*, vol. 597, pp. 666–671, Sep 2021.

[66] M. Langevin, "Recombinaison et diffusion des ions gazeux," *Journal de Physique Théorique et Appliquée*, vol. 4, no. 1, pp. 322–333, 1905.

[67] G. Adriaenssens and V. Arkhipov, "Non-Langevin recombination in disordered materials with random potential distributions," *Solid State Communications*, vol. 103, pp. 541–543, Sep 1997.

[68] A. Pivrikas, G. Juška, A. J. Mozer, M. Scharber, K. Arlauskas, N. S. Sariciftci, H. Stubb, and R. Österbacka, "Bimolecular recombination coefficient as a sensitive testing parameter for low-mobility solar-cell materials," *Physical Review Letters*, vol. 94, May 2005.

[69] W. Shockley, "The theory of p-n junctions in semiconductors and p-n junction transistors," *Bell System Technical Journal*, vol. 28, pp. 435–489, Jul 1949.

[70] R. A. Street, M. Schoendorf, A. Roy, and J. H. Lee, "Interface state recombination in organic solar cells," *Physical Review B*, vol. 81, May 2010.

[71] P. Schilinsky, C. Waldauf, J. Hauch, and C. J. Brabec, "Simulation of light intensity dependent current characteristics of polymer solar cells," *Journal of Applied Physics*, vol. 95, pp. 2816–2819, Mar 2004.

[72] P. Kumar, S. C. Jain, V. Kumar, S. Chand, and R. P. Tandon, "A model for the current-voltage characteristics of organic bulk heterojunction solar cells," *Journal of Physics D: Applied Physics*, vol. 42, p. 055102, Feb 2009.

[73] A. M. Goodman and A. Rose, "Double extraction of uniformly generated electron-hole pairs from insulators with noninjecting contacts," *Journal of Applied Physics*, vol. 42, pp. 2823–2830, Jun 1971.

[74] T. Kirchartz, V. Huhn, A. Gerber, B. E. Pieters, and U. Rau, "Electroluminescence analysis of solar cells and solar modules," in *Advanced Characterization Techniques for Thin Film Solar Cells*, pp. 71–92, Wiley-VCH Verlag GmbH & Co. KGaA, Jul 2016.

[75] T. Unold and L. Gütay, "Photoluminescence analysis of thin-film solar cells," in *Advanced Characterization Techniques for Thin Film Solar Cells*, pp. 275–297, Wiley-VCH Verlag GmbH & Co. KGaA, Jul 2016.

[76] L. Perdigón-Toro, L. Q. Phuong, S. Zeiske, K. Vandewal, A. Armin, S. Shoaee, and D. Neher, "Excitons Dominate the Emission from PM6:Y6 Solar Cells, but This Does Not Help the Open-Circuit Voltage of the Device," *ACS Energy Letters*, vol. 6, pp. 557–564, Jan 2021.

[77] J. Yao, T. Kirchartz, M. S. Vezie, M. A. Faist, W. Gong, Z. He, H. Wu, J. Troughton, T. Watson, D. Bryant, and J. Nelson, "Quantifying losses in open-circuit voltage in solution-processable solar cells," *Physical Review Applied*, vol. 4, Jul 2015.

[78] W. Gong, M. A. Faist, N. J. Ekins-Daukes, Z. Xu, D. D. C. Bradley, J. Nelson, and T. Kirchartz, "Influence of energetic disorder on electroluminescence emission in polymer:fullerene solar cells," *Physical Review B*, vol. 86, Jul 2012.

[79] A. Armin, N. Zarrabi, O. J. Sandberg, C. Kaiser, S. Zeiske, W. Li, and P. Meredith, "Limitations of charge transfer state parameterization using photovoltaic external quantum efficiency," *Advanced Energy Materials*, vol. 10, p. 2001828, Sep 2020.

[80] T. Kirchartz, J. Nelson, and U. Rau, "Reciprocity between charge injection and extraction and its influence on the interpretation of electroluminescence spectra in organic solar cells," *Physical Review Applied*, vol. 5, May 2016.

[81] U. Rau, "Superposition and reciprocity in the electroluminescence and photoluminescence of solar cells," *IEEE Journal of Photovoltaics*, vol. 2, pp. 169–172, Apr 2012.

[82] Y. Wang, D. Qian, Y. Cui, H. Zhang, J. Hou, K. Vandewal, T. Kirchartz, and F. Gao, "Optical gaps of organic solar cells as a reference for comparing voltage losses," *Advanced Energy Materials*, vol. 8, p. 1801352, Aug 2018.

[83] K. Vandewal, J. Benduhn, and V. C. Nikolis, "How to determine optical gaps and voltage losses in organic photovoltaic materials," *Sustainable Energy and Fuels*, vol. 2, no. 3, pp. 538–544, 2018.

[84] C. Donolato, "A reciprocity theorem for charge collection," *Applied Physics Letters*, vol. 46, pp. 270–272, Feb 1985.

[85] G. Smestad and H. Ries, "Luminescence and current-voltage characteristics of solar cells and optoelectronic devices," *Solar Energy Materials and Solar Cells*, vol. 25, pp. 51–71, Jan 1992.

[86] R. T. Ross, "Some thermodynamics of photochemical systems," *The Journal of Chemical Physics*, vol. 46, pp. 4590–4593, Jun 1967.

[87] T. Kirchartz, P. Kaienburg, and D. Baran, "Figures of merit guiding research on organic solar cells," *The Journal of Physical Chemistry C*, vol. 122, pp. 5829–5843, Mar 2018.

[88] T. Kirchartz, K. Ding, and U. Rau, "Fundamental electrical characterization of thin-film solar cells," in *Advanced Characterization Techniques for Thin Film Solar Cells*, pp. 41–69, Wiley-VCH Verlag GmbH & Co. KGaA, Jul 2016.

[89] W. Shockley and H. J. Queisser, "Detailed balance limit of efficiency of p-n junction solar cells," *Journal of Applied Physics*, vol. 32, pp. 510–519, Mar 1961.

[90] M. Azzouzi, T. Kirchartz, and J. Nelson, "Factors controlling open-circuit voltage losses in organic solar cells," *Trends in Chemistry*, vol. 1, pp. 49–62, Apr 2019.

[91] A. Armin, W. Li, O. J. Sandberg, Z. Xiao, L. Ding, J. Nelson, D. Neher, K. Vandewal, S. Shoaee, T. Wang, H. Ade, T. Heumüller, C. Brabec, and P. Meredith, "A history and perspective of non-fullerene electron acceptors for organic solar cells," *Advanced Energy Materials*, vol. 11, p. 2003570, Jan 2021.

[92] X.-K. Chen, D. Qian, Y. Wang, T. Kirchartz, W. Tress, H. Yao, J. Yuan, M. Hülsbeck, M. Zhang, Y. Zou, Y. Sun, Y. Li, J. Hou, O. Inganäs, V. Coropceanu, J.-L. Bredas, and F. Gao, "A unified description of non-radiative voltage losses in organic solar cells," *Nature Energy*, vol. 6, pp. 799–806, Jun 2021.

[93] M. Azzouzi, J. Yan, T. Kirchartz, K. Liu, J. Wang, H. Wu, and J. Nelson, "Nonradiative energy losses in bulk-heterojunction organic photovoltaics," *Physical Review X*, vol. 8, Sep 2018.

[94] E. Collado-Fregoso, S. N. Pugliese, M. Wojcik, J. Benduhn, E. Bar-Or, L. P. Toro, U. Hörmann, D. Spoltore, K. Vandewal, J. M. Hodgkiss, and D. Neher, "Energy-gap law for photocurrent generation in fullerene-based organic solar cells: The case of low-donor-content blends," *Journal of the American Chemical Society*, vol. 141, pp. 2329–2341, Jan 2019.

[95] A. Classen, C. L. Chochos, L. Lüer, V. G. Gregoriou, J. Wortmann, A. Osvet, K. Forberich, I. McCulloch, T. Heumüller, and C. J. Brabec, "The role of exciton lifetime for charge generation in organic solar cells at negligible energy-level offsets," *Nature Energy*, vol. 5, pp. 711–719, Aug 2020.

[96] R. A. Marcus, "On the theory of oxidation-reduction reactions involving electron transfer. i," *The Journal of Chemical Physics*, vol. 24, pp. 966–978, May 1956.

[97] R. A. Marcus, "On the theory of oxidation-reduction reactions involving electron transfer. II. applications to data on the rates of isotopic exchange reactions," *The Journal of Chemical Physics*, vol. 26, pp. 867–871, Apr 1957.

[98] R. A. Marcus, "Chemical and electrochemical electron-transfer theory," *Annual Review of Physical Chemistry*, vol. 15, pp. 155–196, Oct 1964.

[99] R. A. Marcus, "Theory, experiment, and reaction rates. a personal view," *The Journal of Physical Chemistry*, vol. 90, pp. 3460–3465, Jul 1986.

[100] R. A. Marcus, "Electron transfer reactions in chemistry. theory and experiment," *Reviews of Modern Physics*, vol. 65, pp. 599–610, Jul 1993.

[101] J. Jortner, "Temperature dependent activation energy for electron transfer between biological molecules," *The Journal of Chemical Physics*, vol. 64, pp. 4860–4867, Jun 1976.

[102] T. Unger, S. Wedler, F.-J. Kahle, U. Scherf, H. Bässler, and A. Köhler, "The impact of driving force and temperature on the electron transfer in donor-acceptor blend systems," *The Journal of Physical Chemistry C*, vol. 121, pp. 22739–22752, Oct 2017.

[103] C. Göhler, M. Saladina, Y. Wang, D. Spoltore, J. Benduhn, K. Leo, and C. Deibel, "Temperature-dependent charge-transfer-state absorption and emission reveal the

dominant role of dynamic disorder in organic solar cells," *Physical Review Applied*, vol. 15, Jun 2021.

[104] X.-K. Chen, V. Coropceanu, and J.-L. Brédas, "Assessing the nature of the charge-transfer electronic states in organic solar cells," *Nature Communications*, vol. 9, Dec 2018.

[105] V. Coropceanu, X.-K. Chen, T. Wang, Z. Zheng, and J.-L. Brédas, "Charge-transfer electronic states in organic solar cells," *Nature Reviews Materials*, vol. 4, pp. 689–707, Sep 2019.

[106] F. D. Eisner, M. Azzouzi, Z. Fei, X. Hou, T. D. Anthopoulos, T. J. S. Dennis, M. Heeney, and J. Nelson, "Hybridization of local exciton and charge-transfer states reduces nonradiative voltage losses in organic solar cells," *Journal of the American Chemical Society*, vol. 141, pp. 6362–6374, Mar 2019.

[107] T. M. Clarke and J. R. Durrant, "Charge photogeneration in organic solar cells," *Chemical Reviews*, vol. 110, pp. 6736–6767, Jan 2010.

[108] V. May and O. Kühn, "Charge and energy transfer dynamics in molecular systems," *Wiley*, Feb 2011.

[109] F.-J. Kahle, A. Rudnick, H. Bässler, and A. Köhler, "How to interpret absorption and fluorescence spectra of charge transfer states in an organic solar cell," *Materials Horizons*, vol. 5, no. 5, pp. 837–848, 2018.

[110] A. Atxabal, T. Arnold, S. Parui, S. Hutsch, E. Zuccatti, R. Llopis, M. Cinchetti, F. Casanova, F. Ortmann, and L. E. Hueso, "Tuning the charge flow between marcus regimes in an organic thin-film device," *Nature Communications*, vol. 10, May 2019.

[111] D. C. Coffey, B. W. Larson, A. W. Hains, J. B. Whitaker, N. Kopidakis, O. V. Boltalina, S. H. Strauss, and G. Rumbles, "An optimal driving force for converting excitons into free carriers in excitonic solar cells," *The Journal of Physical Chemistry C*, vol. 116, pp. 8916–8923, Apr 2012.

[112] R. Ihly, K. S. Mistry, A. J. Ferguson, T. T. Clikeman, B. W. Larson, O. Reid, O. V.

Boltalina, S. H. Strauss, G. Rumbles, and J. L. Blackburn, "Tuning the driving force for exciton dissociation in single-walled carbon nanotube heterojunctions," *Nature Chemistry*, vol. 8, pp. 603–609, Apr 2016.

[113] L. Yuan, L. Wang, A. R. Garrigues, L. Jiang, H. V. Annadata, M. A. Antonana, E. Barco, and C. A. Nijhuis, "Transition from direct to inverted charge transport marcus regions in molecular junctions via molecular orbital gating," *Nature Nanotechnology*, vol. 13, pp. 322–329, Mar 2018.

[114] K. Tvingstedt, K. Vandewal, A. Gadisa, F. Zhang, J. Manca, and O. Inganäs, "Electroluminescence from charge transfer states in polymer solar cells," *Journal of the American Chemical Society*, vol. 131, pp. 11819–11824, Aug 2009.

[115] J. J. Benson-Smith, L. Goris, K. Vandewal, K. Haenen, J. V. Manca, D. Vanderzande, D. D. C. Bradley, and J. Nelson, "Formation of a ground-state charge-transfer complex in polyfluorene/[6,6]-phenyl-c61 butyric acid methyl ester (PCBM) blend films and its role in the function of polymer/PCBM solar cells," *Advanced Functional Materials*, vol. 17, pp. 451–457, Feb 2007.

[116] D. M. Guldi and M. Prato, "Excited-state properties of C60 fullerene derivatives," *Accounts of Chemical Research*, vol. 33, pp. 695–703, Jul 2000.

[117] E. T. Hoke, K. Vandewal, J. A. Bartelt, W. R. Mateker, J. D. Douglas, R. Noriega, K. R. Graham, J. M. J. Fréchet, A. Salleo, and M. D. McGehee, "Recombination in polymer:fullerene solar cells with open-circuit voltages approaching and exceeding 1.0 v," *Advanced Energy Materials*, vol. 3, pp. 220–230, Sep 2012.

[118] P. Wurfel, "The chemical potential of radiation," *Journal of Physics C: Solid State Physics*, vol. 15, pp. 3967–3985, Jun 1982.

[119] K. Tvingstedt, J. Benduhn, and K. Vandewal, "Temperature dependence of the spectral line-width of charge-transfer state emission in organic solar cells; static vs. dynamic disorder," *Materials Horizons*, vol. 7, no. 7, pp. 1888–1900, 2020.

[120] K. Vandewal, J. Benduhn, K. S. Schellhammer, T. Vangerven, J. E. Rückert, F. Piersimoni, R. Scholz, O. Zeika, Y. Fan, S. Barlow, D. Neher, S. R. Marder, J. Manca,

D. Spoltore, G. Cuniberti, and F. Ortmann, "Absorption tails of Donor:C60 blends provide insight into thermally activated charge-transfer processes and polaron relaxation," *Journal of the American Chemical Society*, vol. 139, pp. 1699–1704, Jan 2017.

[121] R. Meerheim, M. Furno, S. Hofmann, B. Lüssem, and K. Leo, "Quantification of energy loss mechanisms in organic light-emitting diodes," *Applied Physics Letters*, vol. 97, p. 253305, Dec 2010.

[122] K. Goushi, K. Yoshida, K. Sato, and C. Adachi, "Organic light-emitting diodes employing efficient reverse intersystem crossing for triplet-to-singlet state conversion," *Nature Photonics*, vol. 6, pp. 253–258, Mar 2012.

[123] L. Xiang, W. Fuxiang, and L. Hui, "Spectrum study of top-emitting organic light-emitting devices with micro-cavity structure," *Journal of Semiconductors*, vol. 30, p. 044007, Apr 2009.

[124] D. P. Puzzo, M. G. Helander, P. G. O'Brien, Z. Wang, N. Soheilnia, N. Kherani, Z. Lu, and G. A. Ozin, "Organic light-emitting diode microcavities from transparent conducting metal oxide photonic crystals," *Nano Letters*, vol. 11, pp. 1457–1462, Mar 2011.

[125] H. F. Wittmann, J. Grüner, R. H. Friend, G. W. C. Spencer, S. C. Moratti, and A. B. Holmes, "Microcavity effect in a single-layer polymer light-emitting diode," *Advanced Materials*, vol. 7, pp. 541–544, Jun 1995.

[126] M. Kovačič, P.-A. Will, B. Lipovšek, M. Topič, S. Lenk, S. Reineke, and J. Krč, "Coupled optical modeling for optimization of organic light-emitting diodes with external outcoupling structures," *ACS Photonics*, vol. 5, pp. 422–430, Dec 2017.

[127] G. F. Burkhard, E. T. Hoke, and M. D. McGehee, "Accounting for interference, scattering, and electrode absorption to make accurate internal quantum efficiency measurements in organic and other thin solar cells," *Advanced Materials*, vol. 22, pp. 3293–3297, May 2010.

[128] J.-F. Salinas, H.-L. Yip, C.-C. Chueh, C.-Z. Li, J.-L. Maldonado, and A. K.-Y. Jen, "Optical design of transparent thin metal electrodes to enhance in-coupling and trap-

ping of light in flexible polymer solar cells," *Advanced Materials*, vol. 24, pp. 6362–6367, Sep 2012.

[129] N. Dahan, Z. Jehl, T. Hildebrandt, J. J. Greffet, J.-F. Guillemoles, D. Lincot, and N. Naghavi, "Optical approaches to improve the photocurrent generation in Cu(In,Ga)Se2 solar cells with absorber thicknesses down to 0.5 um," vol. 112, p. 094902, Nov 2012.

[130] L. Zuo, C.-C. Chueh, Y.-X. Xu, K.-S. Chen, Y. Zang, C.-Z. Li, H. Chen, and A. K. Y. Jen, "Microcavity-enhanced light-trapping for highly efficient organic parallel tandem solar cells," *Advanced Materials*, vol. 26, pp. 6778–6784, Aug 2014.

[131] W. Yu, L. Shen, F. Meng, Y. Long, S. Ruan, and W. Chen, "Effects of the optical microcavity on the performance of ITO-free polymer solar cells with WO3/Ag/WO3 transparent electrode," *Solar Energy Materials and Solar Cells*, vol. 100, pp. 226–230, May 2012.

[132] Y. Long, "Improving optical performance of inverted organic solar cells by microcavity effect," *Applied Physics Letters*, vol. 95, p. 193301, Nov 2009.

[133] N. P. Sergeant, A. Hadipour, B. Niesen, D. Cheyns, P. Heremans, P. Peumans, and B. P. Rand, "Design of transparent anodes for resonant cavity enhanced light harvesting in organic solar cells," *Advanced Materials*, vol. 24, pp. 728–732, Jan 2012.

[134] H.-W. Lin, S.-W. Chiu, L.-Y. Lin, Z.-Y. Hung, Y.-H. Chen, F. Lin, and K.-T. Wong, "Device engineering for highly efficient top-illuminated organic solar cells with microcavity structures," *Advanced Materials*, vol. 24, pp. 2269–2272, Apr 2012.

[135] S. Ullbrich, B. Siegmund, A. Mischok, A. Hofacker, J. Benduhn, D. Spoltore, and K. Vandewal, "Fast organic near-infrared photodetectors based on charge-transfer absorption," *The Journal of Physical Chemistry Letters*, vol. 8, pp. 5621–5625, Nov 2017.

[136] B. Siegmund, A. Mischok, J. Benduhn, O. Zeika, S. Ullbrich, F. Nehm, M. Böhm, D. Spoltore, H. Fröb, C. Körner, K. Leo, and K. Vandewal, "Organic narrowband near-

infrared photodetectors based on intermolecular charge-transfer absorption," *Nature Communications*, vol. 8, Jun 2017.

[137] M. List, T. Sarkar, P. Perkhun, J. Ackermann, C. Luo, and U. Würfel, "Correct determination of charge transfer state energy from luminescence spectra in organic solar cells," *Nature Communications*, vol. 9, Sep 2018.

[138] C. Kaiser, S. Zeiske, P. Meredith, and A. Armin, "Determining ultralow absorption coefficients of organic semiconductors from the sub-bandgap photovoltaic external quantum efficiency," *Advanced Optical Materials*, vol. 8, p. 1901542, Nov 2019.

[139] A. Karki, J. Vollbrecht, A. L. Dixon, N. Schopp, M. Schrock, G. N. M. Reddy, and T.-Q. Nguyen, "Understanding the high performance of over 15% efficiency in single-junction bulk heterojunction organic solar cells," *Advanced Materials*, vol. 31, p. 1903868, Oct 2019.

[140] L. Perdigón-Toro, H. Zhang, A. Markina, J. Yuan, S. M. Hosseini, C. M. Wolff, G. Zuo, M. Stolterfoht, Y. Zou, F. Gao, D. Andrienko, S. Shoaee, and D. Neher, "Barrierless Free Charge Generation in the High-Performance PM6:Y6 Bulk Heterojunction Non-Fullerene Solar Cell," *Advanced Materials*, vol. 32, p. 1906763, Jan 2020.

[141] J. Hou, O. Inganäs, R. H. Friend, and F. Gao, "Organic solar cells based on non-fullerene acceptors," *Nature Materials*, vol. 17, pp. 119–128, Jan 2018.

[142] S. M. Menke, N. A. Ran, G. C. Bazan, and R. H. Friend, "Understanding energy loss in organic solar cells: Toward a new efficiency regime," *Joule*, vol. 2, pp. 25–35, Jan 2018.

[143] D. Baran, T. Kirchartz, S. Wheeler, S. Dimitrov, M. Abdelsamie, J. Gorman, R. S. Ashraf, S. Holliday, A. Wadsworth, N. Gasparini, P. Kaienburg, H. Yan, A. Amassian, C. J. Brabec, J. R. Durrant, and I. McCulloch, "Reduced voltage losses yield 10% efficient fullerene free organic solar cells with >1 V open circuit voltages," *Energy &amp Environmental Science*, vol. 9, no. 12, pp. 3783–3793, 2016.

[144] P. Cheng, M. Zhang, T.-K. Lau, Y. Wu, B. Jia, J. Wang, C. Yan, M. Qin, X. Lu,

and X. Zhan, "Realizing small energy loss of 0.55 eV, high open-circuit voltage >1 V and high efficiency >10% in fullerene-free polymer solar cells via energy driver," *Advanced Materials*, vol. 29, p. 1605216, Jan 2017.

[145] N. A. Ran, J. A. Love, C. J. Takacs, A. Sadhanala, J. K. Beavers, S. D. Collins, Y. Huang, M. Wang, R. H. Friend, G. C. Bazan, and T.-Q. Nguyen, "Harvesting the full potential of photons with organic solar cells," *Advanced Materials*, vol. 28, pp. 1482–1488, Dec 2015.

[146] L. Goris, K. Haenen, M. Nesládek, P. Wagner, D. Vanderzande, L. D. Schepper, J. D'haen, L. Lutsen, and J. V. Manca, "Absorption phenomena in organic thin films for solar cell applications investigated by photothermal deflection spectroscopy," *Journal of Materials Science*, vol. 40, pp. 1413–1418, Mar 2005.

[147] V. Coropceanu, J. Cornil, D. A. da Silva Filho, Y. Olivier, R. Silbey, and J.-L. Brédas, "Charge transport in organic semiconductors," *Chemical Reviews*, vol. 107, pp. 926–952, Mar 2007.

[148] J.-L. Brédas, D. Beljonne, V. Coropceanu, and J. Cornil, "Charge-transfer and energy-transfer processes in π-conjugated oligomers and polymers: A molecular picture," *Chemical Reviews*, vol. 104, pp. 4971–5004, Sep 2004.

[149] F. Fuchs, S. Schmitt, C. Walter, B. Engels, E. M. Herzig, P. Müller-Buschbaum, V. Dyakonov, and C. Deibel, "Vibrational spectroscopy of a low-band-gap donor-acceptor copolymer and blends," *The Journal of Physical Chemistry C*, vol. 121, pp. 19543–19547, Aug 2017.

[150] M. Bixon, J. Jortner, and J. W. Verhoeven, "Lifetimes for radiative charge recombination in donor-acceptor molecules," *Journal of the American Chemical Society*, vol. 116, pp. 7349–7355, Aug 1994.

[151] M. D. Newton, "Quantum chemical probes of electron-transfer kinetics: the nature of donor-acceptor interactions," *Chemical Reviews*, vol. 91, pp. 767–792, Jul 1991.

[152] C.-P. Hsu, "The electronic couplings in electron transfer and excitation energy transfer," *Accounts of Chemical Research*, vol. 42, pp. 509–518, Feb 2009.

[153] Y. Zhao and W. Liang, "Charge transfer in organic molecules for solar cells: theoretical perspective," *Chem. Soc. Rev.*, vol. 41, no. 3, pp. 1075–1087, 2012.

[154] T. Kastinen, D. A. da Silva Filho, L. Paunonen, M. Linares, L. A. R. Junior, O. Cramariuc, and T. I. Hukka, "Electronic couplings and rates of excited state charge transfer processes at poly(thiophene-co-quinoxaline)-PC71BM interfaces: two- versus multi-state treatments," *Physical Chemistry Chemical Physics*, vol. 21, no. 46, pp. 25606–25625, 2019.

[155] M. Panhans, S. Hutsch, J. Benduhn, K. S. Schellhammer, V. C. Nikolis, T. Vangerven, K. Vandewal, and F. Ortmann, "Molecular vibrations reduce the maximum achievable photovoltage in organic solar cells," *Nature Communications*, vol. 11, Mar 2020.

[156] J. Yan, E. Rezasoltani, M. Azzouzi, F. Eisner, and J. Nelson, "Influence of static disorder of charge transfer state on voltage loss in organic photovoltaics," *Nature Communications*, vol. 12, Jun 2021.

[157] Z. Zheng, N. R. Tummala, T. Wang, V. Coropceanu, and J.-L. Brédas, "Charge-transfer states at organic-organic interfaces: Impact of static and dynamic disorders," *Advanced Energy Materials*, vol. 9, p. 1803926, Feb 2019.

[158] B. P. Rand, D. Cheyns, K. Vasseur, N. C. Giebink, S. Mothy, Y. Yi, V. Coropceanu, D. Beljonne, J. Cornil, J.-L. Brédas, and J. Genoe, "The impact of molecular orientation on the photovoltaic properties of a phthalocyanine/fullerene heterojunction," *Advanced Functional Materials*, vol. 22, pp. 2987–2995, Apr 2012.

[159] X.-K. Chen, M. K. Ravva, H. Li, S. M. Ryno, and J.-L. Brédas, "Effect of molecular packing and charge delocalization on the nonradiative recombination of charge-transfer states in organic solar cells," *Advanced Energy Materials*, vol. 6, p. 1601325, Sep 2016.

[160] J.-L. Brédas, J. E. Norton, J. Cornil, and V. Coropceanu, "Molecular understanding of organic solar cells: The challenges," *Accounts of Chemical Research*, vol. 42, pp. 1691–1699, Aug 2009.

[161] Y. L. Lin, M. A. Fusella, and B. P. Rand, "The impact of local morphology on

organic donor/acceptor charge transfer states," *Advanced Energy Materials*, vol. 8, p. 1702816, Jan 2018.

[162] F. Panzer, H. Bässler, and A. Köhler, "Temperature induced order-disorder transition in solutions of conjugated polymers probed by optical spectroscopy," *The Journal of Physical Chemistry Letters*, vol. 8, pp. 114–125, Dec 2016.

[163] D. Qian, Z. Zheng, H. Yao, W. Tress, T. R. Hopper, S. Chen, S. Li, J. Liu, S. Chen, J. Zhang, X.-K. Liu, B. Gao, L. Ouyang, Y. Jin, G. Pozina, I. A. Buyanova, W. M. Chen, O. Inganäs, V. Coropceanu, J.-L. Bredas, H. Yan, J. Hou, F. Zhang, A. A. Bakulin, and F. Gao, "Design rules for minimizing voltage losses in high-efficiency organic solar cells," *Nature Materials*, vol. 17, pp. 703–709, Jul 2018.

[164] M. E. Ziffer, S. B. Jo, H. Zhong, L. Ye, H. Liu, F. Lin, J. Zhang, X. Li, H. W. Ade, A. K.-Y. Jen, and D. S. Ginger, "Long-lived, non-geminate, radiative recombination of photogenerated charges in a polymer/small-molecule acceptor photovoltaic blend," *Journal of the American Chemical Society*, vol. 140, pp. 9996–10008, Jul 2018.

[165] S. Joseph, M. K. Ravva, and J.-L. Bredas, "Charge-transfer dynamics in the lowest excited state of a Pentacene–fullerene complex: Implications for organic solar cells," *The Journal of Physical Chemistry Letters*, vol. 8, pp. 5171–5176, Oct 2017.

[166] G. D'Avino, L. Muccioli, F. Castet, C. Poelking, D. Andrienko, Z. G. Soos, J. Cornil, and D. Beljonne, "Electrostatic phenomena in organic semiconductors: fundamentals and implications for photovoltaics," *Journal of Physics: Condensed Matter*, vol. 28, p. 433002, Sep 2016.

[167] S. Few, J. M. Frost, J. Kirkpatrick, and J. Nelson, "Influence of chemical structure on the charge transfer state spectrum of a polymer:fullerene complex," *The Journal of Physical Chemistry C*, vol. 118, pp. 8253–8261, Apr 2014.

[168] S. Stoll and A. Schweiger, "Easyspin, a comprehensive software package for spectral simulation and analysis in EPR," *Journal of Magnetic Resonance*, vol. 178, pp. 42–55, Jan 2006.

[169] J. Filik, A. W. Ashton, P. C. Y. Chang, P. A. Chater, S. J. Day, M. Drakopoulos, M. W.

Gerring, M. L. Hart, O. V. Magdysyuk, S. Michalik, A. Smith, C. C. Tang, N. J. Terrill, M. T. Wharmby, and H. Wilhelm, "Processing two-dimensional x-ray diffraction and small-angle scattering data in DAWN 2," *Journal of Applied Crystallography*, vol. 50, pp. 959–966, May 2017.

[170] D.-M. Smilgies, "Scherrer grain-size analysis adapted to grazing-incidence scattering with area detectors," *Journal of Applied Crystallography*, vol. 42, pp. 1030–1034, Oct 2009.

[171] J. I. Langford and A. J. C. Wilson, "Scherrer after sixty years: A survey and some new results in the determination of crystallite size," *Journal of Applied Crystallography*, vol. 11, pp. 102–113, Apr 1978.

[172] S. Hirata and M. Head-Gordon, "Time-dependent density functional theory within the tamm-dancoff approximation," *Chemical Physics Letters*, vol. 314, pp. 291–299, Dec 1999.

[173] E. Cho, V. Coropceanu, and J.-L. Brédas, "Electronic structure of multicomponent organic molecular materials: Evaluation of range-separated hybrid functionals," *Journal of Chemical Theory and Computation*, vol. 16, pp. 3712–3719, Apr 2020.

[174] Z. Zheng, D. A. Egger, J.-L. Brédas, L. Kronik, and V. Coropceanu, "Effect of solid-state polarization on charge-transfer excitations and transport levels at organic interfaces from a screened range-separated hybrid functional," *The Journal of Physical Chemistry Letters*, vol. 8, pp. 3277–3283, Jul 2017.

[175] H. Ren, J.-D. Chen, Y.-Q. Li, and J.-X. Tang, "Recent progress in organic photodetectors and their applications," *Advanced Science*, vol. 8, p. 2002418, Nov 2020.

[176] D. Yang, X. Zhou, and D. Ma, "Fast response organic photodetectors with high detectivity based on rubrene and c60," *Organic Electronics*, vol. 14, pp. 3019–3023, Nov 2013.

[177] Y. Wang, J. Kublitski, S. Xing, F. Dollinger, D. Spoltore, J. Benduhn, and K. Leo, "Narrowband organic photodetectors - towards miniaturized, spectroscopic sensing," *Materials Horizons*, vol. 9, no. 1, pp. 220–251, 2022.

[178] S. Zeiske, C. Kaiser, P. Meredith, and A. Armin, "Sensitivity of sub-bandgap external quantum efficiency measurements of solar cells under electrical and light bias," *ACS Photonics*, vol. 7, pp. 256–264, Dec 2019.

[179] T. yi Li, J. Benduhn, Y. Li, F. Jaiser, D. Spoltore, O. Zeika, Z. Ma, D. Neher, K. Vandewal, and K. Leo, "Boron dipyrromethene (bodipy) with meso-perfluorinated alkyl substituents as near infrared donors in organic solar cells," *Journal of Materials Chemistry A*, vol. 6, no. 38, pp. 18583–18591, 2018.

[180] V. C. Nikolis, Y. Dong, J. Kublitski, J. Benduhn, X. Zheng, C. Huang, A. C. Yüzer, M. Ince, D. Spoltore, J. R. Durrant, A. A. Bakulin, and K. Vandewal, "Field effect versus driving force: Charge generation in small-molecule organic solar cells," *Advanced Energy Materials*, vol. 10, p. 2002124, Nov 2020.

[181] M. Azzouzi, N. P. Gallop, F. Eisner, J. Yan, X. Zheng, H. Cha, Q. He, Z. Fei, M. Heeney, A. A. Bakulin, and J. Nelson, "Reconciling models of interfacial state kinetics and device performance in organic solar cells: impact of the energy offsets on the power conversion efficiency," *Energy and Environmental Science*, vol. 15, no. 3, pp. 1256–1270, 2022.

[182] J. Benduhn, F. Piersimoni, G. Londi, A. Kirch, J. Widmer, C. Koerner, D. Beljonne, D. Neher, D. Spoltore, and K. Vandewal, "Impact of triplet excited states on the open-circuit voltage of organic solar cells," *Advanced Energy Materials*, vol. 8, p. 1800451, Apr 2018.

[183] I. Ramirez, M. Causa', Y. Zhong, N. Banerji, and M. Riede, "Key tradeoffs limiting the performance of organic photovoltaics," *Advanced Energy Materials*, vol. 8, p. 1703551, May 2018.

[184] S. Li, L. Zhan, C. Sun, H. Zhu, G. Zhou, W. Yang, M. Shi, C.-Z. Li, J. Hou, Y. Li, and H. Chen, "Highly efficient fullerene-free organic solar cells operate at near zero highest occupied molecular orbital offsets," *Journal of the American Chemical Society*, vol. 141, pp. 3073–3082, Jan 2019.

[185] R. Wang, J. Yuan, R. Wang, G. Han, T. Huang, W. Huang, J. Xue, H.-C. Wang, C. Zhang, C. Zhu, P. Cheng, D. Meng, Y. Yi, K.-H. Wei, Y. Zou, and Y. Yang,

"Rational tuning of molecular interaction and energy level alignment enables high-performance organic photovoltaics," *Advanced Materials*, vol. 31, p. 1904215, Sep 2019.

[186] Y. Cui, Y. Xu, H. Yao, P. Bi, L. Hong, J. Zhang, Y. Zu, T. Zhang, J. Qin, J. Ren, Z. Chen, C. He, X. Hao, Z. Wei, and J. Hou, "Single-junction organic photovoltaic cell with 19% efficiency," *Advanced Materials*, vol. 33, p. 2102420, Aug 2021.

[187] Y. Firdaus, V. M. L. Corre, S. Karuthedath, W. Liu, A. Markina, W. Huang, S. Chattopadhyay, M. M. Nahid, M. I. Nugraha, Y. Lin, A. Seitkhan, A. Basu, W. Zhang, I. McCulloch, H. Ade, J. Labram, F. Laquai, D. Andrienko, L. J. A. Koster, and T. D. Anthopoulos, "Long-range exciton diffusion in molecular non-fullerene acceptors," *Nature Communications*, vol. 11, Oct 2020.

[188] H. Brinkmann, C. Kelting, S. Makarov, O. Tsaryova, G. Schnurpfeil, D. Wöhrle, and D. Schlettwein, "Fluorinated phthalocyanines as molecular semiconductor thin films," *physica status solidi (a)*, vol. 205, pp. 409–420, Mar 2008.

[189] M. Brendel, S. Krause, A. Steindamm, A. K. Topczak, S. Sundarraj, P. Erk, S. Höhla, N. Fruehauf, N. Koch, and J. Pflaum, "The effect of gradual fluorination on the properties of FnZnPc thin films and FnZnPc/C60 bilayer photovoltaic cells," *Advanced Functional Materials*, vol. 25, pp. 1565–1573, Feb 2015.

[190] J. Meiss, A. Merten, M. Hein, C. Schünemann, S. Schäfer, M. Tietze, C. Uhrich, M. Pfeiffer, K. Leo, and M. Riede, "Fluorinated zinc phthalocyanine as donor for efficient vacuum-deposited organic solar cells," *Advanced Functional Materials*, vol. 22, pp. 405–414, Nov 2011.

[191] K. Ding, X. Liu, and S. R. Forrest, "Charge transfer and collection in dilute organic donor-acceptor heterojunction blends," *Nano Letters*, vol. 18, pp. 3180–3184, Apr 2018.

[192] A. Melianas, V. Pranculis, D. Spoltore, J. Benduhn, O. Inganäs, V. Gulbinas, K. Vandewal, and M. Kemerink, "Charge transport in pure and mixed phases in organic solar cells," *Advanced Energy Materials*, vol. 7, p. 1700888, Jul 2017.

[193] M. L. Tietze, W. Tress, S. Pfützner, C. Schünemann, L. Burtone, M. Riede, K. Leo, K. Vandewal, S. Olthof, P. Schulz, and A. Kahn, "Correlation of open-circuit voltage and energy levels in zinc-phthalocyanine:C60 bulk heterojunction solar cells with varied mixing ratio," *Physical Review B*, vol. 88, Aug 2013.

[194] T. Lee, A. Sanzogni, N. Zhangzhou, P. L. Burn, and A. E. Mark, "Morphology of a bulk heterojunction photovoltaic cell with low donor concentration," *ACS Applied Materials and Interfaces*, vol. 10, pp. 32413–32419, Aug 2018.

[195] M. Causa, I. Ramirez, J. F. Martinez Hardigree, M. Riede, and N. Banerji, "Femtosecond dynamics of photoexcited C60 films," *The Journal of Physical Chemistry Letters*, vol. 9, no. 8, pp. 1885–1892, 2018. PMID: 29569924.

[196] I. Akimoto, M. Ashida, and K. Kan'no, "Luminescence from c60 single crystals in glassy phase under site-selective excitation," *Chemical Physics Letters*, vol. 292, pp. 561–566, Aug 1998.

[197] Y. Yi, V. Coropceanu, and J.-L. Brédas, "Exciton-dissociation and charge-recombination processes in pentacene/C60 solar cells: Theoretical insight into the impact of interface geometry," *Journal of the American Chemical Society*, vol. 131, pp. 15777–15783, Oct 2009.

[198] P. S. Vincett, E. M. Voigt, and K. E. Rieckhoff, "Phosphorescence and fluorescence of phthalocyanines," *The Journal of Chemical Physics*, vol. 55, pp. 4131–4140, Oct 1971.

[199] J. Savolainen, D. van der Linden, N. Dijkhuizen, and J. L. Herek, "Characterizing the functional dynamics of zinc phthalocyanine from femtoseconds to nanoseconds," *Journal of Photochemistry and Photobiology A: Chemistry*, vol. 196, pp. 99–105, Apr 2008.

[200] G. Orlandi and F. Negri, "Electronic states and transitions in c60 and c70 fullerenes," *Photochemical and Photobiological Sciences*, vol. 1, pp. 289–308, Apr 2002.

[201] S. Kazaoui, N. Minami, Y. Tanabe, H. J. Byrne, A. Eilmes, and P. Petelenz, "Compre-

hensive analysis of intermolecular charge transfer excited states in c60 and c70 films," *Physical Review B*, vol. 58, pp. 7689–7700, Sep 1998.

[202] C.-R. Zhang, J. S. Sears, B. Yang, S. G. Aziz, V. Coropceanu, and J.-L. Brédas, "Theoretical study of the local and charge-transfer excitations in model complexes of pentacene-C60 using tuned range-separated hybrid functionals," *Journal of Chemical Theory and Computation*, vol. 10, pp. 2379–2388, May 2014.

[203] J. Niklas, S. Beaupré, M. Leclerc, T. Xu, L. Yu, A. Sperlich, V. Dyakonov, and O. G. Poluektov, "Photoinduced dynamics of charge separation: From photosynthesis to polymer-fullerene bulk heterojunctions," *The Journal of Physical Chemistry B*, vol. 119, pp. 7407–7416, Jan 2015.

[204] J. Niklas and O. G. Poluektov, "Charge transfer processes in OPV materials as revealed by EPR spectroscopy," *Advanced Energy Materials*, vol. 7, p. 1602226, Mar 2017.

[205] A. Privitera, J. Grüne, A. Karki, W. K. Myers, V. Dyakonov, T.-Q. Nguyen, M. K. Riede, R. H. Friend, A. Sperlich, and A. J. Gillett, "Geminate and nongeminate pathways for triplet exciton formation in organic solar cells," *Advanced Energy Materials*, vol. 12, p. 2103944, Mar 2022.

[206] A. Privitera, R. Warren, G. Londi, P. Kaienburg, J. Liu, A. Sperlich, A. E. Lauritzen, O. Thimm, A. Ardavan, D. Beljonne, and M. Riede, "Electron spin as fingerprint for charge generation and transport in doped organic semiconductors," *Journal of Materials Chemistry C*, vol. 9, no. 8, pp. 2944–2954, 2021.

[207] A. F. Bartelt, C. Strothkämper, W. Schindler, K. Fostiropoulos, and R. Eichberger, "Morphology effects on charge generation and recombination dynamics at ZnPc:C60 bulk hetero-junctions using time-resolved terahertz spectroscopy," *Applied Physics Letters*, vol. 99, p. 143304, Oct 2011.

[208] M. Righetto, A. Privitera, F. Carraro, L. Bolzonello, C. Ferrante, L. Franco, and R. Bozio, "Engineering interactions in QDs-PCBM blends: a surface chemistry approach," *Nanoscale*, vol. 10, no. 25, pp. 11913–11922, 2018.

[209] C. M. Wolff, P. Caprioglio, M. Stolterfoht, and D. Neher, "Nonradiative recombination in perovskite solar cells: The role of interfaces," *Advanced Materials*, vol. 31, p. 1902762, Oct 2019.

[210] M. C. Scharber, D. Mühlbacher, M. Koppe, P. Denk, C. Waldauf, A. J. Heeger, and C. J. Brabec, "Design rules for donors in bulk-heterojunction solar cells - towards 10% energy-conversion efficiency," *Advanced Materials*, vol. 18, pp. 789–794, Mar 2006.

[211] S. Duhm, G. Heimel, I. Salzmann, H. Glowatzki, R. L. Johnson, A. Vollmer, J. P. Rabe, and N. Koch, "Orientation-dependent ionization energies and interface dipoles in ordered molecular assemblies," *Nature Materials*, vol. 7, pp. 326–332, Feb 2008.

[212] F. Piersimoni, S. Chambon, K. Vandewal, R. Mens, T. Boonen, A. Gadisa, M. Izquierdo, S. Filippone, B. Ruttens, J. D'Haen, N. Martin, L. Lutsen, D. Vanderzande, P. Adriaensens, and J. V. Manca, "Influence of fullerene ordering on the energy of the charge-transfer state and open-circuit voltage in polymer:fullerene solar cells," *The Journal of Physical Chemistry C*, vol. 115, pp. 10873–10880, May 2011.

[213] F. C. Jamieson, E. B. Domingo, T. McCarthy-Ward, M. Heeney, N. Stingelin, and J. R. Durrant, "Fullerene crystallisation as a key driver of charge separation in polymer/fullerene bulk heterojunction solar cells," *Chem. Sci.*, vol. 3, no. 2, pp. 485–492, 2012.

[214] D. Veldman, O. Ipek, S. C. J. Meskers, J. Sweelssen, M. M. Koetse, S. C. Veenstra, J. M. Kroon, S. S. van Bavel, J. Loos, and R. A. J. Janssen, "Compositional and electric field dependence of the dissociation of charge transfer excitons in alternating polyfluorene copolymer/fullerene blends," *Journal of the American Chemical Society*, vol. 130, pp. 7721–7735, May 2008.

[215] C. Poelking, M. Tietze, C. Elschner, S. Olthof, D. Hertel, B. Baumeier, F. Würthner, K. Meerholz, K. Leo, and D. Andrienko, "Impact of mesoscale order on open-circuit voltage in organic solar cells," *Nature Materials*, vol. 14, pp. 434–439, Dec 2014.

[216] C. Poelking and D. Andrienko, "Long-range embedding of molecular ions and ex-

citations in a polarizable molecular environment," *Journal of Chemical Theory and Computation*, vol. 12, pp. 4516–4523, Aug 2016.

[217] N. Ueno, "Tuning organic band structures with coulomb interactions," *Science*, vol. 352, pp. 1395–1396, Jun 2016.

[218] S. Verlaak, D. Beljonne, D. Cheyns, C. Rolin, M. Linares, F. Castet, J. Cornil, and P. Heremans, "Electronic structure and geminate pair energetics at organic-organic interfaces: The case of Pentacene/C60 heterojunctions," *Advanced Functional Materials*, vol. 19, pp. 3809–3814, Dec 2009.

[219] R. Warren, A. Privitera, P. Kaienburg, A. E. Lauritzen, O. Thimm, J. Nelson, and M. Riede, "Controlling energy levels and fermi level en route to fully tailored energetics in organic semiconductors," *Nature Communications*, vol. 10, Dec 2019.

[220] C. Schünemann, C. Elschner, A. Levin, M. Levichkova, K. Leo, and M. Riede, "Zinc phthalocyanine — influence of substrate temperature, film thickness, and kind of substrate on the morphology," *Thin Solid Films*, vol. 519, pp. 3939–3945, Mar. 2011.

[221] C. Schünemann, D. Wynands, K.-J. Eichhorn, M. Stamm, K. Leo, and M. Riede, "Evaluation and control of the orientation of small molecules for strongly absorbing organic thin films," *The Journal of Physical Chemistry C*, vol. 117, pp. 11600–11609, May 2013.

[222] W. Tress, "Open circuit voltage and IV curve shape of ZnPc:C60 solar cells with varied mixing ratio and hole transport layer," *Journal of Photonics for Energy*, vol. 1, p. 011114, Jan 2011.

[223] S. D. Dimitrov and J. R. Durrant, "Materials design considerations for charge generation in organic solar cells," *Chemistry of Materials*, vol. 26, pp. 616–630, Oct 2013.

[224] B. F. Wright, K. Sunahara, A. Furube, A. Nattestad, T. M. Clarke, G. C. Bazan, J. D. Azoulay, and A. J. Mozer, "Driving force dependence of electron transfer kinetics and yield in low-band-gap polymer donor-acceptor organic photovoltaic blends," *The Journal of Physical Chemistry C*, vol. 119, pp. 12829–12837, May 2015.

[225] Z. Huang, Y. Shi, Y. Chang, C. Yang, M. Lv, Y. Shen, Y. Liu, J. Zhang, K. Lu, and

Z. Wei, "Low nonradiative energy losses within 0.2 eV in efficient non-fullerene all-small-molecule organic solar cells," *Journal of Materials Chemistry C*, vol. 10, no. 7, pp. 2800–2806, 2022.

[226] S. Albrecht, K. Vandewal, J. R. Tumbleston, F. S. U. Fischer, J. D. Douglas, J. M. J. Fréchet, S. Ludwigs, H. Ade, A. Salleo, and D. Neher, "On the efficiency of charge transfer state splitting in polymer:fullerene solar cells," *Advanced Materials*, vol. 26, pp. 2533–2539, Feb 2014.

[227] T. Linderl, T. Zechel, A. Hofmann, T. Sato, K. Shimizu, H. Ishii, and W. Brütting, "Crystalline versus amorphous donor-acceptor blends: Influence of layer morphology on the charge-transfer density of states," *Physical Review Applied*, vol. 13, Feb 2020.

[228] P. Kaienburg, U. Rau, and T. Kirchartz, "Extracting information about the electronic quality of organic solar-cell absorbers from fill factor and thickness," *Physical Review Applied*, vol. 6, Aug 2016.

[229] T. L. Derrien, A. E. Lauritzen, P. Kaienburg, J. F. M. Hardigree, C. Nicklin, and M. Riede, "In situ observations of the growth mode of vacuum-deposited α-sexithiophene," *The Journal of Physical Chemistry C*, vol. 124, no. 22, pp. 11863–11869, 2020.

[230] Y. Dong, V. C. Nikolis, F. Talnack, Y.-C. Chin, J. Benduhn, G. Londi, J. Kublitski, X. Zheng, S. C. B. Mannsfeld, D. Spoltore, L. Muccioli, J. Li, X. Blase, D. Beljonne, J.-S. Kim, A. A. Bakulin, G. D'Avino, J. R. Durrant, and K. Vandewal, "Orientation dependent molecular electrostatics drives efficient charge generation in homojunction organic solar cells," *Nature Communications*, vol. 11, Sep 2020.

[231] M. Abbas and N. Tekin, "Balanced charge carrier mobilities in bulk heterojunction organic solar cells," *Applied Physics Letters*, vol. 101, p. 073302, Aug 2012.

[232] P. Müller-Buschbaum, "The active layer morphology of organic solar cells probed with grazing incidence scattering techniques," *Advanced Materials*, vol. 26, pp. 7692–7709, Feb 2014.

[233] Z. Peng, L. Ye, and H. Ade, "Understanding, quantifying, and controlling the molec-

ular ordering of semiconducting polymers: from novices to experts and amorphous to perfect crystals," *Materials Horizons*, vol. 9, no. 2, pp. 577–606, 2022.

[234] M. Abdelaal, M. H. Abdellatif, M. Riede, and G. Bassioni, "Studying the effect of high substrate temperature on the microstructure of vacuum evaporated TAPC:C60 organic solar thin films," *Materials*, vol. 14, p. 1733, Apr 2021.

[235] J. Nitta, K. Miwa, N. Komiya, E. Annese, J. Fujii, S. Ono, and K. Sakamoto, "The actual electronic band structure of a rubrene single crystal," *Scientific Reports*, vol. 9, Jul 2019.

[236] K. A. McGarry, W. Xie, C. Sutton, C. Risko, Y. Wu, V. G. Young, J.-L. Brédas, C. D. Frisbie, and C. J. Douglas, "Rubrene-based single-crystal organic semiconductors: Synthesis, electronic structure, and charge-transport properties," *Chemistry of Materials*, vol. 25, pp. 2254–2263, May 2013.

[237] S. de Fátima Curcino da Silva, D. A. Turchetti, E. M. Therézio, J. R. Tozoni, L. Akcelrud, and A. Marletta, "Temperature effect on the electron-vibrational mode coupling of a fully conjugated polyfluorene derivative," *Physical Chemistry Chemical Physics*, vol. 21, no. 30, pp. 16779–16784, 2019.

[238] M. A. Saidani, A. Benfredj, S. Romdhane, F. Kouki, and H. Bouchriha, "Role of intermolecular coupling and electron-nuclear coupling in the photophysics of oligothiophenes," *Physical Review B*, vol. 86, Oct 2012.

[239] A. L. Khan, M. J. Banach, and A. Köhler, "Control of beta-phase formation in polyfluorene thin films via Franck-Condon analysis," *Synthetic Metals*, vol. 139, pp. 905–907, Oct 2003.

[240] P. K. H. Ho, J.-S. Kim, N. Tessler, and R. H. Friend, "Photoluminescence of poly(p-phenylenevinylene)-silica nanocomposites: Evidence for dual emission by Franck-Condon analysis," *The Journal of Chemical Physics*, vol. 115, pp. 2709–2720, Aug 2001.

[241] X. Liu, K. Ding, A. Panda, and S. R. Forrest, "Charge transfer states in dilute donor-

acceptor blend organic heterojunctions," *ACS Nano*, vol. 10, pp. 7619–7626, Aug 2016.

[242] C. Kästner, K. Vandewal, D. A. M. Egbe, and H. Hoppe, "Revelation of interfacial energetics in organic multiheterojunctions," *Advanced Science*, vol. 4, p. 1600331, Dec 2016.

[243] G. O. N. Ndjawa, K. R. Graham, S. Mollinger, D. M. Wu, D. Hanifi, R. Prasanna, B. D. Rose, S. Dey, L. Yu, J.-L. Brédas, M. D. McGehee, A. Salleo, and A. Amassian, "Open-circuit voltage in organic solar cells: The impacts of donor semicrystallinity and coexistence of multiple interfacial charge-transfer bands," *Advanced Energy Materials*, vol. 7, p. 1601995, Jan 2017.

[244] A. K. Pandey, "Highly efficient spin-conversion effect leading to energy up-converted electroluminescence in singlet fission photovoltaics," *Scientific Reports*, vol. 5, Jan 2015.

[245] J. Yuan, Y. Zhang, L. Zhou, G. Zhang, H.-L. Yip, T.-K. Lau, X. Lu, C. Zhu, H. Peng, P. A. Johnson, M. Leclerc, Y. Cao, J. Ulanski, Y. Li, and Y. Zou, "Single-junction organic solar cell with over 15% efficiency using fused-ring acceptor with electron-deficient core," *Joule*, vol. 3, pp. 1140–1151, Apr 2019.

[246] M. Zhang, L. Zhu, G. Zhou, T. Hao, C. Qiu, Z. Zhao, Q. Hu, B. W. Larson, H. Zhu, Z. Ma, Z. Tang, W. Feng, Y. Zhang, T. P. Russell, and F. Liu, "Single-layered organic photovoltaics with double cascading charge transport pathways: 18% efficiencies," *Nature Communications*, vol. 12, Jan 2021.

[247] J. Wu, J. Lee, Y.-C. Chin, H. Yao, H. Cha, J. Luke, J. Hou, J.-S. Kim, and J. R. Durrant, "Exceptionally low charge trapping enables highly efficient organic bulk heterojunction solar cells," *Energy & Environmental Science*, vol. 13, no. 8, pp. 2422–2430, 2020.

[248] N. R. Tummala, Z. Zheng, S. G. Aziz, V. Coropceanu, and J.-L. Brédas, "Static and dynamic energetic disorders in the C60, PC61BM, C70, and PC71BM fullerenes," *The Journal of Physical Chemistry Letters*, vol. 6, pp. 3657–3662, Sep 2015.

[249] G. Kupgan, X.-K. Chen, and J.-L. Brédas, "Low energetic disorder in small-molecule non-fullerene electron acceptors," *ACS Materials Letters*, vol. 1, pp. 350–353, Aug 2019.

[250] Z. Jia, Z. Chen, X. Chen, L. Bai, H. Zhu, and Y. M. Yang, "Understanding of the nearly linear tunable open-circuit voltages in ternary organic solar cells based on two non-fullerene acceptors," *The Journal of Physical Chemistry Letters*, vol. 12, pp. 151–156, Dec 2020.

[251] T. L. Derrien, A. E. Lauritzen, P. Kaienburg, E. Hancox, C. Nicklin, and M. Riede, "Interfacial rearrangements and strain evolution in the thin film growth of ZnPc on glass," *Physical Review Materials*, vol. 6, Mar 2022.

[252] A. Barbon, M. Brustolon, and E. E. van Faassen, "Photoexcited spin triplet states in zinc phthalocyanine studied by transient EPR," *Physical Chemistry Chemical Physics*, vol. 3, pp. 5342–5347, Nov 2001.

[253] S. Richert, C. E. Tait, and C. R. Timmel, "Delocalisation of photoexcited triplet states probed by transient EPR and hyperfine spectroscopy," *Journal of Magnetic Resonance*, vol. 280, pp. 103–116, Jul 2017.

[254] T. Biskup, "Structure-function relationship of organic semiconductors: Detailed insights from time-resolved EPR spectroscopy," *Frontiers in Chemistry*, vol. 7, Feb 2019.

[255] F. Yang, K. Sun, and S. R. Forrest, "Efficient solar cells using all-organic nanocrystalline networks," *Advanced Materials*, vol. 19, pp. 4166–4171, Dec 2007.

[256] R. Fitzner, E. Mena-Osteritz, A. Mishra, G. Schulz, E. Reinold, M. Weil, C. Körner, H. Ziehlke, C. Elschner, K. Leo, M. Riede, M. Pfeiffer, C. Uhrich, and P. Bäuerle, "Correlation of π-conjugated oligomer structure with film morphology and organic solar cell performance," *Journal of the American Chemical Society*, vol. 134, pp. 11064–11067, Jun 2012.

A | Appendix

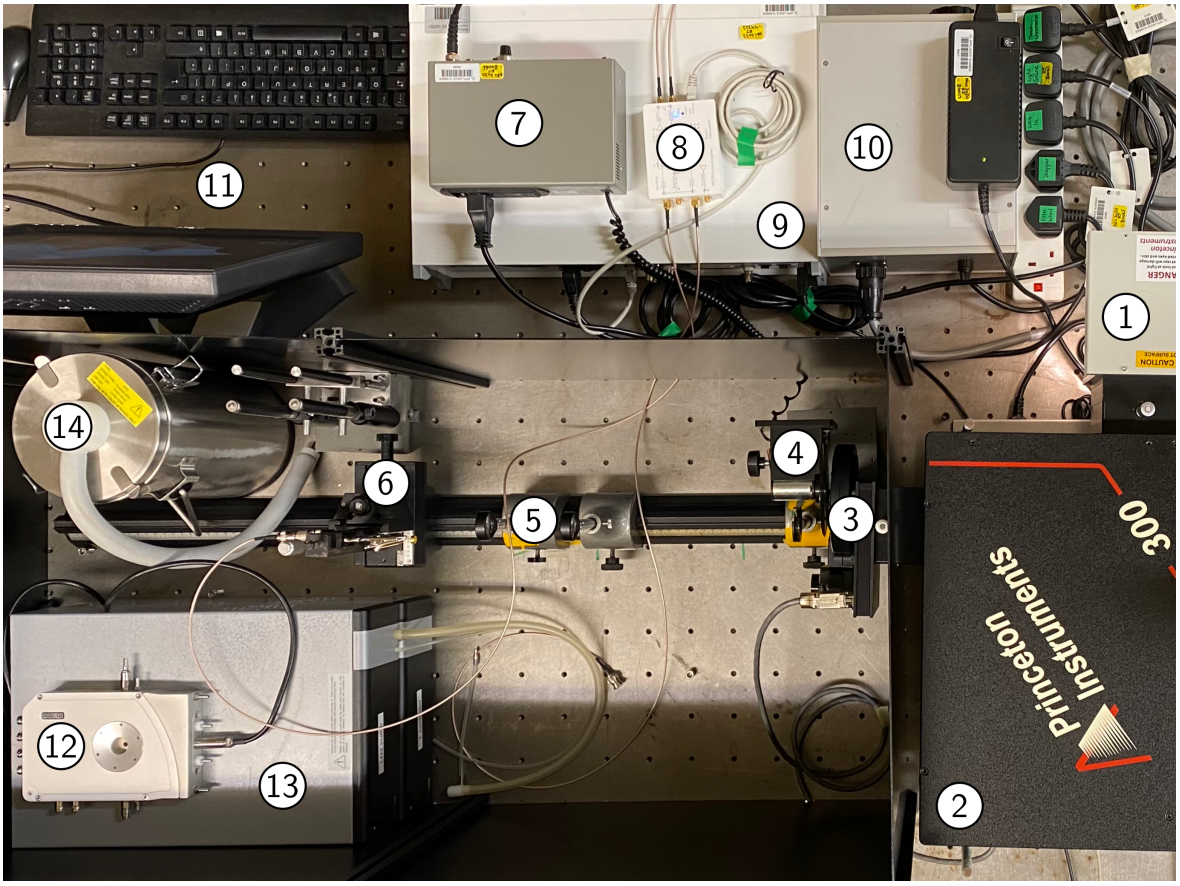


Figure A.1: Photo of the custom-built sensitive EQE setup used in this work. The individual components are numbered as (1) tungsten-halogen light source, (2) monochromator, (3) filter wheels, (4) chopper wheel, (5) focusing lenses, (6) sample holder, (7) chopper wheel power supply, (8) preamplifier, (9) Lock-In amplifier, (10) light source power supply, (11) measurement computer, (12) cryostat for temperature-dependence measurements, (13) temperature controller and liquid nitrogen pump, (14) liquid nitrogen dewar.

B | Appendix

B.1 GIWAXS Analysis

Grazing incidence wide-angle X-ray scattering (GIWAXS) was carried out by Andreas E. Lauritzen and Dr. Thomas Derrien to characterize the microstructure and crystallinity of neat F_xZnPc films and dilute donor F_xZnPc:C_{60} blends. Figure B.1 shows the 2D reciprocal space maps of the investigated systems.

All neat films show crystalline features, in particular a strong out-of-plane peak indexed as the (200) peak, in line with previous work [251]. This indicates that the preferential orientation of the F_xZnPc molecules is with their long axis aligned roughly parallel to the out-of-plane axis direction. The peak broadening along the azimuthal angle is observed for all neat films and indicates a significant spread in the orientation of crystalline domains. At least one in-plane scattering feature attributed to the $\pi - \pi$ stacking (010) peak is also seen, along with a secondary in-plane scattering feature for neat ZnPc. Increased fluorination is concomitant with increased spacing along the long axis stacking direction. F_8ZnPc and F_{16}ZnPc show a decreased $\pi - \pi$ stacking d-spacing compared to ZnPc and F_4ZnPc.

The low-donor films show no crystalline features attributable to C_{60} and only faint (200) scattering features around the out-of-plane direction. The lack of scattering from C_{60}, which is the dominant molecular species in the blended films, indicates that the presence of the F_xZnPc interrupts C_{60} packing in all cases. Thus, at low donor content, all donor molecules are surrounded by acceptors and donor aggregation is largely suppressed.

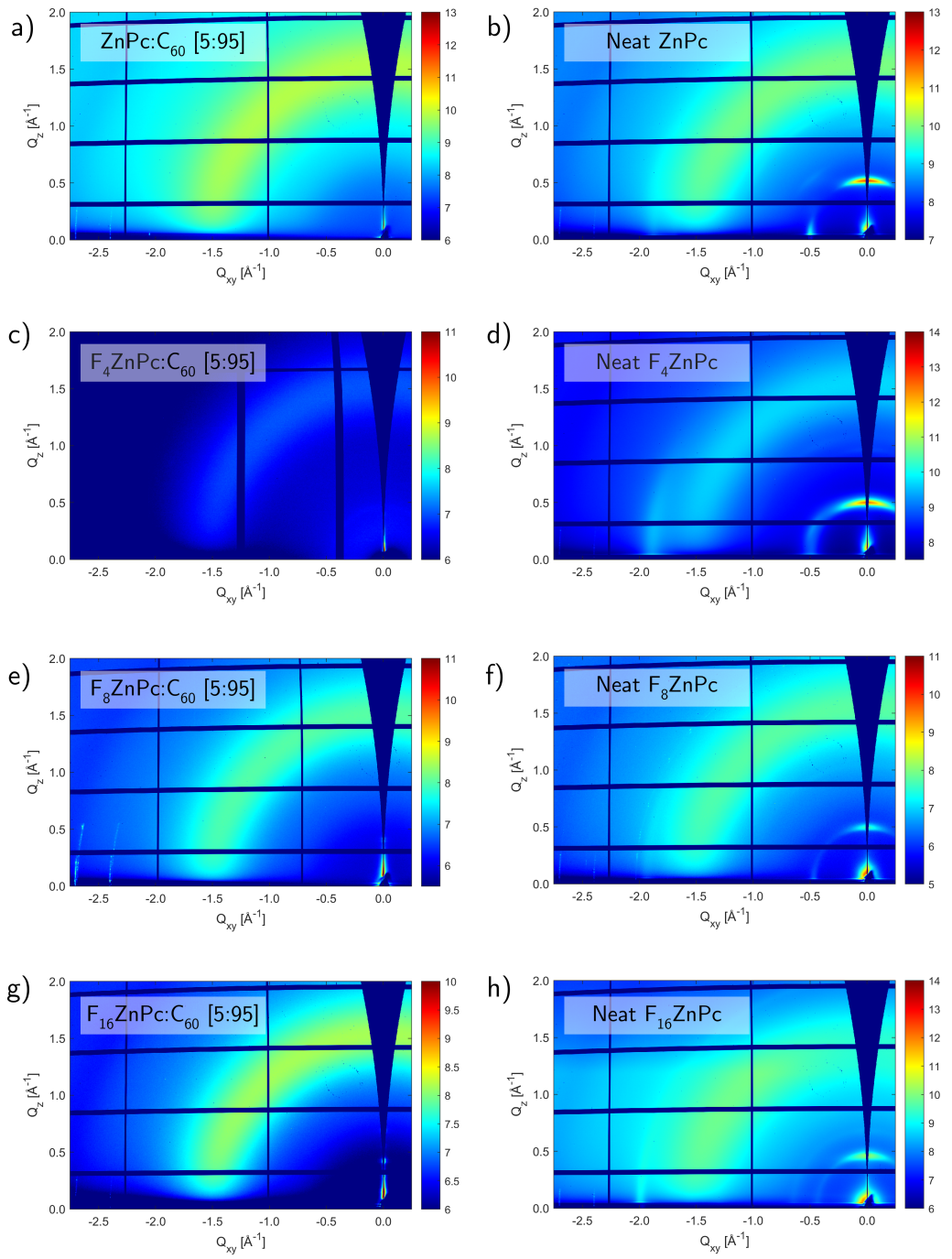


Figure B.1: 2D GIWAXS reciprocal space maps of 50 nm thin film samples on quartz. The first column shows scattering of the dilute $F_xZnPc:C_{60}$ blends, the second column shows scattering of neat donor films. The primary out-of-plane peak is indexed as the (200) peak and the primary in-plane peak is indexed as the (010) peak. The GIWAXS measurements and analysis were performed by Andreas E. Lauritzen and Dr. Thomas Derrien.

B.2 DFT Calculations

Table B.1: Calculated singlet and triplet energies of isolated ZnPc:C_{60} complexes as a function of dielectric constant (ε). The DFT calculations were performed by Dr. Veaceslav Coropceanu and Dr. Eunkyung Cho.

State	**[eV]**	**ε=2**	**ε=3**	**ε=3.5**	**ε=4**
S1	CT	1.46	1.36	1.32	1.30
S2	CT	1.46	1.36	1.32	1.30
S3	CT	1.53	1.41	1.37	1.34
S4	LE-C_{60}	2.22	2.15	2.13	2.12
S5	LE-C_{60}	2.23	2.16	2.14	2.13
S6	LE-C_{60}	2.23	2.17	2.15	2.14
S7	LE-C_{60}	2.23	2.17	2.15	2.14
S8	LE-C_{60}	2.24	2.18	2.16	2.15
S9	LE-C_{60}	2.25	2.19	2.17	2.15
S10	LE-C_{60}	2.25	2.19	2.17	2.16
S11	LE-C_{60}	2.26	2.20	2.18	2.17
S12	LE-C_{60}	2.26	2.21	2.20	2.18
S13	LE-C_{60}	2.27	2.21	2.19	2.19
S14	LE-ZnPc	2.27	2.25	2.25	2.25
S15	LE-ZnPc	2.27	2.26	2.25	2.25
T1	LE-ZnPc	1.21	1.21	1.21	1.20
T2	LE-ZnPc	1.22	1.23	1.23	1.22
T3	CT	1.47	1.38	1.35	1.34
T4	CT	1.50	1.40	1.37	1.34
T5	CT	1.53	1.41	1.39	1.38
T6	LE-C_{60}	1.82	1.79	1.78	1.77
T7	LE-C_{60}	1.83	1.79	1.78	1.78
T8	LE-C_{60}	1.83	1.80	1.79	1.78
T9	LE-C_{60}	2.05	1.99	1.98	1.97
T10	LE-C_{60}	2.05	1.99	1.98	1.97

Table B.2: Calculated singlet and triplet energies of isolated F_4ZnPc:C_{60} complexes as a function of dielectric constant (ε). The DFT calculations were performed by Dr. Veaceslav Coropceanu and Dr. Eunkyung Cho.

State	**[eV]**	**ε=2**	**ε=3**	**ε=3.5**	**ε=4**
S1	CT	1.50	1.39	1.36	1.34
S2	CT	1.50	1.39	1.36	1.34
S3	CT	1.57	1.45	1.41	1.39
S4	LE-C_{60}	2.21	2.16	2.14	2.12
S5	LE-C_{60}	2.22	2.16	2.14	2.13
S6	LE-C_{60}	2.22	2.17	2.15	2.14
S7	LE-C_{60}	2.23	2.17	2.15	2.14
S8	LE-C_{60}	2.23	2.18	2.16	2.15
S9	LE-C_{60}	2.23	2.19	2.17	2.16
S10	LE-C_{60}	2.25	2.19	2.17	2.16
S11	LE-C_{60}	2.25	2.20	2.18	2.17
S12	LE-C_{60}	2.25	2.21	2.19	2.18
S13	LE-C_{60}	2.26	2.21	2.19	2.18
S14	LE-F_4ZnPc	2.27	2.21	2.20	2.20
S15	LE-F_4ZnPc	2.27	2.22	2.21	2.21
T1	LE-F_4ZnPc	1.20	1.20	1.20	1.20
T2	LE-F_4ZnPc	1.20	1.21	1.21	1.21
T3	CT	1.50	1.41	1.38	1.36
T4	CT	1.54	1.44	1.41	1.38
T5	CT	1.57	1.44	1.42	1.40
T6	LE-C_{60}	1.83	1.79	1.78	1.77
T7	LE-C_{60}	1.83	1.79	1.78	1.78
T8	LE-C_{60}	1.83	1.80	1.79	1.78
T9	LE-C_{60}	2.05	2.00	1.98	1.97
T10	LE-C_{60}	2.05	2.00	1.98	1.97

Table B.3: Calculated singlet and triplet energies of isolated F_8ZnPc:C_{60} complexes as a function of dielectric constant (ε). The DFT calculations were performed by Dr. Veaceslav Coropceanu and Dr. Eunkyung Cho.

State	**[eV]**	**ε=2**	**ε=3**	**ε=3.5**	**ε=4**
S1	CT	1.61	1.52	1.49	1.47
S2	CT	1.62	1.52	1.49	1.47
S3	CT	1.70	1.58	1.55	1.52
S4	LE-C_{60}	2.21	2.15	2.13	2.12
S5	LE-C_{60}	2.22	2.16	2.14	2.13
S6	LE-C_{60}	2.22	2.16	2.14	2.13
S7	LE-C_{60}	2.22	2.16	2.15	2.13
S8	LE-C_{60}	2.24	2.18	2.17	2.15
S9	LE-C_{60}	2.24	2.19	2.17	2.16
S10	LE-C_{60}	2.25	2.19	2.17	2.16
S11	LE-C_{60}	2.25	2.19	2.18	2.17
S12	LE-C_{60}	2.26	2.21	2.19	2.18
S13	LE-C_{60}	2.26	2.21	2.19	2.18
S14	LE-F_8ZnPc	2.27	2.27	2.27	2.27
S15	LE-F_8ZnPc	2.29	2.28	2.27	2.27
T1	LE-F_8ZnPc	1.24	1.25	1.25	1.25
T2	LE-F_8ZnPc	1.25	1.26	1.26	1.27
T3	CT	1.62	1.52	1.50	1.48
T4	CT	1.65	1.56	1.53	1.51
T5	CT	1.69	1.58	1.54	1.52
T6	LE-C_{60}	1.82	1.79	1.78	1.77
T7	LE-C_{60}	1.83	1.79	1.78	1.78
T8	LE-C_{60}	1.83	1.79	1.78	1.78
T9	LE-C_{60}	2.04	1.99	1.98	1.97
T10	LE-C_{60}	2.04	1.99	1.98	1.97

Table B.4: Calculated singlet and triplet energies of isolated F_{16}ZnPc:C_{60} complexes as a function of dielectric constant (ε). The DFT calculations were performed by Dr. Veaceslav Coropceanu and Dr. Eunkyung Cho.

State	**[eV]**	**ε=2**	**ε=3**	**ε=3.5**	**ε=4**
S1	CT	1.60	1.50	1.47	1.45
S2	CT	1.60	1.51	1.48	1.46
S3	CT	1.70	1.58	1.55	1.52
S4	LE-F_{16}ZnPc	2.16	2.14	2.13	2.12
S5	LE-F_{16}ZnPc	2.18	2.15	2.13	2.12
S6	LE-C_{60}	2.20	2.15	2.14	2.13
S7	LE-C_{60}	2.20	2.16	2.14	2.13
S8	LE-C_{60}	2.21	2.16	2.15	2.14
S9	LE-C_{60}	2.21	2.17	2.17	2.16
S10	LE-C_{60}	2.24	2.18	2.17	2.16
S11	LE-C_{60}	2.24	2.19	2.17	2.16
S12	LE-C_{60}	2.24	2.19	2.18	2.16
S13	LE-C_{60}	2.25	2.19	2.18	2.17
S14	LE-C_{60}	2.25	2.20	2.19	2.17
S15	LE-C_{60}	2.25	2.20	2.19	2.17
T1	LE-F_{16}ZnPc	1.18	1.18	1.19	1.19
T2	LE-F_{16}ZnPc	1.18	1.19	1.19	1.19
T3	CT	1.60	1.51	1.48	1.46
T4	CT	1.64	1.54	1.52	1.49
T5	CT	1.69	1.57	1.54	1.51
T6	LE-C_{60}	1.82	1.79	1.78	1.77
T7	LE-C_{60}	1.82	1.79	1.78	1.77
T8	LE-C_{60}	1.82	1.79	1.78	1.78
T9	LE-C_{60}	2.03	1.98	1.97	1.96
T10	LE-C_{60}	2.03	1.99	1.97	1.96

Table B.5: Calculated LUMO and HOMO energies for isolated F_xZnPc and C_{60} molecules as a function of dielectric constant (ε). The DFT calculations were performed by Dr. Veaceslav Coropceanu and Dr. Eunkyung Cho.

	ε	**ZnPc**	**F_4ZnPc**	**F_8ZnPc**	**F_{16}ZnPc**	**C_{60}**
LUMO	2	-2.43	-2.63	-2.92	-3.25	-2.95
	3	-2.65	-2.85	-3.13	-3.45	-3.19
	3.5	-2.71	-2.91	-3.19	-3.51	-3.25
	4	-2.76	-2.95	-3.23	-3.55	-3.30
HOMO	2	-5.41	-5.54	-5.90	-6.06	-6.61
	3	-5.20	-5.34	-5.69	-5.86	-6.36
	3.5	-5.14	-5.28	-5.64	-5.80	-6.29
	4	-5.10	-5.23	-5.59	-5.76	-6.23

Table B.6: DFT calculations of transition dipole moments between LE singlet and GS states (μ_{LE-GS}), difference between the dipole moments of CT and GS states ($\Delta\mu_{CT-GS}$), and electronic coupling between CT and ground states (V_{CT-GS}), and between CT and LE states (V_{CT-LE}) for isolated F_xZnPc:C_{60} complexes using a two-state approach. The DFT calculations were performed by Dr. Veaceslav Coropceanu and Dr. Eunkyung Cho.

	ZnPc:C_{60}	**F_4ZnPc:C_{60}**	**F_8ZnPc:C_{60}**	**F_{16}ZnPc:C_{60}**
μ_{LE-GS} / D	6.48	6.53	6.58	7.47
$\Delta\mu_{CT-GS}$ / D	22.9	22.1	21.8	20.3
V_{CT-GS} / eV	65	75	84	101
V_{CT-LE} / eV	165	102	144	116

Table B.7: Parameters used for the three-state vibronic fits of the EQE spectra of dilute ZnPc:C_{60} and F_4ZnPc:C_{60}: CT and LE energies (E_{CT} and E_{LE}), energy difference between LE and CT states (ΔE_{LE-CT}), transition dipole moments of LE states (μ_{LE-GS}), state dipole moments of CT states (μ_{CT}), electronic coupling between CT and ground states (V_{CT-GS}), and between CT and LE states (V_{LE-CT}), frequencies of low and high energy vibrational modes (LF and HF), and vibronic coupling constants (g) corresponding to LE or CT states for the LF or HF vibrational mode. The parameters marked with an asterisk are fixed during the fitting process. All other parameters are fitted. The three-state vibronic fits were performed by Dr. Veaceslav Coropceanu and Dr. Eunkyung Cho.

	ZnPc:C_{60}	**F_4ZnPc:C_{60}**
E_{CT} / eV	1.38	1.45
E_{LE} / eV	1.69	1.65
ΔE_{LE-CT} / eV	0.31	0.20
*μ_{LE-GS} / D	6.48	6.53
*μ_{CT} / D	22.9	22.1
*V_{CT-GS} / eV	0.065	0.075
V_{LE-CT} / eV	0.090	0.081
*LF / cm^{-1}	100	100
*HF / cm^{-1}	1200	1200
g_{LF}^{LE}	2.74	2.74
g_{HF}^{LE}	0.56	0.56
g_{LF}^{CT}	4.18	5.00
g_{HF}^{CT}	0.85	1.02

B.3 EPR Analysis

Dr. Alberto Privitera carried out trEPR at 80 K by using 532 nm laser excitation on the neat donor films (Figure B.2). All spectra show two main species: (1) a spectrally narrow signal in neat absorption or emission around 345 mT, which can be attributed to photogenerated free charges, and (2) a broad signal ranging from about 320 to 370 mT which can be attributed to local F_xZnPc triplet states. The weak signal of the photogenerated charges highlights that charges are generated following laser excitation. Even without an acceptor molecule, the neat films show weak but appreciable photoactivity. The best-fit simulation values are reported in Table B.8 and discussed in the following.

A comparison of our results for neat ZnPc with those reported by Barbon et al. for ZnPc powder highlights a lower D value in our film [252]. Since, in first approximation, the D value is inversely proportional to the cubed delocalization r of the triplet state ($\mathrm{D} \sim r^{-3}$) [253], a lower D value suggests that triplet excitons are slightly more delocalized in our blends. This is probably due to the defined stacking and preferential ordering of the evaporated ZnPc layer, which favors exciton delocalization [206]. A partial ordering is also suggested by the preferential ordering parameter that needs to be included in the simulation [254]. Regarding the F_xZnPc films, their D values are larger ($505 - 535$ MHz) than for non-fluorinated ZnPc (387 MHz). This might suggest a lower delocalization of triplet states to neighboring molecules, possibly due to the presence of bulky fluorine atoms which hinder intermolecular exciton delocalization.

Notably, the spin-populations of the triplet sublevels show that in all neat donor films the triplet states are typical for inter-system crossing (ISC) triplets. This result can be rationalized considering that in the neat films most of the singlet excitons do not dissociate and undergo ISC before recombining to the ground state [65], [254]. Only the F_8ZnPc film shows a contribution of a geminate BET triplet in addition to ISC. This suggests that after weak photogeneration, some charges geminately recombine to low-lying triplet states in this blend. This process is energetically favorable since the triplet state is energetically located below the CT state. The same behavior is also observed for films of pure $PC_{60}BM$ or $PC_{70}BM$ and, while unique among the investigated F_xZnPc materials, not unusual.

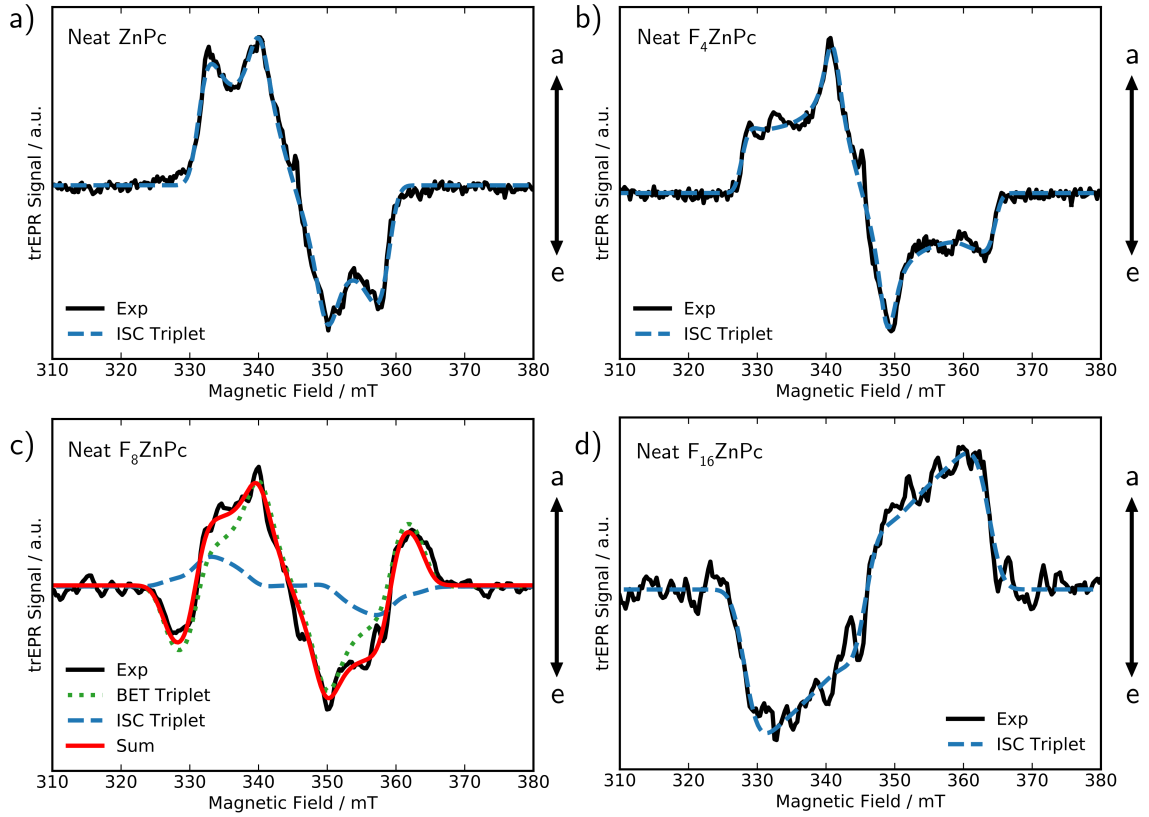


Figure B.2: Time-resolved EPR spectra (black line) and best-fit simulations (red line) of neat F_xZnPc films. The trEPR spectra were recorded at 80 K after a 532 nm laser pulse (integration window $0.8 - 1.2$ s). Absorption (a) is up, and emission (e) is down. All spectra show two main species: (1) a narrow signal in neat absorption or emission centered around 345 mT which can be attributed to photogenerated charges and (2) a broad signal ranging from about 320 to 370 mT which can be attributed to triplet states. In the case of neat ZnPc, F_4ZnPc, and F_{16}ZnPc, triplet states are populated through inter-system crossing (ISC) while neat F_8ZnPc shows both an inter-system crossing and a back electron transfer (BET) contribution. The values of the best-fit simulations are reported in Table B.8.The trEPR measurements and analysis were performed by Dr. Alberto Privitera.

Table B.8: Best-fit values obtained for the trEPR spectra of neat F_xZnPc films. For each film, the populating mechanism of the triplet states and the ZFS parameters are reported. The zero-field splitting (ZFS) parameters are given in absolute value units of MHz. ISC populations order (p_1, p_2, p_3) is from low-to-high energy zero-field states. Only Lorentzian broadening was considered for both ISC and BET triplets to not over-parameterize the fitting; the linewidth is reported in units of mT. The relative weight of ISC and BET triplets is also reported. Finally, for the simulations of ISC triplets of ZnPc and F_4ZnPc a preferential ordering contribution is needed, which suggests preferential ordering of the crystallites with respect to the substrate. The trEPR measurements and analysis were performed by Dr. Alberto Privitera.

	Triplet Species	**[D E] / MHz**	**[p_1, p_2, p_3]**	**LW_{ISC} / mT**	**[p_{-1}, p_0, p_{+1}]**	**LW_{BET} / mT**	**$weight_{ISC}$:$weight_{BET}$**	**Order**
ZnPc	ISC	[387 36]	[0.48 0.19 0.33]	2.52			1:0	0.64
F_4ZnPc	ISC	[516 97]	[0.45 0.21 0.33]	1.9			1:0	0.09
F_8ZnPc	ISC+BET	[535 87]	[0.46 0.47 0.07]	3.4	[1 0 1]	3.2	0.22:0.78	
F_{16}ZnPc	ISC	[505 150]	[0.25 0.38 0.36]	3.5			1:0	

Table B.9: Best-fit values obtained for the trEPR spectra of the dilute F_xZnPc:C_{60} blends. For each film, the populating mechanism of the triplet states and the zero-field splitting (ZFS) parameters are reported. The ZFS parameters are given in absolute value units of MHz. From the ZFS parameters, we can assign all observed triplets to the donor (D) as no acceptor (A) triplet signals were found for the blends. ISC populations order (p_1, p_2, p_3) is from low-to-high energy zero-field states. BET populations show a lower population of the p_0 level with respect to p_{-1} and p_{+1}. Only Lorentzian broadening was considered for both ISC and BET triplets to not over-parameterize the fitting; the linewidth is reported in units of mT. The relative weight of ISC and BET triplets is also reported. The trEPR measurements and analysis were performed by Dr. Alberto Privitera.

	Triplet Species	**[D E] / MHz**	**[p_1, p_2, p_3]**	**LW_{ISC} / mT**	**[p_{-1}, p_0, p_{+1}]**	**LW_{BET} / mT**	**$weight_{ISC}$:$weight_{BET}$**
ZnPc:C_{60}	BET	[583 107]			[1 0 1]	3.7	0:1
F_4ZnPc:C_{60}	ISC+BET	[646 108]	[0.20 0.38 0.42]	2.2	[1 0 1]	2.3	0.46:0.54
F_8ZnPc:C_{60}	ISC+BET	[670 112]	[0.7 0.05 0.26]	4	[1 0 1]	3.9	0.48:0.52
F_{16}ZnPc:C_{60}	ISC+BET	[592 115]	[0.58 0.14 0.28]	3.7	[1 0 1]	2.6	0.79:0.21

C | Appendix

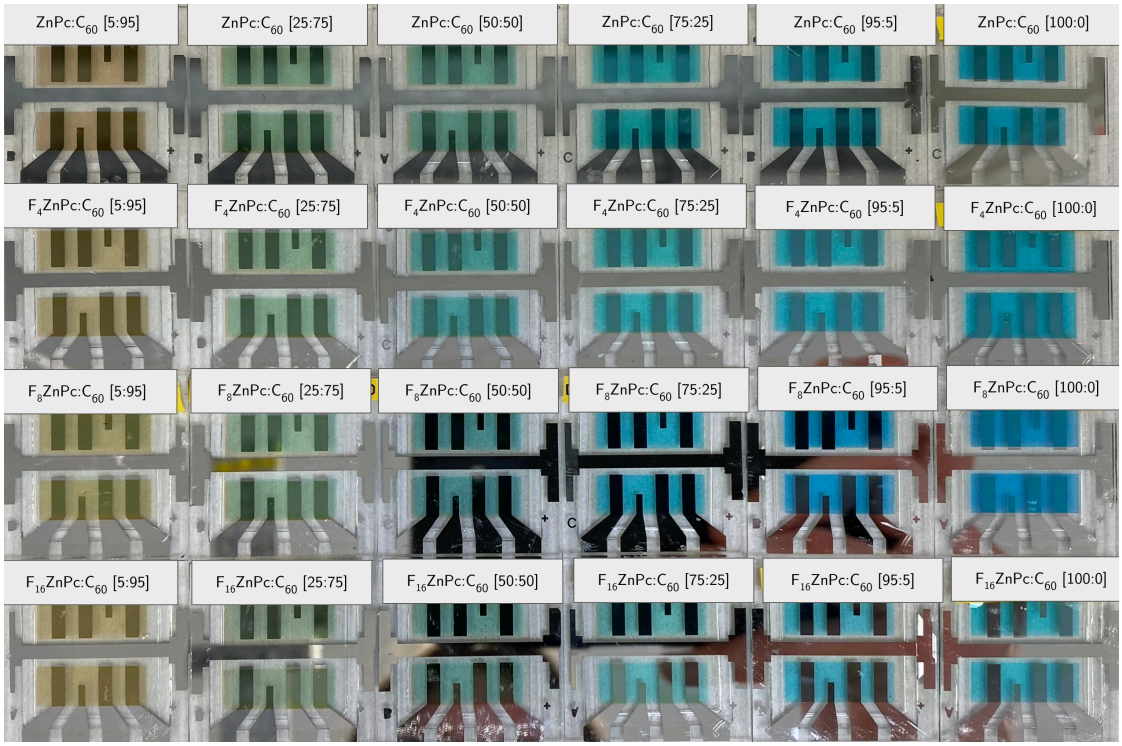


Figure C.1: Photo of the $F_xZnPc:C_{60}$ samples studied in the Chapter 7.

Table C.1: Current density-voltage ($J-V$) characteristics, CT state energies (E_{CT}) and donor singlet energies (E_{S_1}) of the F_xZnPc:C_{60} concentration series. The $J-V$ behavior was measured under 1 Sun illumination and at room temperature. The last column indicates how many devices were measured to determine the $J-V$ performance statistics. The data was not mismatch corrected. E_{S_1} and E_{CT} were fit from the EQE using classical Marcus theory as outlined in Chapter 5.

Material Blend	J_{SC} / mA/cm^{-2}	V_{OC} / V	FF	E_{CT} / eV	E_{S_1} / eV	#
C_{60}	0.86 ± 0.16	1.25 ± 0.09	0.30 ± 0.01			30
ZnPc:C_{60} [5:95]	3.61 ± 0.14	0.76 ± 0.01	0.39 ± 0.01	1.38 ± 0.01	1.68 ± 0.01	3
ZnPc:C_{60} [25:75]	6.46 ± 0.41	0.50 ± 0.06	0.50 ± 0.03	1.23 ± 0.01	1.56 ± 0.02	6
ZnPc:C_{60} [50:50]	5.90 ± 0.21	0.46 ± 0.03	0.50 ± 0.01	1.21 ± 0.01	1.53 ± 0.01	11
ZnPc:C_{60} [75:25]	4.96 ± 0.01	0.50 ± 0.00	0.39 ± 0.01	1.21 ± 0.01	1.50 ± 0.01	1
ZnPc:C_{60} [95:5]	1.36 ± 0.06	0.60 ± 0.00	0.26 ± 0.00	1.22 ± 0.01	1.52 ± 0.01	6
ZnPc:C_{60} [100:0]	0.43 ± 0.03	0.74 ± 0.08	0.37 ± 0.00	1.38 ± 0.01	1.55 ± 0.01	5
F_4ZnPc:C_{60} [5:95]	3.07 ± 0.19	0.88 ± 0.02	0.33 ± 0.01	1.45 ± 0.01	1.59 ± 0.01	29
F_4ZnPc:C_{60} [25:75]	6.28 ± 0.19	0.76 ± 0.00	0.49 ± 0.00	1.40 ± 0.01	1.49 ± 0.01	15
F_4ZnPc:C_{60} [50:50]	6.72 ± 0.27	0.73 ± 0.01	0.49 ± 0.02	1.41 ± 0.01	1.52 ± 0.04	7
F_4ZnPc:C_{60} [75:25]	4.46 ± 0.17	0.74 ± 0.01	0.39 ± 0.01	1.36 ± 0.01	1.51 ± 0.02	9
F_4ZnPc:C_{60} [95:5]	1.04 ± 0.03	0.76 ± 0.01	0.26 ± 0.00	1.40 ± 0.01	1.54 ± 0.01	5
F_4ZnPc:C_{60} [100:0]	0.05 ± 0.00	0.79 ± 0.01	0.27 ± 0.01	1.41 ± 0.01	1.56 ± 0.01	20
F_8ZnPc:C_{60} [5:95]	1.02 ± 0.05	1.13 ± 0.03	0.30 ± 0.00	1.59 ± 0.01	1.73 ± 0.01	12
F_8ZnPc:C_{60} [25:75]	0.46 ± 0.05	1.09 ± 0.01	0.27 ± 0.00	1.58 ± 0.01	1.72 ± 0.02	15
F_8ZnPc:C_{60} [50:50]	0.19 ± 0.02	1.00 ± 0.02	0.27 ± 0.01	1.55 ± 0.01	1.70 ± 0.06	14
F_8ZnPc:C_{60} [75:25]	0.07 ± 0.01	0.89 ± 0.01	0.30 ± 0.01	1.48 ± 0.01	1.63 ± 0.01	4
F_8ZnPc:C_{60} [95:5]	0.28 ± 0.04	0.72 ± 0.03	0.29 ± 0.01	1.43 ± 0.01	1.57 ± 0.01	15
F_8ZnPc:C_{60} [100:0]	0.57 ± 0.07	0.65 ± 0.02	0.31 ± 0.01	1.42 ± 0.01	1.57 ± 0.01	14
F_{16}ZnPc:C_{60} [5:95]	0.82 ± 0.05	1.21 ± 0.02	0.29 ± 0.00	1.61 ± 0.01	1.71 ± 0.01	15
F_{16}ZnPc:C_{60} [25:75]	0.50 ± 0.02	0.81 ± 0.06	0.22 ± 0.01	1.48 ± 0.01	1.67 ± 0.01	4
F_{16}ZnPc:C_{60} [50:50]	0.51 ± 0.15	0.73 ± 0.05	0.26 ± 0.01	1.46 ± 0.01	1.62 ± 0.01	11
F_{16}ZnPc:C_{60} [75:25]	0.28 ± 0.02	0.57 ± 0.04	0.36 ± 0.01	1.37 ± 0.01	1.49 ± 0.01	11
F_{16}ZnPc:C_{60} [95:5]	0.35 ± 0.07	0.35 ± 0.01	0.27 ± 0.05	1.38 ± 0.01	1.48 ± 0.01	2
F_{16}ZnPc:C_{60} [100:0]	0.63 ± 0.07	0.33 ± 0.03	0.37 ± 0.02	1.40 ± 0.01	1.48 ± 0.01	17

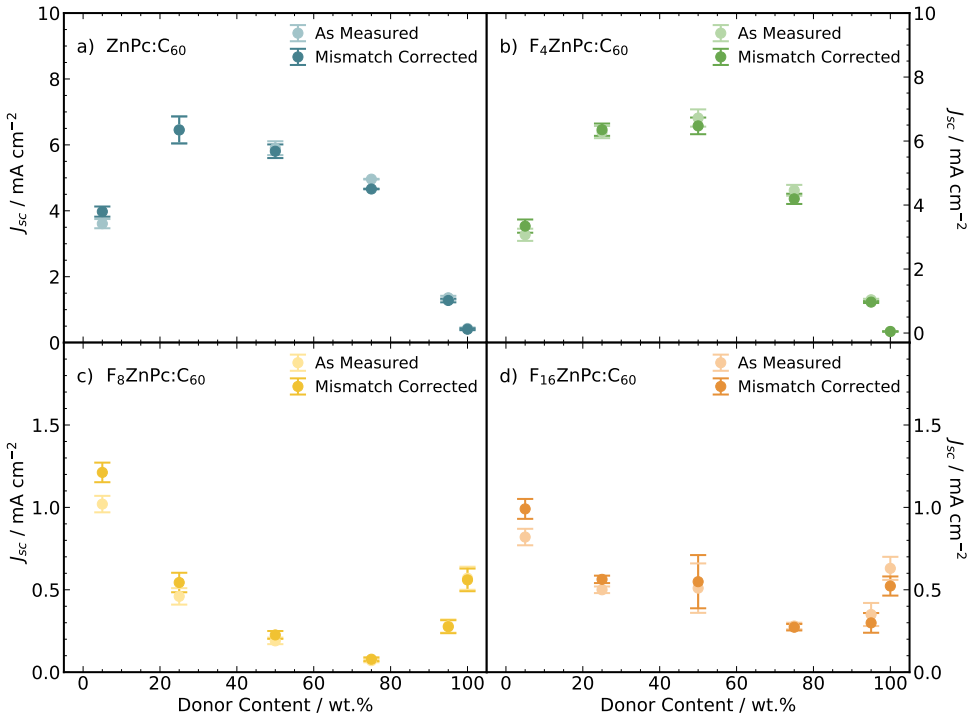


Figure C.2: Comparison of the short-circuit current density (J_{sc}) of the $F_xZnPc:C_{60}$ blends as measured and after spectral mismatch correction.

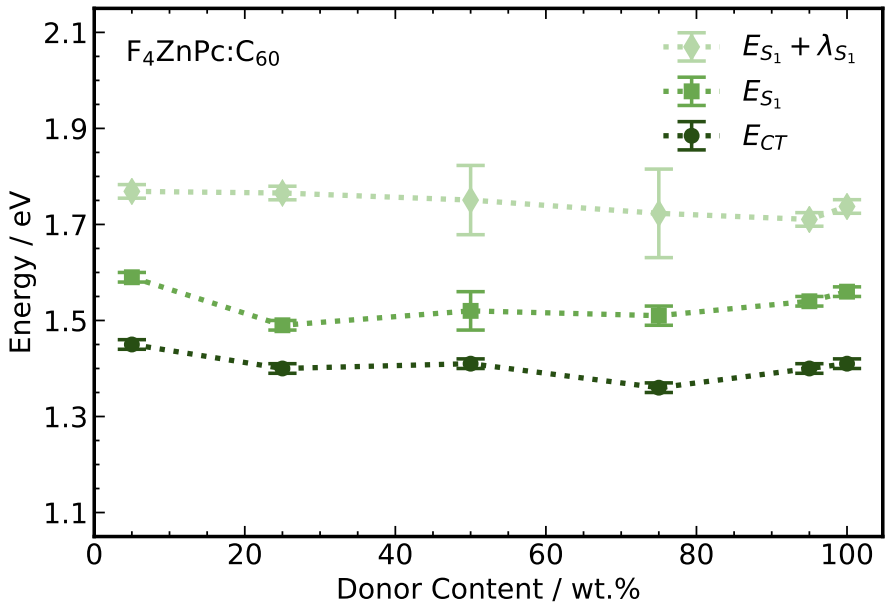


Figure C.3: CT state energy (E_{CT}) and donor singlet energy (E_{S1}) as a function of $F_4ZnPc:C_{60}$ mixing ratio. E_{CT} and E_{S1} were both fit from the EQE using classical Marcus theory as outlined in Chapter 5. For comparison, the sum of E_{S1} and the reorganization energy (λ_{S_1}) of the $S_0 \rightarrow S_1$ transition is shown.

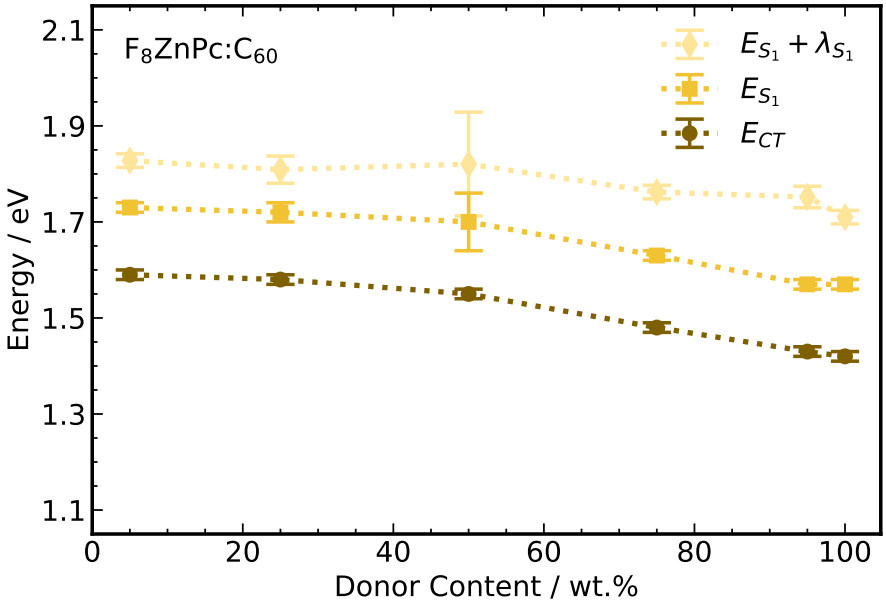


Figure C.4: CT state energy (E_{CT}) and donor singlet energy (E_{S1}) as a function of F_8ZnPc:C_{60} mixing ratio. E_{CT} and E_{S1} were both fit from the EQE using classical Marcus theory as outlined in Chapter 5. For comparison, the sum of E_{S1} and the reorganization energy (λ_{S_1}) of the $S_0 \rightarrow S_1$ transition is shown.

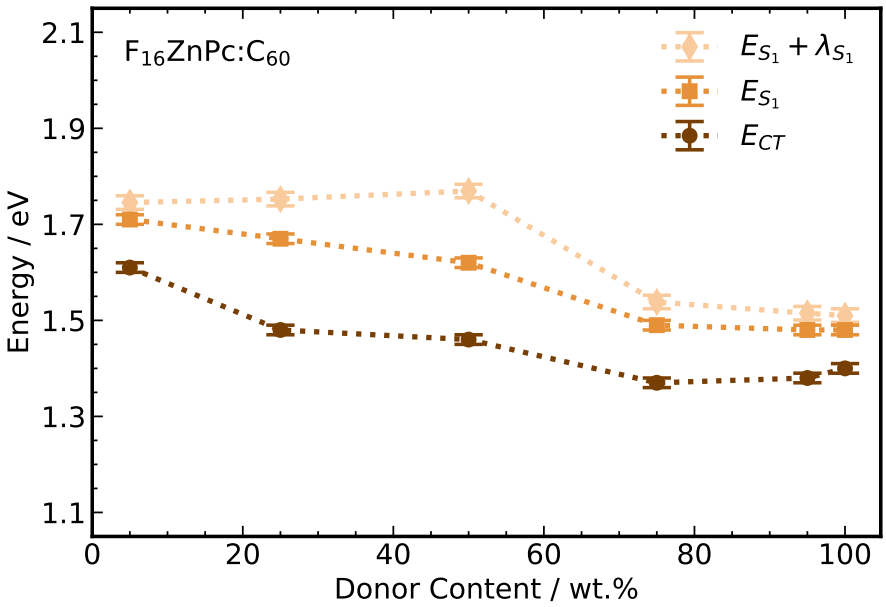


Figure C.5: CT state energy (E_{CT}) and donor singlet energy (E_{S1}) as a function of F_{16}ZnPc:C_{60} mixing ratio. E_{CT} and E_{S1} were both fit from the EQE using classical Marcus theory as outlined in Chapter 5. For comparison, the sum of E_{S1} and the reorganization energy (λ_{S_1}) of the $S_0 \rightarrow S_1$ transition is shown.

D | Appendix



Figure D.1: Photo of the disorder samples studied in the Chapter 8.

Table D.1: Electronic quality (Q) [228] and Scharber efficiency (η_{Sch}) [210] for different donor:C_{60} blends. The values were either calculated for this work by Dr. Pascal Kaienburg or reproduced with permission under the Creative Commons License from reference [2]. The last column indicates the original source of the device data.

Material Blend	**Thickness / nm**	Q / $cm^{1.6}V^{-2}s^{1.2}$	η_{Sch} / %	**Reference**
α-6T:C_{60} [1:1]	50	0.13	6.3	this work
CuPc:C_{60} [1:1]	50	0.17	6.6	this work
CuPc:C_{60}	38	0.77	6.3	[255]
DCV5T:C_{60} [2:1]	50	0.04	10.1	[2]
DCV5T:C_{60} [2:1]	30 2:1	0.1	10.5	[256]
TAPC:C_{60} [1:19]	60	0.26	1	[49]
DTDCPB:C_{60} [2:1]	50	0.16	11.1	[2]
DTDCPB:C_{60} [2:1]	135	0.51	11.2	[2]
HB194:C_{60} [2:1]	50	0.07	9.2	[2]
HB194:C_{60} [2:1]	100	0.09	8.7	[2]
F_4ZnPc:C_{60} [2:1]	50	0.16	10	[2]
F_4ZnPc:C_{60} [2:1]	100	0.94	10.6	[2]
ZnPc:C_{60} [2:1]	50	0.26	6.4	[2]
ZnPc:C_{60} [2:1]	100	1.18	6.9	[2]

Table D.2: Current density-voltage ($J-V$) characteristics, CT state energies (E_{CT}), donor singlet energies (E_{S_1}), CT state reorganization energies (λ_{CT}), and static disorder (σ_S) of the donor:C_{60} devices studied in Chapter 8. The $J-V$ behavior was measured under simulated 1 Sun illumination and at room temperature. The last column indicates how many devices were measured to determine the $J-V$ performance statistics. The data was not mismatch corrected. E_{S_1} (E_{CT}) was fit from the EQE using classical Marcus (semi-classical MLJ) theory as outlined in Chapter 5. λ_{CT} and σ_S were determined via the temperature dependence of the EQE linewidth as outlined in Chapter 8.

Material Blend	J_{SC} / mA/cm^{-2}	V_{OC} / V	FF	E_{CT} / eV	E_{S_1} / eV	λ_{CT} / eV	σ_S / eV	#
TAPC:C_{60} [5:95]	4.46 ± 0.34	0.92 ± 0.02	0.55 ± 0.02	1.46 ± 0.04	1.78 ± 0.01	0.090 ± 0.003	0.061 ± 0.001	12
TAPC:C_{60} [50:50]	0.48 ± 0.05	0.74 ± 0.03	0.23 ± 0.07	1.45 ± 0.01	1.70 ± 0.01	0.097 ± 0.008	0.074 ± 0.002	18
TAPC:C_{60} [95:5]	0.00 ± 0.00	0.83 ± 0.09	0.20 ± 0.02	1.54 ± 0.02	1.78 ± 0.00	0.094 ± 0.004	0.065 ± 0.002	3
α-6T:C_{60} [5:95]	4.16 ± 0.22	0.93 ± 0.01	0.45 ± 0.06	1.54 ± 0.05	1.78 ± 0.00	0.029 ± 0.002	0.108 ± 0.000	11
α-6T:C_{60} [50:50]	2.74 ± 0.18	0.46 ± 0.00	0.42 ± 0.01	1.12 ± 0.09	1.45 ± 0.02	0.075 ± 0.009	0.115 ± 0.002	13
α-6T:C_{60} [95:5]	0.18 ± 0.02	0.54 ± 0.01	0.17 ± 0.01	1.37 ± 0.18	1.29 ± 0.05	0.057 ± 0.005	0.132 ± 0.001	11
CuPc:C_{60} [5:95]	1.09 ± 0.05	0.74 ± 0.02	0.30 ± 0.01	1.44 ± 0.09	1.69 ± 0.01	0.056 ± 0.004	0.101 ± 0.001	21
CuPc:C_{60} [50:50]	7.43 ± 0.35	0.48 ± 0.00	0.38 ± 0.02	1.19 ± 0.05	1.5 ± 0.00	0.068 ± 0.007	0.099 ± 0.001	18
CuPc:C_{60} [95:5]	0.91 ± 0.03	0.56 ± 0.02	0.26 ± 0.00	1.28 ± 0.12	1.56 ± 0.00	0.110 ± 0.021	0.104 ± 0.005	12
Rubrene:C_{60} [5:95]	2.55 ± 0.18	0.99 ± 0.01	0.30 ± 0.00	1.48 ± 0.04	1.79 ± 0.00	0.029 ± 0.006	0.053 ± 0.003	11
Rubrene:C_{60} [50:50]	1.10 ± 0.07	0.78 ± 0.03	0.23 ± 0.00	1.49 ± 0.03	1.62 ± 0.00	0.029 ± 0.000	0.067 ± 0.000	10
Rubrene:C_{60} [95:5]	0.02 ± 0.00	1.20 ± 0.13	0.18 ± 0.02	1.54 ± 0.02	2.23 ± 0.00	0.013 ± 0.006	0.092 ± 0.002	8
DCV5T:C_{60} [5:95]	2.84 ± 0.08	0.92 ± 0.02	0.27 ± 0.00	1.68 ± 0.00	1.79 ± 0.00	0.014 ± 0.002	0.043 ± 0.001	6
DCV5T:C_{60} [50:50]	8.71 ± 0.25	0.95 ± 0.03	0.38 ± 0.01	1.55 ± 0.03	1.74 ± 0.00	0.090 ± 0.003	0.091 ± 0.001	11
DCV5T:C_{60} [95:5]	0.46 ± 0.04	0.94 ± 0.01	0.15 ± 0.01	1.57 ± 0.02	1.71 ± 0.00	0.052 ± 0.005	0.039 ± 0.003	10

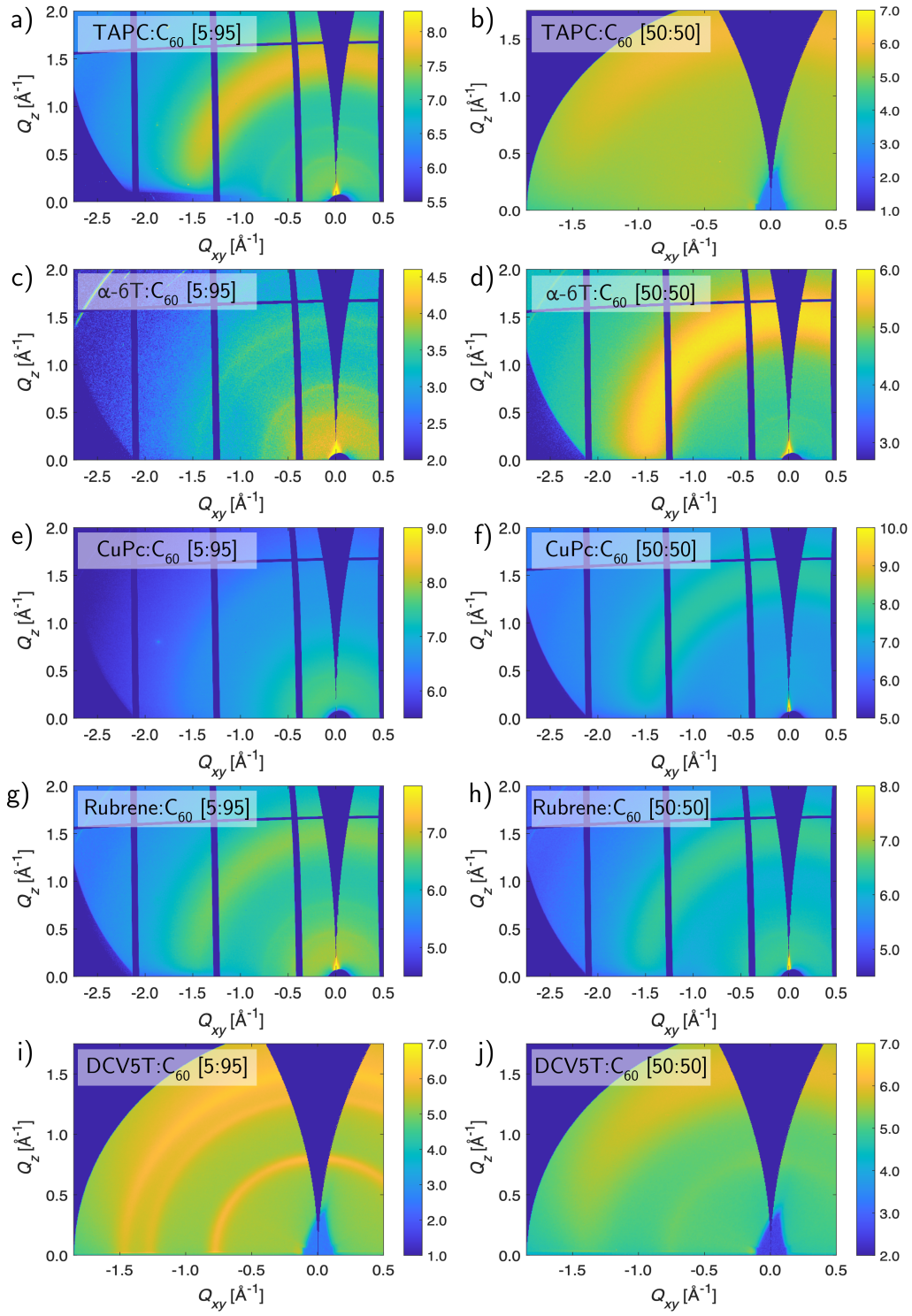


Figure D.2: 2D GIWAXS reciprocal space maps of 50 nm thin film samples on quartz. The first column shows scattering of the dilute donor:C_{60} blends, the second column shows scattering of intermixed donor:C_{60} films. The visual differences in the scattering maps arise because the samples were measured at two different beamtimes, as outlined in Chapter 4. The GIWAXS measurements were carried out by Andreas E. Lauritzen, Olivia Gough, and Irfan Habib, and the GIWAXS analysis was carried out by Andreas E. Lauritzen.

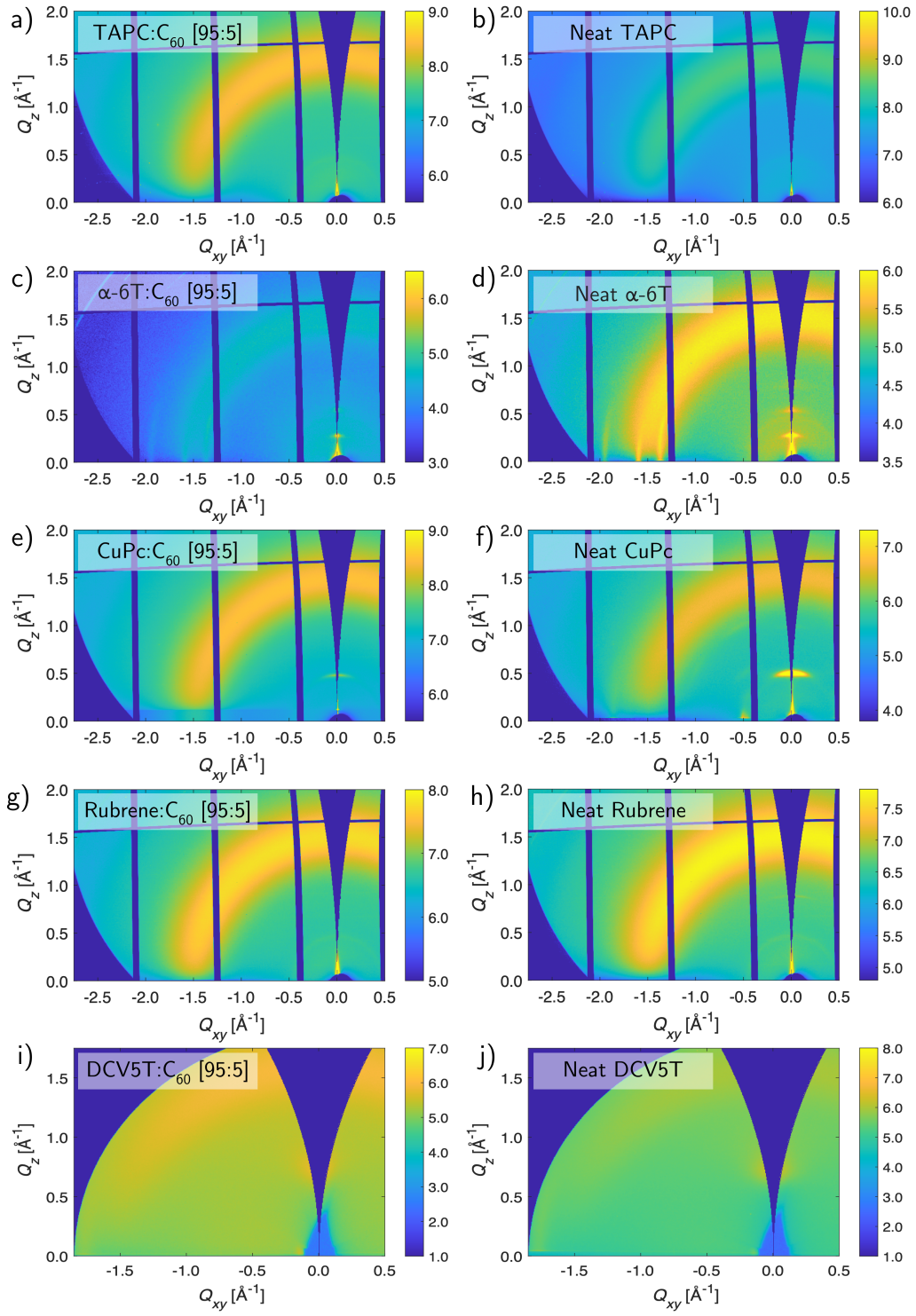


Figure D.3: 2D GIWAXS reciprocal space maps of 50 nm thin film samples on quartz. The first column shows scattering of the dilute acceptor blends, the second column shows scattering of neat donor films. The visual differences in the scattering maps arise because the samples were measured at two different beamtimes, as outlined in Chapter 4. The GIWAXS measurements were carried out by Andreas E. Lauritzen, Olivia Gough, and Irfan Habib, and the GIWAXS analysis was carried out by Andreas E. Lauritzen.

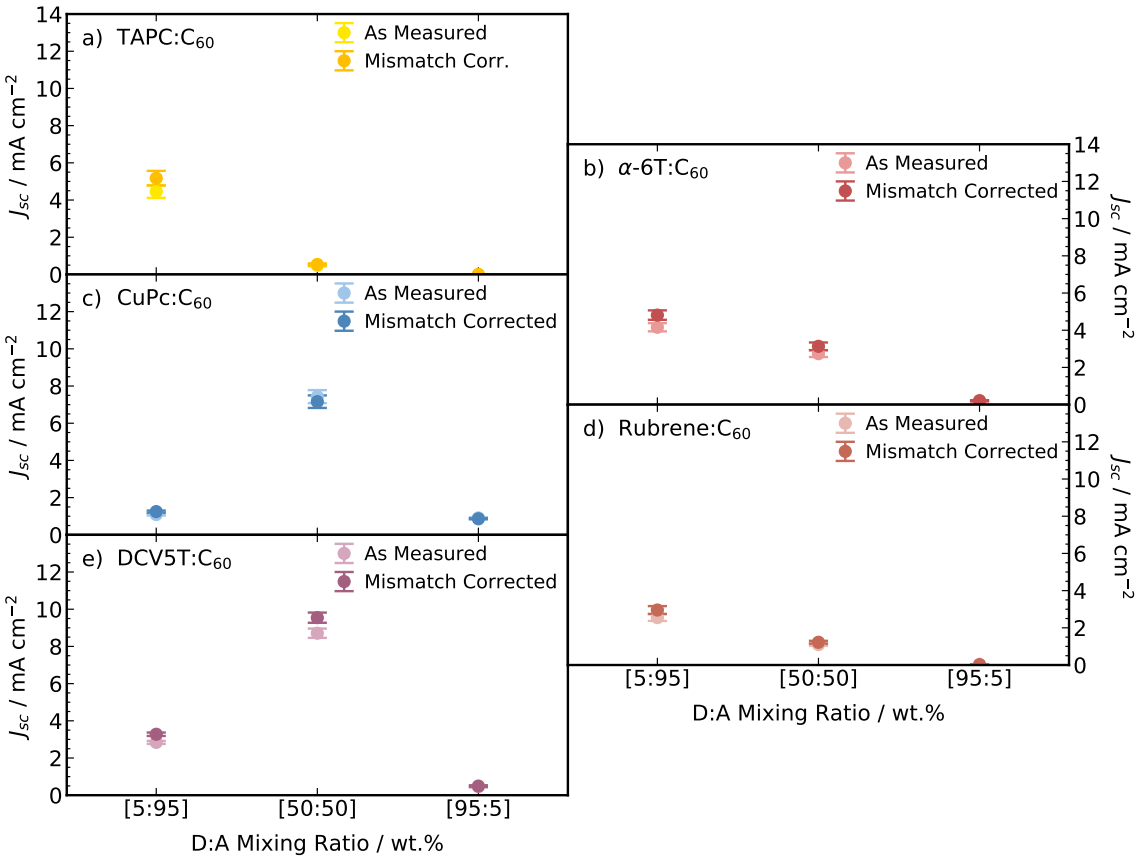


Figure D.4: Comparison of the short-circuit current density (J_{sc}) of the donor:C_{60} blends as measured and after spectral mismatch correction.

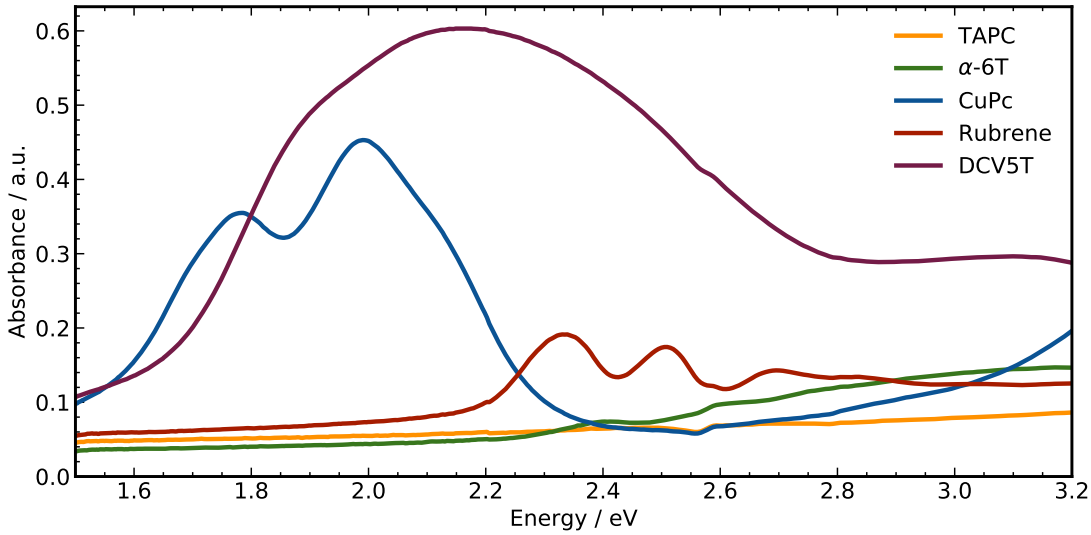


Figure D.5: Absorbance of neat films of the donor molecules studied in Chapter 8. All films consist of 50 nm thick layers deposited via vacuum thermal deposition on quartz substrates. The absorbance spectra were determined via UV-Vis-NIR measurements in transmission mode as outlined in Chapter 4.

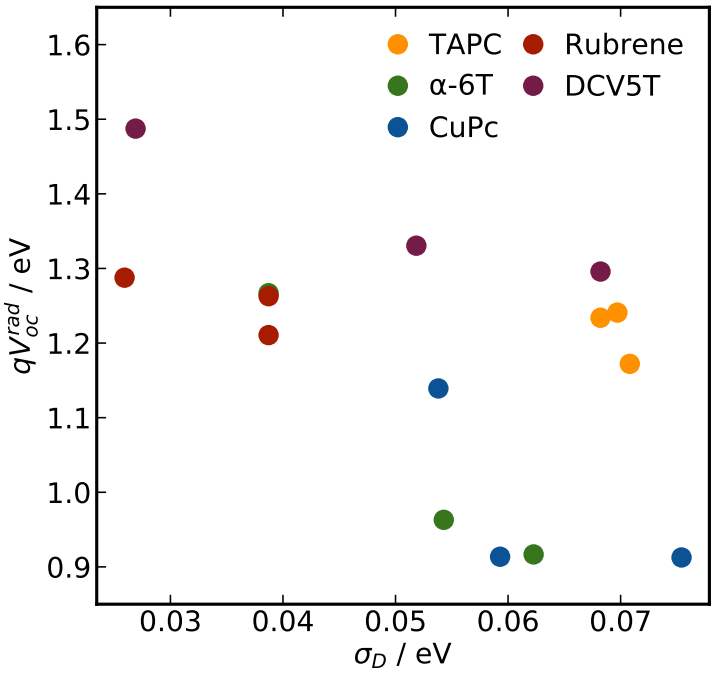


Figure D.6: Radiative limit (qV_{oc}^{rad}) as a function of dynamic disorder (σ_D) for all D:C_{60} blends studied in Chapter 8. Each donor system (encompassing different D:C_{60} mixing ratios) is shown with a different color. The dynamic disorder was calculated at 300 K.

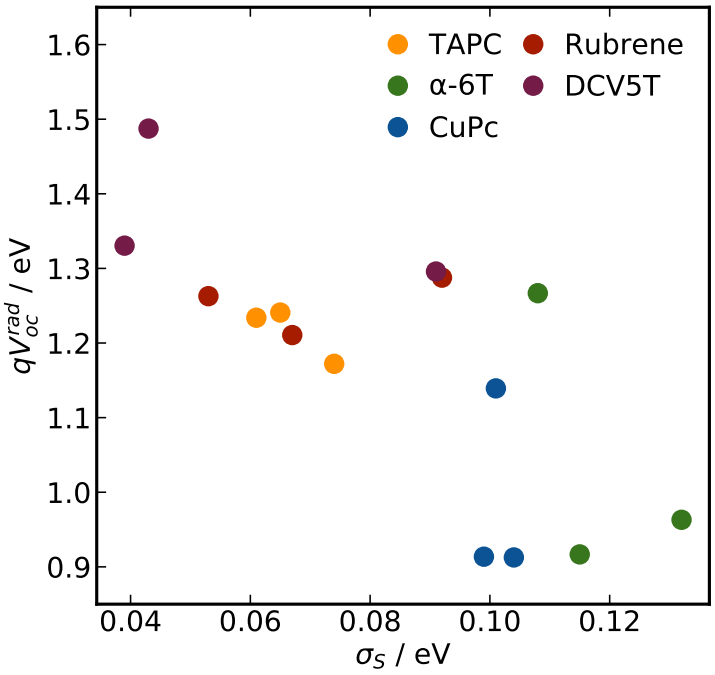


Figure D.7: Radiative limit (qV_{oc}^{rad}) as a function of static disorder (σ_S) for all D:C_{60} blends studied in Chapter 8. Each donor system (encompassing different D:C_{60} mixing ratios) is shown with a different color.

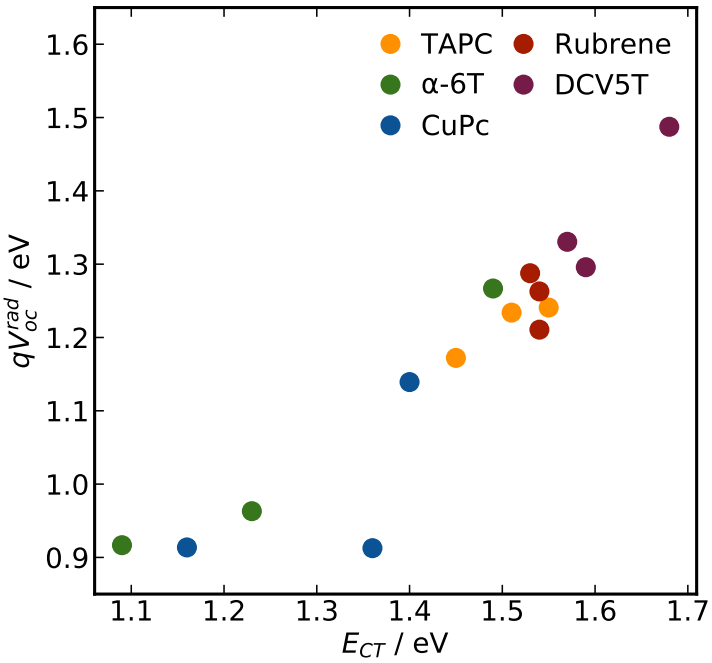


Figure D.8: Radiative limit (qV_{oc}^{rad}) as a function of the disorder corrected CT state energy (E_{CT}) for all D:C_{60} blends studied in Chapter 8. Each donor system (encompassing different D:C_{60} mixing ratios) is shown with a different color.